

# A Continuous-Wave Second Harmonic Gyrotron Oscillator at 460 GHz

by

Melissa Kristen Hornstein

B.S., Rutgers University (1999)

S.M., Massachusetts Institute of Technology (2001)

Submitted to the Department of Electrical Engineering and Computer  
Science

in partial fulfillment of the requirements for the degree of

Doctor of Philosophy

at the

MASSACHUSETTS INSTITUTE OF TECHNOLOGY

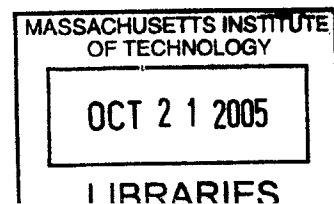
June 2005

© Massachusetts Institute of Technology 2005. All rights reserved.

Author .....  
Department of Electrical Engineering and Computer Science  
May 16, 2005

Certified by .....  
Richard J. Temkin  
Senior Research Scientist, Department of Physics  
Thesis Supervisor

Accepted by .....  
Arthur C. Smith  
Chairman, Department Committee on Graduate Students



ARCHIVES



# A Continuous-Wave Second Harmonic Gyrotron Oscillator at 460 GHz

by

Melissa Kristen Hornstein

Submitted to the Department of Electrical Engineering and Computer Science  
on May 16, 2005, in partial fulfillment of the  
requirements for the degree of  
Doctor of Philosophy

## Abstract

We report the short pulse and CW operation of a 460 GHz gyrotron oscillator both at the fundamental (near 230 GHz) and second harmonic (near 460 GHz) of electron cyclotron resonance. During operation in a complete CW regime with 12.4 kV beam voltage and 135 mA beam current, the gyrotron generates a record 8 W of power in the second harmonic  $TE_{0,6,1}$  mode at 458.6 GHz. Design at high frequency, second harmonic, and low beam power is challenging because the latter two involve lower gain than at fundamental modes and all three necessitate higher  $Q$  cavities. Under complete computer control, the gyrotron has stably operated continuously for over an hour near 460 GHz. Diagnostic radiation pattern measurements of the beam using an array of pyroelectric sensors show a bi-Gaussian beam with 4% ellipticity. Operation in the fundamental modes, including the  $TE_{0,3,1}$  mode at 237.91 GHz and the  $TE_{2,3,1}$  at 233.15 GHz, is observed at peak output powers up to 70 W. CW studies of the fundamental  $TE_{2,3}$  mode at low voltage reveal that the mode can be excited with less than 7 W of beam power at less than 3.5 kV. Further, we demonstrate broadband continuous frequency tuning of the fundamental modes of the oscillator over a range of more than 2 GHz through variation of the magnetic field alone. We interpret these results in terms of smooth transitions between higher order axial modes of the resonator.

In a related experiment, second harmonic (in addition to fundamental) operation of a nominally 250 GHz gyrotron oscillator was characterized to verify the possibility of second harmonic excitation at 460 GHz. The characterization experiments yielded results of extremely low second harmonic start oscillation currents, as low as 12 mA, and have been interpreted as an unintentionally high  $Q$  cavity. A computer-controlled stable CW source, the 250 GHz gyrotron was the first gyro-device specifically designed with the purpose of seamless integration into an NMR spectrometer. Under complete computer control, the gyrotron's operation for over 10 days has been observed, yielding a power stability of better than 1% and frequency stability of better than 400 Hz. Overmoded corrugated waveguide was designed and implemented to enable low loss quasi-Gaussian transmission. In conjunction with the corrugated waveguide, a quasi-optical directional coupler was designed and implemented to enable feedback

on the forward (and reflected) power to further stabilize the signal.

Radiation intensity patterns were compared using four techniques: thermal paper, liquid crystal paper, an array of pyroelectric sensors, and a mechanized scanner. The liquid crystalline technique was adapted from a technique employed in temperature measurements in electronic devices. Originally employed for use in diagnosing laser beams, we demonstrate the first use of a pyroelectric camera at millimeter frequencies.

A study of the overmoded microwave transmission and mode conversion system of a 140 GHz gyrotron oscillator, the first in a series of DNP gyrotrons, is also presented. The losses were characterized under a succession of iterative configurations for optimization of power transmission, including the design and implementation of a new  $TE_{0,1}$  to  $TE_{1,1}$  waveguide mode converter. The result of this study was a reduction of the total loss of the transmission system from nearly 9 dB to 4.5 dB.

In addition to becoming a milestone in high frequency second harmonic design, the successful completion of the 460 GHz gyrotron experiment will allow the highest field DNP experiments to date. The success of experiments on three gyrotron oscillators, at 460, 250, and 140 GHz makes an important contribution to the body of knowledge on the development of high frequency, CW, second harmonic, and low power gyrotrons.

Thesis Supervisor: Richard J. Temkin

Title: Senior Research Scientist, Department of Physics

## Acknowledgments

I would like to acknowledge my thesis supervisor Richard Temkin; my first supervisor Kenneth Kreischer for accepting me on to the project; Director of the Francis Bitter Magnet Laboratory Professor Robert Griffin; Vikram Bajaj of the Griffin Group for our many collaborations on DNP and gyrotrons at 250 and 460 GHz, teaching me about NMR and DNP; my thesis committee, Professors Qing Hu and Ronald Parker; Professor Jin Au Kong, my academic advisor; Ivan Mastovsky for the technical aspects of my experiment, including drawing and assembling the components of the tube, William Mulligan for electrical assistance including power supplies and the high voltage modulator; Paul Woskov (Associate Head, Plasma Technology and Systems Division) for our collaborations at 250 GHz; Michael Shapiro, Head of the Gyrotron Group, for theoretical assistance; Jeffrey Bryant, Ajay Thakkar, Ronald DeRocher, Peter Allen, and Michael Mullins of the Francis Bitter Magnet Laboratory for technical and machining assistance; Catherine Fiore and Amanda Hubbard of the Plasma Science and Fusion Center; Robert Childs for the use of his boroscope in troubleshooting my experiment and for his knowledge on vacuum systems and William Byford for electrical assistance, both of the Plasma Science and Fusion Center; John Machuzak, James Anderson, Jagadishwar Sirigiri, Stephen Korbly, and Jeffrey Vieregg of the Gyrotron Group; Melanie Rosay, Kan-Nian Hu, and Volker Weis of the Griffin Group; Alexander Vlasov of the University of Maryland and SAIC for elucidating MAGY.



# Contents

<b>1</b>	<b>Introduction</b>	<b>27</b>
1.1	Terahertz . . . . .	27
1.1.1	State-of-the-art . . . . .	27
1.1.2	Interactions with matter . . . . .	29
1.2	Cyclotron Resonance Masers . . . . .	30
1.2.1	Harmonic considerations . . . . .	31
1.2.2	History . . . . .	32
1.2.3	Operating Principles . . . . .	32
1.2.4	State-of-the-art . . . . .	33
1.3	Dynamic Nuclear Polarization . . . . .	34
1.4	Thesis Outline . . . . .	35
<b>2</b>	<b>Theory</b>	<b>37</b>
2.1	Introduction . . . . .	37
2.2	CRM Interaction . . . . .	38
2.2.1	Harmonic CRM Interaction . . . . .	40
2.3	Kinetic Theory . . . . .	42
2.3.1	Linearized Dispersion Relation . . . . .	43
2.4	Single-Particle Theory . . . . .	46
2.4.1	Start Oscillation Current . . . . .	49
2.4.2	Ohmic Losses . . . . .	50
2.5	Quantum Mechanical Basis of the Cyclotron Resonance Maser . . . . .	51
2.6	Waveguide Theory . . . . .	55
2.7	Numerical Methods . . . . .	57
2.7.1	Cold Cavity . . . . .	58
2.7.2	Starting Current Calculation Including Beam Effects . . . . .	60
2.7.3	MAGY . . . . .	61
2.7.4	EGUN . . . . .	63
2.8	Sensitivity-Enhanced Nuclear Magnetic Resonance . . . . .	64

2.8.1	Chemical Shift . . . . .	65
2.8.2	Nuclear Magnetic Resonance in the Solid State . . . . .	66
2.8.3	Dynamic Nuclear Polarization . . . . .	67
2.9	Discussion . . . . .	68
<b>3</b>	<b>Experimental Setup and Diagnostics</b>	<b>69</b>
3.1	Diagnostics . . . . .	69
3.1.1	High Frequency Detection . . . . .	69
3.1.2	Power Measurement . . . . .	73
3.1.3	Radiation Pattern Measurement . . . . .	75
3.1.4	Time-Domain Signal Measurement . . . . .	77
3.1.5	Vacuum Diagnostics . . . . .	79
3.1.6	Thermal Load Measurement . . . . .	83
3.1.7	Small-Signal Detection . . . . .	85
3.1.8	Cold Test . . . . .	86
3.2	Equipment . . . . .	87
3.2.1	Pulsed Equipment . . . . .	87
3.2.2	CW Equipment . . . . .	90
<b>4</b>	<b>Design of a 460 GHz Second Harmonic Gyrotron Oscillator</b>	<b>91</b>
4.1	Target Specifications . . . . .	91
4.1.1	Dynamic Nuclear Polarization . . . . .	91
4.2	Second Harmonic Considerations . . . . .	95
4.2.1	Mode Competition . . . . .	95
4.2.2	Start Oscillation Current . . . . .	97
4.2.3	Ohmic Losses . . . . .	99
4.3	Components . . . . .	100
4.3.1	Electron Gun . . . . .	100
4.3.2	Magnet System . . . . .	106
4.3.3	Interaction Structure . . . . .	111
4.3.4	Quasi-Optical Mode Converter . . . . .	112
4.3.5	Vacuum System . . . . .	114
4.3.6	Vacuum Output Window . . . . .	115
4.3.7	Collector . . . . .	116
4.4	Control System . . . . .	118
4.4.1	Software . . . . .	118
4.4.2	Interlocks . . . . .	121
4.5	Discussion . . . . .	121



<b>5</b>	<b>460 GHz Second Harmonic Experiments</b>	<b>123</b>
5.1	Short Pulse Experiment [1] . . . . .	123
5.1.1	Mode Map . . . . .	125
5.1.2	Start Oscillation Current . . . . .	127
5.1.3	Second Harmonic . . . . .	130
5.1.4	Power in Fundamental $TE_{0,3}$ Mode . . . . .	132
5.1.5	Broadband Continuous Frequency Tuning . . . . .	136
5.2	CW Experiment . . . . .	141
5.2.1	Mode Map . . . . .	145
5.2.2	Second Harmonic . . . . .	146
5.2.3	Frequency Pulling . . . . .	147
5.2.4	Ohmic Losses . . . . .	149
5.2.5	Homodyne Measurements . . . . .	155
5.2.6	Low Voltage Fundamental $TE_{2,3}$ Mode . . . . .	156
5.2.7	Hollow Dielectric Waveguide . . . . .	161
5.2.8	Radiation Patterns . . . . .	167
5.2.9	Stability . . . . .	168
5.3	Low Power $Q$ Measurements of the 460 GHz Cavity . . . . .	169
5.4	Discussion . . . . .	174
<b>6</b>	<b>250 GHz Gyrotron Experiments</b>	<b>177</b>
6.1	Characterization of the 250 GHz Gyrotron . . . . .	178
6.1.1	$TE_{0,3}$ Operating Mode . . . . .	179
6.1.2	Frequency Pulling . . . . .	181
6.1.3	Radiation Patterns . . . . .	182
6.1.4	CW Long-term Stability and Control . . . . .	187
6.1.5	Linewidth . . . . .	188
6.2	Low Second Harmonic Starting Currents . . . . .	190
6.3	Corrugated Waveguide and Directional Coupler Experiment [2] . . . . .	200
6.3.1	Introduction . . . . .	200
6.3.2	Component Design . . . . .	201
6.3.3	Cold Tests . . . . .	207
6.3.4	Measurements with Gyrotron . . . . .	210
6.3.5	Conclusions . . . . .	214
6.4	Discussion . . . . .	215

<b>7</b>	<b>Transmission System of a 140 GHz Gyrotron Oscillator</b>	<b>217</b>
7.1	Two-Dimensional Radiation Pattern Measurements . . . . .	220
7.1.1	Gyrotron Radiation Pattern Measurements . . . . .	220
7.1.2	Old Mode Converter Radiation Pattern Measurements . . . . .	226
7.1.3	New Mode Converter Radiation Pattern Measurements . . . . .	229
7.2	Modifications to the 140 GHz Transmission System . . . . .	235
7.2.1	Design of a New $TE_{0,1}$ - $TE_{1,1}$ Waveguide Mode Converter . . . . .	235
7.2.2	Overmoded Miter Bend Near Probe . . . . .	238
7.2.3	Oblique Gyrotron Beam . . . . .	239
7.2.4	Beat . . . . .	240
7.2.5	Corrugated Waveguide . . . . .	240
7.2.6	Theoretical Transmission Line Losses . . . . .	242
7.2.7	Summary of Experimental Losses . . . . .	245
7.3	Summary and Discussion . . . . .	245
<b>8</b>	<b>Conclusions</b>	<b>249</b>
8.1	460 GHz Second Harmonic Gyrotron Oscillator . . . . .	249
8.2	250 GHz Gyrotron Oscillator Experiments . . . . .	250
8.3	140 GHz Gyrotron Oscillator Experiments . . . . .	251
8.4	Gyrotron Comparisons . . . . .	252
8.4.1	Frequency Pulling . . . . .	252
8.4.2	Radiation Patterns . . . . .	252
8.5	Future Work . . . . .	253

# List of Figures

1-1	State of the art in CW terahertz sources. . . . .	28
1-2	The interactions of the bands of the electromagnetic spectrum with matter. . . . .	29
1-3	(a) Typical gyrotron oscillator cavity with electron beam, (b) RF field profile with single axial maximum, (c) phase, and (d) applied DC magnetic field. . . . .	33
2-1	Simulation of a non-uniform electron phase distribution which occurs due to the interaction of a relativistic electron beam with a transverse electric field $E$ , situated in a static magnetic field $B_0$ . The beamlets, with Larmor radius $r_L$ , represent snapshots in phase space in both axial locations throughout the interaction structure (from $z = 0$ to $z = L$ ) and time [3]. . . . .	39
2-2	Cross-section of the beam geometry in the interaction region of a cylindrical resonant gyrotron cavity operating in the $TE_{0,n}$ mode for (a) initial random phasing of electrons in their cyclotron orbits (b) electrons bunched in phase in their cyclotron orbits. . . . .	40
2-3	Electron motion for resonance at (a) second and (b) third cyclotron harmonics. The solid line shows the initial trajectory of electrons and the electric field is represented by dashed lines. Adapted from [4]. . .	42
2-4	Dispersion diagram of a gyrotron oscillator showing the region of interaction between the fast waveguide mode and the beam cyclotron modes. (a) Fundamental beam cyclotron mode and waveguide mode intersect at fundamental resonance. The dots represent the longitudinal cavity modes. The intersection of the beam cyclotron modes with waveguide modes at negative values of $k_z$ causes the excitation of backward wave oscillations. (b) The intersection of the third harmonic of the cyclotron mode with the waveguide mode gives rise to a third harmonic interaction. . . . .	43

2-5	Cyclotron resonance for varying values of the parameter $k = \frac{n\hbar\Omega_c^2}{2\mu c^2}$ according to equation (2.84), where terms of order $(\hbar\Omega_c/m_0c)^2$ have been neglected. Note that a completely absorptive line is recovered in the non-relativistic limit. . . . .	54
2-6	Intensity patterns of the five lowest order transverse electric (TE) waveguide modes; (a) TE <sub>1,1</sub> , (b) TE <sub>2,1</sub> , (c) TE <sub>0,1</sub> , (d) TE <sub>3,1</sub> , and (e) TE <sub>4,1</sub> . . . . .	58
2-7	Operating frequency shift with reference frequency offset. The convergent solution is located at the origin. . . . .	61
3-1	Block diagram of a heterodyne receiver used as a millimeter and sub-millimeter wavelength frequency measurement system. . . . .	70
3-2	Insertion loss of the IF and LO from the diplexer (Pacific Millimeter Products, Model No. MD5, S/N 008). The IF band is flat from DC to 12 GHz and the LO band is flat over 20 to 40 GHz [5]. . . . .	71
3-3	Photograph of the frequency system, picturing the oscilloscope, frequency counter, and power supply on the right, and the local oscillator, amplifiers, and filter on the left (inside the boxes). The horn, mixer, and attenuator are not depicted. . . . .	71
3-4	Intermediate frequency signal for the second harmonic TE <sub>2,6,1</sub> mode at 456 GHz using the frequency measurement system. . . . .	72
3-5	Reflectivity of the laser calorimeter, as measured by a dispersive Fourier transform spectrometer [6, 7]. . . . .	73
3-6	Block diagram of near- and far-field scanner. . . . .	75
3-7	Typical time-domain diode signal of the TE <sub>0,3,1</sub> mode at the voltage and current shown in Figures 3-14 and 3-8 and 8.58 T. . . . .	77
3-8	Typical collector and body current signals using a Rogowski current monitor. The corresponding voltage pulse is shown in Fig. 3-14. The signal corresponds to the TE <sub>0,3,1</sub> mode at 8.58 T, and the diode trace shown in Figure 3-7. . . . .	78
3-9	Typical RGA traces at the end of a bakeout when the tube is at 100°C (top) and room temperature (bottom). . . . .	81
3-10	Relationship between the current drawn from 8 L/s Varian-style ion pumps operated at 3.5 kV and the vacuum pressure in Torr. . . . .	83
3-11	Thermistor resistance measuring circuit. . . . .	85
3-12	Far-field radiation scan of the cylindrical TE <sub>1,1</sub> output of the BWO at 41 cm. . . . .	86

3-13	Power drift over frequency of the BWO. . . . .	87
3-14	Typical voltage pulse from the high voltage modulator. The corresponding current trace is shown in Fig. 3-8. The signal corresponds to the TE <sub>0,3,1</sub> mode at 8.58 T, and the diode trace shown in Figure 3-7. . . . .	88
3-15	Calibration of the cathode voltage readout. . . . .	88
3-16	Photograph of (a) the front end of the high voltage modulator (b) the CW gyrotron console, showing the cryogenic temperature monitors, liquid cryogen level monitor, ion pump controllers, CW switching high voltage power supply, gun coil power supply, computer controls, and superconducting magnet power supply. . . . .	89
4-1	(a) Photograph of the gyrotron tube free-standing (b) Cross-sectional schematic of the cylindrically symmetric 460 GHz gyrotron tube, not shown to scale, indicating key components. . . . .	92
4-2	Photograph of the author and the 460 GHz gyrotron located in the bore of the superconducting magnet. . . . .	93
4-3	Chart of the TE mode indices up to to $\nu_{mp} = 30$ for the fundamental modes and $\nu_{mp} = 60$ for the second harmonic modes. . . . .	96
4-4	Coupling factor for (a) the TE <sub>0,6</sub> and TE <sub>2,6</sub> second harmonic modes of both rotations and (b) the nearby competing co- and counter-rotating TE <sub>2,3</sub> and TE <sub>8,1</sub> fundamental modes. . . . .	96
4-5	Starting currents at 12 kV and alpha and spread parameters taken from EGUN simulations ( <i>c.f.</i> Fig. 4-9). In the case where the alpha from the EGUN simulation is undefined, an beam alpha of 2.0 and corresponding velocity spread is used. Solid lines represent second harmonic modes and dotted lines fundamental modes. . . . .	98
4-6	Theoretical RF efficiency in the 460 GHz gyrotron cavity. . . . .	99
4-7	Photographs of the (a) cathode and (b) anode. . . . .	100
4-8	(a) Test data on the 460 GHz cathode (Semicon, Model No. BGC-101 S/N 0001969) by J. Tarter [8] (b) Current-voltage data for various cathode temperatures. . . . .	101
4-9	(a) Velocity pitch factor and (b) transverse velocity spread for the low-voltage, diode-type gun used in the 460 GHz gyrotron experiment. Each curve is derived from EGUN simulations of the gun geometry conducted as a function of voltage and magnetic field. . . . .	102

4-10	Simulation of the evolution of the transverse and axial velocities of the electrons accelerated at 12 kV in the 460 GHz gyrotron experiment using the EGUN electron optics and gun design program. The simulation includes the electron trajectories, equipotential lines, cathode and anode geometries, and 8.4 T applied magnetic field of the gun region.	103
4-11	(a) Transverse (solid line) and longitudinal (dashed line) electron beam velocity and transverse spread (dotted line) and (b) electron beam velocity pitch factor predictions by EGUN.	104
4-12	Millisecond pulse tests of the Spellman high voltage power supply over a 700 k $\Omega$ resistive load. The red waveforms indicate the high voltage response and the blue lines are the driving pulse shape for pulses of length (a) 5 ms, (b) 20 ms, (c) 100 ms, and (d) 20 ms.	105
4-13	Comparison of measured axial field profile ( $\times$ 's) to Cryomagnetics (solid line) magnetic field profile.	106
4-14	Superconducting magnet drawings, designed by Cryomagnetics, Inc. [9].	107
4-15	Fringe-field plot for the 700 MHz/89 mm superconducting NMR magnet system (Magnex Scientific, Model No. 700/89-4463) [10].	111
4-16	(a) Cross-sectional schematic of the cylindrical 460 GHz gyrotron cavity with the axial radiation field profile for the second harmonic TE <sub>0,6,1</sub> resonator mode. (b) Intensity pattern of the TE <sub>0,6</sub> design mode.	112
4-17	Photograph of the cavity, waveguide, and internal quasi-optical mode converter (launcher, focusing mirror, and steering mirror). The ruler is set at 2 cm and its position approximately corresponds to the location of the electroformed interaction cavity.	113
4-18	Schematic of the quasi-optical internal mode converter showing calculated design parameters (a) side view (b) front view, adapted from [11].	113
4-19	Transmission of second harmonic and fundamental modes through 1.9990 mm (a) and 1.9736 mm (b) thick Corning 7980 fused silica gyrotron windows.	115
4-20	Photograph of the window through the cross-bore of the superconducting magnet. The mode converter is visible.	116
4-21	Schematic of the collector including the electron beam and water cooling circuit.	117
4-22	Front panel of the LabVIEW control system. (a) Event driven control (b) Signal monitoring and PID feedback control.	119

5-1	Voltage, diode voltage, collector current, and body current traces of the $TE_{2,6,1}$ second harmonic mode at 12.5 kV, 100 mA, and 8.34 T. . . . .	124
5-2	Mode map for the design mode and nearby competing fundamental $TE_{2,3}$ mode for beam voltage and cavity magnetic field at 100 mA. The gun coil has been optimized for each point. . . . .	126
5-3	(a) Summary of experimental starting current data (b) measured frequency vs. magnetic field recorded for resonant cavity modes from 5.6 to 9.2 T and up to 15 kV and 160 mA. Open symbols denote fundamental modes and filled-in symbols denote second harmonic modes. . . . .	128
5-4	Intensity patterns of the (a) $TE_{2,2}$ , (b) $TE_{4,2}$ , (c) $TE_{2,3}$ , (d) $TE_{0,3}$ , and (e) $TE_{5,2}$ fundamental waveguide modes. . . . .	128
5-5	Second harmonic $TE_{2,6,1}$ and $TE_{0,6,1}$ start oscillation current data (points) compared with linear theory (solid lines) at 13.1 kV. . . . .	129
5-6	Intensity patterns of the (a) $TE_{2,6}$ and (b) $TE_{0,6}$ second harmonic waveguide modes. . . . .	130
5-7	Efficiency of the $TE_{2,6}$ second harmonic mode at 100 mA (a) as a function of main magnetic field and (b) as a function of voltage. . . . .	131
5-8	Efficiency of the $TE_{0,6}$ second harmonic mode at 100 mA (a) as a function of main magnetic field and (b) as a function of voltage. . . . .	132
5-9	Frequency pulling of the (a) $TE_{0,6}$ and (b) $TE_{2,6}$ second harmonic modes. . . . .	133
5-10	IF signal of 261 MHz with LO frequency of 25.360 GHz at the eighteenth harmonic yields a second harmonic $TE_{2,6}$ frequency of 456.219 GHz at 8.34 T, 12.5 kV, and 100 mA. . . . .	133
5-11	Contour plot of (a) measured peak power data of the fundamental $TE_{0,3,q}$ modes in watts as a function of beam current and magnetic field using a pyroelectric detector. The electron gun was pulsed for several microseconds at a repetition rate of approximately 30 Hz with 9 kV. The power level was calibrated using a calorimeter. (b) MAGY simulated power at experimental conditions. . . . .	134
5-12	Power in the $TE_{0,3}$ mode detected by a laser calorimeter at 9 kV, 100 mA, repetition rate 30 Hz, and pulse length 2.8 $\mu$ s. These data were used to calibrate the pyroelectric detector data shown in Fig. 5-11(a). . . . .	135
5-13	Mode competition between the $TE_{0,3}$ and parasitic $TE_{2,3}$ fundamental modes. . . . .	136

5-14	(a) Start oscillation currents, (b) frequency tuning, and (c) df/dB normalized to the frequency at the minimum start current versus magnetic field normalized to the field at the minimum start current of fundamental modes from 7.8 to 9.2 T. . . . .	138
5-15	Dispersion diagram showing the region of interaction between the unperturbed $TE_{5,2}$ waveguide dispersion curve and the experimentally observed Doppler shifted beam cyclotron modes. The intersection of the beam cyclotron modes with the waveguide mode at negative values of $k_z$ implies interaction of the beam with a backward propagating wave.	140
5-16	Linear theory (solid circles) and MAGY simulation (solid triangles) using EGUN calculated parameters of the frequency tuning of the $TE_{5,2,q}$ modes compared to the experiment (+). The dotted line is the relativistic cyclotron frequency. . . . .	140
5-17	Linear theory (lines) using EGUN calculated parameters of the starting currents of the $TE_{5,2,q}$ modes compared to the experimental data (diamonds). . . . .	141
5-18	Self-consistent axial field and phase profiles for $TE_{5,2,q}$ modes with $q \geq 1$ as calculated from MAGY. The cavity geometry is indicated above each column, and we have displayed the normalized voltage amplitude. The frequency increases from 246.0 GHz in (a) to 248.1 GHz in (h). . . . .	142
5-19	Self-consistent axial field profiles for $TE_{5,2,q}$ modes with $q \geq 1$ as calculated from MAGY (solid lines) compared with cold cavity (dashed lines) and sinusoidal (dotted lines) field profiles. The cavity geometry is indicated above the column. . . . .	142
5-20	Spatial dependence of the power throughout the cavity (in the $TE_{5,2}$ mode) at three magnetic fields. At frequencies greater than that of the $TE_{5,2,1}$ cold cavity mode, there is a spatial oscillation pattern which we interpret as the interference of the backward propagating wave with its non-synchronous reflection [12]. . . . .	143
5-21	Mode map for the design mode and nearby competing fundamental $TE_{2,3}$ mode at 12.4 kV and 100 mA for the cavity and cathode magnetic fields. . . . .	145
5-22	CW output power measured in the $TE_{0,6}$ second harmonic mode as a function of (a) beam current, (b) main magnetic field, (c) voltage, and (d) cathode magnetic field. Unless otherwise indicated, the experimental parameters are 12.4 kV, 100 mA and 8.384 T. . . . .	148



5-23	EGUN simulations for varying cathode magnetic fields at 12.4 kV and 100 mA. . . . .	149
5-24	Frequency tuning of the $TE_{0,6}$ second harmonic mode with (a) beam current, (b) main magnetic field, (c) voltage, and (d) cathode magnetic field. Unless otherwise indicated, the experimental parameters are 12.4 kV, 100 mA and 8.384 T. . . . .	150
5-25	Theoretical RF efficiency as a function of the conductivity of copper and diffractive $Q$ for the second harmonic $TE_{0,6,1}$ mode. The calculation assumes alternately a diffractive $Q$ of 31,000 and half the conductivity of ideal copper. . . . .	152
5-26	Cavity thermal load and RF efficiency as a function of measured output power using cavity thermal load measurement for the second harmonic $TE_{0,6,1}$ mode. . . . .	153
5-27	Block diagram of a simple homodyne detector [13]. . . . .	153
5-28	Homodyne measurements of the technical noise for the second harmonic $TE_{0,6,1}$ mode. . . . .	154
5-29	CW output power in the $TE_{2,3}$ mode as a function of beam current at 3.5 kV and 8.38 T. . . . .	156
5-30	CW start current data in the $TE_{2,3}$ mode at 3.5 kV compared to linear theory using alpha 2.5 and 10% transverse velocity spread. . . . .	157
5-31	CW output power and frequency in the $TE_{2,3}$ mode as a function of magnetic field for 50 mA and 3.5 kV. . . . .	157
5-32	Contour plot of measured CW power data of the fundamental $TE_{2,3,q}$ modes in watts as a function of beam current and magnetic field. . .	158
5-33	Heterodyne measured frequencies of the axial $TE_{2,3,q}$ fundamental modes at low voltage as a function of beam current and magnetic field. . . .	159
5-34	(a) Experiment (homodyne) compared to (b) MAGY simulation of the $TE_{2,3,q}$ fundamental modes at low voltage (3.5 kV) and 8.42 T depicting multiple frequencies separated by 400 MHz corresponding to consecutive longitudinal modes (c) and its corresponding time domain. . . . .	160
5-35	Homodyne frequency data for the $TE_{2,3,q}$ fundamental modes at low voltage (3.5 kV) and 8.42 T as a function of beam current. . . . .	161

5-36	Theoretical attenuation (in dB/m) versus frequency of the $HE_{1,1}$ mode in (a) 1.27 cm, 2.54 cm, 3.81 cm and 5.08 cm diameter dielectric waveguide with refractive index $n = 1.5$ (b) 2.54 cm diameter dielectric waveguide with refractive index of $n = 1.01, n = 1.02, n = 1.1, n = 1.2,$ and $n = 2$ . Measured attenuation in 2.54 cm G10 epoxyglass is marked with pluses. . . . .	162
5-37	Contour plot of the theoretical attenuation (in dB/m) versus refractive index and radius of the $HE_{1,1}$ mode at 460 GHz in hollow dielectric waveguide. . . . .	163
5-38	Plot of the experimental attenuation (in dB) versus length at 460 GHz in a variety of 2.54 cm diameter hollow dielectric waveguide. . . . .	164
5-39	Logarithmic radiation intensity pattern (in normalized dB) of the mode-converted $TE_{0,6}$ mode captured by a pyroelectric camera (a) two dimensional (b) one dimensional in the horizontal and vertical dimensions at the peak. . . . .	165
5-40	Linear radiation intensity patterns of the mode-converted (a) $TE_{0,6}$ (b) $TE_{2,6}$ (c) $TE_{2,3}$ and (d) $TE_{2,2}$ modes captured by a pyroelectric camera. 166	
5-41	Linear radiation intensity pattern of the mode-converted $TE_{0,6}$ mode (a) smoothed data captured by a pyroelectric camera (b) Gaussian fit (c) difference between experiment and fit. . . . .	166
5-42	Two separate one hour duration stability tests of the (a) power, (b) pressure, (c) beam voltage, (d) heater current, (e) beam current, and (f) gun coil current for the $TE_{0,6}$ second harmonic mode at 458 GHz using a diode (left) and calorimeter (right) to monitor the output power. 170	
5-43	Stability of the (a) power, (b) pressure, (c) beam voltage, (d) heater current, (e) beam current, and (f) gun coil current over the period of one hour for the $TE_{2,3}$ fundamental mode at 233 GHz using a diode to monitor the output power. . . . .	171
5-44	Statistical analysis of power fluctuations from setpoint for the diode controlled $TE_{0,6}$ hour long run. The solid line is a Gaussian fit to the data. . . . .	171
5-45	Arrangement of equipment for the 460 GHz cavity $Q$ measurements. .	172
5-46	Measurement of a high $Q$ mode around (a) 163.9 GHz (b) 157.2 GHz. 173	
5-47	MAGY run at 13.1 kV, 100 mA, and 8.39 T showing mode cooperation between the $TE_{0,6}$ and $TE_{2,3}$ modes effectively lowers the starting current of the $TE_{2,3}$ fundamental mode due to pre-bunching of the beam by the $TE_{0,6}$ second harmonic mode. . . . .	175

6-1	Aerial photograph of the 250 GHz gyrotron, corrugated transmission system, and 380 MHz NMR magnet. . . . .	178
6-2	Photograph of the 250 GHz quasi-optical directional coupler. . . . .	178
6-3	Frequency and power of the operating $TE_{0,3,2}$ mode as a function of magnetic field. . . . .	180
6-4	Power in the operating $TE_{0,3,2}$ mode as a function of beam current. . . . .	180
6-5	Frequency pulling of the operating $TE_{0,3,2}$ mode by changing (a) the main magnetic field, (b) the gun magnetic field, and (c) the beam voltage. . . . .	181
6-6	Intensity radiation pattern of the Gaussian output of the gyrotron operating in the $TE_{0,3,2}$ mode as recorded by liquid crystal paper for (a) the gyrotron output and (b) and (c) after lengths of corrugated waveguide. . . . .	183
6-7	Intensity radiation pattern of the Gaussian output of the gyrotron operating $TE_{0,3,2}$ mode as recorded by a pyroelectric camera (a) linear (b) logarithmic (normalized dB). . . . .	184
6-8	Linear radiation intensity pattern of (a) the mode-converted $TE_{0,3}$ mode captured by a pyroelectric camera (b) Gaussian fit (c) difference between experiment and fit. . . . .	185
6-9	Stability of the $TE_{0,3,2}$ operating mode over an hour of the (a) cathode voltage and beam current, (b) heater voltage and current, (c) pressure, and (d) power and frequency. . . . .	186
6-10	Representative transient response of the gyrotron to (a) positive and (b) negative step in the control voltage. The dashed line is a sigmoidal fit to the data from which optimal PID parameters were estimated. Note oscillations in the output power which persist even though the system is not under proportional regulation for these measurements. . . . .	188
6-11	Response of the system to (a) sudden and (b) controlled termination of running power supplies. In (a), a power failure caused the accidental shutdown of the high voltage and heater supplies following three hours of CW operation, while, in (b), the high voltage output was gradually reduced over a period of 10–15 s, and the heater supply voltage was reduced over a period of thirty minutes, both following thirteen hours of CW operation. . . . .	189
6-12	Linewidth measurement of the operating $TE_{0,3,2}$ mode using the frequency measurement system. . . . .	189
6-13	Homodyne measurement of the operating $TE_{0,3,2}$ mode. . . . .	190

6-14	Intensity patterns of the harmonic modes observed in the 250 GHz experiment: (a) $TE_{0,4}$ , (b) $TE_{2,4}$ , (c) $TE_{3,4}$ , (d) $TE_{1,5}$ , and the fundamental waveguide mode (e) $TE_{8,1}$ . . . . .	191
6-15	Summary of experimental starting current data vs. magnetic field recorded for resonant cavity modes from 5.8 to 9.2 T and up to 120 mA. Open symbols denote fundamental modes and filled-in symbols denote second harmonic modes. . . . .	192
6-16	Summary of experimental frequency tuning data vs. magnetic field recorded for resonant cavity modes from 5.8 to 9 T near the starting current. Open symbols denote fundamental modes and filled-in symbols denote second harmonic modes. . . . .	193
6-17	Coupling factor for the $TE_{0,3}$ operating mode and the co-rotating $TE_{8,1}$ fundamental mode. The operating electron beam radius is 1.018 mm. . . . .	195
6-18	Electron beam shifted by the distance $D$ (solid line) in the coordinate system of the resonator. The on-axis electron beam is indicated by the dashed circle. . . . .	195
6-19	Ratio of off-axis to on-axis starting currents for observed (a) fundamental modes and (b) second harmonic modes. Off-axis starting currents for observed (c) fundamental modes and (d) second harmonic modes. The counter-rotating modes are represented by dashed lines. . . . .	196
6-20	Theoretical RF efficiency as a function of the conductivity of copper and diffractive $Q$ for the fundamental $TE_{0,3,1}$ mode. . . . .	198
6-21	Cold cavity simulation showing the cavity and RF profile for the 250 GHz gyrotron cavity (a) without and (b) with an iris. . . . .	198
6-22	Starting currents for the second harmonic $TE_{3,4,1}$ mode using linear and non-linear theory and for the case of the design cavity (lines) and with an iris added before the output uptaper (dotted lines). The percentages indicate the velocity spread simulated. . . . .	199
6-23	250 GHz transmission line layout for DNP experiments. . . . .	201
6-24	Calculated coupling efficiency of an elliptical Gaussian beam of $10.04 \times 13.76$ mm waist cross section to a circular waveguide $HE_{1,1}$ mode. . . . .	202
6-25	Design of the directional coupler fabricated from two corrugated waveguide corners that mate along the diagonal to hold the beamsplitter. One corner with a flat mirror along the diagonal would make a $90^\circ$ waveguide miter bend. . . . .	203

6-26	Scattered radiation patterns ( $P_s/P_o \times 10^3$ ) at 250 GHz by (a) one wire (36 gauge) and by (b) a ten wire array. The wires are arrayed with a spacing of $1/4\lambda$ along the vertical axis of this figure with the wire axis normal to the figure plane. The incident beam is $45^\circ$ from normal to the wire array plane with a $HE_{1,1}$ beam profile corresponding to corrugated waveguide with $ka = 58$ . . . . .	205
6-27	View of 10-wire, gauge 36 beamsplitter stretched across the diagonal face of the corrugated 4-port directional coupler block. . . . .	206
6-28	The 248 GHz heterodyne receiver used for cold test measurements. . . . .	207
6-29	Cold test transmission measurements of the 22 mm diameter corrugated waveguide without and with two versions of the directional coupler.	208
6-30	Calculated quartz ( $n=1.955$ ) beamsplitter reflectivity for a beam incidence at $45^\circ$ for the two orthogonal polarization cases and two thicknesses. . . . .	208
6-31	Three hour CW test of the quartz directional coupler stability, (a) normalized ratio of forward coupled signal and gyrotron power shown in (b). . . . .	211
7-1	Schematic of the 140 GHz gyrotron oscillator indicating key components. The gyrotron tube is parallel to the plane of the floor. . . . .	218
7-2	Schematic of the 140 GHz external transmission system, consisting of a $TE_{0,1}$ - $TE_{1,1}$ snake mode converter, overmoded cylindrical copper waveguide with two miter bends, a taper to fundamental waveguide, a circular to rectangular transition, a directional coupler, and a fundamental waveguide bend, terminating at a 211 MHz ( $^1H$ )/140 GHz (electron cyclotron) DNP probe. . . . .	219
7-3	(a) Schematic of the $TE_{0,1}$ - $TE_{1,1}$ snake mode converter, where $a$ is the average waveguide radius, $\delta$ is the perturbation, $r(z) = a + \delta(z)$ , $d$ is a period, and $L$ is the total length (b) close-up of one period [14]. . . . .	219
7-4	(a) Photograph of the author and the setup for measuring the radiation mode patterns. The gyrotron is located off-screen to the left, and a miter bend steers the radiation toward the scanner. The scanner is located to the right and is covered with Eccosorb to prevent reflections. (b) Block diagram of the setup for measuring the radiation mode patterns. . . . .	221
7-5	Liquid crystal recording of the $TE_{0,1}$ gyrotron output. . . . .	221

7-6	(a) Horizontal and (b) vertical polarizations of the gyrotron output at $z = 5.08$ cm; (c) horizontal and (d) vertical polarizations of $TE_{0,1}$ theoretical intensity; normalized dB contour plot . . . . .	222
7-7	Gyrotron output at $z = 5.08$ cm, (a) $y = 0$ ; (b) $x = 0$ ; the solid line represents the theoretical values, the $\times$ 's the vertical polarization, and the $+$ 's the horizontal polarization . . . . .	223
7-8	Sum of horizontal and vertical polarizations at $z = 5.08$ cm of (a) gyrotron output, (b) theoretical $TE_{0,1}$ waveguide mode, (c) snake output, and (d) theoretical $TE_{1,1}$ waveguide mode in a normalized dB contour plot . . . . .	224
7-9	(a) Horizontal and (b) vertical polarizations of the snake output at $z = 5.08$ cm; (c) horizontal and (d) vertical polarizations of $TE_{1,1}$ theoretical intensity; normalized dB contour plot . . . . .	225
7-10	Snake output at $z = 5.08$ cm, (a) $y = 0$ ; (b) $x = 0$ ; the solid line represents the theoretical values, the $\times$ 's the vertical polarization, and the $+$ 's the horizontal polarization . . . . .	226
7-11	Statistical analysis of the mode converter radiation pattern assuming two modes present in the output, the $TE_{1,1}$ and $TE_{0,1}$ , and phase difference. Confidence levels are indicated by solid lines. . . . .	228
7-12	Coordinate system for calculating the radiation from a circular hollow pipe [15]. . . . .	230
7-13	Setup of the apparatus for the 1D radiation scans. . . . .	230
7-14	Far-field radiation scan of the output of the new snake at 41 cm using the BWO as the source. The vertical polarization is represented by $\times$ 's, the horizontal polarization by $+$ 's, and the theory is shown by the solid line. The theoretical mode content of the snake is in the upper right-hand corner. . . . .	232
7-15	Far-field radiation scan of the output of the new snake at 41 cm using the 140 GHz gyrotron as the source. The vertical polarization is represented by $\times$ 's, the horizontal polarization by $+$ 's, and the theory is shown by the solid line. The theoretical mode content of the snake is in the upper right-hand corner. . . . .	233
7-16	Far-field radiation scan of the output of the old snake in the forward configuration at 41 cm using the BWO as the source. The vertical polarization is represented by $\times$ 's, the horizontal polarization by $+$ 's, and the theory is shown by the solid line. The mode content of the theory data is in the upper right-hand corner. . . . .	234

7-17	Far-field radiation scan of the output of the old snake in the reverse configuration at 41 cm using the BWO as the source. The vertical polarization is represented by $\times$ 's, the horizontal polarization by $+$ 's, and the theory is shown by the solid line. The mode content of the theory data is in the upper right-hand corner. . . . .	234
7-18	Photograph of the 140 GHz overmoded miter bend assembly in the insertion loss test setup. The chopper is on the labjack on the left side and the receiver is located on the bottom. . . . .	238
7-19	Corrugated waveguide transmission system for the 140 GHz gyrotron by Thomas Keating, Ltd. [16]. . . . .	241





# List of Tables

1.1	High frequency CW gyrotron oscillators . . . . .	33
1.2	High frequency DNP/EPR gyrotron oscillators . . . . .	34
3.1	Atomic mass units of residual gases present in the system measured with the RGA. . . . .	80
3.2	Flow parameters for the Proteus sensors of the 460 GHz gyrotron [17].	85
4.1	Gyrotron stability requirements for DNP/NMR spectrometer [18] . .	94
4.2	Gyrotron design parameters . . . . .	95
4.3	Specifications of the gyrotron magnet . . . . .	109
4.4	Cavity design and fabrication dimensions . . . . .	112
4.5	Quasi-optical mode converter parameters . . . . .	114
5.1	Short pulse experimental operating parameters . . . . .	123
5.2	Minimum start current, and magnetic field and frequency for minimum starting current of $q = 1$ modes from linear theory [19] using EGUN calculated parameters of Fig. 4-9(a) and (b) vs. experiment . . . . .	129
5.3	CW experimental operating parameters . . . . .	143
5.4	Frequency dependence on operating parameters . . . . .	147
5.5	Measured and theoretical ohmic losses in the gyrotron cavity at 458 GHz	152
5.6	Design and measured parameters from the ohmic loss measurement of the gyrotron cavity at 458 GHz . . . . .	152
5.7	Cold cavity frequencies of the $TE_{2,3,q}$ modes . . . . .	159
5.8	Measured and theoretical losses in 2.54 cm diameter G10 epoxyglass hollow dielectric waveguides . . . . .	162
5.9	Measured losses in various 2.54 cm diameter hollow dielectric waveguides at 460 GHz . . . . .	164
5.10	Beam waists of the mode converted radiation fields from Fig. 5-40 as calculated by the best fit Gaussian . . . . .	167

5.11	Stability of the second harmonic $TE_{0,6}$ and fundamental $TE_{2,3}$ modes in the 460 GHz gyrotron . . . . .	169
5.12	Cold test data and cold cavity simulation parameters of the $TE_{0,2,q}$ and $TE_{2,2,q}$ cavity modes. . . . .	172
6.1	Frequency dependence on operating parameters of the 250 GHz gyrotron in the $TE_{0,3,2}$ operating mode . . . . .	182
6.2	Beam waist of the gyrotron output radiation field from the pyroelectric camera and liquid crystal method . . . . .	184
6.3	Stability of the 250 GHz operating parameters . . . . .	187
6.4	Second harmonic modes observed in the 250 GHz gyrotron. . . . .	191
6.5	Frequency tuning for the observed modes between 5.8 and 9 T in the 250 GHz gyrotron. . . . .	193
6.6	Minimum start current, and magnetic field and frequency for minimum starting current of $q = 1$ modes from linear theory [19] vs. experiment	194
6.7	Thermal load measurements on the 250 GHz gyrotron [20] . . . . .	197
6.8	Cold test insertion loss measurement results with $248 \pm 4$ GHz radiometer	209
6.9	250 GHz gyrotron beam measurements . . . . .	212
7.1	Measured snake parameters . . . . .	220
7.2	Theoretical mode content of the radiation field from a $TE_{1,1}$ to $TE_{0,1}$ mode conversion in the new snake. . . . .	231
7.3	Theoretical mode content of the radiation field from a $TE_{0,1}$ to $TE_{1,1}$ mode conversion in the new snake. . . . .	232
7.4	Inputs to the two-mode approach . . . . .	237
7.5	Optimum two-mode approach snake parameters . . . . .	237
7.6	Conversion efficiency of the snake in the multi-mode approach . . . .	238
7.7	140 GHz theoretical transmission line losses for transmission of the $TE_{0,1}$ , $TE_{1,1}$ , and $HE_{1,1}$ modes. . . . .	244
7.8	Losses in the 140 GHz transmission line in four configurations. . . . .	245
8.1	Frequency dependence on operating parameters . . . . .	252

# Chapter 1

## Introduction

### 1.1 Terahertz

The terahertz or submillimeter band of the electromagnetic spectrum, corresponding to frequencies between 300 and 3,000 GHz, is of considerable interest for applications in spectroscopy, communications, high-resolution RADAR, and imaging [21, 22]. Potential applications are nevertheless frustrated by a historical dearth of sources that yield appreciable powers in this frequency regime. On the one hand, near-infrared lasers are capable of delivering moderate peak power at very high frequencies, but they do not yet scale to intermediate frequencies; on the other hand, conventional vacuum electron devices such as the klystron and traveling wave tube (TWT) operate at very high output powers in the tens of gigahertz, but the physical dimensions of their interaction structures (*i.e.* the region of interaction with the electron beam) necessarily scale with the wavelength. The resulting increase in power density with increasing frequency limits the reliability and utility of these devices above 140 GHz.

#### 1.1.1 State-of-the-art

Figure 1-1 is a chart of source technology capable of generating high average power at submillimeter wavelengths. Unlike charts detailing the theoretical device capabilities, this chart is composed from data of actual continuous wave devices. The high average power devices fall into two broad categories, vacuum electron devices and lasers. Of the conventional vacuum electron devices, the carcinotron (also known as the backward wave oscillator or BWO) has carved out a niche as a compact and commercially available source generating frequencies over the 1 THz mark. In the BWO, an electron beam, focused by a magnet, passes through a periodic metallic structure and induces an electromagnetic wave, which moves in the opposite direc-

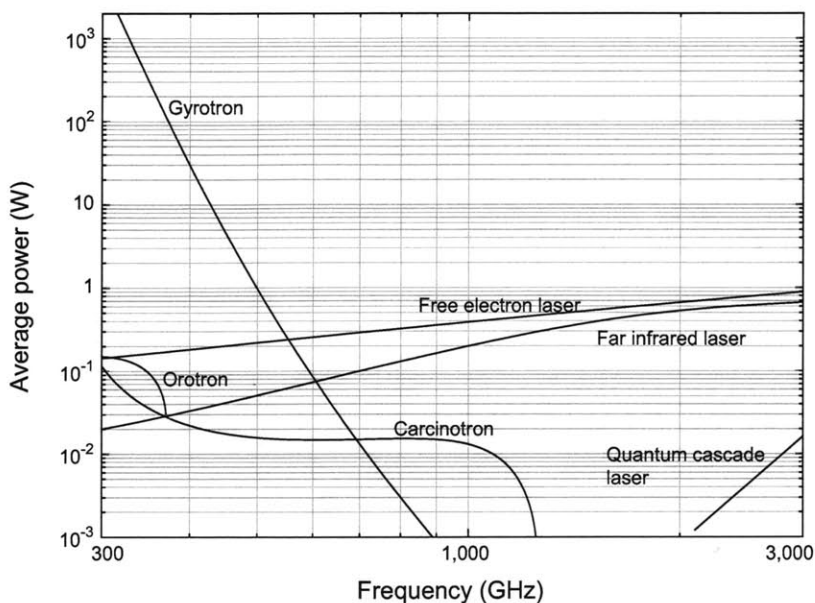


Figure 1-1: State of the art in CW terahertz sources.

tion to the electron beam. A wide frequency tuning range is available by controlling the collector potential. Unfortunately its output power at high frequencies is limited to between milliwatts and tens of milliwatts since its interaction structure is on the order of a wavelength. The far infrared (FIR) laser also seems to span the terahertz band, however has a key drawback; in a FIR laser, the frequency depends on gas type and therefore not all frequencies can be successfully generated. The quantum cascade laser (QCL), on the other hand, does not suffer from this drawback; its operating wavelength is determined by the layer thickness rather than material composition. In the QCL, electrons cascade down a series of identical energy steps (called “quantum wells”) built into the material during crystal growth, emitting a photon at each step. Compared to diode lasers which emit only one photon over a similar cycle, it is potentially many times more powerful [23]. The present state-of-the-art for quantum cascade lasers at submillimeter wavelengths is 50 mW CW at 3.5 THz. The free electron laser is a vacuum electron device in which an electron beam traverses a periodic wiggler magnetic field and emits radiation. Since it requires an accelerator, its primary disadvantage is its extremely large size. A promising technology which may be extended throughout the regime is the gyrotron oscillator, which is capable of very high average power operation throughout millimeter wavelengths.

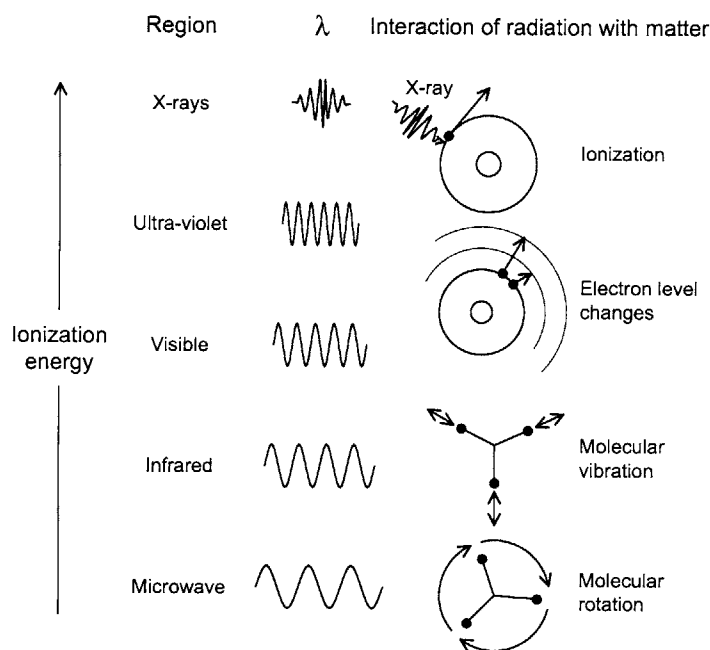


Figure 1-2: The interactions of the bands of the electromagnetic spectrum with matter.

### 1.1.2 Interactions with matter

The interactions of the bands of the electromagnetic spectrum have varying effects upon the matter with which they interact, leading to many effects which can be harnessed for scientific applications. In this work we are interested in the effects of submillimeter radiation on matter, which tend to be less obvious than those of other bands of the electromagnetic spectrum.

X-rays (and the far ultraviolet) are classified as ionizing radiation since the quantum energies of x-ray photons are too high to be absorbed in electron transitions between states, and therefore can interact with an electron only by knocking it completely out of the atom (*c.f.* Fig. 1-2). When all of the energy is given to an electron, this is called “photoionization”; when partial energy is given to a photon and the remainder to a lower energy photon this is known as “Compton scattering,” which results in a longer wavelength x-ray. The primary mechanism for the absorption of visible light photons (and near ultraviolet photons below the ionization energy) is through the elevation of electrons to higher energy levels (*c.f.* Fig. 1-2). For the visible wavelengths, we are familiar with this effect as the production of light which can be viewed by the naked eye.

The infrared region broadly covers a range of frequencies extending from the red, low frequency end of the visible spectrum (750 nm) to the far infrared (about 100  $\mu$

m). The quantum energy of infrared photons is in the range of energies separating the quantum states of molecular vibrations (*c.f.* Fig.1-2). While infrared is absorbed more strongly than microwaves, it is absorbed less strongly than visible light, resulting primarily in heating since it increases molecular vibrational activity. Infrared radiation can penetrate matter further than visible light.

The quantum energy of microwave photons is in the range of energies separating the quantum states of molecular rotation and torsion (*c.f.* Fig. 1-2). The interaction of microwaves with dielectric matter results in rotation of the molecules and which in turn generate heat from the molecular motion. A practical example is the cooking of food in a microwave oven. Most matter is transparent to microwaves, a feature which allows them to propagate over long distances and be useful for communications and radar. Another interaction of matter with microwaves involving a homogeneous magnetic field is described later in the section on nuclear magnetic resonance.

The submillimeter band includes frequencies ranging from 300 GHz to 3 THz, and is often (though not always) synonymous with “terahertz.” Submillimeter photons also interact with molecular rotations. While the rotational interactions with matter begin with the microwave frequencies, their strengths grow as the cube of the frequency until they reach a maximum between several hundred gigahertz and a few terahertz before dropping exponentially [21]. The molecular rotations of the submillimeter band cause complex attenuation with the Earth’s atmosphere which compromise applications requiring atmospheric propagation. However the same rotational interactions provide strong absorptions and emissions crucial for molecular science. Another interaction of matter with terahertz involving a homogeneous magnetic field is described later in the section on dynamic nuclear polarization.

## 1.2 Cyclotron Resonance Masers

Gyrotrons, also known as cyclotron resonance masers, are robust devices. Unlike so-called “slow-wave” microwave devices, “fast-wave” devices such as gyrotron oscillators and amplifiers rely on a resonance between the modes of an interaction structure (such as the transverse electric modes of a cylindrical cavity) and the electron beam in a magnetic field. The resonator can be overmoded and, as such, can have physical dimensions which are much larger than the operating wavelength. This permits high peak and average power operation even at elevated frequencies without risk of damage to the interaction structure [24]. Indeed, gyrotrons routinely achieve megawatt power levels at frequencies between 100 and 170 GHz, where plasma heating for fusion is the driving application [25]. The highest frequency achieved by a gyrotron oscillator

to date is 889 GHz at Fukui University in Japan [26]. More recent applications in spectroscopy, such as high field dynamic nuclear polarization (DNP) [27] and electron paramagnetic resonance (EPR) require lower peak power, but high average power continuous duty (7-10 days CW) operation and high stability of the frequency and output power.

### 1.2.1 Harmonic considerations

Superconducting magnet technology is one limiting factor in high frequency gyrotron design. At fields up to 10 T, magnets which have wide room temperature bores generally employ the NbTi superconducting technology; from 10 T to 22 T (corresponding to a range of fundamental electron cyclotron frequency from 280 to 616 GHz), it is necessary to use the Nb<sub>3</sub>Sn conductor which considerably elevates the cost of the superconducting magnet. Resistive DC Bitter magnets, consisting of copper “Bitter” plates conceived by Francis Bitter, are currently available up to 33 T and have been used in gyrotron experiments up to 14 T [28], while hybrid magnets, combining Bitter and superconducting technology up to 45 T, though both magnet types are mainly experimental devices. Pulsed magnets can generate fields even higher, and up to 30 T have been generated synchronously with pulsed gyrotron operation [29]. This limitation can be alleviated by operating the gyrotron at a harmonic of electron cyclotron resonance, for which the  $n^{\text{th}}$  harmonic will deliver  $n$  times the fundamental frequency for a given magnetic field. However, the harmonic interaction is inherently less efficient than the fundamental interaction due to elevated ohmic losses. It also suffers from the additional complication of mode competition and requires much higher beam currents in order to initiate oscillation. To a large extent, these difficulties can be obviated through appropriate design.

Indeed, while there has been much development of the gyrotron oscillator for fusion applications, its high frequency operation has not been similarly explored and promises to open new areas of growth. To alleviate the dense mode competition of the higher harmonic modes with the fundamental, novel cavity designs can be utilized in the place of conventional open cylindrical tapered resonators. One such mode-selective cavity is a photonic band gap (PBG) interaction structure, consisting of an array of metal rods parallel to the electron beam, where one or more rods have been removed from the center of the array to allow passage of the beam [30]. A high order transverse electric (TE) mode can exist in the “defect” if its resonant frequency lies in the band gap of the PBG structure, where the band gap can be adjusted through the geometry of the rods such that the resonant frequencies of the other modes lie in the passband of the lattice and leak out. Another novel cavity design

uses an iris, a small reduction in radius extending below cutoff, to enhance the second harmonic mode (and subsequently lower its start oscillation current) by increasing its  $Q$  while the fundamental  $Q$  remains unchanged [31]. This implementation reduces the harmonic start current. The high ohmic losses inherent in a high power, high frequency gyrotron can severely compromise the structural integrity of the interaction structure. A cryogenically cooled cavity could be employed to alleviate the thermal load. In accelerator cavities, it has been shown that copper losses can be reduced by factors of between three and five at cryogenic temperatures [32].

### 1.2.2 History

The development of the gyrotron would not have been possible without the accumulated knowledge generated by the occurrence of numerous historical, theoretical, scientific, engineering, and physical events. To assign a concrete starting point, one can argue that the ball was set in motion in 1864 with the existence of electromagnetic waves predicted by James Clerk Maxwell. The existence of electromagnetic waves remained theoretical until 1888 when Heinrich Hertz experimentally demonstrated their existence by building an apparatus to produce radio waves. Subsequent technical advances include the invention of a three-electrode vacuum tube (called the “triode”) by Lee de Forest in 1906. This was followed by the invention of the magnetron in 1921 by the American physicist Albert Wallace Hull, of the klystron in 1937 by the American brothers Russell and Sigurd Varian, and of the traveling wave tube in 1943 by R. Kompfner. In 1958 and 1959, theoretical investigations on the generation of microwaves through the electron cyclotron resonance maser interaction were carried out simultaneously by R. Twiss [33], J. Schneider [34], and A. Gaponov [35]. Finally, the earliest version of the gyrotron was developed in Russian circa 1965.

### 1.2.3 Operating Principles

The gyrotron, as with all microwave sources, is based on the conversion of electron beam energy into microwave radiation using a resonant structure. In many cases, an annular electron beam is produced by a magnetron injection gun and travels through a resonant cavity, located at the center of the superconducting magnet. The magnetic field causes the electrons to gyrate and thus emit radiation. If the magnetic field and cavity are tuned to match the beam parameters, the rotational energy of the electron beam will couple into a resonant cavity transverse electric mode. Figure 1-3 shows a typical cylindrical tapered gyrotron oscillator cavity of length  $L$  and radius  $r_{\text{cavity}}$  with electron beam, axial RF field profile with phase  $\phi$  in the presence of an applied



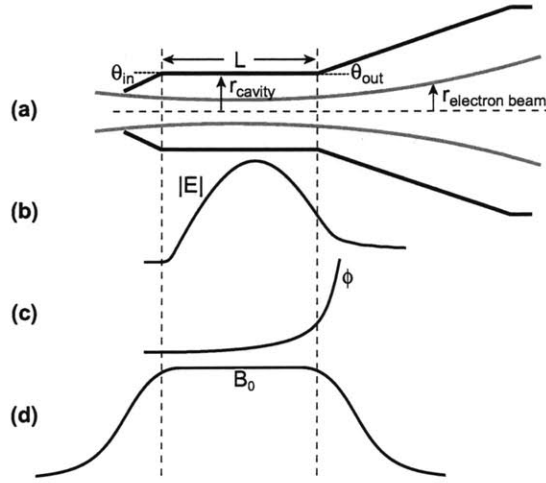


Figure 1-3: (a) Typical gyrotron oscillator cavity with electron beam, (b) RF field profile with single axial maximum, (c) phase, and (d) applied DC magnetic field.

Table 1.1: High frequency CW gyrotron oscillators

Source	Year	Freq. (GHz)	Cycl. harm.	Mode ( $TE_{m,p,q}$ )	V (kV)	I (A)	P (W)	Duty cycle (%)
MIT [1]	2004	460	2	$TE_{0,6,1}$	12.4	0.13	8	100
Sydney [36]	1993	350	2	$TE_{1,7,1}$	10	0.063	0.23	100
IAP [37]	1973	326	2	$TE_{2,3,1}$	27	0.9	1,500	100
Fukui [38]	1999	301	1	$TE_{0,3,1}$	14	0.08	17	100
Sydney [36]	1993	264	1	$TE_{4,4,1}$	10	0.05	30	100
IAP [39]	1988	250	2	$TE_{6,5,1}$	23.3	1	900	100
MIT [40]	1998	250	1	$TE_{0,3,1}$	11.8	0.049	25	100

DC magnetic field with amplitude  $B_0$ . When the interaction is completed, the spent beam leaves the cavity and propagates to the collector where it is intercepted. The microwaves are transmitted from the cavity through an output waveguide, and in some cases can be transformed in an internal mode converter, before exiting the gyrotron through a vacuum window. Past the window, the beam can then be propagated down a transmission line, usually a cylindrical waveguide, to its place of use.

#### 1.2.4 State-of-the-art

Very few experiments have been done on high frequency gyrotrons (above 250 GHz) because of the high magnetic field required, and even fewer experiments at high fre-

Table 1.2: High frequency DNP/EPR gyrotron oscillators

Source	Year	Freq. (GHz)	Cycl. harm.	Mode ( $TE_{m,p,q}$ )	V (kV)	I (A)	P (W)	Duty cycle (%)
MIT [1]	2004	460	2	$TE_{0,6,1}$	12.4	0.13	8	100
Fukui [29]	1999	301	1	$TE_{0,3,1}$	14	0.08	17	100
MIT [40]	1998	250	1	$TE_{0,3,1}$	11.8	0.049	25	100
MIT [41, 42]	1993	140	1	$TE_{0,3,1}$	12.5	0.026	10	33

quencies have been conducted in CW mode. The state-of-the-art in high frequency CW gyrotron oscillators is detailed in Table 1.1. Second harmonic gyrotrons suffer in efficiency, and low power second harmonic gyrotrons even more so; the highest efficiencies come from the gyrotrons with highest beam power. To the author’s knowledge, this work presents the highest power continuous-wave gyrotron results at this frequency to date.

### 1.3 Dynamic Nuclear Polarization

The gyrotron oscillator design presented in this work will permit the precise control of the output power and frequency that is necessary for applications to sensitivity-enhanced magnetic resonance spectroscopy through dynamic nuclear polarization (DNP). Originally employed to produce spin polarized targets for nuclear scattering experiments, DNP is a technique through which the greater Zeeman polarization of the electrons is transferred to the nuclei, in this case to enhance the sensitivity of a subsequent NMR experiment by up to two orders of magnitude. DNP requires irradiation of the sample with 1–10 W of power near the electron Larmor frequency (which is close to the electron cyclotron frequency) [27].

This technology will extend the applicability of DNP techniques to frequencies much higher than was previously possible. Table 1.2 enumerates the three gyrotrons in the world used for dynamic nuclear polarization and one for electron spin resonance. The DNP gyrotrons were constructed at MIT and operate at 140 [41, 42], 250 [40], and 460 GHz [1] at the first, first, and second harmonics respectively. The 140 GHz gyrotron operates in a long pulse regime and the 250 and 460 GHz gyrotrons are fully CW, with continuous operation of the 250 GHz gyrotron for over 10 days. The gyrotrons all produce low output powers of several watts average, reflecting the requirements of the DNP experiment.

## 1.4 Thesis Outline

This thesis is organized in eight chapters with three main parts. The introductory material, including the introduction and background theory, are contained in Chapters one and two. Chapters three and four are equipment related, in both the description and design of components and systems. Chapters five, six, and seven contain the experimental research on three gyrotron oscillators, at 460, 250, and 140 GHz, where the author designed and constructed the first.

Chapter one introduces the subject of gyrotrons, high frequency sources and applications.

Chapter two reviews the relevant theoretical basis for understanding this experimental work. Classical and quantum mechanical theories of the cyclotron resonance maser interaction are presented. Several numerical methods used for design and analysis of gyrotron oscillators are reviewed.

Chapter three enumerates the experimental setup and diagnostics required for the experiments. Novel characteristics and observations by the author of the diagnostic systems as relates to the thesis work are also presented.

Chapter four describes the author's design of key components and systems of the 460 GHz second harmonic gyrotron oscillator.

In Chapter five, we present the title thesiswork, continuous-wave and pulsed results from a 460 GHz gyrotron oscillator designed to operate continuously at the second electron cyclotron harmonic at low voltages and output powers of between several watts and several tens of watts [1]. Further, we have demonstrated that continuous tuning of the gyrotron oscillator over a range of nearly 2 GHz at constant output power is possible by changing the magnetic field alone. The detailed studies of a low voltage fundamental  $TE_{2,3}$  mode reveal that the mode can be excited with less than 7 W of beam power at less than 3.5 kV.

In Chapter six, we present a set of characterization and long-term stability experiments performed on the 250 GHz gyrotron oscillator. The design and implementation of novel components such as the overmoded directional coupler [2] and overmoded corrugated waveguide are also presented. The very low second harmonic starting currents obtained in the 250 GHz gyrotron characterization experiments have been analyzed.

Chapter seven describes the author's work done on the 140 GHz gyrotron oscillator to increase its efficiency, including the modification of several key components in the transmission system and design of a new  $TE_{0,1}$  to  $TE_{1,1}$  waveguide mode converter.

Finally, Chapter eight contains the discussion and conclusions drawn from this entire body of work and the direction of future work.



# Chapter 2

## Theory

*Several sections of this chapter will appear in [43].*

### 2.1 Introduction

The fundamental cyclotron resonance maser (CRM) interaction can be understood by examining the electrons in phase space as a function of time. In order to do so, we regard the electron beam as a charged fluid or plasma, following the treatments in [44, 45]. First, we observe that electrons obeying the equations of motion and have a velocity which is separable into an angular component orthogonal to the beam axis,

$$v_{\perp} = v_{\perp}(r, \phi) \quad (2.1)$$

and one parallel to it,  $v_z$ . In this frame,  $v_{\perp}$  is usually larger than  $v_z$ , and both are constants of the motion. Now we will determine if the gyrotory motion is sufficient to generate microwave radiation. For the  $k^{\text{th}}$  electron located at  $(r, \phi_0 + \Omega t, 0)$  and moving with  $v_{\perp}$  at time  $t = 0$ , the electron current is spatially localized according to [44]:

$$J_{\phi} = -ev_{\perp}\delta(r - r_0)\delta(\phi - (\phi_0 + \Omega t))\delta(z). \quad (2.2)$$

A Fourier transform of (2.2) with respect to  $\phi$  gives:

$$J_{\phi} = -\frac{ev_{\perp}}{2\pi}\delta(r - r_0)\delta(z) \sum_{n=-\infty}^{\infty} e^{in(\phi - \phi_0) - in\Omega t} \quad (2.3)$$

Considering a large number,  $N$ , of electrons which are uniformly distributed in phase, (2.3) becomes

$$J_\phi = -\frac{ev_\perp}{2\pi}\delta(r-r_0)\delta(z)\sum_{n=-\infty}^{\infty}e^{in(\phi-\Omega t)}\sum_{k=1}^N e^{-in\phi_{0k}}. \quad (2.4)$$

This expression contains factors oscillating at the cyclotron frequency and its harmonics. We now take an ensemble average over all electron orbits; in the limit where  $N$  approaches infinity, the second sum becomes oscillatory and only the  $n = 0$  term survives, yielding

$$J_\phi = -\frac{Nev_\perp}{2\pi}\delta(r-r_0)\delta(z). \quad (2.5)$$

This indicates that, under the assumption of a uniform charge distribution, that there is no alternating current. Therefore, an electron beam which is uniform in phase space cannot produce an rf field under these conditions.

## 2.2 CRM Interaction

The electromagnetic radiation in a gyrotron is produced by the interaction of a mildly relativistic gyrating electron beam and transverse electric (TE) wave near cutoff in an overmoded cavity resonator situated in a DC magnetic field. The oscillation frequency  $\omega$  of a  $\text{TE}_{m,p,q}$  mode of a cylindrical cavity of effective length  $L$  and radius  $r_0$  is given by

$$\frac{\omega^2}{c^2} = k^2 = k_\perp^2 + k_z^2 \quad (2.6)$$

where  $k_\perp (= \nu_{mp}/r_0)$  and  $k_z (= q\pi/L \ll k_\perp)$  are the transverse and longitudinal propagation constants of the  $\text{TE}_{m,p,q}$  wave,  $c$  is the velocity of light,  $\nu_{mp}$  is the  $p^{\text{th}}$  root of  $J'_m(x)$ , and  $m$ ,  $p$ , and  $q$  are, respectively, the azimuthal, radial, and axial mode numbers. The resonance condition for the excitation of the cyclotron resonance maser instability is satisfied when  $\omega$  and  $k_z$  in (2.6) satisfy the beam mode dispersion relation,

$$\omega - k_z\beta_{z0}c \approx n\omega_{c0} \quad (2.7)$$

where

$$\omega_{c0} = \frac{eB_0}{\gamma m_e} \quad (2.8)$$

is the relativistic cyclotron frequency,  $\gamma = (1 - \beta_{z0}^2 - \beta_{\perp 0}^2)^{-1/2}$  is the relativistic mass factor,  $m_e$  and  $e$  are the electron rest mass and charge,  $\beta_{\perp 0}$  and  $\beta_{z0}$  are, respectively, the transverse and longitudinal velocities of the electrons normalized to the velocity

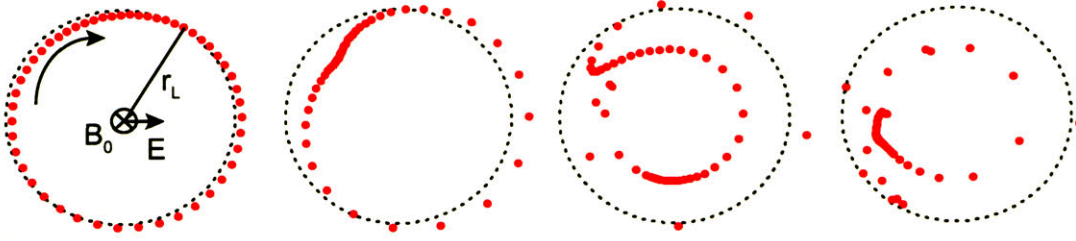


Figure 2-1: Simulation of a non-uniform electron phase distribution which occurs due to the interaction of a relativistic electron beam with a transverse electric field  $E$ , situated in a static magnetic field  $B_0$ . The beamlets, with Larmor radius  $r_L$ , represent snapshots in phase space in both axial locations throughout the interaction structure (from  $z = 0$  to  $z = L$ ) and time [3].

of light,  $n$  is the cyclotron harmonic number,  $B_0$  is the magnitude of the static axial magnetic field, and the subscript “0” denotes that the value is taken at the start of the interaction region.

Previously we saw that an electron beam which is uniform in phase space could not produce an rf field. However, a mildly relativistic interaction between an electron beam and a magnetic field in a resonator can produce a non-uniform, bunched, phase distribution which permits the generation of an oscillating RF field. The phase space is defined in the reference frame of the RF field (*e.g.* TE modes of an interaction cavity), which are assumed *a priori* to exist (*c.f.* Fig. 2-1). When entering the cavity, the electrons have an initially uniform azimuthal phase distribution and gyrate at the cyclotron frequency,  $\omega_c$ . This is depicted in Fig. 2-2 (a). Since the cyclotron frequency depends on the relativistic factor,  $\gamma$ , through (2.8), the electron will either gain or lose energy depending on its phase with respect to the RF field. Those electrons which are accelerated by the field gain energy, rotate at a lower frequency, and lag behind in phase; conversely, electrons which are decelerated by the field lose energy, rotate faster, and gain in phase. After a certain interaction time, the electrons are no longer uniformly distributed in phase (*c.f.* Fig. 2-2(b)). If the frequency of the RF electric field  $\omega_{RF}$  is slightly larger than the electron cyclotron frequency  $\omega_c$ , the electrons transfer a fraction of their rotational energy to the growing RF field (*c.f.* Fig. 2-1). Practically, this condition can be met by tuning the main magnetic field  $B_0$  to match the cavity radius. In the reverse case of  $\omega_c > \omega_{RF}$ , the wave loses energy to the electrons, an effect which can be productively exploited to produce a gyrotron amplifier. After the transverse energy is extracted from the electrons, they are no longer in phase (they lose their synchronism) with the RF wave,  $\omega_c$  has increased, and the interaction saturates.

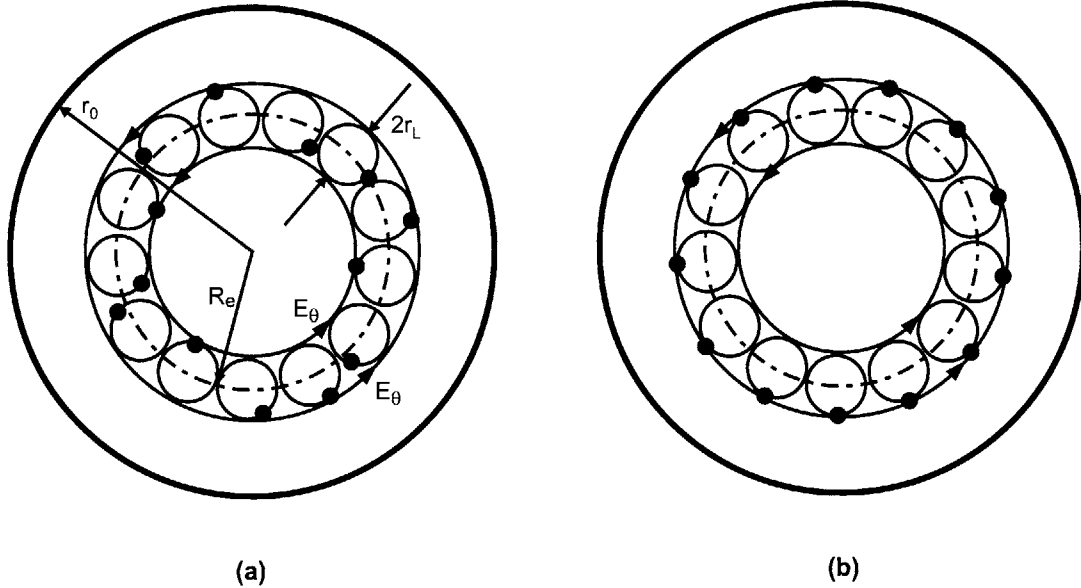


Figure 2-2: Cross-section of the beam geometry in the interaction region of a cylindrical resonant gyrotron cavity operating in the  $TE_{0,n}$  mode for (a) initial random phasing of electrons in their cyclotron orbits (b) electrons bunched in phase in their cyclotron orbits.

### 2.2.1 Harmonic CRM Interaction

In the previous section we considered only the case of fundamental electron cyclotron resonance. However, from the beam mode dispersion relation in (2.7), it is evident that the frequency of the electromagnetic field can be approximately equal to any integer harmonic  $n$  times the cyclotron frequency. The electric field can be expanded into a Fourier series in the polar coordinate system whose origin is the guiding center of electrons [4]

$$\mathbf{E}(r, \theta) = \sum \mathbf{E}_l(r) \exp(-il\theta) \quad (2.9)$$

where the  $l^{\text{th}}$  harmonic of this series describes the field rotating with an angular frequency  $\omega/l$ . The largest cumulative effect upon the electron motion is caused by the synchronous  $n^{\text{th}}$  azimuthal harmonic. Since the gyroradius is much smaller than the wavelength, the synchronous field has a quasi-static structure on the electron orbit and can be represented as a rotating  $n^{\text{th}}$  order multipole, where a dipole corresponds to fundamental cyclotron resonance, quadrupole to the second harmonic, hexapole to the third harmonic (*c.f.* Fig. 2-3), etc.

It can be demonstrated, following [46], that the component of the rf field which is synchronous with the gyrating electrons at the  $n^{\text{th}}$  cyclotron harmonic has a structure of an  $n$ -order rotating multipole. Consider a system of cylindrical symmetry where



the boundary condition at the resonator walls is given by  $\partial/\partial z = 0$ . The transverse field structure of a mode in this system can be determined by the membrane function  $\Psi$ , which satisfies the Helmholtz equation

$$\Delta_{\perp} \Psi + k_{\perp}^2 \Psi = 0. \quad (2.10)$$

If we take an arbitrary point  $(x_0, y_0)$  as the center of the local polar coordinates  $(r, \theta)$ , the membrane function can be expanded around this point into the Fourier series

$$\Psi = \sum_{l=-\infty}^{l=\infty} \Psi_l(r) e^{-il\theta}. \quad (2.11)$$

Since the rf fields under consideration are proportional to  $e^{i\omega t}$ , each sum in the series in (2.15) represents a rotating field. Following from the Helmholtz equation, the radial structure of the membrane function  $\Psi_l(r)$  in polar coordinates can be described by the Bessel function

$$\Psi_l(r) = L_l J_{|l|}(k_{\perp} r), \quad (2.12)$$

with the coefficients  $L_l$ <sup>1</sup>. Near the local center of the coordinate system (*i.e.* for very small  $r$ ), the Bessel function in (2.12) can be approximated as

$$J_{|l|}(k_{\perp} r) \simeq \left( \frac{1}{|l|!} \right) \left( \frac{k_{\perp} r}{2} \right)^{|l|}, \quad (2.13)$$

corresponding to a reduction of the Helmholtz equation to the Laplace equation

$$\Delta_{\perp} \Psi = 0. \quad (2.14)$$

In this limit, the Fourier series of the membrane function in (2.11) becomes the Taylor series,

$$\Psi = \Psi(x_0, y_0) + \sum_{l=-\infty}^{l=-1} \frac{L_l}{|l|!} \left( \frac{\rho}{2} \right)^{|l|} + \sum_{l=1}^{\infty} \frac{L_l}{|l|!} \left( \frac{\rho^*}{2} \right)^l, \quad (2.15)$$

where  $\rho = k_{\perp} [(x - x_0) + i(y - y_0)]$ . Therefore, it follows that the synchronous field for which the rf field frequency  $\omega$  is close to  $n\omega_e$  is proportional to  $|\rho|^n$ .

In summary, in order to have a harmonic interaction, the electric field must vary across the electron Larmor radius. Conversely, if the electric field does not vary across

---

<sup>1</sup>The coefficients  $L_l$  can be derived from [47] with the use of integral representations for the membrane and Bessel functions, where the action of the angle operator  $\hat{\nabla} = \frac{\partial}{\partial(k_{\perp} x)} + i \frac{\partial}{\partial(k_{\perp} y)}$  on the membrane function (2.15), accounting for the relations  $\hat{\nabla} \rho = 0$  and  $\hat{\nabla}^* \rho = 2$ , yields  $L_l = \hat{\nabla}^{*|l|} \Psi(x, y)$  for  $l < 0$  and  $L_l = \hat{\nabla}^{|l|} \Psi(x, y)$  for  $l > 0$ .

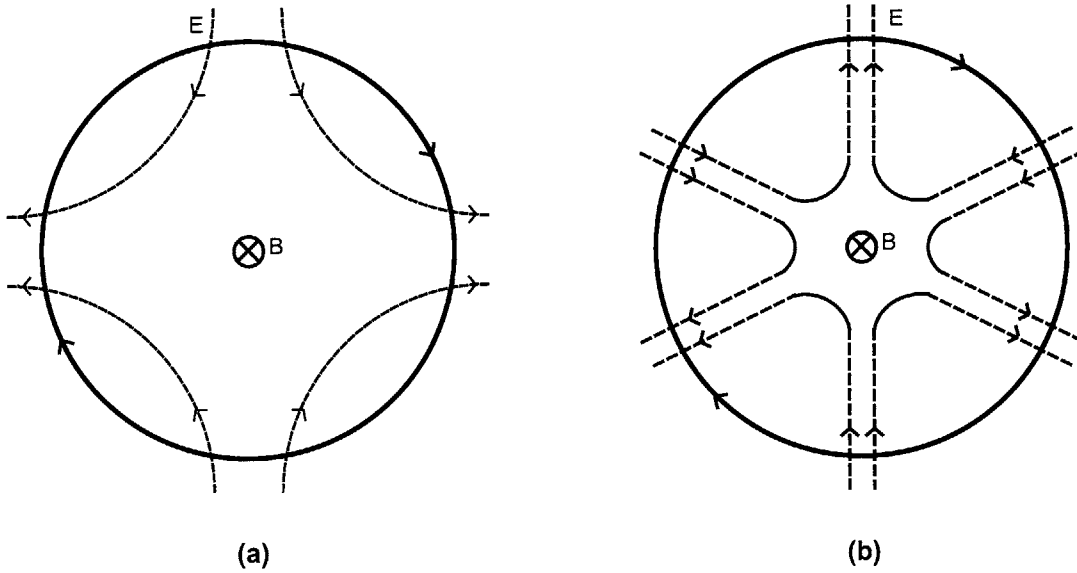


Figure 2-3: Electron motion for resonance at (a) second and (b) third cyclotron harmonics. The solid line shows the initial trajectory of electrons and the electric field is represented by dashed lines. Adapted from [4].

the Larmor orbit only the fundamental interaction term will be nonzero. In a second harmonic interaction, two phase bunches will be formed. In general, when operating at the  $n^{\text{th}}$  cyclotron harmonic, up to  $n$  bunches may be formed [48]. The modified gain and resonance conditions for operation at the  $n^{\text{th}}$  cyclotron harmonic are

$$\omega > n\omega_c \quad (2.16)$$

$$\omega \simeq n\omega_c \quad (2.17)$$

respectively.

## 2.3 Kinetic Theory

In the fluid theory treatment of a plasma, the dependent variables are functions of only four independent variables,  $x$ ,  $y$ ,  $z$ , and  $t$ , and the velocity distribution of all species is assumed to be Maxwellian. However, for species with non-Maxwellian distributions this assumption is inadequate. Therefore the kinetic theory adds three more independent variables,  $v_x$ ,  $v_y$ , and  $v_z$  to explicitly treat the velocity distribution, in our case of the electrons [49].

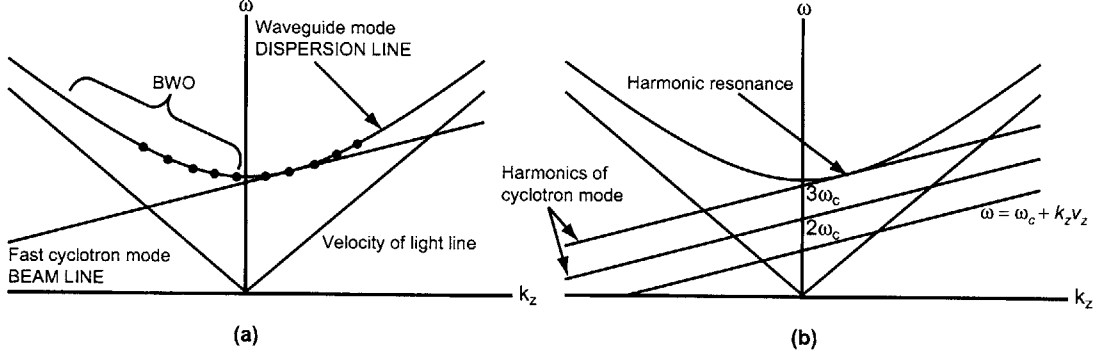


Figure 2-4: Dispersion diagram of a gyrotron oscillator showing the region of interaction between the fast waveguide mode and the beam cyclotron modes. (a) Fundamental beam cyclotron mode and waveguide mode intersect at fundamental resonance. The dots represent the longitudinal cavity modes. The intersection of the beam cyclotron modes with waveguide modes at negative values of  $k_z$  causes the excitation of backward wave oscillations. (b) The intersection of the third harmonic of the cyclotron mode with the waveguide mode gives rise to a third harmonic interaction.

### 2.3.1 Linearized Dispersion Relation

The coupled dispersion relation for TE modes in a cylindrical waveguide has been derived using a kinetic approach for an electron beam drifting in a cylindrical waveguide with an applied axial magnetic field. This theory is detailed in [50, 51, 52, 53] and is insightful in predicting the regime of dominance of the CRM instability over the competing Weibel instability.

The present treatment follows the derivation of [52] and uses the MKS conventions for TE modes in cylindrical waveguide, assuming that the beam is sufficiently tenuous that its space charge electric field can be neglected, and the spatial structure of the waveguide mode is unaffected by the presence of the beam. We also assume that the beam interacts with a single  $TE_{m,p}$  mode.

A linear dispersion relation can be derived by solving the linearized relativistic Vlasov-Boltzmann equation with the perturbed electron distribution function in the presence of an electromagnetic wave. The linearized relativistic Vlasov-Boltzmann equation is given by

$$\frac{df_1}{dt}(\mathbf{r}, \mathbf{p}, t) = e(\mathbf{E} + \mathbf{v} \times \mathbf{B}) \cdot \nabla_p f_0(\mathbf{r}, \mathbf{p}, t) \quad (2.18)$$

where, since  $f$  is a function of seven variables,

$$\frac{df}{dt} = \frac{\partial f}{\partial t} + \frac{\partial f}{\partial x} \frac{dx}{dt} + \frac{\partial f}{\partial y} \frac{dy}{dt} + \frac{\partial f}{\partial z} \frac{dz}{dt} + \frac{\partial f}{\partial v_x} \frac{dv_x}{dt} + \frac{\partial f}{\partial v_y} \frac{dv_y}{dt} + \frac{\partial f}{\partial v_z} \frac{dv_z}{dt} \quad (2.19)$$

thus the operator  $\frac{d}{dt}$  is defined as

$$\frac{d}{dt} \equiv \frac{\partial}{\partial t} + \mathbf{v} \cdot \nabla - e\mathbf{v} \times B_0 \hat{\mathbf{z}} \cdot \nabla_p \quad (2.20)$$

$\nabla_p$  is the gradient in momentum space,

$$\nabla_p = \frac{\partial}{\partial \mathbf{p}} = \hat{\mathbf{x}} \frac{\partial}{\partial p_x} + \hat{\mathbf{y}} \frac{\partial}{\partial p_y} + \hat{\mathbf{z}} \frac{\partial}{\partial p_z} \quad (2.21)$$

$f$  is the electron distribution function,  $\mathbf{v}$  and  $\mathbf{p}$  are the electron velocity and momentum, and  $\mathbf{E}$  and  $\mathbf{B}$  are the waveguide RF fields.

From Maxwell's equations, the linearized wave equation with a source present for a TE mode can be written as

$$\nabla^2 \mathbf{H}_1 - \frac{1}{c^2} \frac{\partial^2}{\partial t^2} \mathbf{H}_1 = \nabla \times \mathbf{J}_1 \quad (2.22)$$

and the perturbed current density is given by

$$\mathbf{J}_1 = -e \int f_1 \mathbf{v}_1 d^3 p. \quad (2.23)$$

The distribution function can be represented as the sum of an equilibrium term  $f_0$  and a perturbation  $f_1$ ,

$$f(\mathbf{r}, \mathbf{p}, t) = f_0(\mathbf{r}, \mathbf{p}) + f_1(\mathbf{r}, \mathbf{p}, t) \quad (2.24)$$

and the distribution function of the unperturbed electron beam can be represented as

$$f_0 = \sigma_0 h_0(r_0) g_0(p_\perp, p_z) \quad (2.25)$$

where for a cold, thin annular beam with no momentum spread and no guiding center spread,  $h_0$  and  $g_0$  are given by

$$h_0(r_0) = A_b \frac{1}{r_0} \delta(r_0 - r_b) \quad (2.26)$$

$$g_0(p_\perp, p_z) = \frac{1}{2\pi p_\perp} \delta(p_\perp - p_{\perp 0}) \delta(p_z - p_{z0}) \quad (2.27)$$

where  $A_b$  is the area of the beam cross-section,  $r_b$  is the average beam radius, and  $p_{\perp 0}$  and  $p_{z0}$  are the average transverse and longitudinal momentum, respectively.

Using standard procedures, the cold beam dispersion relation for a  $\text{TE}_{m,p}$  mode

can be obtained by solving (2.18), (2.22), and (2.23);

$$(\omega^2 - k_{\perp}^2 c^2 - k_z^2 c^2) = -\frac{f_{bw}\omega_p^2}{K_{mp}\gamma_0} \left[ \frac{(\omega^2 - k_z^2 c^2) \beta_{\perp 0}^2 H_{nm}}{\left(\omega - k_z v_{z0} - \frac{s\omega_c}{\gamma_0}\right)^2} - \frac{(\omega - k_z v_{z0}) Q_{nm}}{\left(\omega - k_z v_{z0} - \frac{s\omega_c}{\gamma_0}\right)} \right] \quad (2.28)$$

where  $H_{nm}$ ,  $Q_{nm}$ , and  $K_{mp}$  are defined as

$$H_{nm} = J_{n-m}^2(k_{\perp} r_0) J_n'^2(k_{\perp} r_L) \quad (2.29)$$

$$Q_{nm} = 2J_{n-m}^2(k_{\perp} r_0) [J_n'^2(k_{\perp} r_L) + k_{\perp} r_L J_n'(k_{\perp} r_L) J_n''(k_{\perp} r_L)] \quad (2.30)$$

$$K_{mp} = \left(1 - \frac{m^2}{\nu_{mp}^2}\right) J_m^2(\nu_{mp}) \quad (2.31)$$

$\nu_{mp}$  is the  $p^{\text{th}}$  zero of  $J_m'$ , the beam-waveguide fill factor is given by

$$f_{bw} = \frac{A_b}{\pi r_w^2} \quad (2.32)$$

and the plasma frequency is given by

$$\omega_p^2 = \frac{\sigma_0 e^2 \mu_0 c^2}{m_0}. \quad (2.33)$$

From the dispersion relation we learn that two bunching mechanisms are simultaneously present, an axial bunching due to  $\Delta v_z$  and an azimuthal bunching due to  $\Delta\gamma$  [50]. The azimuthal bunching is known as the cyclotron resonance maser (CRM) instability and the axial bunching is known as the Weibel instability [54, 55]. The regime where azimuthal bunching dominates is characterized by [50]

$$\frac{\omega^2}{k_z^2} > c^2 \quad (2.34)$$

and the regime where axial bunching dominates is characterized by

$$\frac{\omega^2}{k_z^2} < c^2. \quad (2.35)$$

It is interesting to note that the relativistic effects of the CRM instability may be dominant at nonrelativistic energies [50].

The dispersion relation (2.28) is valid for any  $\text{TE}_{m,p}$  mode and with harmonic number  $n$ . In comparison of (2.28) and its non-relativistic cousin, it is evident that

the  $\omega^2$  in the numerator of the first term of the R.H.S. of (2.28) is due to the inclusion of the relativistic mass factor  $\gamma$  and results in the cyclotron resonance maser instability [50]. The second term of the R.H.S. of (2.28) imposes a threshold beam energy for the cyclotron resonance maser instability [51].

## 2.4 Single-Particle Theory

While a dense plasma has many properties of a fluid, as shown in the kinetic theory of the previous section, a low density plasma can also be described by single-particle trajectories, and collective effects become unimportant. A single-particle description of the gyrotron oscillator can be found in [56, 4, 57, 58], and this section will closely follow the derivations in [58].

For an electron moving in a uniform electric and magnetic field, its motion will be the sum of a circular Larmor motion with a drift of guiding center. The equations for the momentum and energy of a single electron can be expressed as

$$\frac{d\mathbf{p}}{dt} = -e(\mathbf{E} + \mathbf{v} \times \mathbf{B}) \quad (2.36)$$

$$\frac{d\mathcal{E}}{dt} = -e\mathbf{v} \cdot \mathbf{E} \quad (2.37)$$

where  $\mathcal{E}$  ( $= \gamma mc^2$ ) is the electron energy,  $\mathbf{p}$  ( $= \gamma m\mathbf{v}$ ) is the electron momentum, and  $\gamma$  ( $= 1/\sqrt{1 - v^2/c^2}$ ) is the relativistic factor.

With a uniform magnetic field  $\mathbf{B}_0\hat{\mathbf{z}}$  in the axial direction, these equations describe a simple harmonic oscillator, where the charged particle then obeys the following parametric equations of motion:

$$x = x_0 + r_L \cos(\omega_c t + \phi) \quad (2.38)$$

$$y = y_0 + r_L \sin(\omega_c t + \phi) \quad (2.39)$$

$$z = z_0 + \gamma t. \quad (2.40)$$

The particle traces out a helical path gyrating at the relativistic cyclotron frequency,

$$\omega_c = \frac{eB_0}{\gamma m} \quad (2.41)$$

about a guiding center with a gyration (Larmor) radius of

$$r_L = \frac{v_\perp}{\omega_c} = \frac{\gamma m v_\perp}{eB_0}. \quad (2.42)$$

Redefining the dependent and independent variables according to [4],  $u$  and  $\zeta$  become the normalized energy and axial position variables, respectively;

$$u \equiv \frac{2}{\beta_{\perp 0}^2} \left( 1 - \frac{\gamma}{\gamma_0} \right) \quad (2.43)$$

$$\zeta \equiv \pi \left( \frac{\beta_{\perp 0}^2}{\beta_{z0}} \right) \left( \frac{z}{\lambda} \right) \quad (2.44)$$

and the normalized interaction length becomes

$$\mu \equiv \pi \left( \frac{\beta_{\perp 0}^2}{\beta_{z0}} \right) \left( \frac{L}{\lambda} \right) \quad (2.45)$$

where  $\beta_{\perp 0}$  ( $= v_{\perp 0}/c$ ) is the normalized transverse velocity of the electrons,  $L$  is the effective length over which the interaction occurs,  $\lambda$  is the wavelength, and the subscript 0 denotes the initial value of the quantity under consideration in the interaction region.

Using this transformation and for a weakly relativistic electron beam characterized by  $n\beta_{\perp 0}^2 \ll 1$ , the equations of motion in (2.36) and (2.37) can be re-written as [58]

$$\frac{du}{d\zeta} = 2Ff(\zeta)(1-u)^{\frac{n}{2}} \sin \theta \quad (2.46)$$

$$\frac{d\theta}{d\zeta} = \Delta - u - nFf(\zeta)(1-u)^{\frac{n}{2}-1} \cos \theta \quad (2.47)$$

where the slow-time scale phase variable  $\theta$  has been introduced,

$$\theta = \omega t - n\phi \quad (2.48)$$

with  $\phi$  being the phase of the electron in its Larmor orbit,  $n$  is the cyclotron harmonic number, and  $F$  is the normalized field amplitude defined by

$$F \equiv \frac{E_0}{B_0} \beta_{\perp 0}^{n-4} \left( \frac{n^{n-1}}{n! 2^{n-1}} \right) J_{m \pm n}(k_{\perp} R_e). \quad (2.49)$$

The minus and plus signs in the Bessel function subscript correspond to the co- and counter-rotations of the rf field,  $E_0$  is the amplitude of the electric field,  $B_0$  is the magnitude of the static axial magnetic field,  $n$  is the cyclotron harmonic number,  $k_{\perp}$  ( $= \nu_{mp}/r_0$ ) is the transverse propagation constant,  $R_e$  is the average beam radius,  $m$  is the radial index of the TE mode, and  $J$  is the Bessel function of the first kind. The longitudinal field profile described by  $f(\zeta)$  is an arbitrary function, but is often approximated by a Gaussian for field distributions with a single axial maximum or

a sinusoid, for axially varying fields. The initial conditions are  $\theta = \theta_0 \in [0, 2\pi)$  and  $u = 0$ . The detuning parameter is given by

$$\Delta = \frac{2}{\beta_{\perp}^2} \left( 1 - \frac{n\omega_c}{\omega} \right). \quad (2.50)$$

The electronic efficiency of the gyrotron oscillator is given by

$$\eta \equiv \frac{\gamma_0 - \gamma}{\gamma_0 - 1} = \left[ \frac{\beta_{\perp 0}^2}{2(1 - \gamma_0^{-1})} \right] \eta_{\perp}. \quad (2.51)$$

The transverse efficiency is the fraction of transverse electron energy transferred to the resonator field. Expressed as

$$\eta_{\perp} = \langle u(\zeta_{\text{out}}) \rangle_{\theta_0} \quad (2.52)$$

it depends only on three parameters:  $F$ ,  $\mu$ , and  $\Delta$ . The position  $\zeta_{\text{out}}$  is the end of the resonator and the brackets  $\langle \rangle_{\theta_0}$  denote an average over initial phase. When the efficiency is optimized with respect to the magnetic field parameter  $\Delta$ , the optimal value is denoted as  $\Delta_{\text{opt}}$ . The transverse efficiency then depends upon only  $F$  and  $\mu$ . Isoefficiency contour plots have been generated for the first five cyclotron harmonics as  $\eta_{\perp}(F, \mu)$  and  $\eta_{\perp}(I, \mu)$  in [59]. For the second harmonic interaction, peak perpendicular efficiencies of over 70% are theoretically possible [58].

The total quality factor of the cavity,  $Q_T$ , is related to the total stored energy  $U$  of the mode and the average power  $P$  dissipated per radian of the mode as

$$Q_T = \frac{\omega U}{P}. \quad (2.53)$$

The dissipated power  $P$ , or the total stored energy of the resonator, can be expressed as

$$P = \eta I_A V = \frac{mc^2}{e} \frac{\gamma_0 \beta_{\perp 0}^2}{2} \eta_{\perp} I_A \quad (2.54)$$

where  $I_A$  is the beam current in amperes and  $V$  is the cathode voltage in volts. The beam current can be related to the field amplitude  $F$  by an energy balance equation,

$$F^2 = \eta_{\perp} I. \quad (2.55)$$

We assume that the axial field profile has a single axial maximum and can be approx-



imated by a Gaussian of the form

$$f(\zeta) = e^{-(k_z z)^2} = e^{-(2\zeta/u)^2} \quad (2.56)$$

where  $k_z = 2/L$ . The normalized current parameter  $I$  for a Gaussian axial field profile can be written as

$$I = 0.238 \times 10^{-3} \left( \frac{Q_T I_A}{\gamma_0} \right) \beta_{\perp 0}^{2(n-3)} \left( \frac{\lambda}{L} \right) \left( \frac{n^n}{2^n n!} \right)^2 C_{m,p}^2 \quad (2.57)$$

where  $C_{m,p}$  is the beam-wave coupling factor

$$C_{m,p}^2 = \frac{J_{m\pm n}^2(k_{\perp} R_e)}{(\nu_{mp}^2 - m^2) J_m^2(\nu_{mp})}. \quad (2.58)$$

The “ $\pm$ ” sign in (2.58) refers to the counter- and co-rotating  $\text{TE}_{m,p}$  waves, respectively.

## 2.4.1 Start Oscillation Current

The starting current is defined as the minimum electron beam current needed to overcome the dissipative processes in the cavity and excite a given transverse electric mode. This threshold is obtained on energy conservation grounds by equating the dissipative relationship implied in (2.53) with the beam-wave power transfer governed by

$$P = -\frac{1}{2} \text{Re} \left\{ \int \mathbf{E}^* \cdot \mathbf{J} \, d\mathbf{r} \, d\mathbf{p} \right\} \quad (2.59)$$

where  $\mathbf{E}$  is the cavity electric field,  $\mathbf{J}$  ( $= e\mathbf{v}f(\mathbf{r}, \mathbf{p}, t)$ ) is the current density, and  $f(\mathbf{r}, \mathbf{p}, t)$  is the electron distribution function.

From the linear theory of the gyrotron oscillator, the start oscillation current of a gyrotron operating in the  $n^{\text{th}}$  cyclotron harmonic is given in terms of the normalized current parameter  $I$ , by [45, 58]

$$I = I_{\text{st}}(\Delta, \mu) = \frac{4}{\pi \mu^2} \frac{e^{2x^2}}{\mu x - n} \quad (2.60)$$

where  $x = \mu\Delta/4$ . Since the starting current is a function of both the detuning parameter  $\Delta$  and  $\mu$ , we can minimize (2.60) with respect to  $\Delta$  to obtain  $I_{\text{st}}(\Delta_{\text{min}})$ ,

yielding an  $x$  parameter,

$$x = x_{\min} = \frac{1}{2} \left( \frac{n}{\mu} + \sqrt{\frac{n^2}{\mu^2} + 1} \right). \quad (2.61)$$

For both the fundamental and second electron cyclotron harmonic, the minimum starting current, in amperes, for a Gaussian axial field profile with a single axial maximum, as a function of the magnetic field detuning can be simplified to

$$I_{\text{start}}(\Delta, \mu) = 8.56 \times 10^4 \frac{\exp \left[ \frac{1}{8} (\mu\Delta)^2 \right]}{\mu^2 (\mu^2 \Delta - 4n)} \left( \frac{\gamma_0}{Q_T} \right) \beta_{10}^{2(3-n)} \times \left( \frac{L}{\lambda} \right) C_{m,p}^{-2} \quad (2.62)$$

and  $R_e$  is the electron beam radius. A similar theory, derived for the case of fixed sinusoidal axial field profiles, can be applied to calculate linear starting currents for higher order axial modes [60].

## 2.4.2 Ohmic Losses

The total efficiency of a gyrotron is the ratio of the output rf power to the input beam power,

$$\eta_{\text{out}} = \frac{P_{\text{out}}}{P_{\text{in}}} = \eta_{\text{el}} \times \eta_Q. \quad (2.63)$$

The electronic efficiency,  $\eta_{\text{el}}$ , accounts for the fraction of beam power in the perpendicular direction and  $\eta_Q$  is the reduction due to ohmic losses [61]. The electronic efficiency is given by

$$\eta_{\text{el}} = \frac{\beta_0^2}{2(1 - \gamma_0^{-1})} \eta_{\perp} \quad (2.64)$$

and  $\eta_Q$  is the reduction in efficiency due to ohmic losses given by

$$\eta_Q = 1 - \frac{Q_T}{Q_{\text{ohm}}}. \quad (2.65)$$

The total  $Q$  of a resonant cavity is given by

$$\frac{1}{Q_T} = \frac{1}{Q_{\text{ohm}}} + \frac{1}{Q_{\text{diff}}}. \quad (2.66)$$

The ohmic  $Q$  of a  $\text{TE}_{m,p}$  mode is given by

$$Q_{\text{ohm}} = \frac{r_0}{\delta} \left( 1 - \frac{m^2}{\nu_{mp}^2} \right) \quad (2.67)$$

where  $\delta (= (\pi f \mu_0 \sigma)^{-\frac{1}{2}})$  is the skin depth. The diffractive  $Q$  for modes which have minimal diffraction losses and only one field variation on the length of the resonator is given by

$$Q_D = 4\pi \frac{\left(\frac{L}{\lambda}\right)^2}{1 - |R_{1,2}|}, \quad (2.68)$$

where  $R_{1,2}$  is the wave reflection coefficient of the input and output cross-sections of a resonator.

In a long wavelength gyrotron, the total  $Q$  is approximately equivalent to the diffractive  $Q$ , resulting in negligible ohmic losses. However at short wavelengths, the ohmic losses can severely reduce the output power of a gyrotron.

## 2.5 Quantum Mechanical Basis of the Cyclotron Resonance Maser

Up to now, we have classically treated the cyclotron resonance maser interaction. However, from a quantized viewpoint, radiation occurs by stimulated emission within the quantized eigenspectrum of the electron in a magnetic field. The motion of a charged particle in a magnetic field was first treated by Landau. The magnetic field,  $\mathbf{B}(\mathbf{r})$ , is defined up to the gradient of an arbitrary function through the vector potential,  $\mathbf{A}(\mathbf{r})$ ,

$$\mathbf{B}(\mathbf{r}) = \nabla \times \mathbf{A}(\mathbf{r}). \quad (2.69)$$

The Hamiltonian operator and the operator for the particle velocity are then given in (2.70) and (2.71):

$$\mathcal{H} = \frac{1}{2\mu} (\mathbf{P} - e\mathbf{A})^2 \quad (2.70)$$

$$\mathbf{V} = \frac{1}{\mu} (\mathbf{P} - e\mathbf{A}) \quad (2.71)$$

For  $\mathbf{B}(\mathbf{r}) = \hat{\mathbf{z}}B_z$  and motion perpendicular to the magnetic field, (2.70) becomes

$$\mathcal{H} = \frac{\mu}{2} (V_x^2 + V_y^2). \quad (2.72)$$

Commutators of elements of the velocity operator can be derived from canonical commutation relations; for the problem constructed, they are given in (2.73) and

(2.74),

$$[V_x, V_z] = [V_y, V_z] = 0 \quad (2.73)$$

$$[V_x, V_y] = -i \frac{\hbar \Omega_c}{\mu} \quad (2.74)$$

in which  $\Omega_c = eB_z/\mu$ .

The eigenspectrum of (2.72) can be obtained by analogy to the one-dimensional harmonic oscillator. In particular, we define,

$$X = \sqrt{\frac{\mu}{\hbar \Omega_c}} V_x \quad (2.75)$$

$$P = \sqrt{\frac{\mu}{\hbar \Omega_c}} V_y \quad (2.76)$$

such that the operators  $X$  and  $P$  now obey,

$$[X, P] = i \quad (2.77)$$

and the Hamiltonian (2.72) is now identical to that of the one-dimensional harmonic oscillator,

$$\mathcal{H} = \frac{\hbar \Omega_c}{2} (X^2 + P^2). \quad (2.78)$$

In (2.78), the classical cyclotron resonance frequency is given by

$$\Omega_c = e \frac{B_z}{\mu}. \quad (2.79)$$

The eigenvalues of (2.72), defining motion in the plane orthogonal to the magnetic field, are

$$E = \left( n + \frac{1}{2} \right) \hbar \Omega_c. \quad (2.80)$$

This harmonic quantization of the energy of a charged particle moving in a homogeneous magnetic field is named for Landau. We now consider the possibility that an ensemble of initially monoenergetic electrons can lose energy to an electromagnetic field in the presence of a strong magnetic field, a situation corresponding to stimulated emission. The energy absorbed by an electron from the radiation field over the interaction time,  $t$ , is

$$W = \hbar [\omega_{n,n+1} P_{n,n+1} - \omega_{n,n-1} P_{n,n-1}]. \quad (2.81)$$

The transition probabilities,  $P_{n,n+1}$  and  $P_{n,n-1}$ , which appear in (2.81) are given by expressions of the form

$$P_{n,n+1} = \frac{E_0^2 t^2}{\hbar^2} \mu_{n,n+1}^2 g_\omega(\omega_{n,n+1}), \quad (2.82)$$

where  $\mu_{n,n+1}$  is the transition dipole moment for the harmonic oscillator,  $E_0$  is the magnitude of the electric field, and  $g_\omega(\omega_{n,n+1})$  is an approximate lineshape function, given by,

$$g_\omega(\omega_{n,n+1}) \simeq \frac{\sin^2 \left( (\omega_{n,n+1} - \omega) \frac{t}{2} \right)}{\left( (\omega_{n,n+1} - \omega) \frac{t}{2} \right)^2}, \quad (2.83)$$

where, in (2.83), we have neglected the counter-rotating component of the electric field. Substituting (2.83) into (2.81), we can obtain an expression for the total energy absorbed by the electron in terms of fundamental parameters of the system:

$$W \simeq \frac{e^2 E_0^2 t^2}{2\mu} [n(g_\omega(\omega_{n,n+1}) - g_\omega(\omega_{n,n-1})) + g_\omega(\omega_{n,n+1})] \quad (2.84)$$

From (2.84), it is clear that energy can only be given up to the field if the quantity  $(g_\omega(\omega_{n,n+1}) - g_\omega(\omega_{n,n-1}))$  is negative. However, we have already shown in (2.80) that the eigenvalues of the electron in a magnetic field are evenly spaced, and hence  $g_\omega(\omega_{n,n+1}) = g_\omega(\omega_{n,n-1}) = g_\omega(\Omega_c)$ , which implies that  $W$  is purely absorptive. By this reasoning, there can be no loss of energy to the field and no cyclotron resonance maser effect unless the eigenspectrum of the electron in a magnetic field is anharmonic. Fortunately, such a situation can arise for a relativistic electron in a homogeneous magnetic field [62, 63, 64, 34]. In this case, the electron obeys the Dirac equation,

$$\left( \gamma_\mu \partial_\mu + \frac{mc}{\hbar} \right) \psi = 0 \quad (2.85)$$

which, in the presence of an electromagnetic field, becomes:

$$\left( \partial_\mu - \frac{ie}{\hbar c} A_\mu \right) \gamma_\mu \psi + \frac{mc}{\hbar} \psi = 0. \quad (2.86)$$

In (2.86), we have made the usual Gauge-invariant, Lorentz-covariant substitution for the electromagnetic field in the form  $-i\hbar\partial_\mu \rightarrow -i\hbar\partial_\mu - eA_\mu/c$ . In the correct gauge and using appropriate explicit representations of the matrices  $\gamma_\mu$ , the problem in (2.86) can be solved in analogy to the Schrödinger harmonic oscillator using transfor-

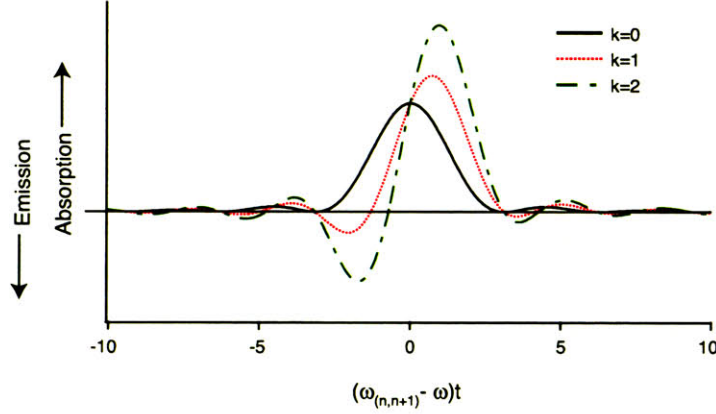


Figure 2-5: Cyclotron resonance for varying values of the parameter  $k = \frac{n\hbar\Omega_c^2}{2\mu c^2}$  according to equation (2.84), where terms of order  $(\hbar\Omega_c/m_0c)^2$  have been neglected. Note that a completely absorptive line is recovered in the non-relativistic limit.

mations very similar to those defined in (2.75) and (2.76) for the non-relativistic case.<sup>2</sup> The solution to (2.86) requires that the kinetic energy of the electron be quantized according to,

$$E \simeq m_0c^2 \sqrt{\left[1 + 2 \left(n + \frac{1}{2}\right) \left(\frac{\hbar\Omega_c}{m_0c^2}\right)\right]} - m_0c^2 \quad (2.90)$$

where  $m_0$  is the electron rest mass and all other parameters have been defined in the non-relativistic solution. The important consequence of this result is that the energy levels of the relativistic electron are not evenly spaced, and hence we can expect stimulated emission as defined in (2.84). For our purposes, this means that radiation can be produced from even a weakly relativistic beam of electrons, as shown in Figure 2-5. The gyrotron oscillator is one realization of a cyclotron resonance maser based on this effect.

<sup>2</sup>Specifically, if we use an explicit representation of the Dirac matrices as

$$\gamma_0 = \begin{bmatrix} I & 0 \\ 0 & -I \end{bmatrix} \quad (2.87)$$

$$\vec{\gamma}_0 = \begin{bmatrix} 0 & \vec{\sigma} \\ \vec{\sigma} & 0 \end{bmatrix}, \quad (2.88)$$

set  $A_\mu = (0, 0, B_x, 0)$ , and make the *ansatz*

$$\phi(x) = e^{i(P_y y + P_z z)} f(x), \quad (2.89)$$

for the spinor  $\psi = \begin{bmatrix} \phi \\ \chi \end{bmatrix}$ , then the Dirac problem in two-component representation can be solved by analogy harmonic oscillator problem.

## 2.6 Waveguide Theory

The simplest geometry of a gyrotron resonator is a cylinder consisting of a straight section of length  $L$  and circular cross-section of radius  $r_0$  joined to a linearly uptapered section and a linearly downtapered section at the entrance. Therefore we can use cylindrical waveguide theory to simplify our analysis. Even though these cavities can support many resonant electromagnetic modes, we can simplify still further; gyrotrons are operated close to cutoff with  $k_{\perp} \gg k_z$ , hence transverse magnetic (TM) modes are suppressed in favor of transverse electric (TE) modes. Therefore only the TE modes of the cavity RF field need to be calculated to understand the interaction that takes place in the gyrotron interaction structure.

The fields of a cylindrical circular metallic waveguide cavity in a  $\text{TE}_{m,p}$  mode can be calculated as follows. Starting with Maxwell's equations in differential vector form;

$$\nabla \times \mathbf{E} = -\frac{\partial \mathbf{B}}{\partial t} \quad (2.91)$$

$$\nabla \times \mathbf{H} = \frac{\partial \mathbf{D}}{\partial t} + \mathbf{J} \quad (2.92)$$

$$\nabla \cdot \mathbf{B} = 0 \quad (2.93)$$

$$\nabla \cdot \mathbf{D} = \rho \quad (2.94)$$

we assume a source free environment ( $\mathbf{J} = \rho = 0$ ), a time harmonic form ( $e^{i\omega t}$ ), and the constitutive relations

$$\mathbf{B} = \mu_0 \mathbf{H} \quad (2.95)$$

$$\mathbf{D} = \epsilon_0 \mathbf{E} \quad (2.96)$$

such that Maxwell's equations can be re-written as;

$$\nabla \times \mathbf{E} = -i\omega\mu_0 \mathbf{H} \quad (2.97)$$

$$\nabla \times \mathbf{H} = i\omega\epsilon_0 \mathbf{E} \quad (2.98)$$

$$\nabla \cdot \mathbf{H} = 0 \quad (2.99)$$

$$\nabla \cdot \mathbf{E} = 0. \quad (2.100)$$

By taking the curl of (2.98), substituting in the curl of (2.97), and using the identity  $\epsilon_0\mu_0 = 1/c^2$ , we derive the wave equation,

$$\nabla^2 \mathbf{H} + \frac{\omega^2}{c^2} \mathbf{H} = 0. \quad (2.101)$$

Writing the  $z$ -component of the wave equation in cylindrical coordinates,

$$\frac{\partial^2 H_z}{\partial r^2} + \frac{1}{r} \frac{\partial H_z}{\partial r} + \frac{1}{r^2} \frac{\partial^2 H_z}{\partial \varphi^2} + \frac{\omega^2}{c^2} H_z + \frac{\partial^2 H_z}{\partial z^2} = 0 \quad (2.102)$$

and assuming that  $H_z$  is of the form  $H_z = B(r, \varphi) f(z)$ , we find a generating equation  $H_z$  that is a solution to (2.102)

$$H_z = J_m \left( \frac{\nu_{mp}}{r_0} r \right) e^{im\varphi} f(z). \quad (2.103)$$

Writing Maxwell's equations in terms of each component  $(r, \varphi, z)$ , with  $E_z = 0$  since we are solving for the  $\text{TE}_{m,p}$  case, we can solve for the remainder of the  $E$  and  $H$  components. First we formulate an equation for  $E_r$  in terms of  $H_z$ ,

$$\frac{\partial^2 E_r}{\partial z^2} + \frac{\omega^2}{c^2} E_r = -i\omega\mu_0 \frac{1}{r} \frac{\partial H_z}{\partial \varphi}. \quad (2.104)$$

Substituting (2.103) into (2.104) we solve for  $E_r$ ,

$$E_r = \frac{m}{\omega\epsilon_0} \frac{1}{r} J_m \left( \frac{\nu_{mp}}{r_0} r \right) e^{im\varphi} f(z). \quad (2.105)$$

Now we can also solve for  $H_\varphi$  using

$$H_\varphi = -\frac{1}{\omega\mu_0} \frac{\partial E_r}{\partial z} \quad (2.106)$$

$$= i \frac{mc^2}{\omega^2} \frac{1}{r} J_m \left( \frac{\nu_{mp}}{r_0} r \right) e^{im\varphi} f'(z). \quad (2.107)$$

$E_\varphi$  follows from

$$\frac{\partial^2 E_\varphi}{\partial z^2} - i\omega\mu_0 \frac{\partial H_z}{\partial r} = -\omega^2 \epsilon_0 \mu_0 E_\varphi \quad (2.108)$$

where we can ignore the first term since  $k_z \ll k_\perp$ . Substituting in (2.103),

$$E_\varphi = i \sqrt{\frac{\mu_0}{\epsilon_0}} J'_m \left( \frac{\nu_{mp}}{r_0} r \right) e^{im\varphi} f(z) \quad (2.109)$$

where  $\omega/c \simeq \nu_{mp}/r_0$ . Finally,  $H_r$  can be solved from

$$H_r = \frac{1}{i\omega\mu_0} \frac{\partial E_\varphi}{\partial z} \quad (2.110)$$

$$= \frac{1}{\omega c} J'_m \left( \frac{\nu_{mp}}{r_0} r \right) e^{im\varphi} f'(z). \quad (2.111)$$



Summarizing these results, we have

$$E_r = \frac{m}{\omega \epsilon_0} \frac{1}{r} J_m \left( \frac{\nu_{mp}}{r_0} r \right) e^{im\varphi} f(z) \quad (2.112)$$

$$E_\varphi = i \sqrt{\frac{\mu_0}{\epsilon_0}} J'_m \left( \frac{\nu_{mp}}{r_0} r \right) e^{im\varphi} f(z) \quad (2.113)$$

$$E_z = 0 \quad (2.114)$$

$$H_r = \frac{1}{\omega c} J'_m \left( \frac{\nu_{mp}}{r_0} r \right) e^{im\varphi} f'(z) \quad (2.115)$$

$$H_\varphi = i \frac{mc^2}{\omega^2} \frac{1}{r} J_m \left( \frac{\nu_{mp}}{r_0} r \right) e^{im\varphi} f'(z) \quad (2.116)$$

$$H_z = J_m \left( \frac{\nu_{mp}}{r_0} r \right) e^{im\varphi} f(z) \quad (2.117)$$

where  $\omega$  is the angular resonant frequency,  $r$  is the radial cavity position,  $a$  is the cavity radius,  $k_\perp (= \nu_{mp}/r_0)$  is the transverse wave number,  $\nu_{mp}$  is the  $p^{\text{th}}$  zero of  $J'_m$ ,  $J_m$  is a Bessel function of the ordinary type,  $m$  is the azimuthal mode index, and  $p$  is the radial mode index. The above equations satisfy the boundary conditions of zero tangential  $E$ -field or perpendicular  $H$ -field at the waveguide wall,  $r = r_0$ . For fixed end walls of the resonator (at  $z = 0$  and  $L$ ), the function  $f(z)$  is satisfied by

$$f(z) = \sin \left( \frac{q\pi}{L} z \right) \quad (2.118)$$

for  $q$  and integer larger than zero. For an open resonator, we can use a Gaussian approximation, justified by numerical simulation, that

$$f(z) \approx e^{-4z^2/L^2}. \quad (2.119)$$

Using these equations, intensity patterns of the five lowest order transverse electric (TE) waveguide modes; the  $\text{TE}_{1,1}$ ,  $\text{TE}_{2,1}$ ,  $\text{TE}_{0,1}$ ,  $\text{TE}_{3,1}$ , and  $\text{TE}_{4,1}$ ; have been calculated and are shown in Fig. 2-6.

## 2.7 Numerical Methods

Several academic gyrotron-related computer codes were used for both design and analysis in the course of this work and are described in this section.

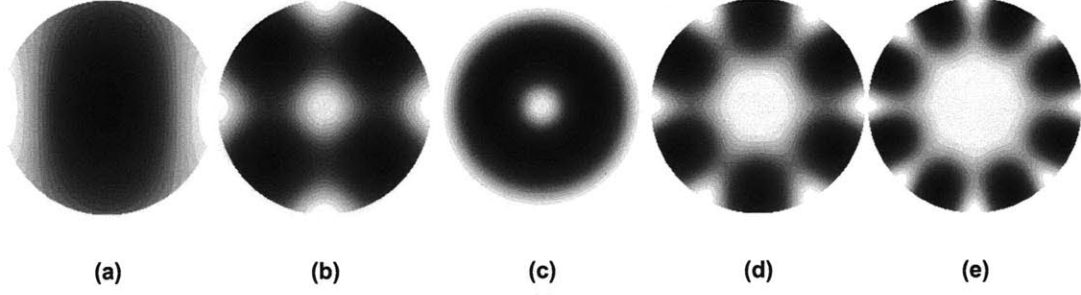


Figure 2-6: Intensity patterns of the five lowest order transverse electric (TE) waveguide modes; (a)  $TE_{1,1}$ , (b)  $TE_{2,1}$ , (c)  $TE_{0,1}$ , (d)  $TE_{3,1}$ , and (e)  $TE_{4,1}$ .

### 2.7.1 Cold Cavity

The cold cavity code solves for the electromagnetic fields of a weakly irregular resonant structure in the absence of an electron beam. The computer code used in this work was developed by [65] and this section follows the description therein. Using weakly irregular waveguide (so-called “cold cavity”) theory [66, 67, 68, 69, 70], we can calculate the resonator eigenfrequencies,  $Q$  values, and axial field functions of TE modes by solving a one-dimensional wave equation of the form

$$\left[ \frac{d^2}{dz^2} + k_z^2(z) \right] f(z) = 0 \quad (2.120)$$

where

$$k_z(z) = \left( \frac{\omega}{c} \right)^2 - k_{\perp}^2(z) \quad (2.121)$$

$f$  is the longitudinal profile function, and  $z$  is the longitudinal coordinate. The radiation conditions at the input and output boundaries of the resonator are of a cutoff wave in the input;

$$\left[ \frac{df(z)}{dz} - jk_z f(z) \right]_{z=z_{\text{in}}} = 0 \quad (2.122)$$

and a propagating wave at the output;

$$\left[ \frac{df(z)}{dz} + jk_z f(z) \right]_{z=z_{\text{out}}} = 0 \quad (2.123)$$

where  $z_{\text{in}}$  is the longitudinal coordinate of the resonator input,  $z_{\text{out}}$  is the position of the cavity output,  $\text{Re}(k_{\perp}) > 0$  when  $\text{Re}(k_{\perp}^2) > 0$  and  $\text{Im}(k_{\perp}) < 0$  when  $\text{Im}(k_{\perp}^2) < 0$ .

The analysis, which is based upon the source-free Maxwell’s equations, relies upon the dimensions of the cavity as well as the indices of the  $TE_{m,p}$  mode, but neglects

coupling to other modes and the perturbing effects of the electron beam. All conditions assume that the resonator cross-section is far from critical and weakly varying in the input ( $z < z_{\text{in}}$ ) and output ( $z > z_{\text{out}}$ ) sections,

$$\text{Re} (k_{\perp}^2) \gg \text{Im} (k_{\perp}^2) \quad (2.124)$$

and

$$\frac{dk_{\perp}}{dz} \ll k_{\perp}^2. \quad (2.125)$$

The solutions of the wave equation in (2.120) which satisfy the boundary conditions in (2.122) and (2.123) have complex eigenfrequencies. Due to a finite  $Q$ , the source-free resonator field functions decay over time as  $\exp[-(\text{Im } \omega)t/2Q]$ . The quality factor is related to the real and imaginary parts of the frequency as

$$Q = \frac{\text{Re } \omega}{2 \text{Im } \omega}. \quad (2.126)$$

The profile function  $f(z)$  is complex and can be expressed as the phasor

$$f(z) = |f|e^{-j\phi(z)} \quad (2.127)$$

where the magnitude  $|f|$  and phase  $\phi$  are given by

$$|f| = \sqrt{(\text{Re } f)^2 + (\text{Im } f)^2} \quad (2.128)$$

$$\phi = -\tan^{-1} \left( \frac{\text{Im } f}{\text{Re } f} \right). \quad (2.129)$$

To numerically solve (2.120), it is convenient to separate the real and imaginary parts to obtain the following pair of second order coupled ordinary differential equations which can be integrated:

$$\left[ \frac{d^2}{dz^2} + \text{Re} \left( \frac{\omega}{c} \right)^2 - k_{\perp}^2 \right] \text{Re } f = \text{Im} \left( \frac{\omega}{c} \right)^2 \text{Im } f \quad (2.130)$$

$$\left[ \frac{d^2}{dz^2} + \text{Re} \left( \frac{\omega}{c} \right)^2 - k_{\perp}^2 \right] \text{Im } f = -\text{Re} \left( \frac{\omega}{c} \right)^2 \text{Re } f \quad (2.131)$$

$$(2.132)$$

The complex eigenfrequency satisfying the output boundary condition (2.123) can be solved using an iterative procedure based on the method of steepest descent [71].

The cold cavity method is very useful in determining the cold cavity resonant frequency of the cavity eigenmode, its axial field function, and the diffractive  $Q$  of

the eigenmode. These quantities will change in the perturbing presence of an energetic electron beam, however this first order approximation is a good starting point for a design and fairly accurate for low power electron beams.

## 2.7.2 Starting Current Calculation Including Beam Effects

A linear theory derived in Section 2.4.1 is used to determine the starting currents of the modes present in a cylindrical gyrotron cavity. The numerical approach uses this existing linear theory and is generalized to include effects of magnetic field tapering, cavity profile, finite beam thickness, velocity spread, and axially dependent beam coupling to the fields of competing modes [19] and was incorporated into a computer code [72].

Following [19], the starting current, including beam effects, can be expressed as

$$I_{\text{st}} = \frac{2\pi (mc^3\gamma_0/e) \cdot (1/\lambda) \int_0^L |f(z)|^2 dz}{[n^n / (2^{n-2}n!)]^2 Q \int_{\beta_{\perp 0} - \Delta\beta_{\perp 0}/2}^{\beta_{\perp 0} + \Delta\beta_{\perp 0}/2} W_{\beta}(\beta_{\perp 0}) \beta_{\perp 0}^{2(n-3)} \langle \chi'' G \rangle_{R_e} d\beta_{\perp 0}}. \quad (2.133)$$

A nonzero radial beam thickness  $\Delta R_e$  causes electrons with different beam radii to have a different coupling impedance to a mode;

$$\varphi(R_e) = \frac{J_{m\pm n}(k_{\perp}R_e)}{J_{m\pm n}(k_{\perp}\bar{R}_e)} \quad (2.134)$$

Since the electron guiding centers follow the magnetic field lines, a tapered magnetic field along the interaction region causes the average radial position of the beam  $\bar{R}_e(z)$  to scale relative to its position at the entrance to the interaction region,

$$\bar{R}_e(z) = \bar{R}_e(0) \sqrt{\frac{B_0(0)}{B_0(z)}}. \quad (2.135)$$

The tapered magnetic field thus indirectly causes variations in the coupling impedance along the axial direction;

$$\phi[\bar{R}_e(z)] \equiv \frac{J_{m\pm n}[k_{\perp}(z)\bar{R}_e(z)]}{J_{m\pm n}[k_{\perp}(0)\bar{R}_e(0)]}. \quad (2.136)$$

In addition to accounting for a tapered magnetic field, this equation also describes the tapering of the cavity wall radius through  $k_{\perp}(z) = \nu/R_0(z)$ . The effects of finite beam thickness and variation of radial beam position are included into the starting current equation through the weighted average of the product of the imaginary part of the

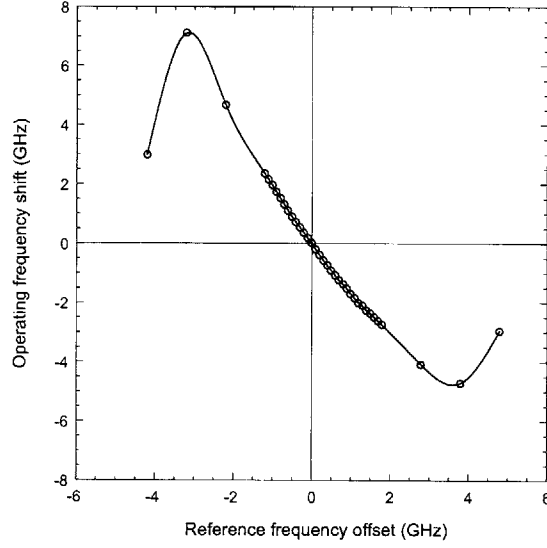


Figure 2-7: Operating frequency shift with reference frequency offset. The convergent solution is located at the origin.

linearized dielectric susceptibility of the electron beam and the coupling impedance over the beam thickness,

$$\begin{aligned} \langle \chi'' G \rangle_{R_e} &= -G(\bar{R}_e(0)) \left( n + \frac{\partial}{\partial \Delta_0} \right) \\ &\times \left| \int_0^{\zeta_{\text{out}}} \hat{f}(\zeta) \int_{\bar{R}_e - \Delta R_e/2}^{\bar{R}_e + \Delta R_e/2} W_R(R_e) \varphi(R_e) dR_e d\zeta \right|^2 \end{aligned} \quad (2.137)$$

where  $G(\bar{R}_e(0))$  is the coupling impedance for the average beam radius at the entrance to the interaction region,  $\hat{f}(\zeta) (= f(\zeta) \cdot \phi(\zeta) \exp(i(\Delta_0 \zeta + \int_0^\zeta \tilde{\Delta} d\zeta')))$ , and  $W_R(R_e)$  is the distribution function for the radial beam spread given by,

$$\int_{\bar{R}_e - \Delta R_e/2}^{\bar{R}_e + \Delta R_e/2} W_R(R_e) dR_e = 1. \quad (2.138)$$

A distribution for the velocity spread  $W_\beta(\beta_{\perp 0})$  is given by

$$\int_{\beta_{\perp 0} - \Delta \beta_{\perp 0}/2}^{\beta_{\perp 0} + \Delta \beta_{\perp 0}/2} W_\beta(\beta_{\perp 0}) d\beta_{\perp 0} = 1. \quad (2.139)$$

### 2.7.3 MAGY

Nonlinear modeling has been performed using the time-dependent simulation code MAGY, developed jointly at the University of Maryland and the Naval Research

Laboratory [73]. In MAGY, the transverse resonator fields are expanded in terms of normal waveguide modes, while the axial fields are expanded in a basis of the divergence of the TE/TM modes in the transverse basis. A self-consistent equation for the axial resonator field is solved in a slowly time-varying approximation. This has a few consequences. First, the simulation time step is related to the cavity fill time and not the RF oscillation period, and much larger time steps than, for example, in PIC codes can be used. Second, convergence of the expansion in the axial basis is non-uniform.

In single mode simulations, we found that MAGY is very sensitive to the choice of initial reference oscillation frequency for the mode. In particular, we found that a reference frequency vastly different from the correct frequency resulted in a convergence to an unphysical quasi-stationary solution in which the axial field was periodically changing as a function of time and the output spectrum was not monochromatic. Further, beam-wave power transfer may not exist in this condition. There is a straightforward mathematical explanation of these features. The reference frequency is used to calculate the interaction between an electromagnetic field and an electron beam. Due to the electron loading of a resonator, the operating frequency of an oscillator cannot be exactly predicted. Given the reference frequency (of which the cold cavity resonant frequency is a good approximation), MAGY will calculate the operating frequency using the slowly varying amplitude approximation.

The current MAGY code calculates a temporal evolution of an electromagnetic field, represented as a sum of modes of local cross-sections, together with the electron beam dynamics. The effect of the electron beam on the electromagnetic field is described in terms of electron sources presented in field equations (the generalized telegrapher's equations). To find the electron sources, the electron equations of motion are solved and electron trajectories calculated. Now, the reference frequency can be used to calculate the phase of the electron with respect to the field or adjusted frequency. While the current MAGY code uses the reference frequency, an older version used the adjusted frequency. While the present code was developed for gyro-amplifiers, where the precise operating frequency is known, it can be used to successfully treat gyro-oscillators when the reference frequency is reasonably close to the operating frequency. Figure 2-7 shows an example of the operating frequency shift as a function of the reference frequency offset. The convergent solution is located at the origin.

## 2.7.4 EGUN

The EGUN electron optics and gun design program is a 2- $\frac{1}{2}$ D code, which means that it solves for fields in two dimensions and particle motion in three [74]. EGUN computes the trajectories of charged particles (in our case electrons) in electrostatic and magnetostatic fields including the effects of space charge and self-magnetic fields. Poisson's equation,

$$\nabla^2\Phi = -\frac{\rho_v}{\epsilon_0} \quad (2.140)$$

where  $\rho_v$  is the volume charge density, is solved by the finite difference method using boundary conditions which are defined by specifying in the geometry the type and position of the boundary. In cylindrical coordinates, the Laplacian of the potential  $\nabla^2\Phi$ , is given by

$$\nabla^2\Phi = \frac{1}{\rho} \frac{\partial}{\partial \rho} \left( \rho \frac{\partial \Phi}{\partial \rho} \right) + \frac{1}{\rho^2} \frac{\partial^2 \Phi}{\partial \phi^2} + \frac{\partial^2 \Phi}{\partial z^2}. \quad (2.141)$$

The electric fields are determined by differentiating the potential distribution,

$$\mathbf{E} = -\nabla\Phi \quad (2.142)$$

where the gradient of the potential in cylindrical coordinates is given by

$$\nabla\Phi = \hat{\rho} \frac{\partial \Phi}{\partial \rho} + \hat{\phi} \frac{1}{\rho} \frac{\partial \Phi}{\partial \phi} + \hat{z} \frac{\partial \Phi}{\partial z}. \quad (2.143)$$

The electron trajectory equations are fully relativistic and take into account all possible electric and magnetic field components. Trajectories are started assuming that Child's law of space-charge limited current holds near the cathode surface,

$$J = \frac{4}{9} \sqrt{\frac{2e}{m}} \frac{\epsilon_0 V^{3/2}}{d^2} \quad (2.144)$$

where  $V$  is the applied voltage between anode and cathode, and  $d$  is the anode to cathode spacing. Space charge forces are realized through appropriate deposition of charge on one cycle followed by another solution of Poisson's equation (2.140) which is in turn followed by another cycle of trajectory calculations.

A typical method of calculating the magnetic field is from an arbitrary configuration of solenoids, where the user specifies a set of point coils by giving their position, radius, and current. The magnetic fields are axially symmetric and the off-axis field components are calculated by a sixth-order expansion of the radial coordinate.

## 2.8 Sensitivity-Enhanced Nuclear Magnetic Resonance

This section presents an overview of sensitivity-enhanced nuclear magnetic resonance, which was the principal motivation for the construction of a gyrotron oscillator at 460 GHz. An introduction to the theory of dynamic nuclear polarization is also presented in the context of nuclear magnetic resonance.

Nuclear magnetic resonance is a powerful and routine spectroscopic technique for the study of structure and dynamics in condensed phases and, in particular, of biological macromolecules. Its principal limitation is low sensitivity; the small nuclear Zeeman energy splittings result in correspondingly small nuclear spin polarization at thermal equilibrium [75]:

$$\frac{N_m}{N} = \frac{e^{-\frac{E_m}{k_B T}}}{\sum_{m=-I}^I e^{-\frac{E_m}{k_B T}}} \quad (2.145)$$

$$\simeq \frac{1 + \frac{m\hbar\gamma B_0}{k_B T}}{2I + 1} \quad (2.146)$$

where  $N_m$  is the number of nuclei in the  $m^{\text{th}}$  state ( $-\frac{1}{2}$  or  $\frac{1}{2}$  for a spin- $\frac{1}{2}$  nucleus),  $N$  is the total number of spins,  $T$  is the absolute temperature,  $k_B$  is the Boltzmann constant,  $E_m$  ( $= -m\hbar\gamma B_0$ ) is the nuclear Zeeman energy,  $\hbar$  ( $= h/2\pi$ ) is Planck's constant,  $B_0$  is the static magnetic field,  $I$  is the nuclear spin angular momentum, where we have taken the high temperature limit in (2.146).

Transitions between Zeeman levels can be stimulated by applied electromagnetic radiation, where the photon energy  $\Delta E$  required to excite a transition between the  $m$  and  $m + 1$  Zeeman states is

$$\Delta E = \hbar\gamma B_0. \quad (2.147)$$

From Planck's law,  $E = \hbar\omega$ , the frequency of the required electromagnetic radiation is given by

$$\omega_0 = \gamma B_0 \quad (2.148)$$

where  $\gamma$ , the gyromagnetic ratio, is measured in units of  $(\text{T}\cdot\text{s})^{-1}$  and is a characteristic constant for a given nucleus. Since protons at room temperature exhibit a spin polarization of less than 0.01% in a field of 5 T [76], we can understand the need for more powerful magnets for use in NMR spectroscopy. Though both solution and solid state NMR suffer from this poor sensitivity, relaxation processes in the solid



state further compromise the time-averaged sensitivity of these experiments by two or three orders of magnitude. The low sensitivity of solid-state NMR complicates the study of biological systems, where sample amounts are limited and spectra are complex.

### 2.8.1 Chemical Shift

The circulating motion of the valence electrons of an atom induced by an external magnetic field causes a secondary magnetic field at the nucleus which opposes the applied field. The precessional frequency is the same as the frequency of electromagnetic radiation required to excite transitions between the Zeeman levels. The effect of the secondary fields is called nuclear shielding. Therefore, the net magnetic field at the nucleus is generally less than the applied field by [75, 77]

$$B = B_0 (1 - \sigma) \quad (2.149)$$

where  $\sigma$  is the average isotropic shielding constant for the nucleus. The effects of shielding on a particular nucleus can be observed through modification of (2.148) as

$$\omega = \gamma (1 - \sigma) B_0. \quad (2.150)$$

Since the resonant frequency is directly proportional to the static magnetic field strength, this relationship presents difficulties in comparing NMR spectra taken on spectrometers operating at different field strengths. The chemical shift was developed to eliminate this problem.

Since the electron density around each nucleus in a molecule varies according to the types of nuclei and bonds in the molecule, the secondary field and therefore the net field at each nucleus will vary accordingly. This phenomenon is called the chemical shift and is a very precise metric of the chemical environment around a nucleus. The chemical shift of a nucleus is the difference between the resonance frequency of the nucleus and a reference signal from a standard molecule, measured in parts per million:

$$\delta = \frac{\Omega - \Omega_{\text{ref}}}{\omega_0} \times 10^6 = (\sigma_{\text{ref}} - \sigma) \times 10^6 \quad (2.151)$$

where  $\Omega$  and  $\Omega_{\text{ref}}$  are the offset frequencies of the signal of interest and the reference signal, respectively.

## 2.8.2 Nuclear Magnetic Resonance in the Solid State

Solid state nuclear magnetic resonance (NMR) is an encompassing method for structure determination in the native biological milieu. Its generality is derived from the freedom from the requirement of crystallization imposed by diffraction methods, and from the requirements of solubility and molecular weight imposed by solution state NMR.

### Chemical shift anisotropy

The magnitude of the chemical shift is related to the extent to which the electrons can shield the nucleus from the applied magnetic field. Where in a spherically symmetric molecule the chemical shift is independent of molecular orientation, the chemical shift in an asymmetric molecule depends on the orientation. In other words, the net magnetic field in the nucleus varies as a function of the orientation of the molecule in the magnetic field. In a nonviscous liquid, the effect of tumbling of the molecules averages out the fields at the various orientations. In a solid, however, the random distribution of fixed orientations results in an NMR spectra consisting of broad spectral lines, where there is a larger signal at lower field strength due to the existence of more perpendicular orientations. This mechanism of line-broadening in solids is referred to as the anisotropic chemical shift (or chemical shift anisotropy – CSA).

### Magic angle spinning

Another reason for broad spectral lines is dipolar broadening. The magnitude of a dipolar interaction, between two spin  $\frac{1}{2}$  nuclei, varies with angle  $\theta$  between the dipole and the applied magnetic field axis  $B_0$  and with the distance  $r$  between the nuclei. The magnetic field experienced by one of the nuclei can be expressed as

$$B = 3 \cos^2 \theta - 1. \quad (2.152)$$

In a solid, the random distribution of orientations of a group of dipoles results in an NMR spectra consisting of broad spectral lines, where there is a larger signal at mid-field strength due to the larger fraction of orientations perpendicular to the  $B_0$  field axis. This phenomenon is called dipolar broadening. As previously, in a nonviscous liquid, the effect of tumbling of the molecules averages out the fields at the various orientations. If the average orientation of the molecules is set to the magic angle  $\theta_m$  ( $= 54.7^\circ$ ), the dipole interaction vanishes. Practically, this can be accomplished by spinning the entire sample at the magic angle  $\theta_m$  with respect to

the static magnetic field  $B_0$  at a spinning rate of thousands of revolutions per second, comparable to the solid state line width.

### 2.8.3 Dynamic Nuclear Polarization

Dynamic nuclear polarization (DNP) is a magnetic resonance technique used to enhance the polarization of nuclei through interactions with the electron spin population. It occurs through a variety of mechanisms, and the mechanism used in solid state NMR involves irradiation of the electron spins at or near their Larmor frequency. The effect was first observed in 1956 by Carver and Slichter [78] and later in 1958 by Abragam and Proctor [79] and was historically applied to enhancement of the polarization of targets in nuclear scattering experiments, and more recently for sensitivity enhancement in high resolution NMR spectroscopy.

Phenomenological expressions for the maximum DNP enhancement due to the solid effect,  $\epsilon_{SE}$ , and thermal mixing,  $\epsilon_{TM}$ , are given by [80]

$$\epsilon_{SE} = \alpha \frac{\gamma_e N_e}{\gamma_n b^3 \delta} \left( \frac{B_1}{B_0} \right)^2 T_{1n} \quad (2.153)$$

$$\epsilon_{TM} = \alpha' \frac{\gamma_e N_e^2}{\gamma_n \delta^2} \left( \frac{B_1^2}{B_0} \right) T_{1n} T_{1e} \quad (2.154)$$

where  $\alpha$  and  $\alpha'$  contain physical constants,  $N_e$  is the density of unpaired electrons,  $\delta$  is the EPR linewidth,  $b$  is the nuclear spin diffusion barrier,  $B_1$  is the microwave field strength,  $T_{1n}$  and  $T_{1e}$  are the nuclear and electron spin-lattice relaxation times, and  $\gamma_{p,e}$  ( $= f_{p,e}/B_0$ ) are the nuclear and electron gyromagnetic ratios, respectively, yielding 42.6 MHz/T for protons and 28.0 GHz/T for electrons. In principle, signal enhancements on the order of  $\gamma_e/\gamma_n$  can be obtained, corresponding to a factor of 657 for  $^1\text{H}$  nuclei and 2,615 for  $^{13}\text{C}$  nuclei.

Though both the solid effect and thermal mixing mechanisms play roles in enhancing the sensitivity, studies show that thermal mixing is the predominant effect. Using a 140 GHz gyrotron, we have previously demonstrated that signal enhancements of several orders of magnitude (100 – 400) are achievable at a magnetic field of 5 T [76, 41, 81, 82, 83, 84]. However, to obtain higher resolution spectra, it is desirable to perform DNP at higher field strengths (9 – 18 T), where NMR is commonly employed today.

There are several problems encountered when performing DNP at high fields. First, the enhancement decreases as  $1/B_0^2$  with increasing static field strength for the solid effect and as  $1/B_0$  for thermal mixing as indicated by (2.153) and (2.154).

Second, relaxation mechanisms responsible for the DNP effect are fundamentally different at higher fields. These problems at high field can be overcome, and significant signal enhancements obtained, by using high radical concentrations and high microwave driving powers. Furthermore, the enhancements scale with the square of the microwave driving field and only inversely with the applied magnetic field. Therefore, large signal enhancements can be achieved, even at high fields (9 – 18 T) if sufficient microwave power (1 – 10 W) is available to drive the polarization transfer.

## 2.9 Discussion

In this chapter, we review the theoretical basis for understanding this experimental work. We described the phenomenological basis for the fundamental and second harmonic cyclotron resonance maser interaction, in addition to several theoretical approaches. We recapitulated the derivation of the linearized dispersion relation from the kinetic theory of gyrotron oscillators, a classical fluid-dynamical theory, in which the electron beam is treated as a plasma and the distribution of electrons is explicitly described. From the linearized single-particle theory, we presented the derivation of the start oscillation current. In the quantum mechanical basis of the cyclotron resonance maser we noted the analog to the classical formalism. We derived the transverse electric and magnetic field components in a cylindrical waveguide. Four main numerical techniques based on the above theories were also described. These computer codes served as design and analysis tools for all of the experiments in this work. Finally, introductory theory pertaining to the application of this work, dynamic nuclear polarization, was presented.

# Chapter 3

## Experimental Setup and Diagnostics

In this chapter we describe the experimental setup and diagnostics that were used in the experiments during the course of this work. All of the components used in the CW experiment (*c.f.* Section 3.2.2) were purchased expressly for the 460 GHz gyrotron experiment, while an existing pulsed setup was used. Diagnostics were required for several areas, including but not limited to power, frequency, time-domain signals, vacuum system, radiation patterns, and cold tests. The main experimental components and diagnostic systems are discussed below.

### 3.1 Diagnostics

This section details the diagnostics used in the gyrotron experiments of this work. Diagnostic systems were used to identify several quantities and qualities of the gyrotron either directly related to design parameters, such as the frequency and power, or indirect factors indicating its health, such as the thermal loading or pressure.

#### 3.1.1 High Frequency Detection

The most important indicator of the second harmonic which separates it from the fundamental is its frequency. The frequency can either directly be measured or can be narrowed into a range by use of a filter. For instance, plexiglass becomes more opaque with increasing frequency. In this section, we describe a heterodyne frequency measurement system, that can accurately measure the frequency to within 1 Hz by phase locking the local oscillator. On the other hand, filter horns, designed and constructed by Spira et. al. [85], can pass frequencies above the cut-off.

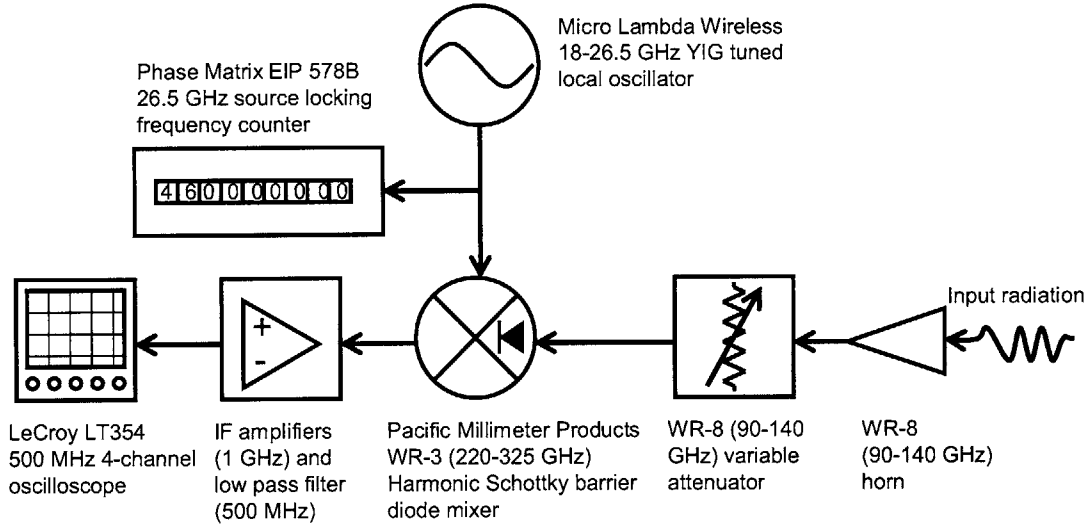


Figure 3-1: Block diagram of a heterodyne receiver used as a millimeter and submillimeter wavelength frequency measurement system.

### Heterodyne frequency measurement system

A heterodyne receiver was built for used in frequency detection in the experiments presented in this thesis. A block diagram of the frequency system is shown in Fig. 3-1. The gyrotron radiation is directed at a WR-8 horn and attenuated through a WR-8 variable attenuator. The WR-8 band corresponds to 90-140 GHz. Thus, the horn permits all frequencies of interest to pass while the attenuator primarily filters out the radiation with frequency less than 140 GHz and provides increasing attenuation as the frequency of the signal decreases. This useful feature allows the high frequency second harmonic radiation near 460 GHz to pass unfettered while eliminating the powerful and possibly damaging fundamental frequencies.

The input radiation is mixed in a WR-3 harmonic Schottky barrier diode (Pacific Millimeter Products, Model No. HM) and diplexer (Pacific Millimeter Products, Model No. MD5) with intermediate frequency (IF) range from DC-12 GHz and local oscillator (LO) range from 20-40 GHz. The diplexer may have dead frequencies (*c.f.* Fig. 3-2), however the broad range of the 18-26.5 GHz GaAs FET YIG-Tuned oscillator (Micro Lambda Wireless, Model No. MLOS-1826PA) connected to the LO port would allow us to tune over multiple of its harmonics in that case. The total RF and LO power input maximum to the harmonic mixer is 100 milliwatts.

The IF signal (the mixer output) is then amplified by a chain of 1 GHz low noise solid-state amplifiers (Mini-Circuits, Model No. ZFL-1000LNB, ZFL-1000B, ZFL-1000VH2B) and the signal above 520 MHz is discarded by a low pass filter (Mini-

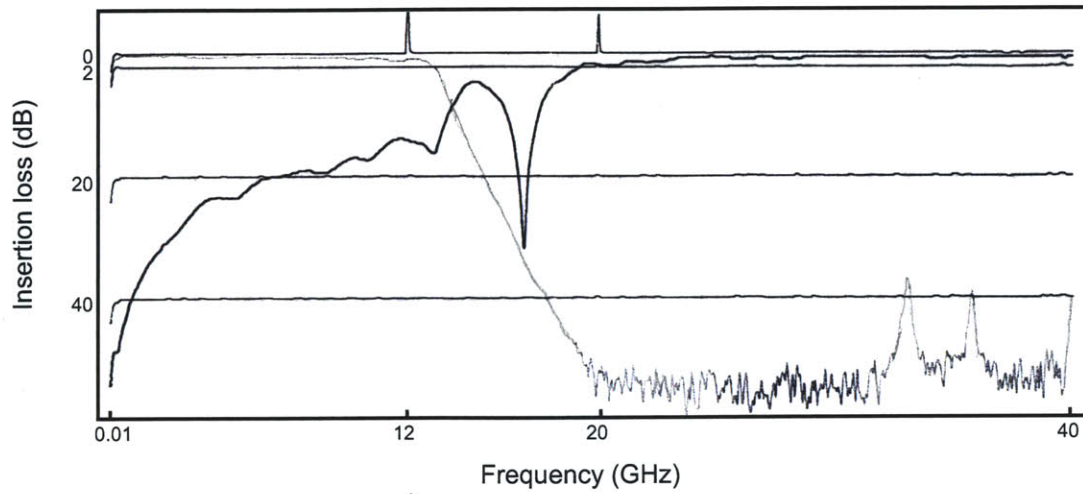


Figure 3-2: Insertion loss of the IF and LO from the diplexer (Pacific Millimeter Products, Model No. MD5, S/N 008). The IF band is flat from DC to 12 GHz and the LO band is flat over 20 to 40 GHz [5].

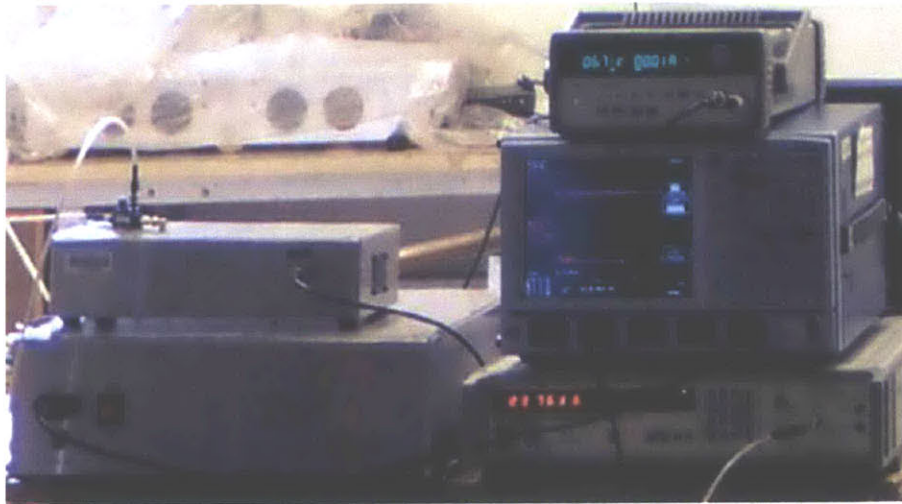


Figure 3-3: Photograph of the frequency system, picturing the oscilloscope, frequency counter, and power supply on the right, and the local oscillator, amplifiers, and filter on the left (inside the boxes). The horn, mixer, and attenuator are not depicted.

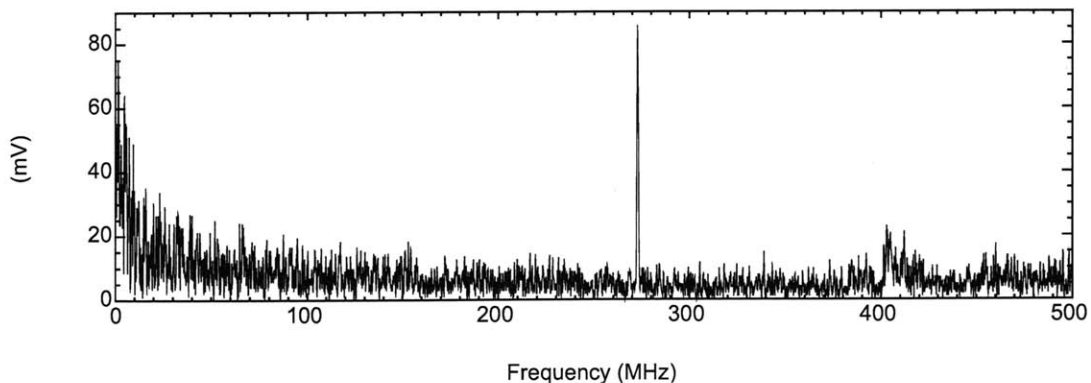


Figure 3-4: Intermediate frequency signal for the second harmonic  $TE_{2,6,1}$  mode at 456 GHz using the frequency measurement system.

Circuits, Model No. SLP-550). The IF and LO connections are made with Microflex 165, a flexible shielded cable with low attenuation in the K band.

A 500 MHz, 4-channel oscilloscope (LeCroy, Model No. LT354) computes a Fast Fourier Transform (FFT) of the filtered IF signal in real time. The local oscillator frequency is tuned such that one of its harmonics (in our case the 9<sup>th</sup> through 18<sup>th</sup>) mixes with the input radiation to produce an intermediate frequency signal in the 0 - 500 MHz range. The IF signal is detected in real time as a pair of peaks by an FFT on the oscilloscope such that through varying the LO, one of the peak lines falls within the 0-500 MHz band. The input frequency then corresponds to

$$f_{in} = n f_{LO_{\pm}} \mp f_{IF_{\pm}} \quad (3.1)$$

where  $f_{IF_{+}}$  and  $f_{IF_{-}}$  are the upper and lower IF sidebands,  $f_{LO_{+}}$  and  $f_{LO_{-}}$  are the corresponding local oscillator frequencies, and  $n$  is the harmonic number. We can eliminate  $f_{in}$  from the set of equations given in (3.1) and solve for the harmonic of the mixer,

$$n = \frac{f_{IF_{+}} + f_{IF_{-}}}{f_{LO_{+}} - f_{LO_{-}}}. \quad (3.2)$$

The frequency counter (Phase Matrix, Model No. EIP 578B) is a source locking microwave frequency counter, with the capability of analog phase locking of any electronically tunable source, in this case our local oscillator, to the accuracy and long term stability of the timebase oscillator in the counter. The result is a highly accurate frequency measurement system, with the capability of resolving the gyrotron frequency to better than 1 MHz. It samples the local oscillator frequency via a narrow band 18-26.5 GHz 20 dB directional coupler (Krytar, Model No. 262220).

The harmonic mixer, its band 220-325 GHz notwithstanding, performs adequately



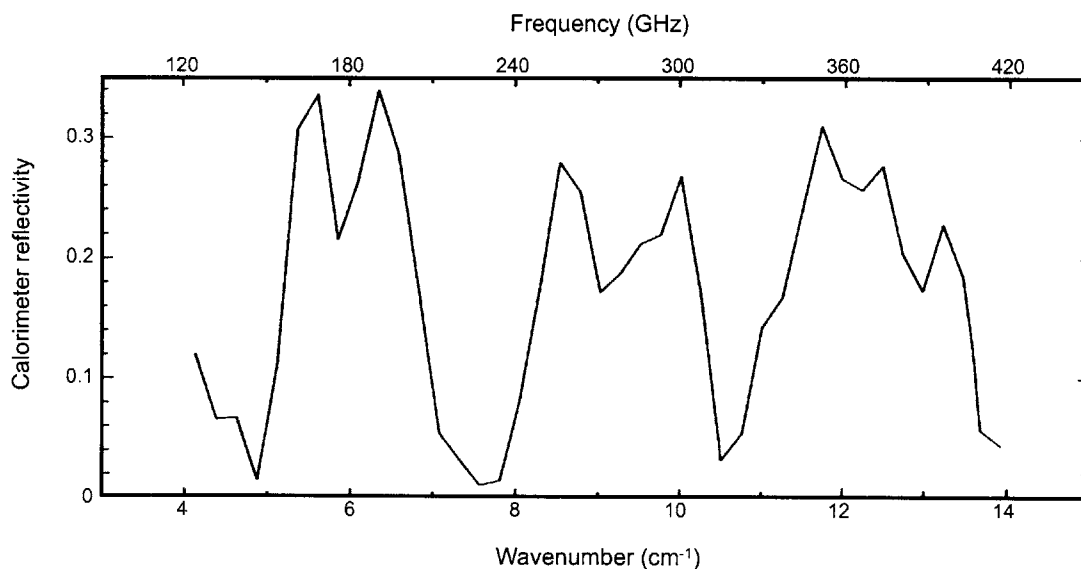


Figure 3-5: Reflectivity of the laser calorimeter, as measured by a dispersive Fourier transform spectrometer [6, 7].

at 460 GHz.

### Filter horns

Custom made filter horns were used to observe the second harmonic radiation near 460 GHz. The horns were used in the submillimeter wave harmonic gyrotron work of Spira et al. [85]. The filter horn assembly consists of a standard WR-3 quick flange connector attached to a section of WR-3 waveguide, followed by a cutoff section and a standard gain (25 dB) WR-3 horn. The three custom made filter horns have cutoff frequencies of 280 GHz, 300 GHz, and 400 GHz. Only two of the horns currently remain in our possession, and measurements indicate that they are those cutoff at 280 and 300 GHz. Since the fundamental modes are all below 250 GHz and the second harmonic modes of interest are around 460 GHz, both should function interchangeably. When using a filter horn, the diode signal was considerably attenuated because a 2.54 cm long WR-3 waveguide flange adapter (Aerowave, Model No. 03-1104) was required to mate the horn to the diode.

### 3.1.2 Power Measurement

The methods of power measurement used in this work were dry calorimetry and pyroelectric detection. Dry calorimetry was primarily used in the CW experiments while pyroelectric detection was useful in measuring the energy per pulse. Wet calorimetry

was also employed in measuring the power absorbed by the cavity and is described in Section 3.1.6.

### **Calorimeter**

Thermoelectric calorimetry was used as a technique to measure the average power in the experiments in this work. The principle of calorimeter laser detection of radiation is that the incident radiation is absorbed either by a surface or a volume absorber, whereupon the absorbed energy is converted to heat which is measured by a thermoelectric sensor [86].

A surface absorbing disc calorimeter with a 2.54 cm aperture (Scientech, Inc., Model No. 36-0001) was used in this work. In a disc calorimeter, heat is typically measured by a thermopile which is located between the absorbing disc and a heat sink. The thermopile generates a potential when the two sides of the device are at different temperatures, where the measured current is proportional to the heat flow.

The laser calorimeter was intended for use with wavelengths in the range of 0.25 to 35 microns. The device was presumably modified to absorb the millimeter wavelengths using the procedure described by Kreisler et al. [87]. The dependence of calorimeter reflectivity on frequency was measured using a dispersive Fourier transform spectrometer, depicted in Fig. 3-5 [6, 7]. For the power measurements performed in this experiment, an average value of 15 % reflectivity was assumed.

Power measurements were made by hooking the calorimeter head onto the end of a 1.9 m cylindrical copper waveguide of 2.54 cm inner diameter. The calorimeter was read by a power energy meter (Scientech, Inc., Model No. 362). The calorimeter head was insulated to shield itself from thermal fluctuations and ambient heat in low average power measurements.

### **Pyroelectric detector**

Pyroelectric detection utilizes special properties of ferroelectric crystals, a class of materials that can be prepared in a state of permanent polarization, to sense changes in temperature due to absorption of radiation. When a ferroelectric material absorbs radiation, the incident energy is converted to heat. The temperature rise causes a corresponding change in the magnitude of electrical polarization of the crystal. This causes a charge separation across the crystal, which is sensed as a current between two electrodes on the faces of the crystal, which continues to flow until both sides reach the same voltage [86, 88].

While pyroelectric detectors cannot be used to measure continuous output since

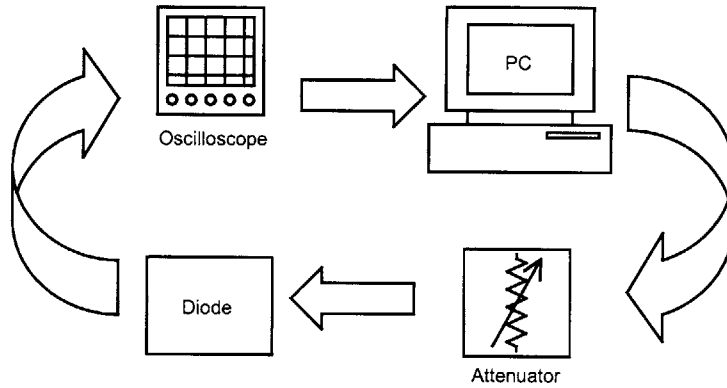


Figure 3-6: Block diagram of near- and far-field scanner.

they respond only to changes in absorbed energy, they were only used in the pulsed gyrotron experiments. The Vector pyroelectric detector used in this work (Scientech, Inc., Model No. PHF09) has an aperture 9 mm in diameter and was used with a Vector digital power meter (Scientech, Inc., Model No. S310).

### 3.1.3 Radiation Pattern Measurement

Several techniques and apparatuses used for measurement of radiation patterns are described in this section. They include a mechanized scanner, a pyroelectric camera consisting of an array of pyroelectric elements, thermal paper, and liquid crystal imaging.

The radiation pattern in the region close to the waveguide differs from the pattern at large distances. The term “near-field”, also known as the induction field, refers to the field pattern that exists close to the waveguide antenna, while the term “far-field”, also known as the radiation field, refers to the field pattern at large distances. Due to the sensitivity or aperture of our available techniques or equipment, the radiation pattern in our experiments is often recorded in the near-field, where the fields still resemble waveguide fields.

#### Mechanized scanner

A 3D motorized data acquisition radiation scanner (*c.f.* Fig. 3-6) was developed by Borchard at MIT [89]. The apparatus consists of an oscilloscope, a PC, a motorized variable attenuator, and a diode. From a systems viewpoint, the scanner consists of a positioning system and an attenuator system. The four-axes positioning system consists of a translational system with a  $y$  and  $x$  axis in addition to a rotational positioning system. The position is set by a stepper motor, which is controlled by the

PC. The sensing apparatus consists of a diode, a Millitech motorized attenuator, a horn. Due to the inherent nonlinearity of the diode, the attenuation level is adjusted until the diode signal reaches a preset level. The diode signal is read on the oscilloscope and sent to the PC, which then adjusts the attenuator. The signal is averaged over several points in order to reduce noise. The attenuation level and positions are written to an output data file when the point is completed.

### **Pyroelectric camera**

A pyroelectric camera laser beam diagnostic system developed by Spiricon, Inc. (Pyrocamera III, Model No. PY-III-C-B, Serial No. 30507) was used for millimeter and submillimeter-wave radiation pattern measurements. While the pyroelectric camera was developed as a diagnostic for infrared laser beams, the spectral response of the pyroelectric array from 0.1 to 100  $\mu\text{m}$  is fairly flat, and the camera has been used at 1,000  $\mu\text{m}$  [90]. At the Thomas Jefferson National Accelerator Facility (Newport News, VA), radiation of wavelengths between 100 and 300  $\mu\text{m}$  from a free electron laser using relativistic electrons from a linear accelerator was imaged using a similar pyroelectric camera [91]. Further, use of the pyroelectric camera at millimeter wavelengths was first demonstrated in a 250 GHz gyrotron [92].

The pyroelectric array consists of 124 by 124 elements where the element spacing is 100  $\mu\text{m}$  by 100  $\mu\text{m}$ . The camera has a relatively small active area of 12.4 by 12.4 mm which is often not large enough to instantaneously image the area of an overmoded waveguide, in our case of 25.4 cm inner diameter. Since pyroelectric crystals can only measure changes in intensity, the camera came fitted with a built-in chopper to enable measurement of CW radiation at chopper frequencies of either 24 Hz or 48 Hz.

The camera has several drawbacks. The camera dynamic range recorded in the measurements of this work was only 10 dB, which is insufficient to reconstruct the phase information of a beam. In addition, the small sensor area is comparable to the beam waist, in our case of the 25.4 mm inner diameter waveguide, and for this reason it is impossible to record far-field radiation patterns.

### **Thermal paper**

Thermal paper, commonly used in facsimile and ATM machines, is a copy paper which employs heat to produce its image. A typical thermal paper consists of a base paper applied with a heat-sensitive chemical coating on its face which darkens when heated. Using an absorbant as a substrate, thermal paper is useful in generating a quick image of a microwave beam and also for finding the axis of the beam. Images

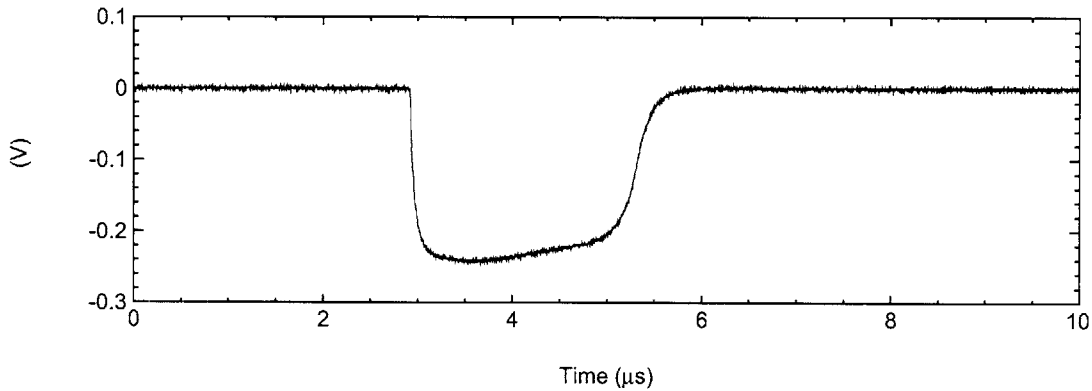


Figure 3-7: Typical time-domain diode signal of the  $TE_{0,3,1}$  mode at the voltage and current shown in Figures 3-14 and 3-8 and 8.58 T.

from thermal paper are shown in Chapter 6.

### Liquid crystal imaging

A novel technique to measure millimeter radiation patterns and recover quantitative intensity information using liquid crystal paper was developed and is described in Chapter 6 and [92].

### 3.1.4 Time-Domain Signal Measurement

Due to the intrinsic nature of short-pulse experiments, key experimental parameters, such as power, beam voltage, and beam current, vary over time. To harness this information, signals in the time domain were recorded. In the case of measuring the power in short pulses, while the average power can be measured with a calorimeter, the pulse shape over time is necessary to reconstruct the peak power. In this section, two devices for recording time-domain signals are detailed: the video detector diode for the microwave pulse shape and the Rogowski current monitor.

#### Video detector diode

A photodiode was used in conjunction with calorimetric and pyroelectric detection in order to measure the peak power of the gyrotron by measuring the microwave pulse shape. Video detectors were used in two waveguide bands, WR-3 (220-325 GHz) and WR-6 (110-170 GHz) (Pacific Millimeter Products, Model No. HD and DD). The detectors use silicon beam lead diodes on a planar stripline circuit and are extremely compact devices, measuring  $1.9 \times 1.9 \times 0.5$  cm. These detectors utilize two diodes

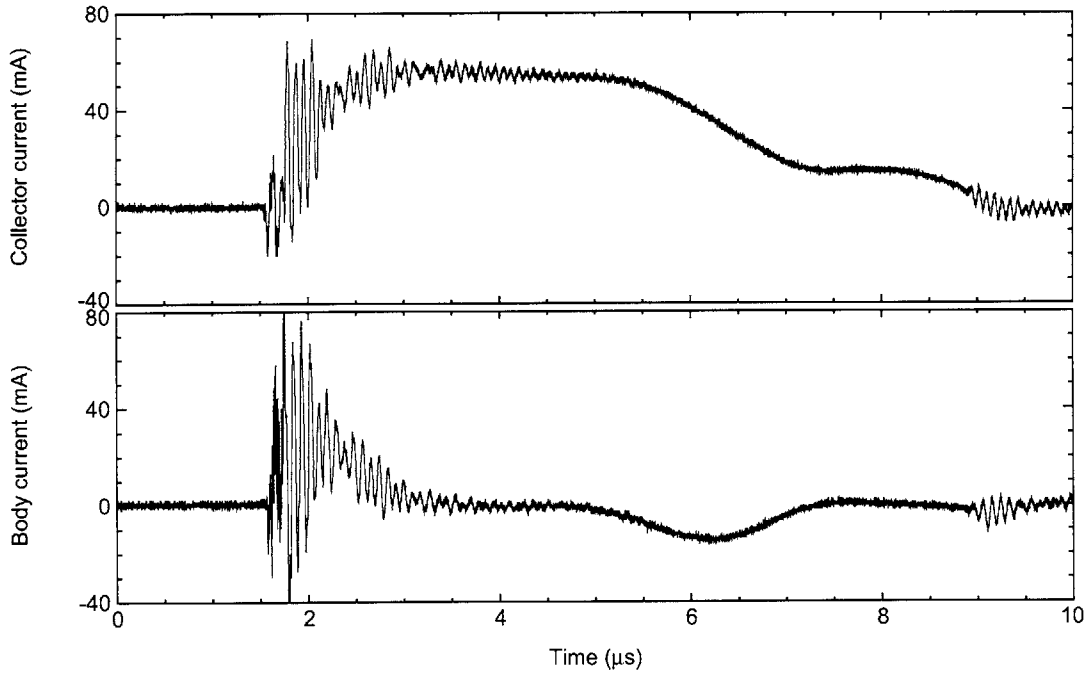


Figure 3-8: Typical collector and body current signals using a Rogowski current monitor. The corresponding voltage pulse is shown in Fig. 3-14. The signal corresponds to the  $TE_{0,3,1}$  mode at 8.58 T, and the diode trace shown in Figure 3-7.

and a matched termination connected to a 3 dB hybrid. When not in use, the diodes are terminated with  $50\Omega$  loads to prevent electrostatic damage.

### Rogowski current monitors

The current monitors used in these experiments are wide-band current transformers which convert an AC or pulse current signal into a proportional voltage signal which can then be displayed on an oscilloscope. Commonly known as a “Rogowski coil”, the current-carrying conductor is passed through the current monitor opening, and its associated magnetic field is used to accurately measure the current without requiring a direct connection. Consequently, this type of current monitor is well-suited to measuring currents on high voltage conductors.

The Rogowski coil is a toroidal coil with an air core which is placed around a current-carrying conductor. An alternating magnetic field is produced by the current, which induces a voltage in the coil proportional to the rate of change of current. The voltage output of the coil is given by [93]

$$V_{\text{out}} = M \frac{dI}{dt}, \quad (3.3)$$

where  $M$  is the mutual inductance of the coil and  $dI/dt$  is the rate of change of the current. To accurately reproduce the current waveform, the output voltage is integrated electronically.

The Rogowski coils used in these experiments (Ion Physics Corp., Model No. CM-100-L) have sensitivity of 1.0 V/A and 43 mm inner diameter. Magnetically coupled current monitors can read currents to very low frequencies but, as shown in (3.3), are intrinsically incapable of reading DC currents. The consequence for pulsed applications is that the output voltage signal decays more quickly than the measured current pulse, resulting in a phenomenon called “droop”. In our current monitors, the droop is rated at 0.035 %/ $\mu$ sec and saturation occurs at the amp-second-product rating of 0.0015 A sec. We also tried to use a model with higher sensitivity (Ion Physics Corp., Model No. CM-500-L), 5.0 V/A, however the droop was 30 %/ $\mu$ sec, which nearly eradicated our current pulse of 3  $\mu$ sec.

### 3.1.5 Vacuum Diagnostics

Characterization of the vacuum environment is important to the operation of a vacuum electron device, and especially so in the case of continuous-wave operation. Since vacuum leaks, both virtual and real, and component outgassing can compromise the performance of the gyrotron, every aspect of construction, from design and choice of materials through preparation, bakeout, and installation procedures as well as during any subsequent handling is critical. In this section, the diagnostic use of residual gas analysis and vacuum pumps are considered in addition to the repair methodology of two differing vacuum leaks.

#### Residual gas analysis

The residual gas analyzer (RGA) is an instrument which can completely characterize a vacuum environment including the detection of all component gases present in addition to the measurement of the total pressure through mass spectrometry. The principle of operation of a mass spectrometer is as follows; a small fraction of the gas molecules are ionized, the resulting ions are separated according to their respective masses, and the ion currents are measured at each mass. Partial pressure measurements are determined with calibration factors by reference to the abundance of the individual mass numbers attributed to each gas type [94].

Residual gas analysis (Stanford Research Systems, Model No. SRS RGA 100) was performed on the 460 GHz gyrotron before, during, and after bakeout in order to determine the vacuum composition and locate vacuum leaks using helium, alcohol,

Table 3.1: Atomic mass units of residual gases present in the system measured with the RGA.

Residual gas	(a.m.u)	Partial pressure ( $10^{-9}$ Torr)			
		Hot/OFF	Hot/ON	Cold/OFF	Cold/ON
Hydrogen	2	154	189	17.0	14.2
Carbon monoxide/dioxide	12	0.349	–	–	–
Nitrogen	14	2.57	5.09	2.31	6.40
Acetone	15	0.997	0.874	–	–
Oxygen	16	1.59	1.47	0.433	0.588
Water	17	1.46	1.24	0.803	0.810
Water	18	3.23	2.87	2.11	2.19
	26	1.61	0.305	–	–
	27	2.46	2.74	–	–
Nitrogen/Carbon dioxide	28	46.5	92.1	48.2	109
Nitrogen	29	1.39	3.11	0.814	1.28
Oxygen	32	1.33	1.03	2.16	2.25
	39	0.880	1.57	–	–
Argon/Air	40	1.66	1.86	1.46	1.67
Turbopump oil	41	1.03	3.41	–	–
	42	–	1.28	–	–
Acetone/Turbopump oil	43	0.943	3.72	–	–
Carbon dioxide	44	0.561	0.443	–	–
Turbopump oil	55	0.676	2.72	–	–
	56	0.208	1.23	–	–
Turbopump oil	57	0.414	1.79	–	–
Turbopump oil	69	–	1.12	–	–
	70	–	0.730	–	–
Turbopump oil	71	–	0.628	–	–
	83	–	0.307	–	–
Krypton	84	–	0.225	–	–
	85	–	0.346	–	–
Xylene, Toluene	91	0.266	0.758	–	–
Oil	97	–	0.595	–	–



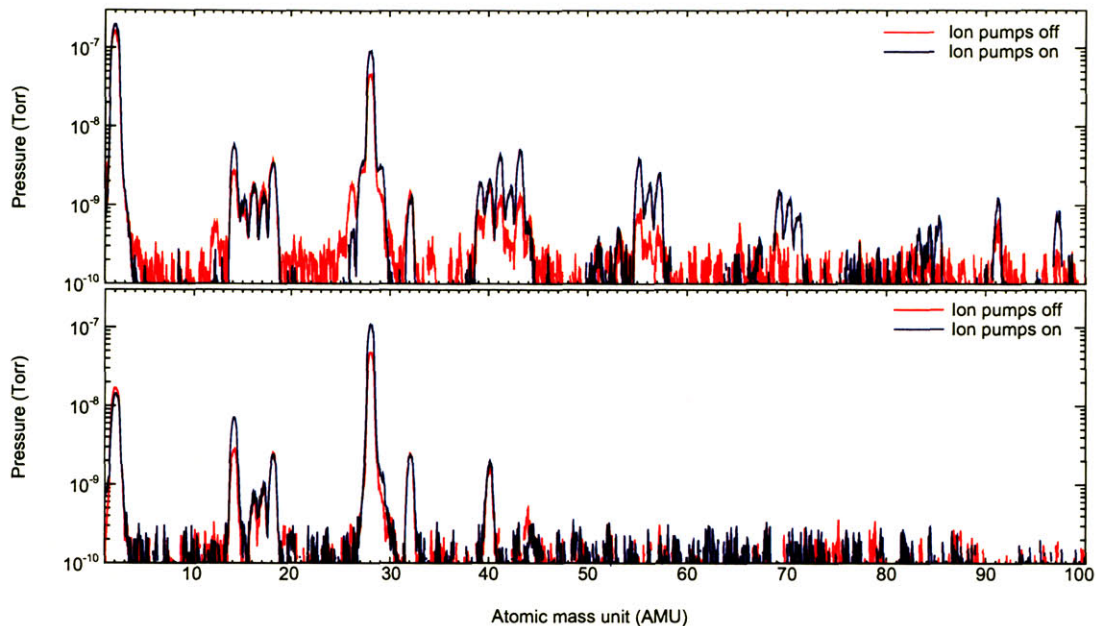


Figure 3-9: Typical RGA traces at the end of a bakeout when the tube is at 100°C (top) and room temperature (bottom).

and acetone. Fig. 3-9 shows the vacuum characterization during a 100°C bakeout following the sealing of a leak in the cavity cooling channel with Glyptal. The partial pressures were recorded for a bakeout temperature of 100°C and at room temperature. The partial pressures were recorded with the ion pumps on and off since the ion pumps are located between the RGA and tube and could affect the measurement. Table 3.1 identifies the residual gases present in the 460 GHz tube under four conditions: at 100°C with the ion pumps off, at 100°C with the ion pumps on, at room temperature with the ion pumps off, and at room temperature with the ion pumps on. While the tube is hot, there are many gases which are immobilized (and therefore not present) when the tube is cold. These include large molecules such as hydrocarbons. In the case where the tube is hot and the ion pumps are on, the partial pressures are higher than when the ion pumps are off. Since the ion pumps are at high temperature, this effect is due to the gases being ejected from the ion pumps through a combination of their pumping action and outgassing due to the heat. When the tube is cold, the gases with low atomic mass dominate (below 40 a.m.u.) and the gas composition is the same with or without ion pumps. In both cases, the highest partial pressures are contributed from hydrogen, air (*i.e.* nitrogen, oxygen, argon, and carbon dioxide) and water vapor.

## **Vacuum repair methodology**

During the course of this work, the 460 GHz gyrotron tube developed several leaks in the ultrahigh vacuum which severely limited its operation due to elevated pressure until vacuum repair could be performed. The repair of an O-ring leak and a weld leak are described here.

A Viton O-ring sealing the vacuum window was replaced with a Helicoflex seal. Helicoflex metal O-rings are designed to provide a high sealing level under high temperatures especially in a vacuum medium. Viton, in addition to contributing to the total gas load of the system through permeation, outgasses when heated and eventually permanently deforms at the high temperatures required for bakeout. Residual gas analysis showed that, during the heating of the window region in the configuration where a Viton O-ring was used to seal the window, periodic spikes of atmospheric composition would enter the vacuum chamber, recurring every few minutes.

All vacuum welds should be leak checked with a helium mass spectrometer to assure that they are vacuum tight for low pressure vacuum. The weld joints need to be properly designed in order to avoid either virtual or real leaks. In the present experiment, an improperly formed weld in the water cooling channel of the cavity became exposed to atmosphere either during bakeout or due to the flowing of water through the circuit. The leak was detected via residual gas analysis and helium mass spectrometry. A red Glyptal mixture with the ratio of between 3:1 and 1:1 Glyptal (Glyptal 1201B Red Enamel) to solvent (Glyptal G1500 thinner) was flowed through the cooling channel with use of pipets, hoses, and gravity. The excess mixture was drained from the cooling channel. The coat of Glyptal was dried overnight with low pressure compressed air and a second coating was applied and dried with the same procedure. Red Glyptal is an all-purpose thick red enamel paint that functions as an excellent vacuum seal to most types of materials by impregnating the leak. In addition, Glyptal is used for many other functions such as electrical insulation and anti-corrosion. During a bakeout following the application of the Glyptal mixture, care was taken to not exceed 150°C in the region of the cooling channel by monitoring the local temperature.

## **Vacuum pumps**

Two ion pump power supplies (Duniway, Model No. Terranova 741) control the 8 L/s diode Varian-style ion pumps (Duniway, Model No. VA-8-DD-M). Figure 3-10 shows the relationship between ion pump current and vacuum pressure for an 8 L/s pump at 3.5 kV. For the Terranova 741 unit, the equation used for calculating pressure from

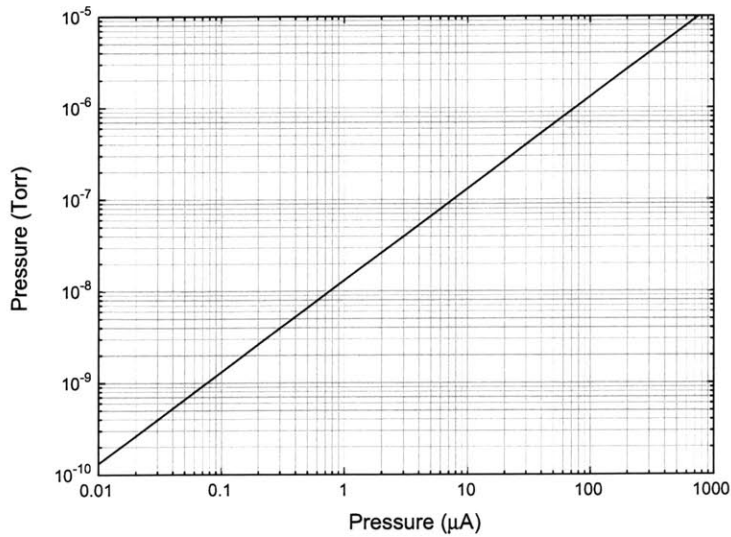


Figure 3-10: Relationship between the current drawn from 8 L/s Varian-style ion pumps operated at 3.5 kV and the vacuum pressure in Torr.

current is [95]

$$P = \frac{K \times I}{S \times V}, \quad (3.4)$$

where  $P$  is the pressure in Torr,  $K$  is a constant equal to 369.6,  $I$  is the current in amps,  $S$  is the pumping speed in liters per second, and  $V$  is the voltage in volts. While the current drawn in a sputter-ion pump is nearly proportional to pressure over a wide range, the proportionality is only approximate. At pressures less than  $1 \times 10^{-8}$  Torr, the current to the Penning discharge is multiple valued, displaying significant hysteresis. Therefore the current drawn depends on whether the pressure is rising or falling. The accuracy of the pressure as indicated by the ion pump current is no better than  $\pm 20\%$ , and that accuracy is only achieved in the pressure range between  $1 \times 10^{-7}$  Torr and  $1 \times 10^{-5}$  Torr.

### 3.1.6 Thermal Load Measurement

Liquid coolant is flowed through several components of the gyrotron as a method of heat removal from the system. If both the flow rate and temperature difference through each component are known, a measurement of the thermal load in that component is possible. The measurement of the thermal load of a specific component is a diagnostic tool which can determine the amount of heat being dissipated in that component. This information provides utility either for structural integrity, such as in the high power loading of the collector, or for scientific reasons, such as with

the measurement of the ohmic losses in the cavity. Using the flow and temperature information, the thermal loading on the cooled and monitored components of the gyrotron can be calculated as

$$\text{Thermal load (W)} = \Delta\text{temp. (K)} \left( 4.2 \frac{\text{J}}{\text{g}} \right) \left( 1 \frac{\text{g}}{\text{cm}^3} \right) \times \left( \text{flow (gpm)} \times 3.785 \frac{\text{L}}{\text{gal}} \right) \left( \frac{1}{60} \frac{\text{min}}{\text{s}} \right) \left( 1,000 \frac{\text{cm}^3}{\text{L}} \right) \quad (3.5)$$

where the specific heat of H<sub>2</sub>O is 4.2 J/g, 1 g of H<sub>2</sub>O is equal to 1 cm<sup>3</sup> H<sub>2</sub>O, and 1 gallon is equivalent to 3.785 L. This calculation is especially useful in determining overheating of a component. In the case of the cavity, the ohmic losses can be directly measured and the ratio of diffractive to ohmic  $Q$  can be estimated by

$$P_{\text{ohmic}} = \frac{Q_{\text{diffractive}}}{Q_{\text{ohmic}}} P_{\text{out}}. \quad (3.6)$$

## Flow

The coolant flow rates are monitored using Proteus Hall-effect flowmeters (Proteus Ind., Model No. 703P24T and 701B24T). Model 701B24T has a flow range of 0.4–3.8 LPM (0.1–1.0 gpm) and separate units are used to monitor the cavity and gun coil flow rate and Model 703P24T has a flow range of 3.0–22 LPM (0.8–6.0 gpm) and is used to monitor the collector flow rate. The nominal flow rates for the collector, cavity, and gun coil are 1, 0.5, and 0.4 gpm. The characteristics of the flowmeters are summarized in Table 3.2.

The principles of operation of the flowmeter are as follows; as liquid flows through the meter, a rotor spins. Magnets in the rotor switch a Hall-effect sensor mounted in the sensor body, and the resulting pulse train is converted by electronics to a voltage that is linearly proportional to the flow rate through a calibration factor. However, due to the use of magnets in the flowmeters, they must be either situated remote to the superconducting magnet or orthogonal to the external magnetic field lines. Therefore, the included temperature sensors cannot accurately measure the thermal load of the gyrotron components due to their distance from the gyrotron.

## Temperature

Inlet and outlet coolant temperatures are then measured by immersed negative temperature coefficient (NTC) thermistors (Omega, Model No. ON-403-PP). Thermistors are electrical resistors whose resistance changes rapidly with temperature. Ther-

Table 3.2: Flow parameters for the Proteus sensors of the 460 GHz gyrotron [17].

	Nominal flow rate (gpm)	Flow range (gpm)	Model No.	Flow sensor material
Collector	1	0.8–6.0	703P24T	Polypropylene
Cavity	0.5	0.1–1.0	701B24T	Brass
Gun coil	0.4	0.1–1.0	701B24T	Brass

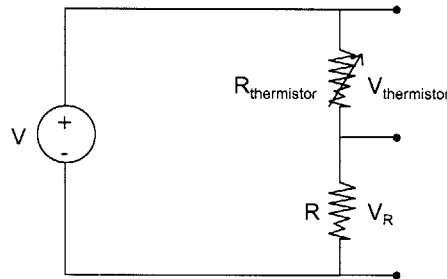


Figure 3-11: Thermistor resistance measuring circuit.

thermistors are usually made from metal oxide semiconductor material encapsulated in an epoxy bead. To operate, they must be supplied with an excitation current and the voltage read across the terminals (*c.f.* Fig. 3-11). Because self  $I^2R$  heating caused by the excitation current itself can raise the temperature of the sensing element in addition to changing the resistance, a low excitation current must be supplied [96]. In the circuit from Fig. 3-11, the thermistor resistance can be calculated as

$$R_{\text{thermistor}} = R \left( \frac{V}{V_R} - 1 \right). \quad (3.7)$$

where  $R$  is a fixed value resistor comparable in value to that of the thermistor.

### 3.1.7 Small-Signal Detection

Lock-in amplifiers are commonly used to accurately detect and measure very small AC signals, even when the small signal may be obscured by noise sources orders of magnitude larger. In our setup, a Stanford Research Systems (Model No. SR830) lock-in amplifier is used in conjunction with an optical chopper whose function is to convert a CW signal into a pulsed signal. The lock-in amplifier uses a phase-sensitive detection technique to identify the component of the signal at a specific reference frequency and phase. Thus all noise at frequencies other than the reference frequency is rejected and will therefore not affect the measurement [97].

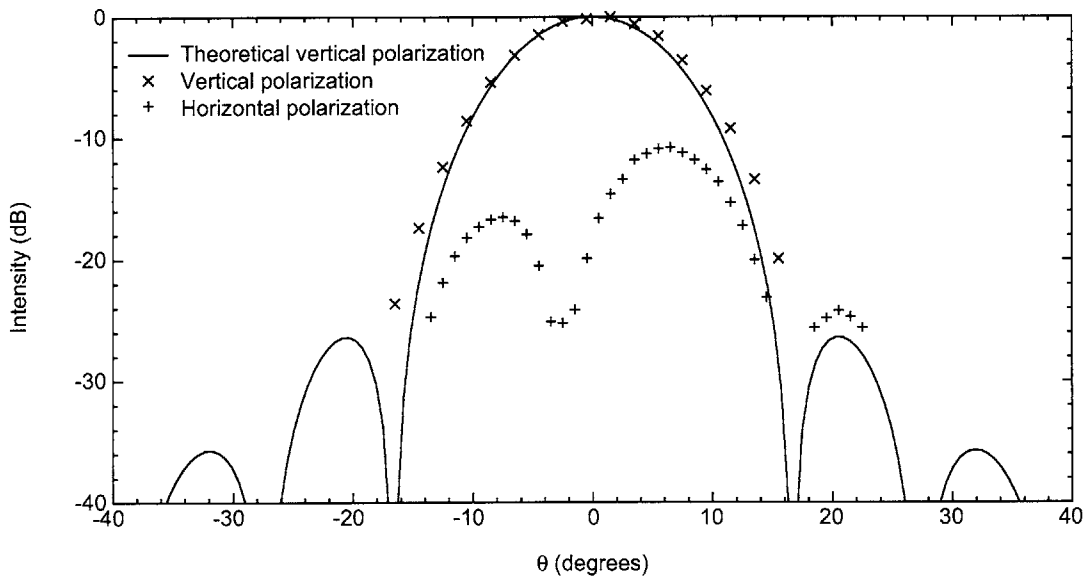


Figure 3-12: Far-field radiation scan of the cylindrical  $TE_{1,1}$  output of the BWO at 41 cm.

### 3.1.8 Cold Test

A “cold test” is a low power measurement of a gyrotron component in an environment outside of the gyrotron, usually performed with a low power source. Conversely, a measurement performed using the gyrotron is referred to as a “hot test.” It can be extremely useful to cold test components internal to the gyrotron such as the cavity or an internal mode converter before they are installed. Low power measurements of the 460 GHz gyrotron cavity were performed with a backward wave oscillator.

#### Backward Wave Oscillator

The backward wave oscillator (BWO), also known as the carcinotron, is a wideband tunable millimeter wave generator. A vacuum electron device, an electron beam which is focused by magnets passes through a periodic metallic structure and induces an electromagnetic wave. The electron beam and the electromagnetic wave move in opposite directions, and the output power is extracted near the electron gun. Wide frequency tuning is available through controlling the collector potential. Since the electrons travel in a medium with a velocity greater than that of the propagating electromagnetic wave, the structure is known as a *slow-wave* structure, where this form of radiation is known as Cherenkov radiation.

A BWO sweeper (Insight Product Company, Model No. IPG-140-178) is capable of generating up to 100 mW of power between 113 and 173 GHz in the rectangular

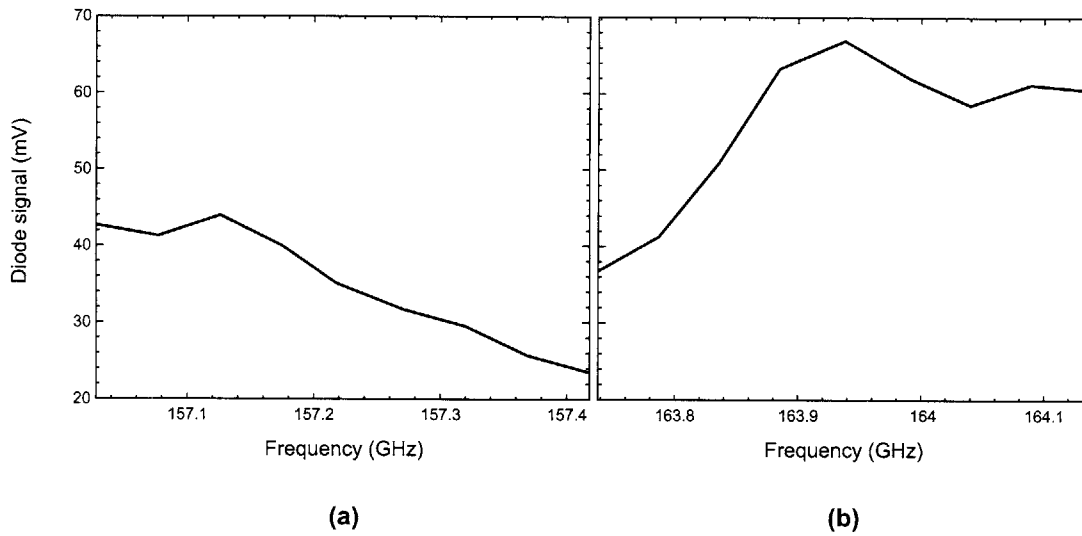


Figure 3-13: Power drift over frequency of the BWO.

TE<sub>1,0</sub> mode. The source is controlled by a voltage corresponding to a frequency which varies by approximately  $\pm 0.5$  GHz from the primary frequency. This variation occurs over time and can be compensated by a “fine tune” adjust knob on the front panel, which sweeps over 1% of the BWO voltage, or roughly 1.5 GHz. The frequency variations by the source introduce an uncertainty in the measurements. In addition, the power of the source is not constant over time or frequency, as shown in Fig. 3-13. Figure 3-12 shows the far-field radiation scan of the output of the BWO at 41 cm in the cylindrical TE<sub>1,1</sub> mode. The vertical polarization is represented by  $\times$ 's, the horizontal polarization by  $+$ 's, and the theory is shown by the solid line.

## 3.2 Equipment

This section summarizes the important functions of the equipment used in both the pulsed gyrotron test setup and the permanent CW gyrotron setup.

### 3.2.1 Pulsed Equipment

The key component in the pulsed gyrotron test setup is the high voltage modulator. The high voltage modulator is capable of operation above 100 kV and 1.2 A operation in 3  $\mu$ s pulses and up to 33 Hz repetition rate. The standard tube modulator consists of a 30 kV, 100 mA DC power supply (Spellman High Voltage Electronics Corp., Model No. RHP-3KW), a tunable pulse forming network (PFN), and thyatron switch, and a pulse transformer with 1:12 turns ratio to step the voltage pulse up to

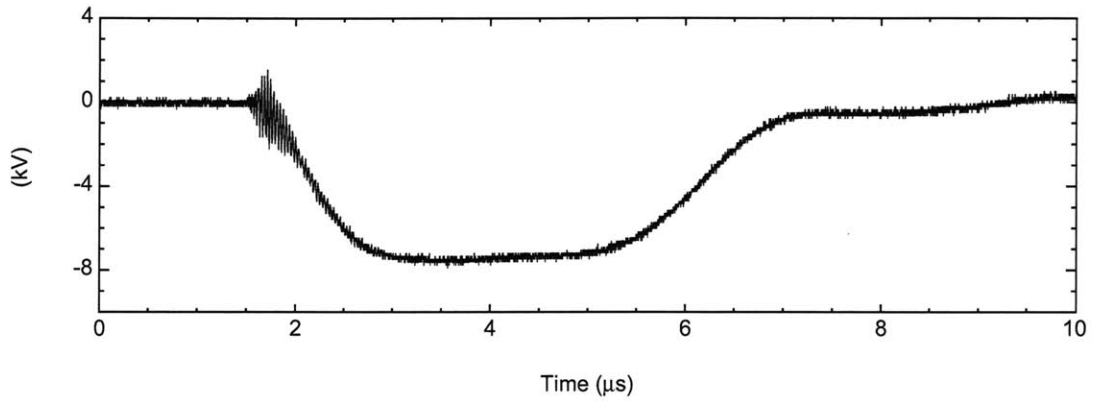


Figure 3-14: Typical voltage pulse from the high voltage modulator. The corresponding current trace is shown in Fig. 3-8. The signal corresponds to the  $TE_{0,3,1}$  mode at 8.58 T, and the diode trace shown in Figure 3-7.

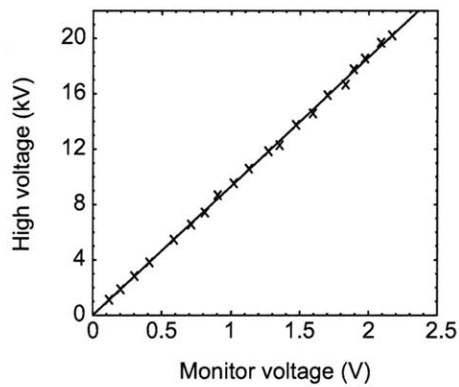
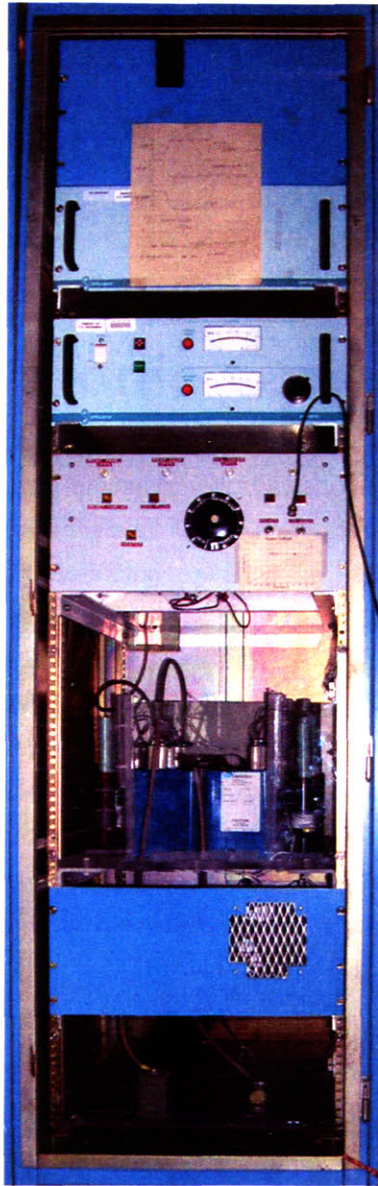
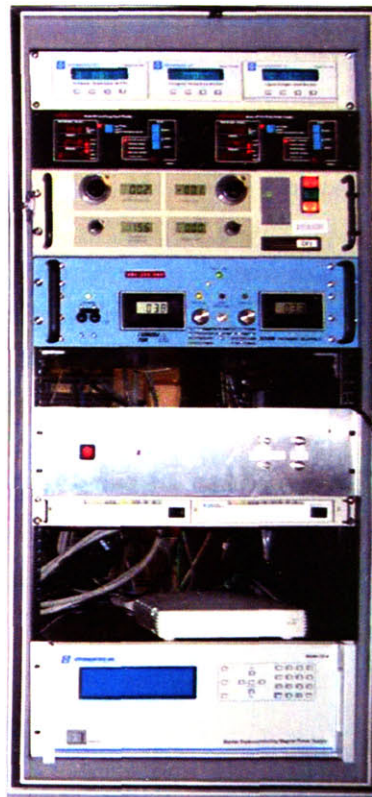


Figure 3-15: Calibration of the cathode voltage readout.





(a)



(b)

Figure 3-16: Photograph of (a) the front end of the high voltage modulator (b) the CW gyrotron console, showing the cryogenic temperature monitors, liquid cryogen level monitor, ion pump controllers, CW switching high voltage power supply, gun coil power supply, computer controls, and superconducting magnet power supply.

the required voltage [98].

The actual voltage and current drawn were limited by the experiment. A photograph of the front end is shown in Fig. 3-16(a). The cathode voltage is measured by a capacitive-resistive divider installed in the modulator oil tank, where the cathode voltage is related to the monitored voltage through a multiplication factor of 9.32 kV/V and was calibrated by a high voltage probe (*c.f.* Fig. 3-15).

A typical voltage pulse from the high voltage modulator is shown in Fig. 3-14. The corresponding current traces are shown in Fig. 3-8. The signal corresponds to the  $TE_{0,3,1}$  mode at 8.58 T, and the diode trace shown in Figure 3-7.

### 3.2.2 CW Equipment

A photograph of the CW gyrotron console is shown in Fig. 3-16(b). From top to bottom, the equipment located in the rack is as follows: two cryogenic temperature monitors (Cryomagnetics, Inc., Model No. TM-600), a liquid cryogen level monitor (Cryomagnetics, Inc., Model No. LM-500), two ion pump controllers (Duniway, Model No. Terranova 741), a CW switching high voltage (and filament) power supply (Spellman High Voltage Electronics Corp., Model No. DF25N3X3177), the gun coil power supply (Lambda EMI, Model No. EMS 40-50), home built control electronics, (National Instruments, Model No. ENET-232/4), (National Instruments, Model No. GPIB-ENET/100), and the superconducting magnetic power supply (Cryomagnetics, Inc., Model No. CS-4-100).

## Chapter 4

# Design of a 460 GHz Second Harmonic Gyrotron Oscillator

The goal of this work is to demonstrate the production of 460 GHz radiation for eventual use in sensitivity-enhanced NMR by dynamic nuclear polarization. In this chapter, we discuss the challenges of building a high frequency continuous-wave submillimeter gyrotron. In order to affordably achieve high frequency with available superconducting magnet technology, the design must be at the second electron cyclotron harmonic. This constraint becomes the primary challenge of the design.

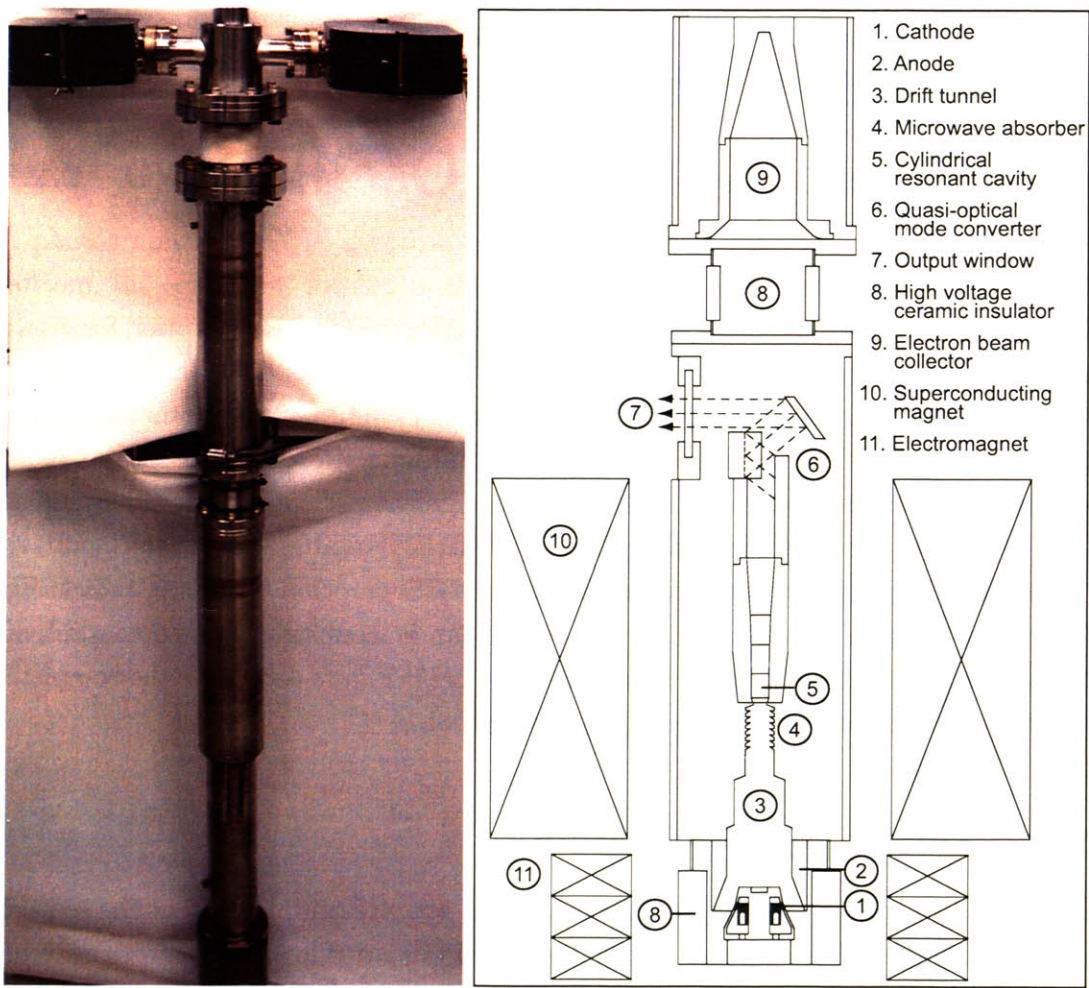
A schematic (not drawn to scale) of the 460 GHz gyrotron oscillator, indicating key components, is shown in Fig. 4-1(b), which can be compared to a photograph of the gyrotron tube free-standing shown in Fig. 4-1(a). Figure 4-2 shows the complete gyrotron in an operational position with the author.

### 4.1 Target Specifications

The 460 GHz gyrotron oscillator was designed to operate continuously at the second electron cyclotron harmonic at low voltages and output powers of between several watts and several tens of watts.

#### 4.1.1 Dynamic Nuclear Polarization

The gyrotron oscillator design will permit the precise control of the output power and frequency that is necessary for applications to sensitivity-enhanced magnetic resonance spectroscopy through dynamic nuclear polarization (DNP). Originally employed to produce spin polarized targets for nuclear scattering experiments, DNP is a technique through which the greater Zeeman polarization of the electrons is trans-



(a)

(b)

Figure 4-1: (a) Photograph of the gyrotron tube free-standing (b) Cross-sectional schematic of the cylindrically symmetric 460 GHz gyrotron tube, not shown to scale, indicating key components.

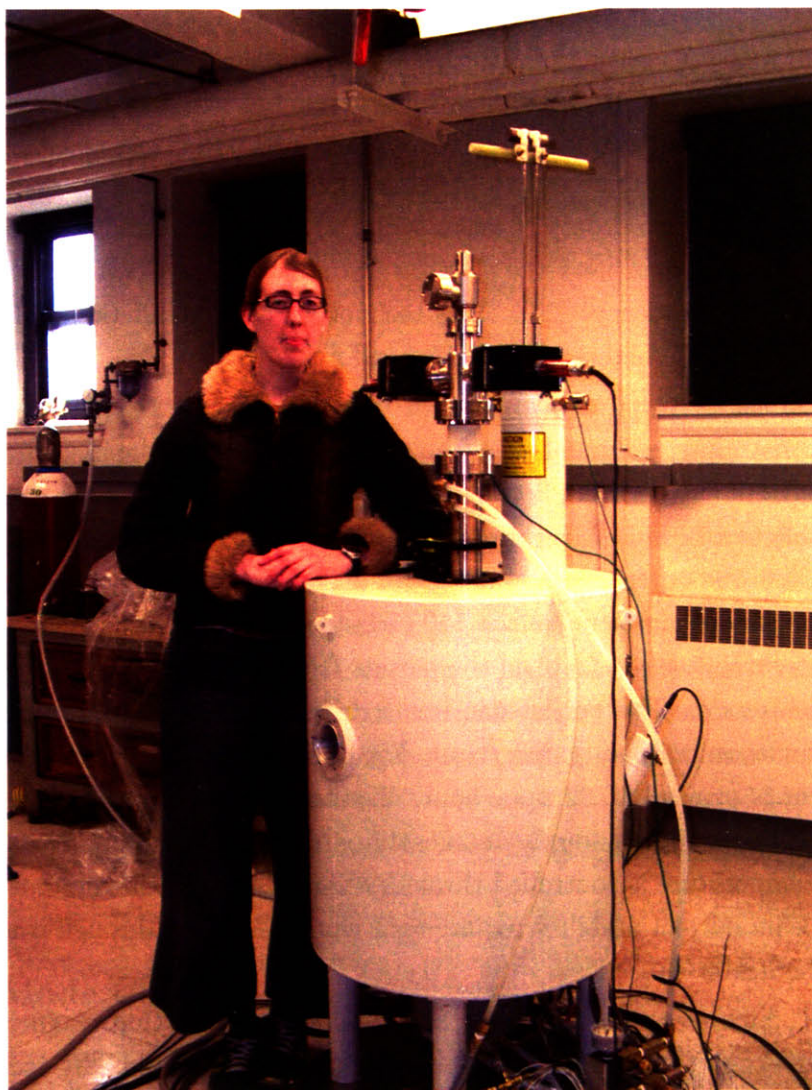


Figure 4-2: Photograph of the author and the 460 GHz gyrotron located in the bore of the superconducting magnet.

Table 4.1: Gyrotron stability requirements for DNP/NMR spectrometer [18]

Parameter	Sensitivity	Stability requirement
Magnetic field	1.1 GHz/T	$5 \times 10^{-3}$ T
Beam voltage	10 MHz/kV	500 V
Cavity temperature	2.2 MHz/ $^{\circ}$ C	2.3 $^{\circ}$ C
Beam current	30 kHz/mA	170 mA

ferred to the nuclei, in this case to enhance the sensitivity of a subsequent NMR experiment by up to two orders of magnitude. DNP requires irradiation of the sample with 1–10 W of power near the electron Larmor frequency (which is close to the electron cyclotron frequency) [27]. This technology will extend the applicability of DNP techniques to the highest frequencies and fields.

Aspects of the gyrotron are constrained by requirements of the NMR spectrometer. These constraints, enumerated in Table 4.1, are related to the frequency stability and bandwidth of the rf power and are based on the assumption that the frequency must be stable to within 50 MHz (in our case, 10 ppm at 460 GHz). The sensitivities are derived from the experimentally measured dependence of the gyrotron’s frequency pulling on system parameters from a 140 GHz gyrotron experiment [18]. The magnetic field constraint sets a limit on the permissible drift of the field while operating in persistence mode. The persistence mode drift rate of the 9 T superconducting gyrotron magnet is less than 1 ppm/hour. For comparison, the drift on the 700 MHz NMR magnet is typically 0.02 ppm/hour. The voltage requirement determines the regulation of the HV power supply and is attainable from commercial manufacturers. The cavity temperature is controlled through a closed refrigeration system with feedback. The beam current stability requirement can be satisfied through computerized control of the heater current.

A 16.4 T, high-resolution, Magnex Scientific superconducting magnet including a sweep coil is the defining component of a nominally 700 MHz NMR spectrometer. The proton frequency of the NMR spectrometer is 700 MHz, corresponding to an electron Larmor frequency of 460 GHz. Taking both the sweep coil and the regions of positive and negative DNP enhancement into account, there is a window of 1.14 GHz over which the dynamic nuclear polarization mechanism can be excited.

Table 4.2 summarizes the gyrotron and cavity design parameters. Notably, the gyrotron was designed for low voltage and current (12 kV, 100 mA) operation in a single second harmonic higher order mode. The DNP experiment requires moderate peak powers but continuous duty cycle operation for periods lasting 7-10 days, during

Table 4.2: Gyrotron design parameters

Frequency	460 GHz	Perp. velocity spread	4 %
Magnetic field	8.4 T	Velocity pitch factor	2
Harmonic number	2	Magnetic compression	28
Mode	TE <sub>0,6,1</sub>	Electron beam radius	1 mm
Accelerating voltage	12 kV	Cavity diffractive Q	31,100
Beam current	100 mA	Cavity ohmic Q	19,400
Cathode radius	5.4 mm	Total cavity Q	12,000

which the output power and frequency must be stable to within 1 % and at least 5 MHz respectively.

## 4.2 Second Harmonic Considerations

Operation of a gyrotron at the second harmonic of the electron cyclotron resonance, which results in approximately twice the fundamental frequency for a given magnetic field, is attractive even when magnet technology is not a limiting factor. Nevertheless, it suffers from three principal challenges: high ohmic losses, which reduce the efficiency, high start currents, which require higher beam power than our experimental design allows, and finally, mode competition. Of these, mode competition from fundamental modes whose starting currents are inherently lower is the primary concern. Due to the density of the mode structure in an overmoded resonator, particularly when higher order longitudinal modes are included, mode competition must be explicitly addressed in the design [99].

### 4.2.1 Mode Competition

In order to operate at this relatively high frequency, we have selected to operate with a second harmonic mode and a lower field (8.4 T) niobium titanium superconducting magnet. However, with increasing frequency, the fundamental (and accordingly harmonic) mode spectrum becomes increasingly dense. Many fundamental electron cyclotron modes have lower starting currents than second harmonic modes and can more efficiently couple to the electron beam, therefore it is critical that the second harmonic design mode must be sufficiently free from such fundamental modes, as well as other second harmonic modes.

Through meticulous design we can ensure that there is a gap in the frequency

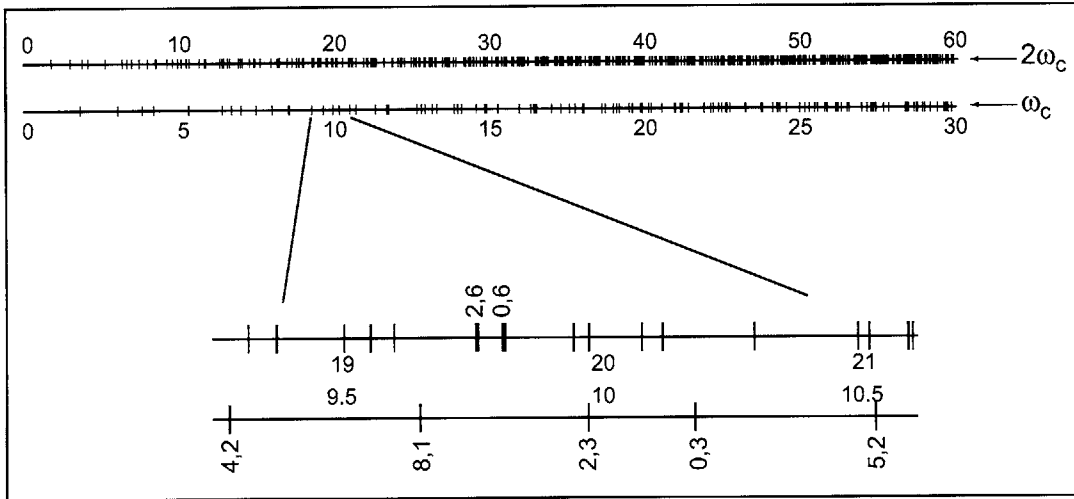


Figure 4-3: Chart of the TE mode indices up to to  $\nu_{mp} = 30$  for the fundamental modes and  $\nu_{mp} = 60$  for the second harmonic modes.

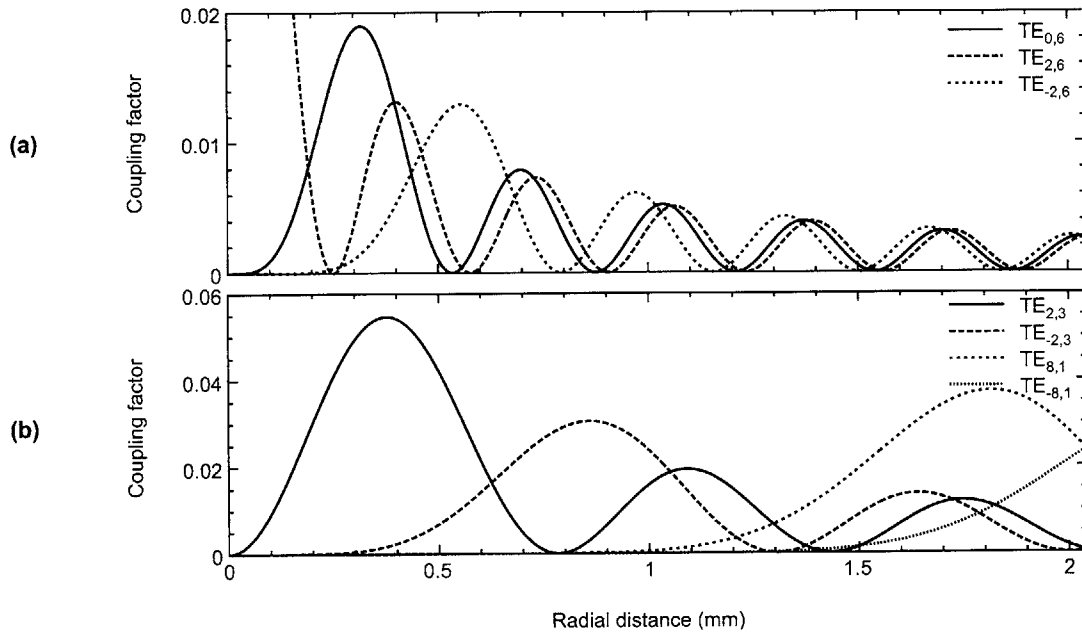


Figure 4-4: Coupling factor for (a) the  $TE_{0,6}$  and  $TE_{2,6}$  second harmonic modes of both rotations and (b) the nearby competing co- and counter-rotating  $TE_{2,3}$  and  $TE_{8,1}$  fundamental modes.



spectrum in which the design mode can be situated. First, recall that for a gyrotron operating near cutoff ( $k_{\perp} \gg k_z$ ) the frequency of a  $\text{TE}_{mp}$  mode can be approximated by

$$f \simeq \frac{c\nu_{mp}}{2\pi r_0} \quad (4.1)$$

Second, from the resonance condition in (2.17), we find that  $\nu_{mp1} \simeq \frac{1}{2}\nu_{mp2}$ , where the subscripts 1 and 2 denote the fundamental and second harmonic modes, respectively. From (4.1), it follows that gaps in the frequency spectrum are a direct result of the spacing of the TE mode indices,  $\nu_{mp}$ . To avoid competition from fundamental modes, we must choose a second harmonic mode where half of the value of its index,  $\frac{1}{2}\nu_{mp2}$ , is located in a sizable gap between consecutive fundamental mode indices ( $\nu_{mp1}$ ).

From inspection of the mode spectrum in Fig. 4-3, the  $\text{TE}_{0,6}$  second harmonic design mode is bounded from the left and right by the fundamental  $\text{TE}_{8,1}$  and  $\text{TE}_{2,3}$  modes. The gap in mode indices where the second harmonic design mode is located linearly translates into a region in the magnetic field where our mode can be excited without competition from the fundamental, since the frequency given in (4.1) is proportional to the cavity magnetic field. In addition, it can be seen from the coupling impedance of the modes in Fig. 4-4 that a beam radius can be chosen such that the  $\text{TE}_{8,1}$  mode does not interfere with excitation of the  $\text{TE}_{0,6}$  design mode, and as such the mode competition can be further diminished.

## 4.2.2 Start Oscillation Current

Another technique to suppress the fundamental modes comes from lowering the starting currents, or the minimum energy of the electron beam needed to excite the operating mode.

The ratio of the second electron cyclotron harmonic,  $I_{2\omega_c}$ , to the fundamental starting current,  $I_{\omega_c}$ , can be approximated from (2.62) as follows;

$$\frac{I_{2\omega_c}}{I_{\omega_c}} = \frac{(L/\lambda)_{\omega_c}^2}{(L/\lambda)_{2\omega_c}^2} \times \frac{1}{\beta_{10}^2} \times \frac{Q_{\omega_c}}{Q_{2\omega_c}} \times \frac{(C_{m,p})_{\omega_c}^2}{(C_{m,p})_{2\omega_c}^2}, \quad (4.2)$$

where the subscript  $\omega_c$  denotes the fundamental mode quantities and  $2\omega_c$  the second harmonic. The first term is approximately  $\frac{1}{4}$  since the number of wavelengths in a cavity of fixed length  $L$  is approximately twice as large at second harmonic as at the fundamental. Due to the low voltage used to accelerate the electrons, the second term, which incorporates the normalized transverse velocity of the electrons, is large; it is about 25 for velocity pitch factor equal to 2 at 12 kV. In practice, this can be mitigated through a design in which the second harmonic  $Q$  is large with respect to

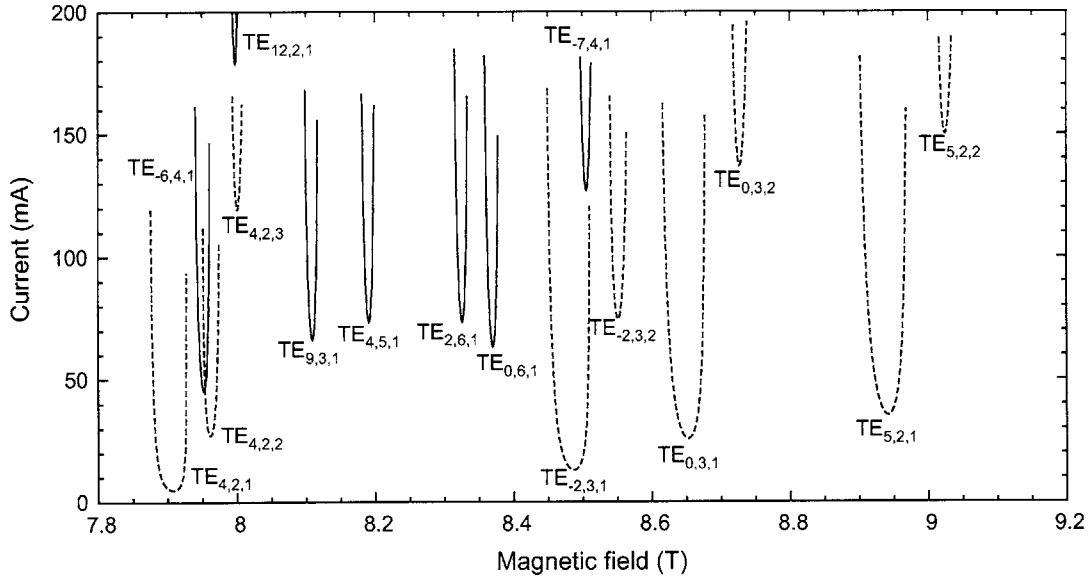


Figure 4-5: Starting currents at 12 kV and alpha and spread parameters taken from EGUN simulations (*c.f.* Fig. 4-9). In the case where the alpha from the EGUN simulation is undefined, an beam alpha of 2.0 and corresponding velocity spread is used. Solid lines represent second harmonic modes and dotted lines fundamental modes.

the competing fundamental mode. In this experiment, the value of the third factor is about  $\frac{1}{3}$ . The fourth factor is the ratio of beam-wave coupling factor  $C_{m,p}^2$  of the modes and depends on the beam radius. It is generally greater than unity because the  $\nu_{mp}^2$  term is smaller at the fundamental than at the second harmonic. In summary, the minimum starting current for the second harmonic modes is generally at least several times higher than the minimum starting current for the fundamental modes.

In the present design, each factor was optimized. A long cavity profile was chosen in order to lower both the second harmonic and fundamental start oscillation currents into a regime where the electron gun is operable. This is discussed further in Section 4.3.3. An operating voltage was chosen for the electron gun where the velocity pitch factor was maximized (thus reducing the second factor). This is discussed further in Section 4.3.1. For the third factor, the input and output tapers of the cavity geometry were optimized, which will be discussed further in Section 4.3.3. Finally, the radius of the electron beam was designed such that the coupling of the second harmonic mode was optimized. Working within the limits of the compression of the electron beam by the magnetic field, the third radial maximum of the  $TE_{0,6}$  mode was designed to interact with an electron beam of radius 1.03 mm inside the interaction cavity resonator (*c.f.* Fig. 4-4). In total, the starting current for the design mode

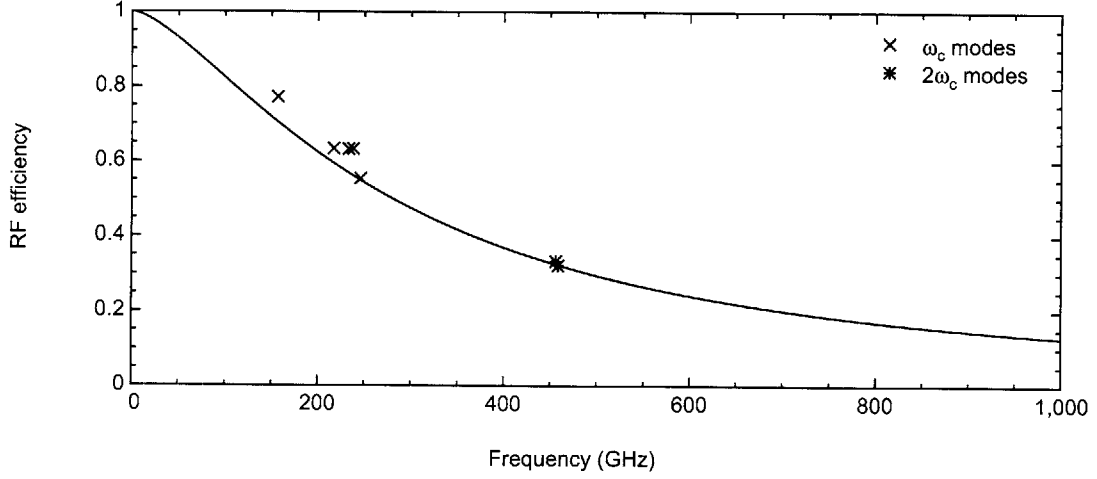


Figure 4-6: Theoretical RF efficiency in the 460 GHz gyrotron cavity.

was lowered to 60 mA.

Fig. 4-5 shows a plot of the starting currents of modes in the vicinity of our design  $TE_{0,6}$  mode versus cavity magnetic field, as obtained by linear theory using beam parameters simulated in EGUN. The starting current depicted for the design mode is about 60 mA at a cavity magnetic field of 8.4 T. Four fundamental modes shown are the  $TE_{4,2}$ ,  $TE_{2,3}$ ,  $TE_{0,3}$ , and the  $TE_{5,2}$  and the remaining modes are second harmonic. The  $TE_{0,6}$  mode is sufficiently far away from the fundamental modes, and the  $TE_{8,1}$  fundamental mode is absent here due to poor beam coupling.

### 4.2.3 Ohmic Losses

Ohmic losses increase rapidly with frequency and become a limiting factor for output power at high frequencies. This can be seen where the diffractive  $Q$  is proportional to the square of the frequency,

$$Q_{\text{diffractive min}} = 4\pi \left(\frac{L}{\lambda}\right)^2 \propto f^2, \quad (4.3)$$

and the ohmic  $Q$  is proportional to the square root of the frequency,

$$Q_{\text{ohmic}} = \frac{r_0}{\delta} \left(1 - \frac{m^2}{\nu^2 m_p}\right) \propto \sqrt{f}. \quad (4.4)$$

The RF efficiency of the cavity is given by

$$\eta_{RF} = \frac{Q_{\text{ohmic}}}{Q_{\text{diffractive}} + Q_{\text{ohmic}}}, \quad (4.5)$$

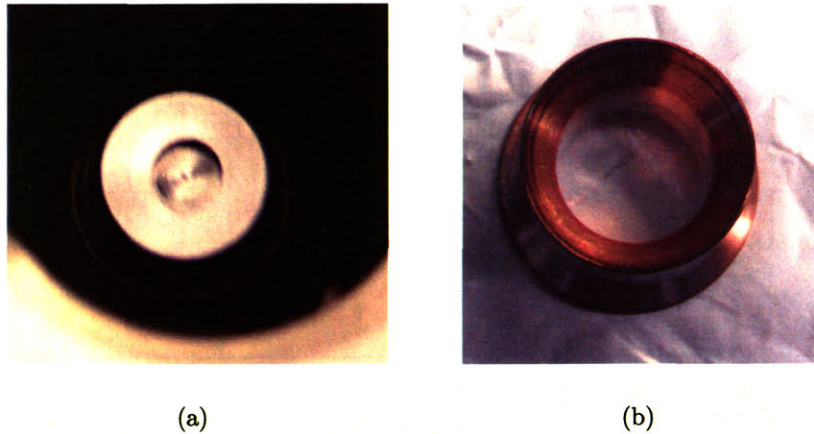


Figure 4-7: Photographs of the (a) cathode and (b) anode.

In the design of the 460 GHz cavity in the  $TE_{0,6,1}$  mode, the extracted power is reduced to 32 % of the generated power due to the ohmic losses in the walls of the cavity. Figure 4-6 shows the ohmic losses as a function of frequency for the 460 GHz cavity, where the  $\times$ 's indicate the fundamental modes and the \*'s are the second harmonic modes.

In order to reduce ohmic losses, the highly overmoded cavities required make mode competition more severe; the mode density increases as the cavity size becomes larger. In lowering the start current through lengthening the cavity, we encounter an elevated diffractive  $Q$ . In reality, the cavity design must be a compromise between several factors.

## 4.3 Components

### 4.3.1 Electron Gun

Many gyrotrons employ a thermionic electron gun called the magnetron injection gun (MIG) to generate a high current annular electron beam. The "M-Type" cathode for such a gun typically consists of a matrix material (*e.g.* tungsten) which is impregnated with rare-earth metals (*e.g.* barium oxide) and other materials in order to reduce the effective work function. To further enhance the emission, an overcoating of other materials such as osmium has been applied, while the exact chemistry is usually considered proprietary to the manufacturer. When the emitter is heated by an AC current, some electrons gain sufficient thermal energy to overcome the work function barrier and are ejected into free space. The cathode is biased to a large negative

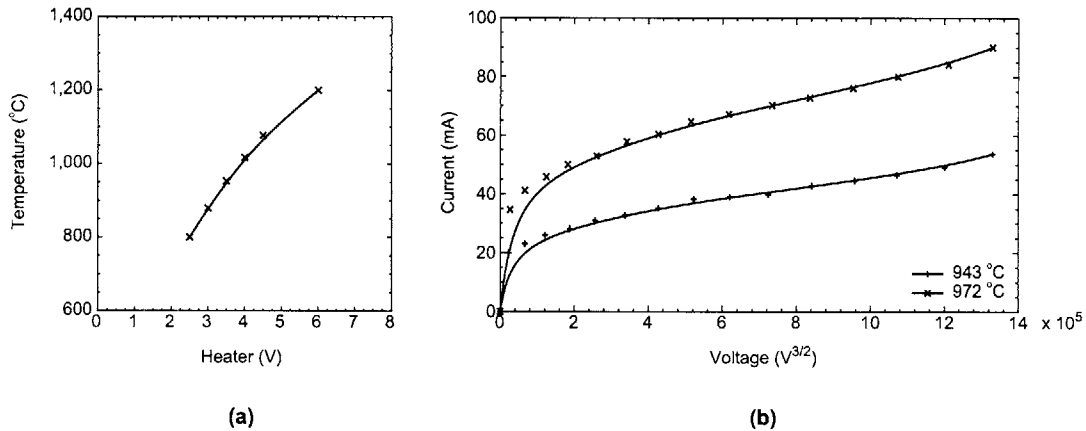


Figure 4-8: (a) Test data on the 460 GHz cathode (Semicon, Model No. BGC-101 S/N 0001969) by J. Tarter [8] (b) Current-voltage data for various cathode temperatures.

voltage relative to the hollow anode, so that the ejected electrons are accelerated toward the anode. The cathode is intended to operate at about 1,000°C for over 10,000 hours.

The 460 GHz emitter (Semicon, Model No. BGC-101 S/N 0001969) is a standard, commercial “M-Type” cathode. Photographs of the anode and cathode are shown in Fig. 4-7. The Semicon cathode test data (*c.f.* Fig. 4-8(a)) obtained with the cathode free standing in bell jar, indicate capability of operation at up to a temperature of 1,200°C corresponding to a filament voltage of approximately 6 V [8]. Degradation of the heater potting material begins when the filament temperature exceeds 1,650°C. The temperature may be estimated by using a ratio of hot to cold resistance to calculate the average filament temperature, where the voltage should be measured as close to the cathode as possible to avoid introducing an error due to the resistance in the leads.

The 250 GHz electron gun was briefly studied to determine its operating characteristics in short pulse operation. Figure 4-8(b) shows the transition between space-charge limited electron emission at lower voltages, and temperature limited emission at higher voltages. It confirms that we operate in the temperature limited regime.

The low voltage, diode-type electron gun employed in this experiment features an electrode design which is modeled after the gun employed in a successful 250 GHz gyrotron experiment [40]. The low operating voltage of less than 15 kV eliminates the need for cumbersome oil cooling and high voltage insulation and reduces the possibility that ionizing radiation will be produced. In addition, the low gun voltage allowed us to use a small ceramic so that the diameter of the gun can fit through the magnet bore. In practice, the electron beam parameters such as the velocity pitch

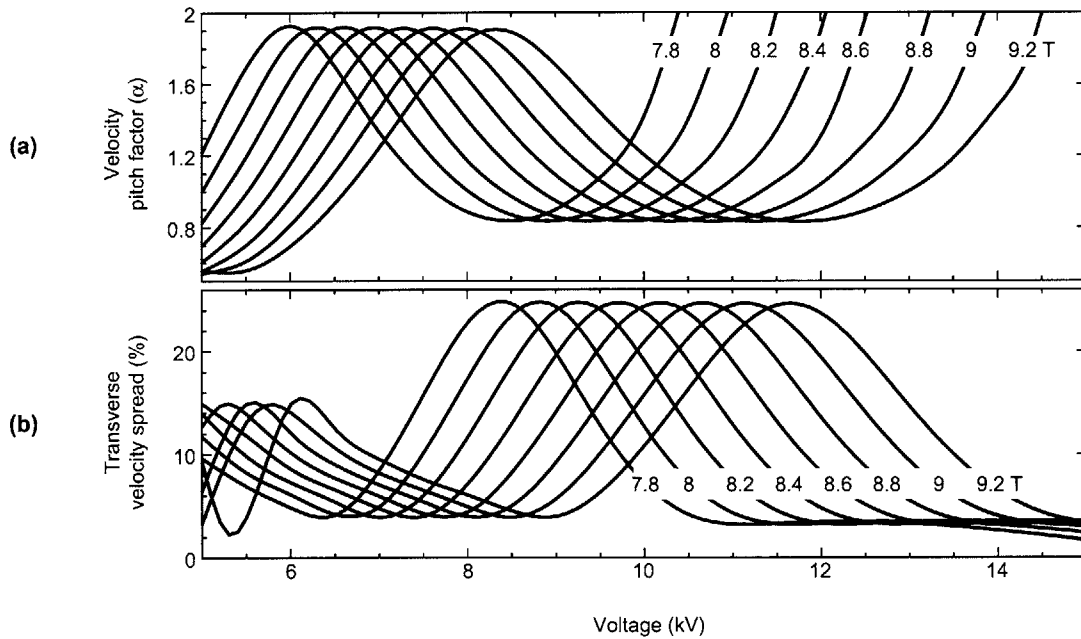


Figure 4-9: (a) Velocity pitch factor and (b) transverse velocity spread for the low-voltage, diode-type gun used in the 460 GHz gyrotron experiment. Each curve is derived from EGUN simulations of the gun geometry conducted as a function of voltage and magnetic field.

factor and velocity spread can be experimentally tuned by an electromagnet shim coil situated around the electron gun through changing the magnetic compression, the ratio of axial magnetic field at the cavity and cathode. Also known as the “gun coil”, it reaches a maximum magnetic field of  $8.5 \times 10^{-2}$  T on axis and serves to fine tune the electron beam characteristics. The reduced complexity of this gun design is achieved at the expense of an increased sensitivity of the electron beam velocity pitch factor and velocity spread to the exact operating parameters. For that reason, characteristics of the electron gun were studied using the EGUN electron optics and gun design program [74] and optimized for the intended operating regime. Figure 4-10(b) depicts a typical simulation of the trajectories followed by electrons accelerated by a 12 kV potential in a gently tapered magnetic field reaching a maximum of 8.4 T in the cavity. A closer view of the electron gun region is shown in Fig. 4-10(a). The transverse rms velocity spread and beam  $\alpha$  (*c.f.* Fig. 4-11) reach 4 % and 2, respectively, in the region of the cavity for the design parameters optimized for second harmonic operation. For operating parameters corresponding to excitation of fundamental modes observed in this experiment, EGUN simulations predict large variations in the velocity spread and velocity pitch ratio with changes in the beam

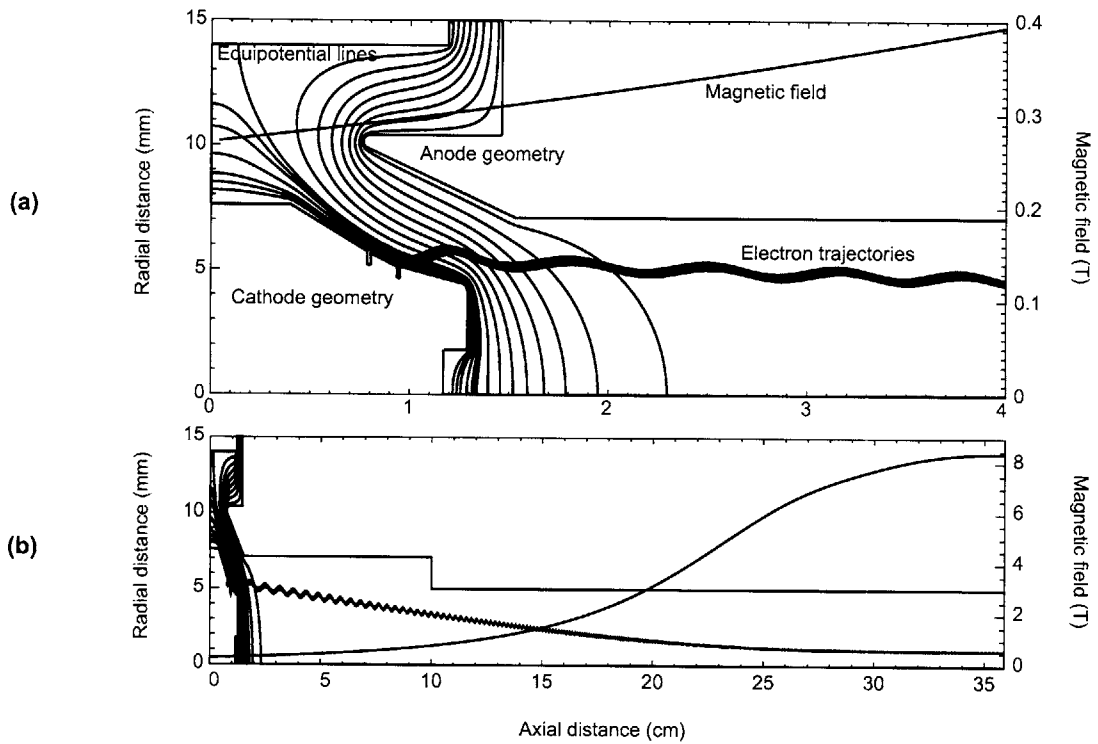


Figure 4-10: Simulation of the evolution of the transverse and axial velocities of the electrons accelerated at 12 kV in the 460 GHz gyrotron experiment using the EGUN electron optics and gun design program. The simulation includes the electron trajectories, equipotential lines, cathode and anode geometries, and 8.4 T applied magnetic field of the gun region.

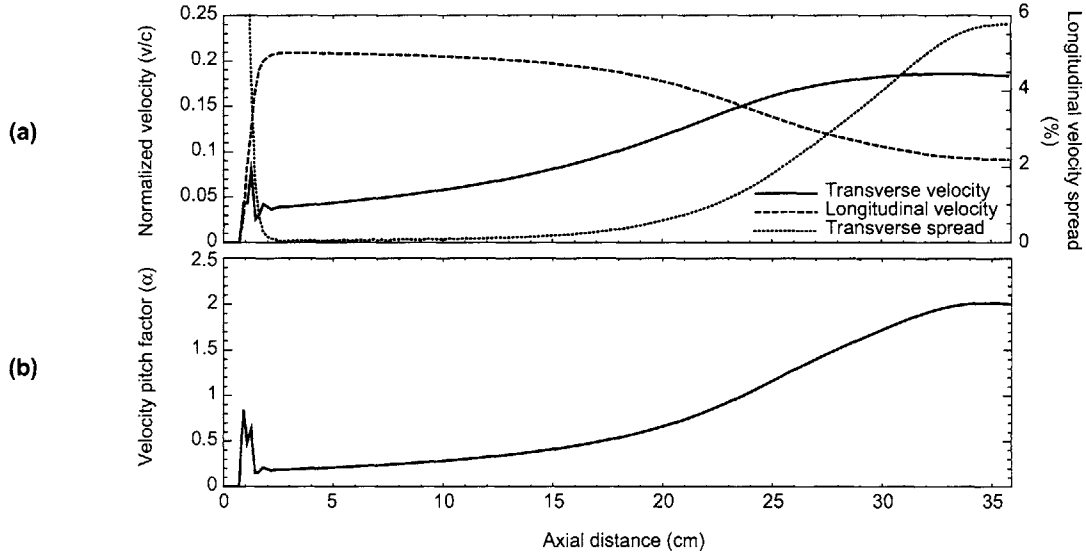


Figure 4-11: (a) Transverse (solid line) and longitudinal (dashed line) electron beam velocity and transverse spread (dotted line) and (b) electron beam velocity pitch factor predictions by EGUN.

voltage and the magnetic field. The results of an EGUN study of this gun over a broader range of operating voltages and magnetic fields are shown in Figure 4-9(a) and (b).

### High voltage power supply

A custom high voltage power supply was commissioned from the Spellman High Voltage Electronics Corporation to generate 25 kV and 200 mA with continuous duty. Model DF25N3X3177 was built in accordance with standard catalog specifications of a Spellman Model DF3 with several MIT modifications [100]. The power supply, originally developed for X-ray tube applications, provides stable, low ripple voltage and current outputs with long term stability of less than 0.01% over 8 hours. To generate high voltage DC, the power supply utilizes a sine wave current source, produced by phase shifting series resonant circuits at switching frequencies greater than 20 kHz and incorporates IGBTs for power switching. The power supply specifications are 25 kV and 192 mA maximum, with the total power limited to 3 kW. The filament supply is configured to operate as a regulated programmable separate power supply, with maximum operating parameters of 5 A and 6 V, and accuracy and linearity of  $\pm 5\%$  or better from 25% to 100% of rated current. The high voltage is of negative polarity and the filament circuit is referenced to the cathode high voltage potential (floating filament). The power supply is locally controllable via front panel potentiometers for



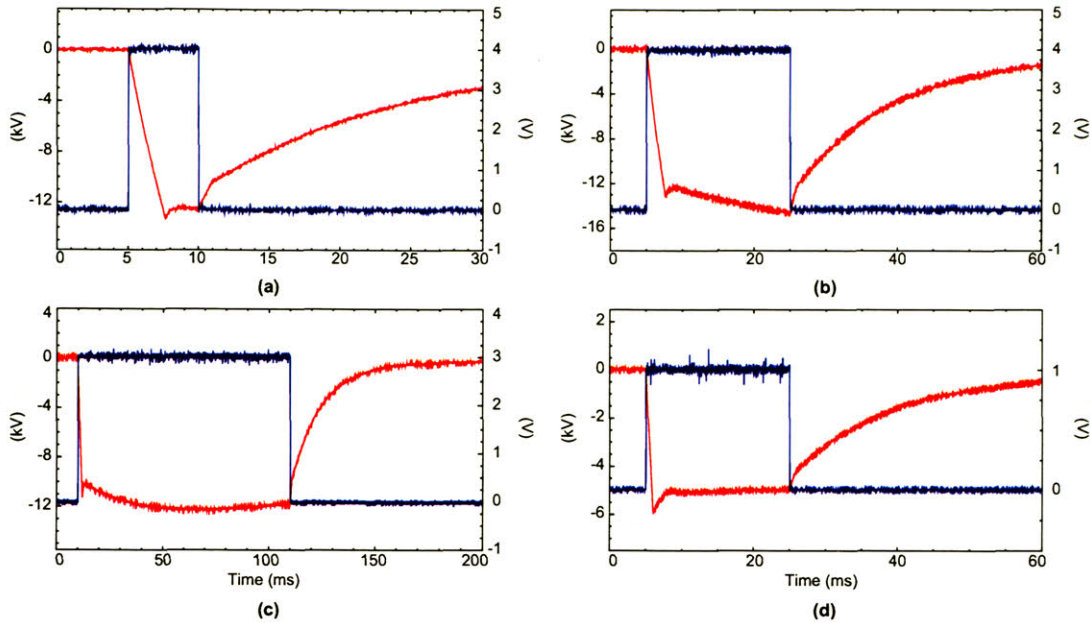


Figure 4-12: Millisecond pulse tests of the Spellman high voltage power supply over a  $700 \text{ k}\Omega$  resistive load. The red waveforms indicate the high voltage response and the blue lines are the driving pulse shape for pulses of length (a) 5 ms, (b) 20 ms, (c) 100 ms, and (d) 20 ms.

the filament current, DC high voltage, and power limit, but can also be controlled remotely via RS-232 or a DB50 analog connector. For reasons known to the manufacturer, the “milliamperes” front panel control knob has been internally reconnected to control the filament current, while the “filament amperes” control knob has no function. Further documentation is available in both the DF3 instructional and RS-232 manuals.

While designed for CW operation, the power supply is capable of crude operation in pulses of at least several milliseconds in length. In Fig. 4-12, we demonstrate several tests for pulses of 5 through 100 ms using a resistive load at 5–16 kV as measured with a high voltage probe. A resistive load of  $700 \text{ k}\Omega$  was selected to model the nominal electron gun operating parameters of 12 kV and a few tens of milliamperes. In Fig. 4-12(a), for a driving pulse of length 10 ms, the rise time to 12 kV is approximately 2.5 ms and the fall time approximately 12 ms, leaving a minimum useable pulse length of approximately 5 ms. For each case there is a voltage overshoot whose amplitude depends on the final pulse amplitude. In addition, on the pulses above 12 kV in Figs. 4-12(a)–(c), the high voltage signal never reaches a steady-state value, which is in contrast to the performance at 5 kV in Fig. 4-12(d). Unfortunately, when the multi-millisecond high voltage pulses were applied to the electron gun of

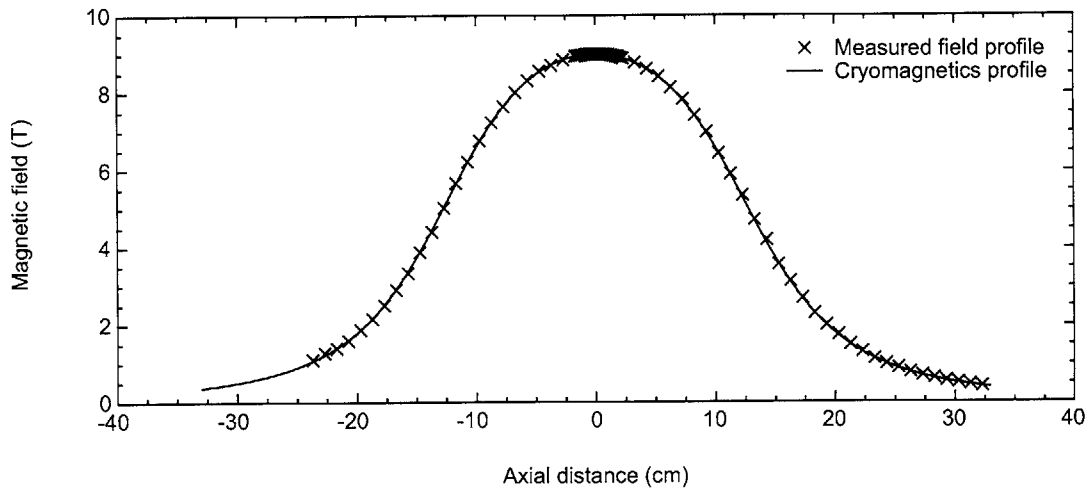


Figure 4-13: Comparison of measured axial field profile (x's) to Cryomagnetics (solid line) magnetic field profile.

the 460 GHz gyrotron at high beam current, the noise and RFI on all signal lines rendered the system inoperable.

### 4.3.2 Magnet System

The characteristics of the magnetic field along the electron trajectories from where they are emitted at the electron gun, through the cavity resonator, to where they are intercepted in the collector region are critical to the operation of a gyrotron. The peak magnetic field occurs in the cavity resonator region, where the field must be homogeneous, however not to the strict requirements of an NMR magnet. The axial magnetic field must fall off to a specified fraction of its maximum intensity in a prescribed manner in the direction of the electron gun. The transverse component of the magnetic field must be minimized in order to ensure good electron transport from the electron gun to the cavity with minimal degradation of the electron beam quality.

The magnet system of the 460 GHz gyrotron consists of a 9.2 T superconducting solenoid (Cryomagnetics, Inc.) to generate the main field and an  $850 \times 10^{-2}$  T solenoid (Ogallala Electronics, Model No. 41C2444-2) to tune the electron characteristics in the gun region.

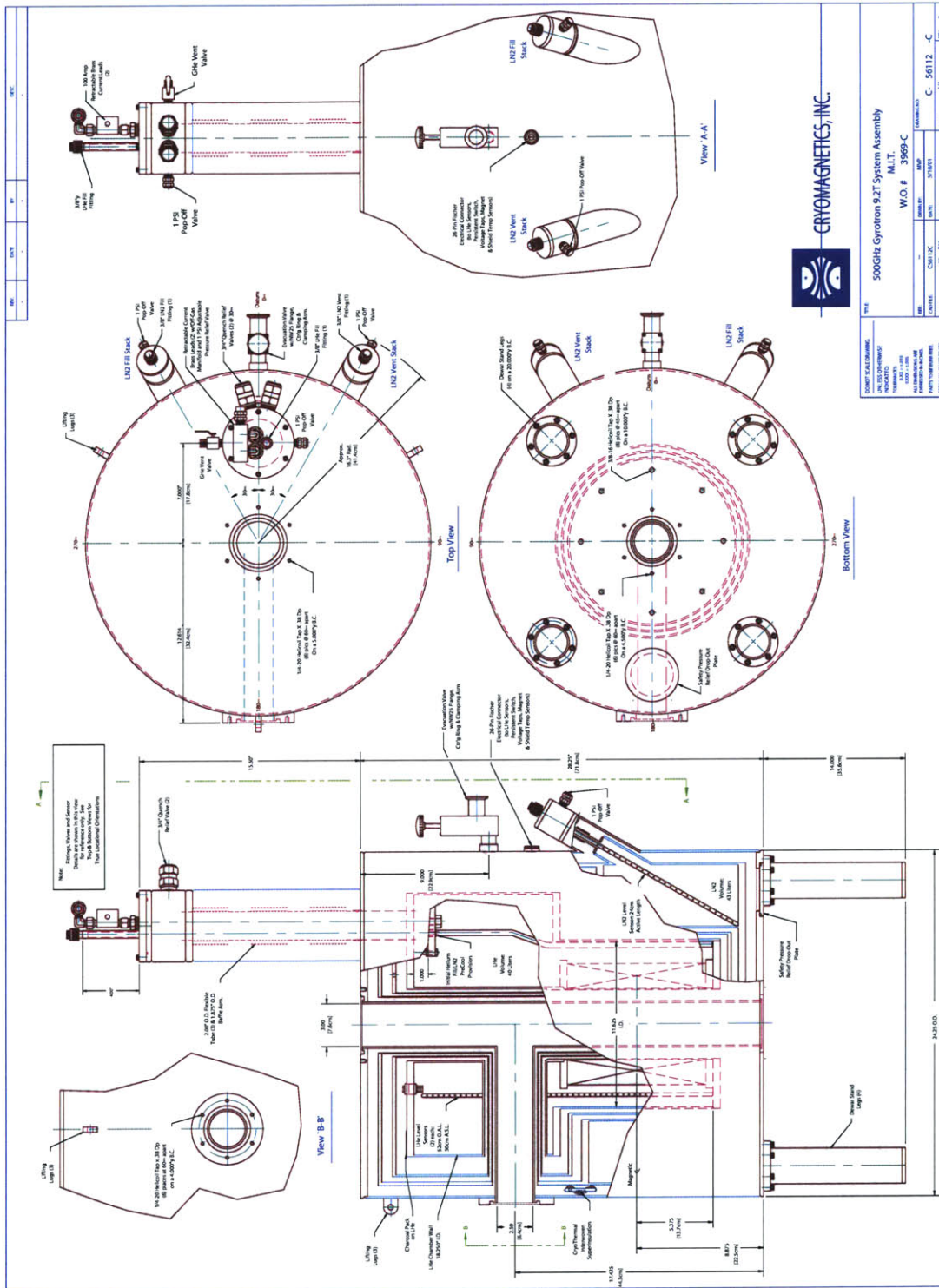


Figure 4-14: Superconducting magnet drawings, designed by Cryomagnetics, Inc. [9].

## Superconducting magnet

Superconducting magnet technology is one limiting factor in high frequency gyrotron design. At fields up to 10 T, magnets with wide room temperature bores commonly employ the NbTi superconducting technology. From 10 T to 22 T (corresponding to a fundamental electron cyclotron frequency from 280 to 616 GHz), the often prohibitively expensive and brittle Nb<sub>3</sub>Sn superconducting wire technology is employed. Resistive DC Bitter magnets, consisting of copper “Bitter” plates conceived by Francis Bitter, are currently available up to 33 T, while hybrid magnets, combining Bitter and superconducting technology up to 45 T, though both types are mainly experimental devices. A frequency of 328 GHz was generated by a gyrotron using a 14 T Bitter magnet [101]. Pulsed magnets can generate fields even higher, and up to 30 T have been generated synchronously with pulsed gyrotron operation [29].

Magnet limitations can be lessened by operating the gyrotron at a harmonic of electron cyclotron resonance, for which the  $n^{\text{th}}$  harmonic will deliver  $n$  times the fundamental frequency for a given magnetic field. While the harmonic interaction is nearly as efficient as the fundamental interaction in theory, less power is extracted from the cavity due to elevated ohmic losses, which increase with the frequency. Harmonic operation also suffers from the additional complication of mode competition and requires much higher beam currents in order to initiate oscillation. In our case, the magnet limitation has been alleviated by operating the gyrotron at a harmonic of electron cyclotron resonance; with an operating field of less than 9 T, the magnet coil can be wound from NbTi wire, which will reduce the cost.

Figure 4-14 is a schematic of the superconducting magnet, designed by Cryomagnetics, Inc. [9], which was used in the 460 GHz gyrotron experiment. The room-temperature bore of the magnet is vertical, and has a diameter of 7.62 cm. In addition, there is a horizontal cross-bore with a diameter of 6.35 cm through which the RF power is extracted from the gyrotron. This horizontal cross-bore is less than 99 cm above the floor. The magnet has a maximum magnetic field of 9.2 T for 4.2 K (liquid helium) operation, with a sufficient margin for 8.4 T design operation, and can be charged to full field in either direction. The homogeneity of the axial field at the center of the magnet coil, for a cylindrical volume with a length of 2.0 cm and a diameter of 1.0 cm, is between 0.3–0.6 %. A field in excess of the design homogeneity is not desirable because it can lead to spurious RF oscillations in the gyrotron which can disrupt operation.

The dependence of the axial magnetic field on axial distance between the cavity and the cathode is of critical importance for the design of gyrotrons. Figure 4-13 is a comparison of the measured axial field profile ( $\times$ 's) to Cryomagnetics (solid line)

Table 4.3: Specifications of the gyrotron magnet

Maximum magnetic field	9.2 T
Operating magnetic field	8.4 T
Warm bore diameter	7.62 cm
Cross bore diameter	6.35 cm
Homogeneity in center on axis	< 0.6 % over 2 cm
Field at gun (z=34 cm)	0.34 T
Maximum field decay	1 ppm/hr
Bore axis tilt wrt. magnetic axis	< 0.3°
Bore axis offset wrt. magnetic axis	< 0.1 cm
Minimum helium refill	28 days
Minimum nitrogen refill	7 days

magnetic field profile. They overlap identically. The cathode is located at the position where the magnetic field has been reduced by a factor of 28 from the peak magnetic field. This occurs at an axial distance of approximately 35 cm below the center of the coil.

The compact dewar has sufficient capacity to allow an interval between liquid helium refills of four weeks and nitrogen refill interval of one week. Liquid nitrogen is used to cool the outer jacket and shields. The liquid helium loss rate in persistence mode is less than 0.03 L/hour, corresponding to a four week refill interval.

The gyrotron is typically operated in persistence mode operation, with the leads removed. The gyrotron magnet remains in persistence mode even when not in operation due to its proximity to several high homogeneity NMR magnets, whose fields are weakly coupled, and a change in field will adversely affect the NMR spectrometer. The magnet decay rate in persistence mode was specified to the vendor (Cryomagnetics, Inc.) to be less than 1 ppm/hr. Due to the narrow width of the second harmonic design mode, a drift of 0.02 T by the superconducting magnet will remove the gyrotron from excitation range. At the specified drift rate, this will occur in three months.

The superconducting magnet system includes several auxiliary components: removable power leads, a persistence switch, a vacuum-jacketed helium transfer line, a removable liquid nitrogen level sensor, and several sensors internal to the magnet: two helium level sensors and three cryothermometers: one each on the inner and outer cryo-shields, and on the magnet itself. Electronic displays of the level (Cryomagnetics, Inc., Model No. LM-500) and temperature (Cryomagnetics, Inc., Model No. TM-600) readings from these sensors are located in the instrument control rack. The power

supply (Cryomagnetics, Inc., Model No. CS-4-100), temperature and level monitors are capable of computer control by National Instruments LabVIEW software.

### Gun coil

A room-temperature auxiliary coil (the “gun coil”) is mounted on the lower side of the dewar, concentric with the magnetic axis of the solenoid. The gun coil is centered on the electron gun cathode and is capable of producing a field of  $8.5 \times 10^{-2}$  T in either an aiding or opposing direction to the main magnetic field direction.

The dewar wall of the superconducting magnet and tapped holes must be mechanically strong enough to withstand the maximum forces between the 9.2 T superconducting coil and the gun coil. The force between the magnets can be calculated by approximating the superconducting coil as a dipole. The maximum magnetic field in the center of the superconducting magnet (at  $z = 0$ ) is 9.2 T. The magnetic field at the center of the gun coil (or the cathode) ( $z = 34.94$  cm) is approximately

$$B_{z=34.94\text{cm}} = \left(\frac{a}{z}\right)^3 B_0 = 0.23 \text{ T} \quad (4.6)$$

where  $a$  ( $= 10.3$  cm) is the effective radius of the dipole approximated by the superconducting coils. The gradient is given by

$$\frac{\partial B}{\partial z} = -\frac{3a^3}{z^4} B_0 = -2.02 \frac{\text{T}}{\text{m}}. \quad (4.7)$$

The force per unit volume on the gun coil is [102]

$$F = m \frac{\partial B}{\partial z} = 136,634 \frac{\text{N}}{\text{m}^3} \quad (4.8)$$

where the magnetic dipole moment  $m$  is

$$m = \frac{\text{maximum gun coil field}}{\mu_0} = \frac{0.085 \text{ T}}{4\pi \times 10^{-7} \text{ H/m}}. \quad (4.9)$$

The gun coil volume is approximately  $2.75 \times 10^{-3}$  m<sup>3</sup>, yielding a total force of 375 N or 84 lb.

### NMR magnet

A 16.4 T, high-resolution, Magnex Scientific superconducting magnet is the key component of a 700 MHz NMR spectrometer. The fringe field of the NMR magnet can adversely affect the sensitive magnetic field at the gyrotron gun in the case of ex-

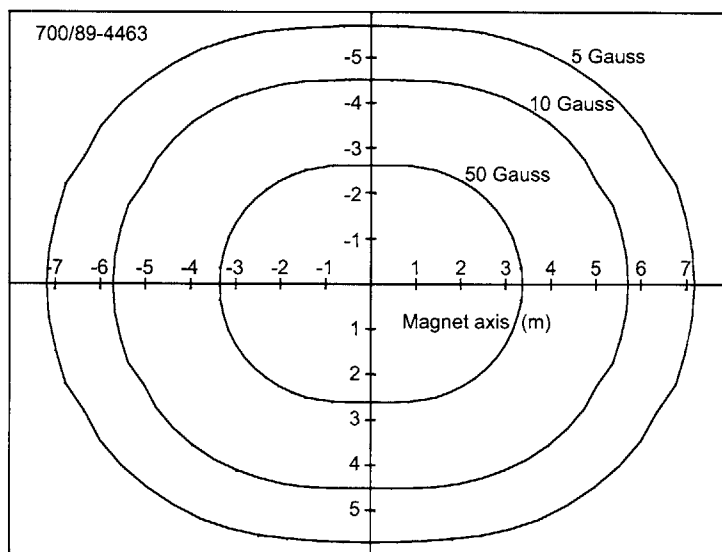


Figure 4-15: Fringe-field plot for the 700 MHz/89 mm superconducting NMR magnet system (Magnex Scientific, Model No. 700/89-4463) [10].

cessive proximity of the gyrotron and NMR magnets, as has been observed with the 250 GHz gyrotron and 380 MHz NMR spectrometer. A simple solution for the 460 GHz gyrotron system is to situate the gyrotron magnet sufficiently far from the NMR magnet. From the fringe-field plot for the 700 MHz superconducting NMR magnet with 89 mm bore in Fig. 4-15, this distance is greater than 6 meters laterally. This will necessitate a lengthened transmission line, however no additional losses should be incurred with an extra length of corrugated waveguide.

### 4.3.3 Interaction Structure

The resonant gyrotron interaction structure is a tapered cavity that was optimized for the  $TE_{0,6,1}$  second harmonic eigenmode at 460 GHz using a cold cavity (electron beam absent) simulation code described in Chapter 2. Figure 4-16(a) is a cross-sectional schematic of the tapered cavity, consisting of a straight section of length 20.5 mm and circular cross-section of radius 2.03 mm joined to a linearly uptapered section at three discrete slopes at the exit ( $0.25^\circ$ ,  $0.56^\circ$ , and  $1.3^\circ$ ) and a linearly downtapered section at the entrance of  $4.7^\circ$ , showing the axial profile of the design mode. A long cavity design was utilized in order to lower the starting current below 100 mA. Shallow output tapers were utilized in order to lower the diffractive  $Q$ . Mode conversion in the input taper was not detected by simulation. The gyrotron cavity was electroformed from oxygen-free (OFC) copper using an aluminum mandrel precision machined to a  $5 \mu\text{m}$  tolerance and  $0.2 \mu\text{m}$  finish. The cavity, uptapers, and connecting waveguide

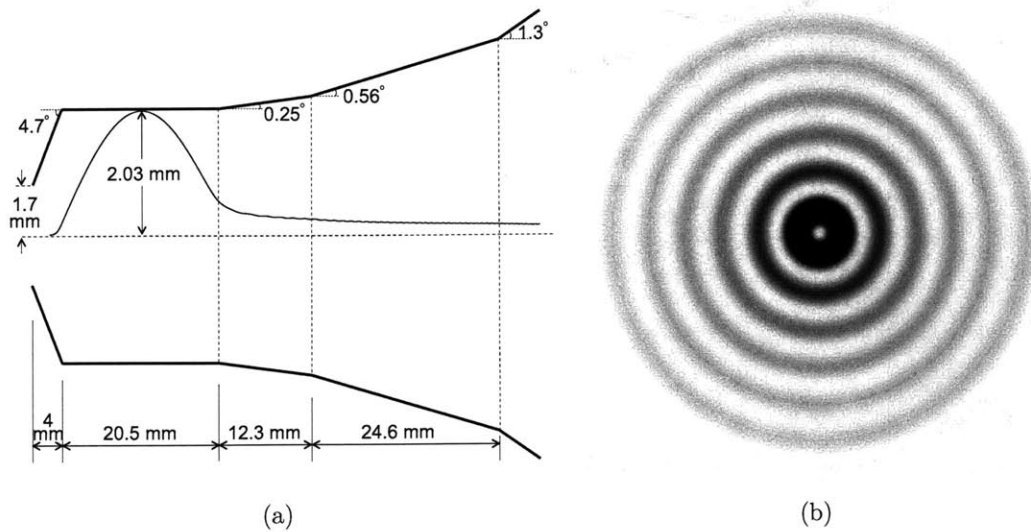


Figure 4-16: (a) Cross-sectional schematic of the cylindrical 460 GHz gyrotron cavity with the axial radiation field profile for the second harmonic  $TE_{0,6,1}$  resonator mode. (b) Intensity pattern of the  $TE_{0,6}$  design mode.

Table 4.4: Cavity design and fabrication dimensions

	Cavity radius
Design	2.035 mm
Fabricated	2.045 mm
Measured	2.041 mm

can be seen in Fig. 4-17. The length of the constant radius section of the cavity is approximately 2 cm.

From the results of the short pulse experiments, we are able to calculate a cavity radius of 2.041 mm to obtain the best fit to the data. This value is 0.3% larger than the design value of 2.035 mm and the difference is within the manufacturing accuracy of the cavity. The cavity design and fabrication dimensions are listed in Table 4.4.

#### 4.3.4 Quasi-Optical Mode Converter

The first element in the quasi-optical transmission line is a quasi-optical antenna. Located internal to the gyrotron and colinear to the cross-bore of the superconducting magnet, its function is to efficiently convert the operating  $TE_{0,6}$  mode waveguide radiation into a freespace Gaussian beam which will then be transmitted out of the vacuum tube to the DNP probe through a transmission line, likely a corrugated



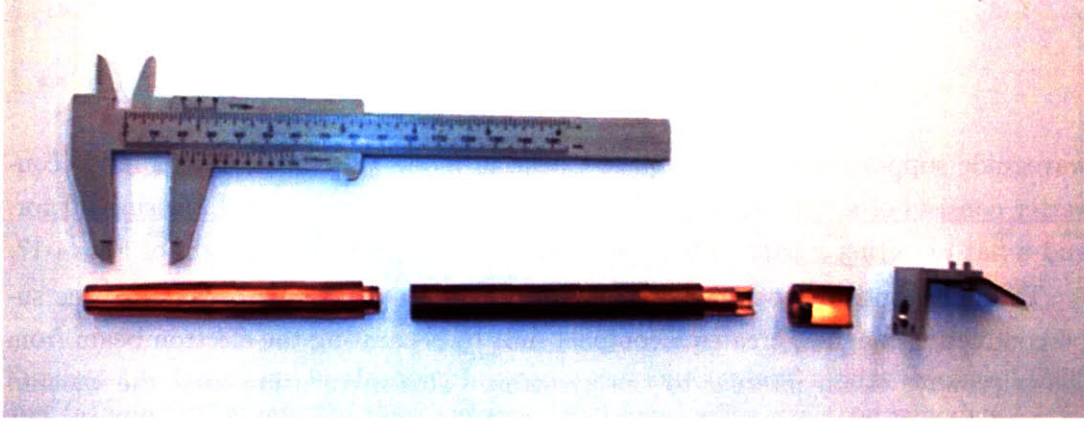


Figure 4-17: Photograph of the cavity, waveguide, and internal quasi-optical mode converter (launcher, focusing mirror, and steering mirror). The ruler is set at 2 cm and its position approximately corresponds to the location of the electroformed interaction cavity.

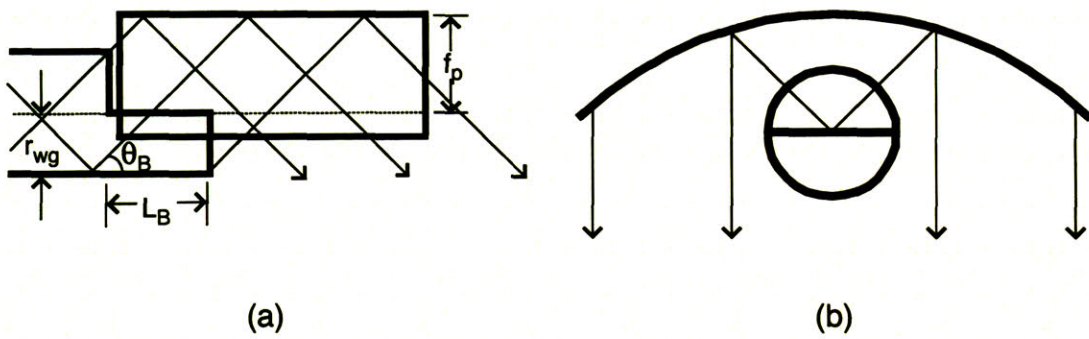


Figure 4-18: Schematic of the quasi-optical internal mode converter showing calculated design parameters (a) side view (b) front view, adapted from [11].

Table 4.5: Quasi-optical mode converter parameters

Brillouin angle $\theta_B$	39.8°
Waveguide radius $r_{wg}$	3.18 mm
Focal length $f_p$	3.87 mm

waveguide supporting the  $HE_{1,1}$  quasi-Gaussian mode. The quasi-optical mode converter consists of a circular waveguide with a step-cut, a cylindrical focusing mirror, and a flat reflecting mirror. These components can be seen in the right of Fig. 4-17.

The quasi-optical mode converter, in conjunction with the cross-bore of the superconducting magnet, creates a compact unit by separating the electron beam from the microwave beam internal to the gyrotron. This in turn increases the vacuum pumping conductance and reduces the ohmic losses in the output waveguide.

The principles of operation are depicted in Fig. 4-18. The waveguide launcher [103] converts the gyrotron output into a linearly polarized beam. Using geometrical optics, the Brillouin angle  $\theta_B$  is determined by

$$\sin \theta_B = \frac{k_{\perp}}{k} = \frac{\nu_{mp}}{kr_{wg}} \quad (4.10)$$

where  $r_{wg}$  is the waveguide radius,  $\nu_{mp}$  ( $= \nu_{0,\delta}$ ) is the mode index, and  $k_{\perp}$  ( $= \nu_{mp}/r_{wg}$ ) is the transverse propagation constant of the  $TE_{m,p,q}$  wave.  $L_B$  ( $= 2a \cot \theta_B$ ) is the length of the step cut. The parabolic reflector molds the beam into a Gaussian shape, and the steering mirror directs the beam through the gyrotron output window out the center of the cross bore of the superconducting magnet. The mode converter was optimized for efficiency and space, such that it fits inside the bore of the magnet and is outside the electron beam radius. Table 4.5 details several key parameters of the quasi-optical mode converter. The mode converter is approximately 80% efficient.

### 4.3.5 Vacuum System

In order to improve the operating reliability of the gyrotron, the gyrotron vacuum tube was designed in a demountable configuration; that is, the tube can be assembled external to the superconducting magnet and inserted or removed from the magnet bore. This feature, made possible by the low voltage electron gun, allows us to process the tube outside of the magnet at much higher temperatures using a bakeout furnace. This method, used by vacuum tube manufacturers for their high-average power tubes, will result in a much lower base pressure and better operation. Another key feature

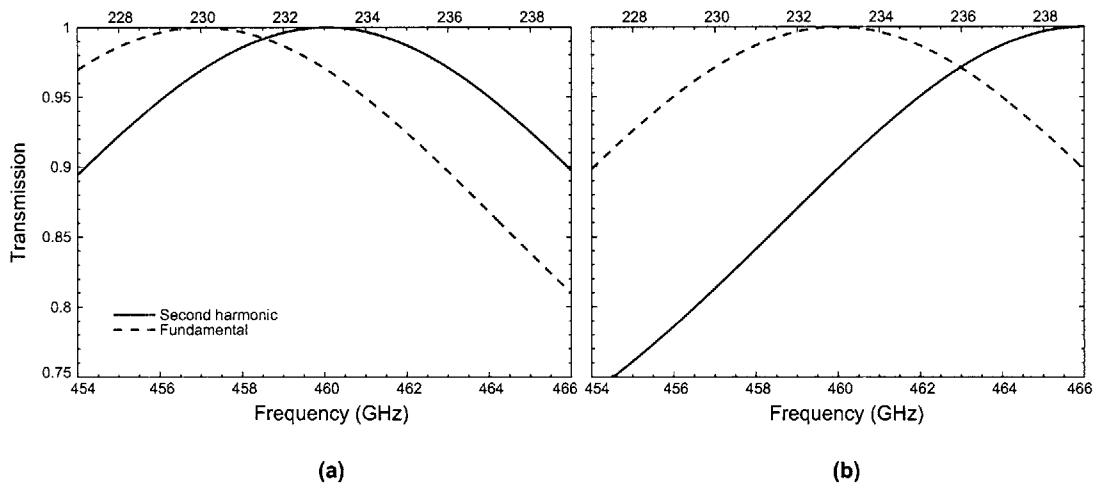


Figure 4-19: Transmission of second harmonic and fundamental modes through 1.9990 mm (a) and 1.9736 mm (b) thick Corning 7980 fused silica gyrotron windows.

of the vacuum system is the separation of the electron beam from the rf beam by the internal mode converter. Due to the separation of beams, a pipe of larger cross-section can be used to connect the vacuum pumps to the tube (in place of a narrow waveguide), thereby increasing the vacuum conductance.

### 4.3.6 Vacuum Output Window

Corning 7980 Fused Silica was chosen as the material for the gyrotron output window due to its wide bandwidth, at a refractive index of approximately 1.956, at the frequencies of interest [104]. Two sets of windows were designed for the gyrotron based upon the premise that partial reflection of the second harmonic mode and total transmission of the fundamental mode may be desirable, in addition to complete transmission of the harmonic mode. In the case of partial reflection of the second harmonic mode, the window reflectivity would cause the  $Q$  of the resonator to increase thereby decreasing its start oscillation current. Similarly, if the competing fundamental mode were to have zero reflection, its  $Q$  would be unaffected. Thus, the first set of windows is matched to the second harmonic mode at 460 GHz and the second set of windows is matched to transmit the competing fundamental mode near 233 GHz ( $TE_{2,3}$ ), as shown in Fig. 4-19. The thicknesses were chosen by modeling the windows as Fabry-Perot interferometers, with frequency-dependent power transmission, given by [105]

$$T = \left[ 1 + \frac{4R}{(1-R)^2} \sin^2 \left( \frac{2\pi d}{\lambda} \right) \right]^{-1}, \quad (4.11)$$

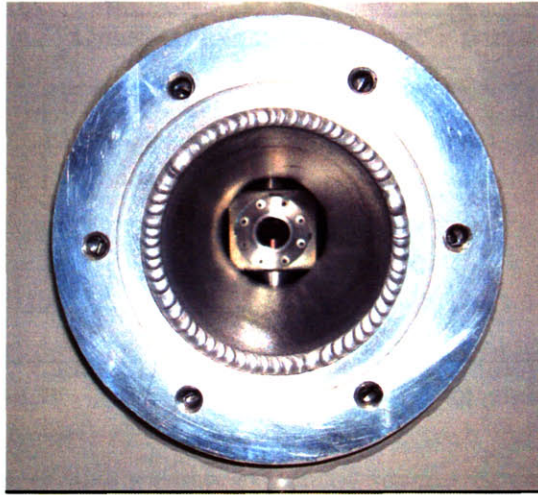


Figure 4-20: Photograph of the window through the cross-bore of the superconducting magnet. The mode converter is visible.

where  $R (= (n - 1)^2 / (n + 1)^2)$  is the reflection coefficient,  $n$  is the index of refraction,  $d$  is the thickness of the window, and  $\lambda (= c / nf)$  is the wavelength in the window medium.

The gyrotron windows were manufactured by Computer Optics, Inc. with specifications of  $3.175 \pm 0.0127$  cm in diameter, thickness of 1.9990 and  $1.9736 \pm 0.0127$  mm, 1 mrad parallelism, and  $5 \lambda$  flatness at 633 nm. The window of thickness 1.9990 mm was installed on the gyrotron for the present experiments, allowing nearly complete transmission of the second harmonic design mode, shown in Fig. 4-19(a). A photograph of the window is visible through the cross-bore of the superconducting magnet in Fig. 4-20.

### 4.3.7 Collector

Under the assumption that in certain situations no RF power will be generated in the cavity, the collector was designed to withstand several kilowatts of the full CW beam power. A schematic of the collector and the cooling circuit is located in Fig. 4-21. For heat removal by flowing water, the fundamental equation relating  $P$ , the power removed in Watts (W), to the volume flow rate  $Q$  in gallons per minute (gpm), and the temperature rise in the water  $\Delta T$  in Kelvin (K) is

$$\Delta T = \frac{0.0038P}{Q}. \quad (4.12)$$

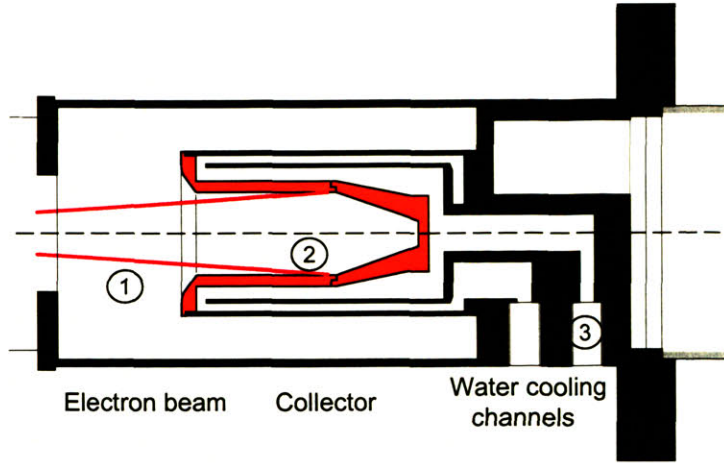


Figure 4-21: Schematic of the collector including the electron beam and water cooling circuit.

For the power removal  $P$  of 1 kW and volume flow rate  $Q$  of 2 gpm, the temperature rise  $\Delta T$  is 1.9 K. This treatment assumes that the entire beam energy is converted into thermal energy which is an upper bound since the beam energy should only become heat as the resistance of the copper of the collector.

Heat transfers across the boundaries of a system when there is a temperature difference between the system and surroundings. In this case, the copper in the collector adjacent to the cooling water is held at the temperature of the water, while the copper being heated by the electron beam is at a different temperature. The temperature differential over the collector wall can be calculated using Fourier's Law,

$$q = \frac{k\Delta T}{L}, \quad (4.13)$$

where  $L$  is the thickness of the collector wall,  $k$  is the thermal conductivity of copper, and  $q$  is the power density. Solving for the temperature differential  $\Delta T$ , we find

$$\Delta T = \frac{qL}{k} \quad (4.14)$$

$$= 47.04 \frac{\text{W}}{\text{cm}^2} \times 0.2794 \text{ cm} \times \left(4 \frac{\text{W}}{\text{cm K}}\right)^{-1} \quad (4.15)$$

$$= 3.28 \text{ K}, \quad (4.16)$$

where the  $L$  ( $= 0.2794 \text{ cm}$ ) is the thickness of collector wall,  $k$  ( $= 4 \text{ W}/(\text{cm K})$ ) is the thermal conductivity of copper, and  $q$  ( $= 47.04 \text{ W}/\text{cm}^2$ ) is the power density. The area over which the 1 kW incident electron beam impacts the collector is calculated

by propagating the beam thickness of the cathode adiabatically to the collector. The area of interception at the collector is calculated as  $21.26 \text{ cm}^2$ .

## 4.4 Control System

A control system has been implemented on the 460 GHz gyrotron [106], modeled after the 250 GHz gyrotron control system [92], using the LabVIEW software package combined with hardware interlocks. Software controls are a necessity in the long-term operation of a gyrotron without continuous user intervention. The 250 GHz gyrotron has operated under complete computer control for over 10 days [92]. The control system described in this section is for the 460 GHz gyrotron.

### 4.4.1 Software

LabVIEW is a graphical programming language that relies upon a graphical user interface environment to program via icons instead of text-based code in order to develop hardware oriented applications. A LabVIEW program is called a “virtual instrument” (or VI) and consists of a front panel and block diagram. The front panel is the graphical user interface with which the user interacts. The block diagram is the code assembled using graphical representations of functions and is invisible to the user while the program is executing much in the same way that a text-based code is also invisible during execution.

The 460 GHz gyrotron control code contains two main virtual instruments which are accessible to the user and several sub-VI's which are accessible only by the main VI's. The first main VI uses event-driven programming to control the parameters of the experiment. An event is an asynchronous notification of an occurrence. In contrast to a procedural program which executes in a sequential predetermined order, the order in which an event-driven program executes depends upon which events occur and the order in which they occur. Using events can significantly reduce the CPU requirements of the program. The second main VI is a procedural program which monitors the acquired signals while also providing an option to control the microwave output via a PID controller.

The front panel of the gyrotron controls is shown in Fig. 4-22. The event driven control VI in Fig. 4-22(a) consists of six events. The six events allow the user to set the high voltage, filament current, and gun coil current within prescribed limits. In addition, they provide software limits on the pressure, high voltage, beam current, collector current, body current, and gun coil. The current and pressure limits can be

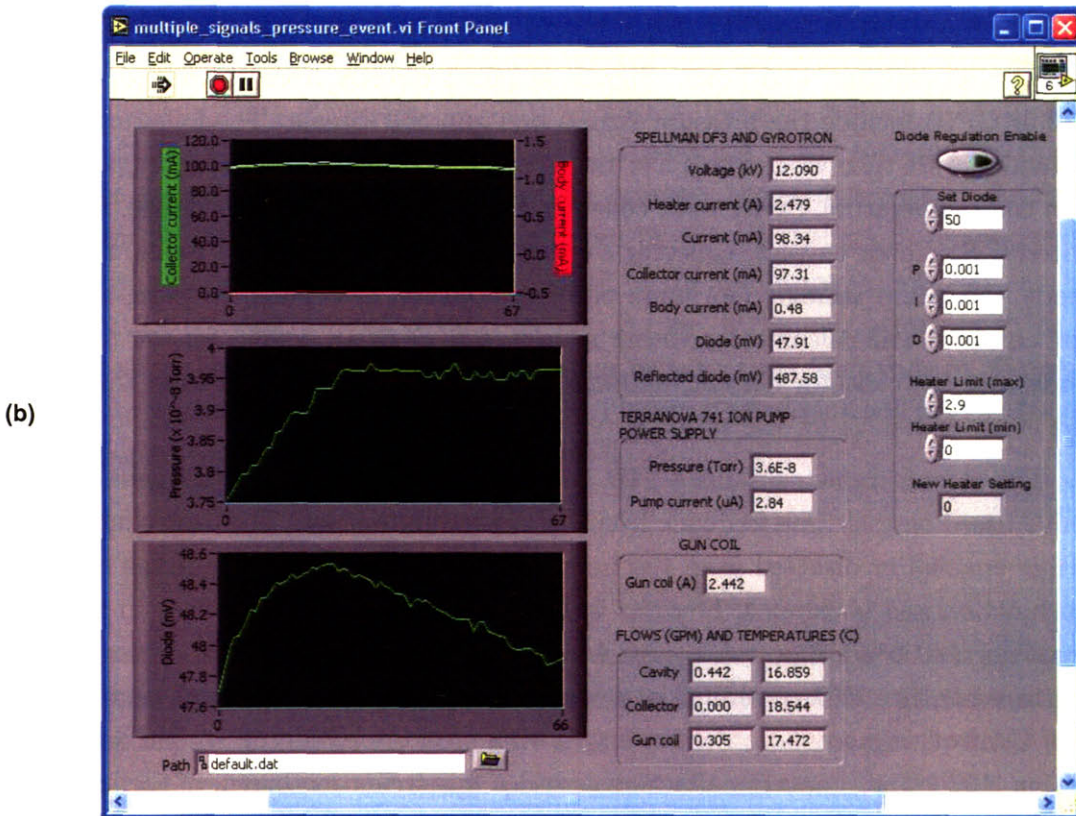
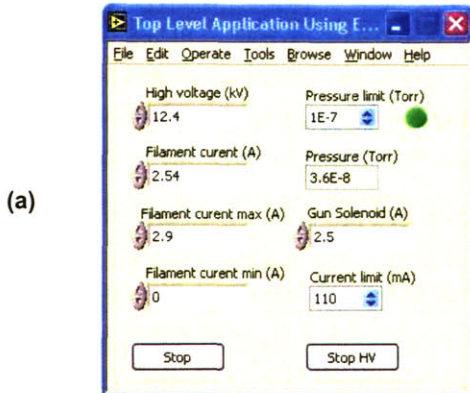


Figure 4-22: Front panel of the LabVIEW control system. (a) Event driven control (b) Signal monitoring and PID feedback control.

set on the front panel while the high voltage and gun coil limits are soft-wired in the block diagram. Event 0 stops the execution of the gyrotron controls when the “Stop” button is depressed. Event 1 allows the user to set the high voltage. Event 2 sets the high voltage to zero when the “Zero HV” button is pushed. Event 3 stops the high voltage if the pressure, body current, collector current, or Spellman current exceed the indicated limits. Event 4 allows the user to set the filament current value. Event 5 allows the user to set the gun coil current value.

The interface for the monitoring/PID VI is shown in Fig. 4-22(b). In this VI, three frames are executed sequentially. The first frame is responsible for gathering all of the analog signals from the DAQ or directly from each device and to plot them on the front panel as either a graph or digital indicator. The signals acquired from the DAQ are sent through a low-pass sixth order Butterworth filter with an infinite impulse response (IIR) and cutoff at 50 Hz. These signals include the high voltage, heater current, Spellman current, collector current, body current, forward diode, reflected diode, temperatures, and flows. Signals acquired directly from the device via RS-232 or GPIB include the pressure signals and gun coil signals. The following signal parameters are then written to a file: time, cavity temperature, collector temperature, gun coil temperature, cavity flow, collector flow, gun coil flow, high voltage, filament current, Spellman current, collector current, body current, forward diode, reflected diode, ion pump voltage, ion pump current, pressure, calculated pressure, and gun coil current. The calculated pressure is derived from (3.4). Values for the pressure, body current, collector current, and supply current are also passed from this VI to the event-driven VI for use as software limits.

The second frame contains a PID controller which controls the filament current value based on real-time feedback from the microwave output. The controller can be either enabled or disabled from the front panel. While disabled, the frame provides no function and is skipped, however when enabled it can make changes to the filament current in addition to changes which can be made in the event driven virtual instrument. The PID controller, also known as “Proportional, Integral, and Derivative Control” is a second order controller with proportional, integral, and derivative action [107]. The proportional action provides a contribution based on the instantaneous value of the control error, the integral action provides a contribution that is proportional to the accumulated error, and the derivative action provides a contribution based on the rate of change of the control error. Using this controller, the microwave output has been held stable to 0.4% over a period of an hour (*c.f.* Sec. 5.2.9).

The third frame provides a 100 ms delay whose purpose is so that the hardware



does not overtax itself by trying to be accessed too frequently or concurrently.

#### 4.4.2 Interlocks

The hardware components for the control system are discussed elsewhere in this document. In addition to the software component there is an interlock system to ensure that the system is not operated in an uncontrolled manner to prevent damage to both the user and the equipment. Hardware interlocks on the high voltage power supply include those from the ion pump power supplies preventing over pressure operation and from the flowmeters preventing operation without cavity, gun coil, or collector water flow. If a trip condition occurs, the high voltage power supply is set in a mode where both the filament and high voltage are set to zero. The power supply must be explicitly reset to continue operation.

In addition to the hardware interlocks there are software interlocks integrated into the control system. These interlocks prevent over setpoint beam current and over setpoint pressure operation. In a trip condition, the high voltage is set to zero and the filament current remains unchanged. The values of the software interlocks should be set such that they will be tripped in advance of the hardware interlocks since the heater is brittle and can be easily damaged by abrupt changes in temperature. There are also out-of-bounds protection on all of the hardware values that can be set using the software control system. In such a case, if the user attempts to set a value greater than the maximum allowed value to any of the high voltage, filament current, or gun coil current, then the maximum or minimum value will instead be set depending on whether it is over or undervalued.

### 4.5 Discussion

The structural basis of the 460 GHz gyrotron design presented is a 250 GHz gyrotron by Kreisler et al. [40]. The important changes lie in the scientific realm, including the operating mode, cavity, mode converter, and a higher axial magnetic field. The main feature/challenge of the design presented is the potential to operate at the second harmonic of the cyclotron frequency. Second harmonic design requires careful analysis in the areas of mode competition, starting current, and ohmic losses.

The choice of operating point was heavily weighted by the experimental requirements of sensitivity-enhanced NMR by dynamic nuclear polarization. The necessary stability has been achieved through design and with a computerized control system.

The important engineering features of the the gyrotron include the cross-bore of

the superconducting magnet, where extraction of the rf power has been separated from the electron beam by an internal quasi-optical mode converter. This feature also allows for increased vacuum pumping conductance. The low voltage electron gun is another important feature which removes the need for oil cooling and enables the tube to be demountable and thus to bake at a higher temperature.

A second harmonic design allowed for the use of a magnet with half the field of a fundamental design. Because of this economic decision, several challenging second harmonic physics issues were considered in the design. The three principal second harmonic challenges overcome in the design were high ohmic losses, high start currents, and mode competition. While the use of a low voltage was an important engineering advantage, it generated physics challenges since the efficiency of the gyrotron is reduced at low beam power and even more severely reduced for the second harmonic.

# Chapter 5

## 460 GHz Second Harmonic Experiments

### 5.1 Short Pulse Experiment [1]

The gyrotron was initially operated with short pulses with duration of 1-3  $\mu\text{s}$  with repetition rate of approximately once per second. In this configuration, we were able to measure the emission characteristics of the gun and to align the electron beam within the tube. The low duty cycle allowed us to study the physics of the microwave generation in the gyrotron while avoiding potential damage due to beam interception or RF heating of internal components. The results of the short pulse experiment have been discussed in [1].

An existing modulator capable of over 100 kV and 1.2 A provided the power to the electron gun in the short pulse tests. Once the electron gun was activated, it produced over 100 mA of current with about 10 watts of input heater power. The optimal electron beam propagation path was determined by translating the position

Table 5.1: Short pulse experimental operating parameters

Experimental parameters	Min.	Max.
Pulse length ( $\mu\text{s}$ )	1	3
Repetition rate (Hz)	1	33
Beam voltage (kV)	0	15
Beam current (mA)	0	160
Main magnetic field	5.6	9.2
$\Delta$ cathode magnetic field (T)	$-8.5 \times 10^{-2}$	$8.5 \times 10^{-2}$

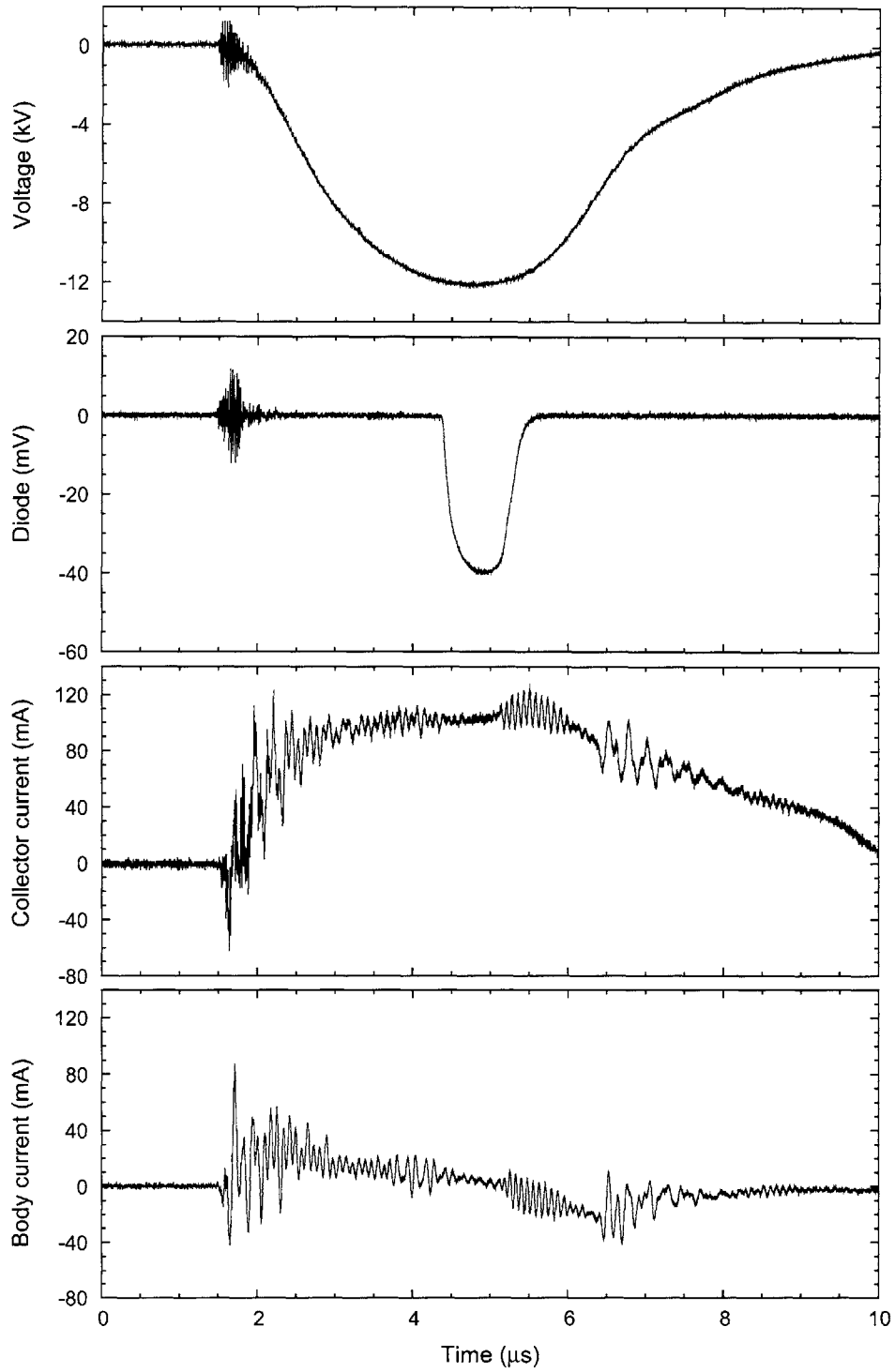


Figure 5-1: Voltage, diode voltage, collector current, and body current traces of the  $\text{TE}_{2,6,1}$  second harmonic mode at 12.5 kV, 100 mA, and 8.34 T.

of the tube in the dimension transverse to the main bore of the magnet. A final position was chosen that maximized the RF power at the second harmonic and also resulted in 100% beam transmission to the collector, that is, zero interception in the body.

A parametric study was conducted to determine the operating parameters of the second harmonic design mode and of the fundamental and second harmonic modes in its vicinity. To this end, operating parameters including the cavity and gun magnetic fields, beam current, and voltage were varied to map out the operating characteristics of the modes. The electron beam voltage and current were varied up to 15 kV and 160 mA while the main magnetic field was varied up to 9.2 T and the gun magnet up to  $\pm 8.5 \times 10^{-2}$  T with respect to the cathode field. The experimental parameters are summarized in Table 5.1. Unless otherwise specified, all measurements were taken at the end of a 2 m long copper waveguide of 2.54 cm inner diameter, which couples directly to the output window.

Figure 5-1 shows an example of typical oscilloscope traces of the electron beam voltage, RF signal, collector current, and body current for the experiment. In this case we show the second harmonic  $TE_{2,6,1}$  mode. The noise and distortions to the pulse shape are due to power supply ripple and the transient response of connecting cables. A small droop in the voltage pulse causes a small corresponding droop in the microwave pulse.

### 5.1.1 Mode Map

A mode map was generated to chart the regions of parameter space in which the modes in the vicinity of the  $TE_{0,6}$  design mode can be excited (*c.f.* Fig. 5-2). Since the design mode is of relatively low order, the modes are spaced apart and there are few possibilities of simultaneously excited modes in the present gyrotron. Most possibilities of excitation of multiple modes at a fixed magnetic field involve changing the beam voltage and compression or during the rising or falling edge of the voltage pulse. In fact, in the region of interest, there are only two possible second harmonic modes, the  $TE_{2,6}$  and  $TE_{0,6}$ , and one competing fundamental mode, the  $TE_{2,3}$ . For the present mode map, we have varied three main parameters, the main magnetic field, the beam voltage, and the cathode magnetic field, to determine the operational limits of each mode. The cavity magnetic field is an obvious parameter choice because the electron cyclotron frequency is directly proportional to it in addition to the proportionality of the detuning parameter. The cathode magnetic field, adjustable through varying the gun coil, affects the magnetic compression which changes the beam radius. Finally, in Fig. 4-9, we see that the electron beam parameters, namely

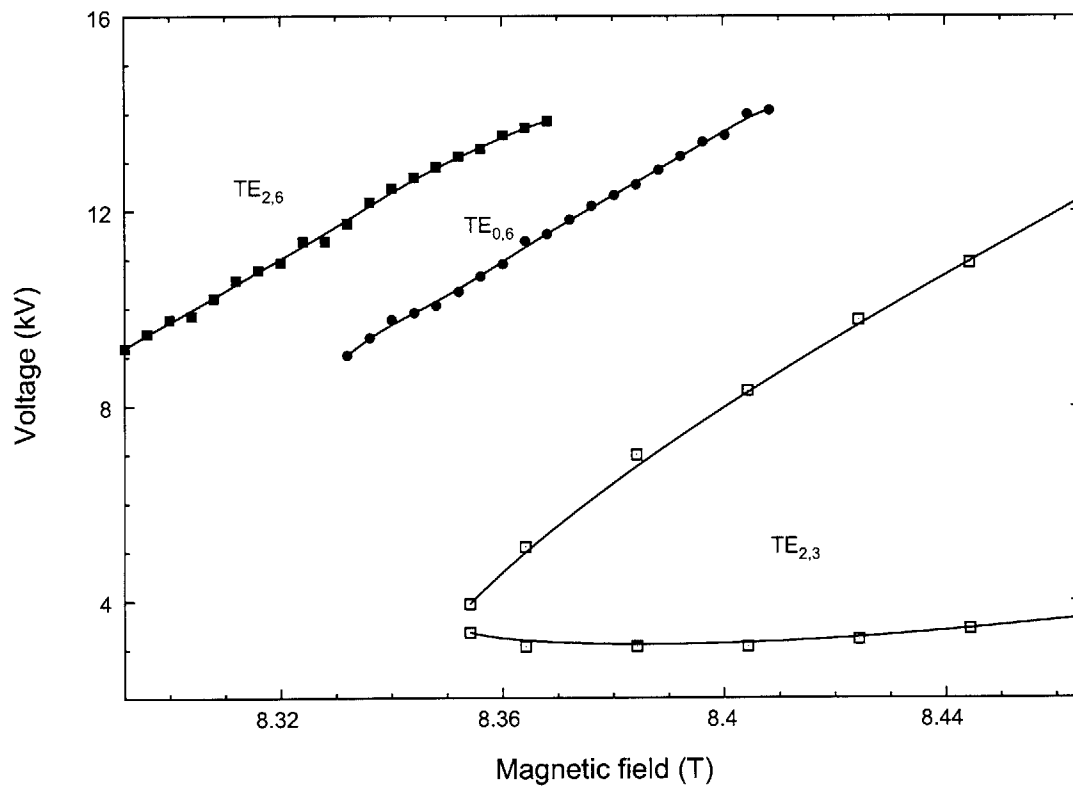


Figure 5-2: Mode map for the design mode and nearby competing fundamental  $TE_{2,3}$  mode for beam voltage and cavity magnetic field at 100 mA. The gun coil has been optimized for each point.

the beam alpha and transverse velocity spread, are extremely sensitive to the beam voltage and cavity and gun magnetic fields.

Figure 5-2 shows the optimum power curves of the  $TE_{2,6}$  and  $TE_{0,6}$  second harmonic modes, which have narrow regions of voltage excitation at a fixed main magnetic field around 1 kV. At the higher magnetic fields for the  $TE_{0,6}$  regime of excitation in short pulse operation, the  $TE_{2,3}$  fundamental mode is excited on the rising and falling edges of the pulse thereby saturating the second harmonic signal. This places an upper limit on the detection of the  $TE_{0,6}$  mode at high magnetic fields. The complete region of excitation of the fundamental  $TE_{2,3}$  mode, over several kilovolts, is shown. For increasing magnetic field, each of the modes presented follows a path of increasing voltage, such that the lowest field point of a mode is also the lowest voltage point. The mode map is similar to the starting current map which determines other facets of the parameter space.

### 5.1.2 Start Oscillation Current

The starting current curves for all modes experimentally observed are shown in Fig. 5-3(a). Five fundamental modes are depicted with open shapes ranging in frequency from 157 to 246 GHz and two second harmonic modes near 460 GHz are shown with filled shapes. Data in each mode were collected at the unique voltage which was optimal for its excitation; these conditions are labeled in Fig. 5-3(a). The theoretical intensity patterns of the fundamental modes observed in the experiment are shown in Fig. 5-4.

We have observed two second harmonic modes in these experiments, the  $TE_{2,6,1}$  and  $TE_{0,6,1}$ , for which theoretically predicted and experimentally measured starting currents show good agreement (Figure 5-5). The starting current curves for the two second harmonic modes experimentally observed, the  $TE_{2,6}$  and  $TE_{0,6}$ , are shown in Fig. 5-5 and are represented by points. The data were collected at 13.1 kV with both a video detector diode and the frequency measurement system described in Sections 3.1.4 and 3.1.1 to ensure the proper mode.

With the linear theory previously described in Chapter 2, we can proceed to analyze the start current data. In all cases, we use the beam parameters that were derived from EGUN simulations. For each mode, we have also calculated the theoretical magnetic field which minimizes the start current and compared it to experiment. In Table 5.2, the experimental start current values of seven observed modes are compared with values calculated from [19] using beam parameters from Fig. 4-9, diffractive  $Q$  from cold cavity theory, and all other values from experiment. The agreement is good, and discrepancies might be explained by the uncertainties in the beam alpha, diffractive

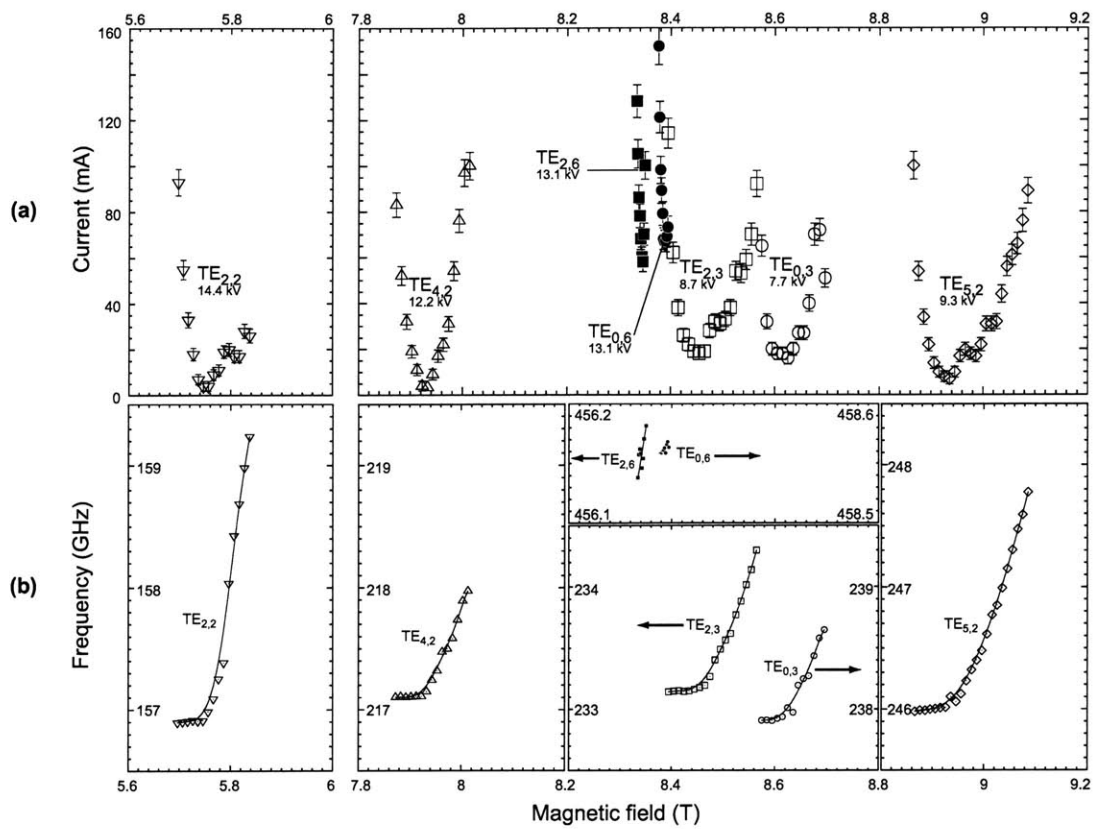


Figure 5-3: (a) Summary of experimental starting current data (b) measured frequency vs. magnetic field recorded for resonant cavity modes from 5.6 to 9.2 T and up to 15 kV and 160 mA. Open symbols denote fundamental modes and filled-in symbols denote second harmonic modes.

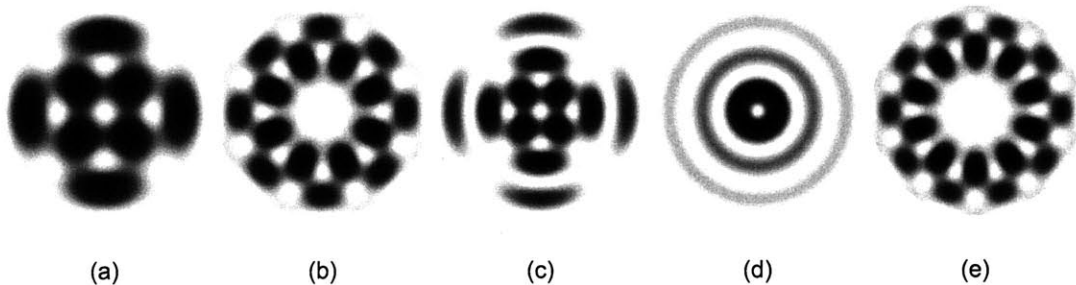


Figure 5-4: Intensity patterns of the (a) TE<sub>2,2</sub>, (b) TE<sub>4,2</sub>, (c) TE<sub>2,3</sub>, (d) TE<sub>0,3</sub>, and (e) TE<sub>5,2</sub> fundamental waveguide modes.



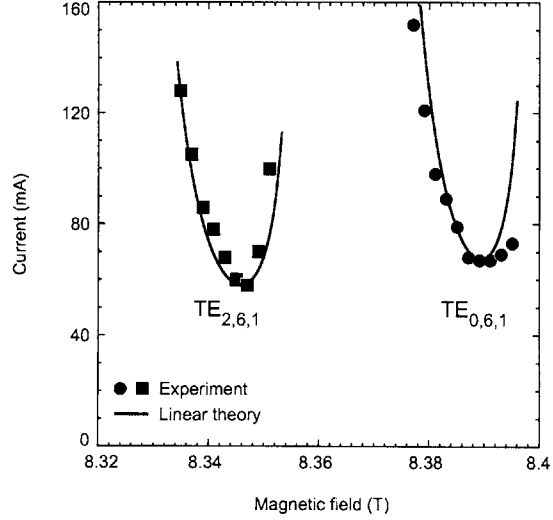


Figure 5-5: Second harmonic  $TE_{2,6,1}$  and  $TE_{0,6,1}$  start oscillation current data (points) compared with linear theory (solid lines) at 13.1 kV.

Table 5.2: Minimum start current, and magnetic field and frequency for minimum starting current of  $q = 1$  modes from linear theory [19] using EGUN calculated parameters of Fig. 4-9(a) and (b) vs. experiment

$TE_{m,p,q}$	Experiment			Theory		
	$B_0$ (T)	$I_{st}$ (mA)	$f$ (GHz)	$B_0$ (T)	$I_{st}$ (mA)	$f$ (GHz)
$TE_{2,2,1}$	5.747	4	156.90	5.746	4	156.89
$TE_{4,2,1}$	7.933	2	217.10	7.926	4	217.09
$TE_{2,6,1}$	8.346	58	456.15	8.345	58	456.15
$TE_{0,6,1}$	8.388	67	458.56	8.390	67	458.56
$TE_{2,3,1}$	8.454	18	233.15	8.433	27	233.15
$TE_{0,3,1}$	8.625	16	237.91	8.605	7	237.92
$TE_{5,2,1}$	8.936	7	246.00	8.915	14	246.01

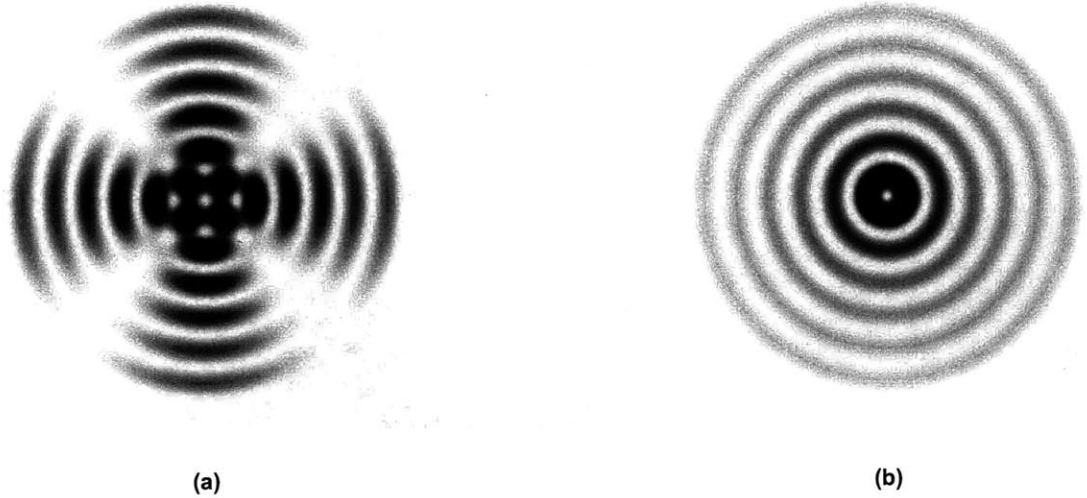


Figure 5-6: Intensity patterns of the (a)  $TE_{2,6}$  and (b)  $TE_{0,6}$  second harmonic waveguide modes.

$Q$ , and experimental conditions such as beam radius and alignment.

We are also able to calculate a cavity radius of 2.041 mm to obtain the best fit to the data. This value is 0.3% larger than the design value of 2.035 mm and the difference is within the manufacturing accuracy of the cavity.

It is clear that the  $TE_{m,p,1}$  modes are excited at the magnetic fields predicted by linear theory [19]. However, the fundamental modes in the experiment have multiple local minima which form a continuous manifold of accessible cavity oscillation states, each one producing monochromatic emission. This phenomenon, which is due to higher order longitudinal states, will be more fully discussed in Section 5.1.5. In short, for fundamental modes, the occurrence of overlapping  $TE_{m,p,q}$  (where  $q$  is larger than one) higher order axial modes broadens the magnetic excitation range. Finally, the very low values of start current observed in the fundamental modes are described by linear theory.

### 5.1.3 Second Harmonic

Initial pulsed power measurements of the  $TE_{2,6,1}$  (456.15 GHz) second harmonic mode indicate signal strengths of several watts with 13 kV and 110 mA. The  $TE_{2,6,1}$  mode was found experimentally to be more isolated from fundamental modes than the  $TE_{0,6,1}$  second harmonic design mode, which was also observed in [108, 109]. Theoretical intensity patterns of the  $TE_{2,6}$  and  $TE_{0,6}$  modes are depicted in Fig. 5-6.

Maps of the efficiency regions of the  $TE_{2,6}$  and  $TE_{0,6}$  second harmonic modes were generated for an array of cathode voltages, cathode magnetic fields, and cavity

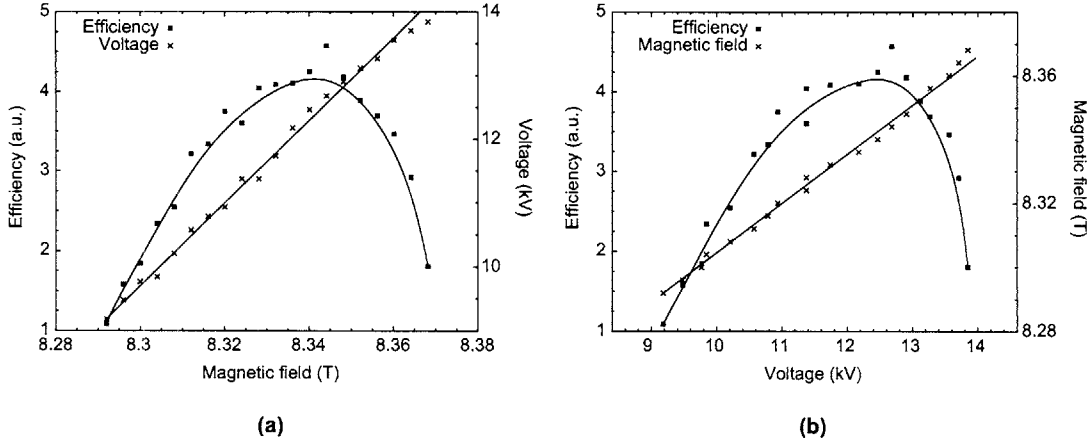


Figure 5-7: Efficiency of the TE<sub>2,6</sub> second harmonic mode at 100 mA (a) as a function of main magnetic field and (b) as a function of voltage.

magnetic fields using the video detector diode described in Sec. 3.1.4. At each magnetic field, the voltage and cathode magnetic field were varied to achieve an optimum diode signal. The results are shown in Figs. 5-7 and 5-8 for the efficiency (in arbitrary units) as a function of cathode voltage, cathode magnetic field, and main magnetic field, where for each main field there is a corresponding optimum voltage. The maximum efficiency point for the TE<sub>2,6</sub> mode occurs near 12.5 kV and 8.34 T and near 12.5 kV and 8.39 T for the TE<sub>0,6</sub> mode. It is apparent that the optimum efficiency curve is linear between voltage and magnetic field. Since the cyclotron frequency is  $\omega_c (= eB/\gamma m_e)$  where  $\gamma (= 1 + V_c/511)$  is the relativistic factor, and the cathode voltage  $V_c$  is in kilovolts, the operating point can be shifted if coordinated changes are implemented in both the main magnetic field  $B$  and the cathode voltage. The TE<sub>0,6</sub> signal was limited at high magnetic fields due to the excitation of the TE<sub>2,3</sub> fundamental mode on the rising and falling edge of the pulse which led to saturation of the detection equipment. The shape of the efficiency curve as a function of voltage or magnetic field is likely due to the idiosyncrasies of the electron gun (*c.f.* Fig. 4-9).

Using the frequency system described in Sec. 3.1.1, several measurements were performed. The frequency pulling of the TE<sub>0,6</sub> and TE<sub>2,6</sub> second harmonic modes with magnetic field are measured in Fig. 5-9. The second harmonic modes do not tune by more than 20-30 MHz, which implies that the long-term frequency will be stable towards drift in the magnetic field. This follows from Fig. 5-5 where we have shown with linear theory that only the first axial variation of the second harmonic modes has been excited in this experiment. This is important in the intended application of this device.

An IF signal of 261 MHz with local oscillator frequency of 25.360 GHz at the

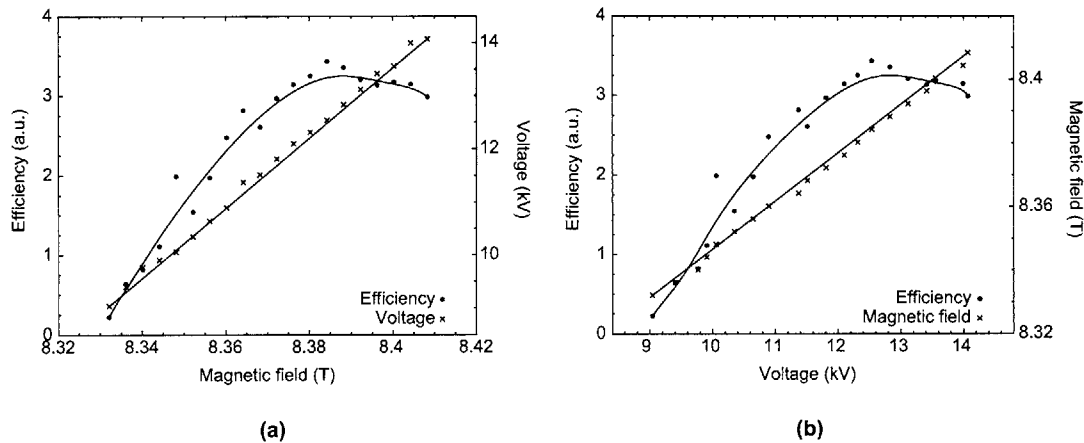


Figure 5-8: Efficiency of the TE<sub>0,6</sub> second harmonic mode at 100 mA (a) as a function of main magnetic field and (b) as a function of voltage.

eighteenth harmonic yields an accurate second harmonic TE<sub>2,6</sub> frequency of 456.219 GHz at 8.34 T, 12.5 kV, and 100 mA, as shown in Fig. 5-10. The second harmonic pulsed linewidth is approximately 3 MHz and is limited by the microsecond length of the rf pulse.

### 5.1.4 Power in Fundamental TE<sub>0,3</sub> Mode

Peak power measurements were made during the microsecond pulsed experiment using both a laser calorimeter and a pyroelectric detector, as described in Section 3.1.2. Figure 5-11(a) depicts measured peak power data of the fundamental TE<sub>0,3,q</sub> modes around 238 GHz as a function of beam current and magnetic field. A pyroelectric detector was used to measure the radiation, and the beam voltage was fixed at 9 kV with microsecond pulse lengths and a repetition rate of approximately 30 Hz. The data were confirmed with calorimetric measurements (*c.f.* Fig. 5-12). Nearly 70 W of peak power were recorded at 237.9 GHz with an efficiency of over 7%.

In principle, the linear theory fails to completely describe the beam-wave dynamics in a real gyrotron due to its assumption of a fixed resonator field structure; in an actual device, the electromagnetic field structure arises due to the interaction of the cavity modes with the moving electromagnetic sources (electrons) and their self-fields. Thus, a complete description necessarily involves the simultaneous self-consistent solution of equations governing the relativistic particle dynamics and the electromagnetic fields. For the simulations presented here, we have used the non-linear, time-dependent simulation code MAGY, developed jointly at the University of Maryland and the Naval Research Laboratory [73]. In MAGY, the resonator transverse fields are expanded

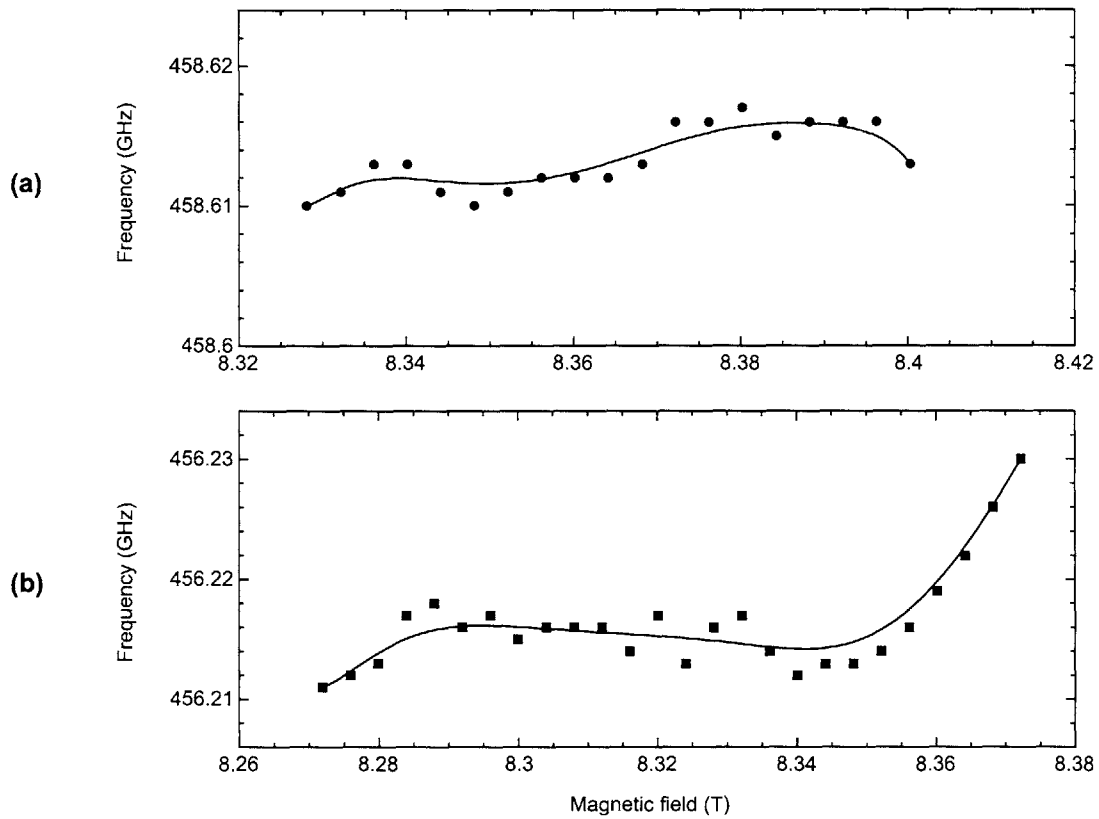


Figure 5-9: Frequency pulling of the (a)  $TE_{0,6}$  and (b)  $TE_{2,6}$  second harmonic modes.

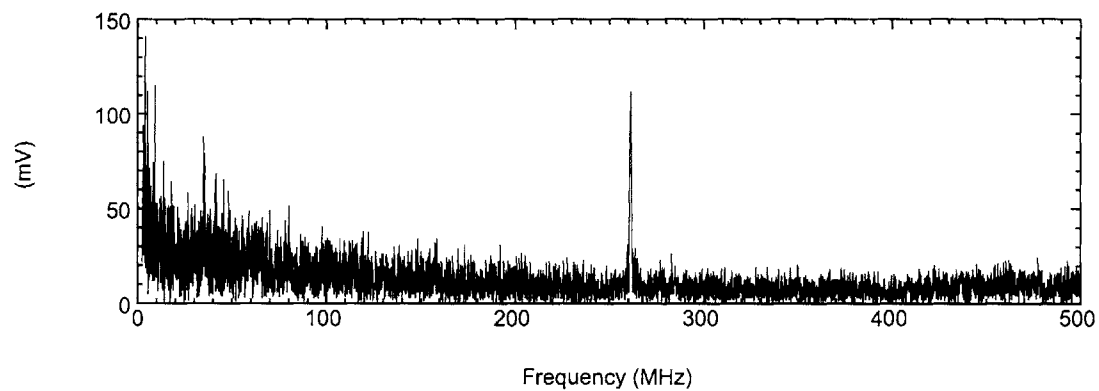


Figure 5-10: IF signal of 261 MHz with LO frequency of 25.360 GHz at the eighteenth harmonic yields a second harmonic  $TE_{2,6}$  frequency of 456.219 GHz at 8.34 T, 12.5 kV, and 100 mA.

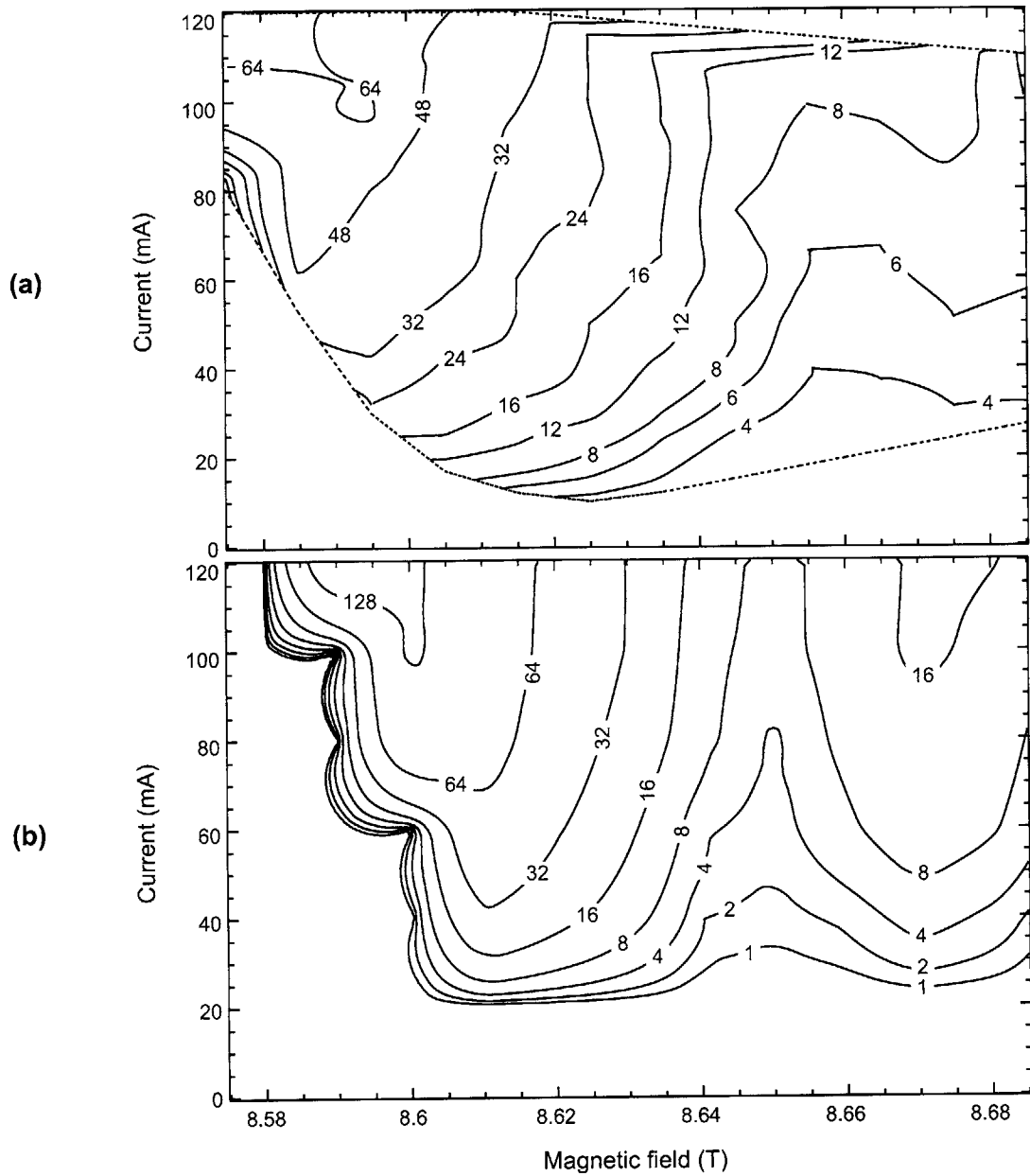


Figure 5-11: Contour plot of (a) measured peak power data of the fundamental  $TE_{0,3,q}$  modes in watts as a function of beam current and magnetic field using a pyroelectric detector. The electron gun was pulsed for several microseconds at a repetition rate of approximately 30 Hz with 9 kV. The power level was calibrated using a calorimeter. (b) MAGY simulated power at experimental conditions.

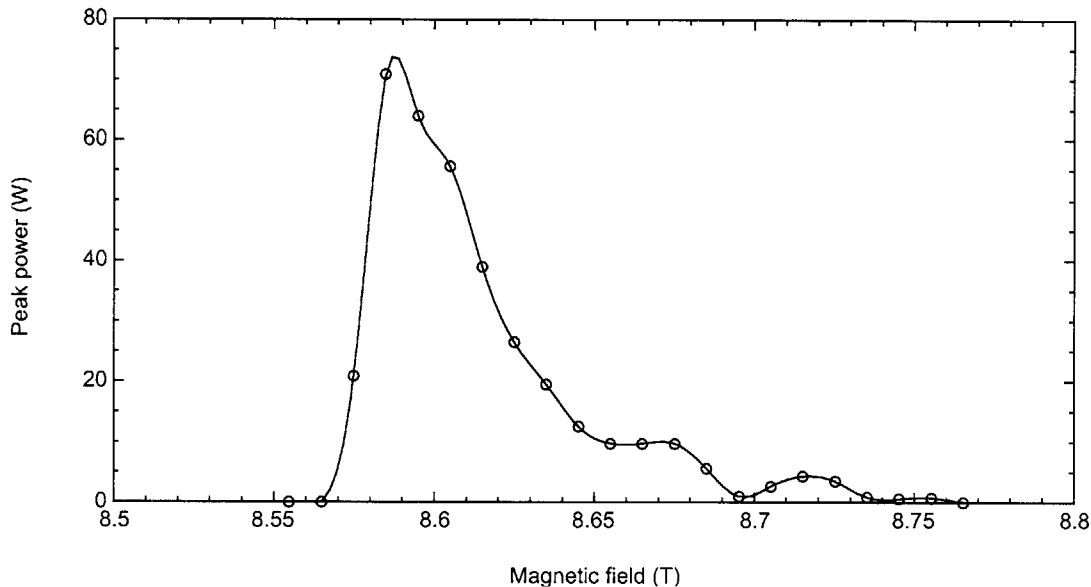


Figure 5-12: Power in the  $TE_{0,3}$  mode detected by a laser calorimeter at 9 kV, 100 mA, repetition rate 30 Hz, and pulse length  $2.8 \mu\text{s}$ . These data were used to calibrate the pyroelectric detector data shown in Fig. 5-11(a).

in a normal mode basis of waveguide modes, and the axial field structure is solved self-consistently in the slowly time-varying approximation. In all the simulations presented here, one or two TE modes were used in the basis. In order to observe steady state dynamics, all modes were forced to oscillate at the frequencies obtained from self-consistent simulations in an iterative adjustment procedure which employs the slope of the field phase evolution as an estimator. The cavity geometry was defined with an axial grid step of of  $9.8 \times 10^{-3}$  cm (1041 points), and with half the conductivity of ideal copper. We have chosen physical parameters to describe the geometry and thermal properties of the beam. This includes, for all simulations, pitch angle, velocity spread, guiding center radius and (where applicable) the spread in guiding center which were obtained from EGUN simulations presented in Figure 4-9(a) and (b). We have systematically increased the EGUN-derived velocity spread according to [110] to account for cathode uniformity, thermal variations, and other effects not explicitly modeled in EGUN. The simulation geometry also involves a slightly tapered magnetic field derived from experimental measurement of the axial field profile. The simulation time step was taken to be 50-150 ps, and we ran the code for 200-2,000 iterations to reach a converged steady state solution.

In simulations of the  $TE_{0,3}$  fundamental mode, MAGY qualitatively reproduces the experimentally observed power distribution (Figure 5-11) but predicts much

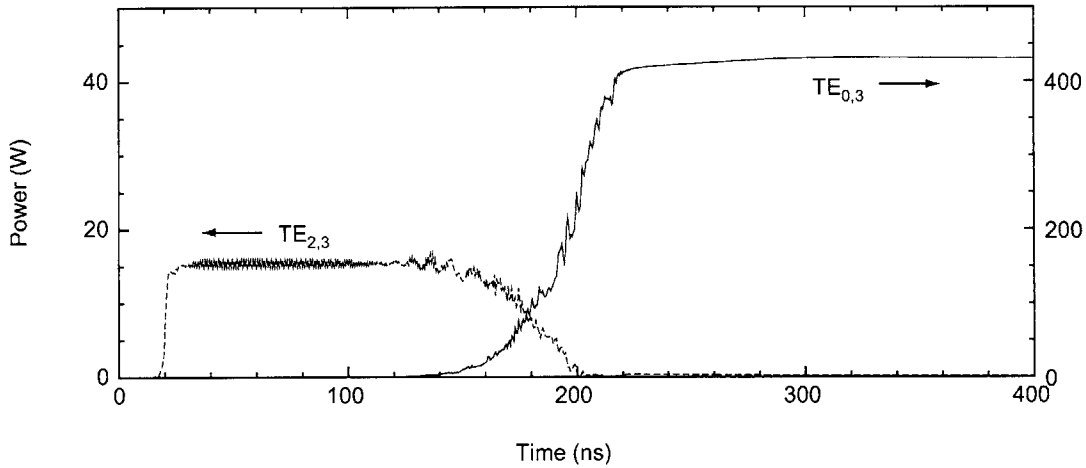


Figure 5-13: Mode competition between the  $TE_{0,3}$  and parasitic  $TE_{2,3}$  fundamental modes.

higher power output than was actually observed. The remaining differences might arise due to higher ohmic losses in the cavity, diffractive and coupling losses in the quasi-optical mode converter, and reduced coupling to the output waveguide, which were not studied in detail in this experiment.

### Mode competition

In the region of magnetic field where the  $TE_{2,3}$  manifold of higher order axial modes co-exists with the  $TE_{0,3,1}$  mode, it is difficult to predict on the basis of linear theory which modes will be excited. MAGY simulations suggest that there is initial mode competition between the  $TE_{2,3,q}$  mode (in the form of a backward-propagating wave oscillation) and the  $TE_{0,3,1}$  mode, but that the  $TE_{0,3,1}$  mode prevails and suppresses the parasitic mode. This is consistent with experimental observation and is shown in Fig. 5-13.

### 5.1.5 Broadband Continuous Frequency Tuning

Broadband continuous frequency tuning was observed as a function of magnetic field for all fundamental modes. A long cavity design was utilized in order to reduce the start current for the second harmonic, in order to meet excitation criteria for a low power gun. In addition to lowering the start current for second harmonic modes, the length of the cavity permits multiple radiation maxima along the axial length of the cylindrical waveguide resonator to be excited. That is, in addition to the  $TE_{m,p,1}$  modes that we expect to excite, there exist a series of  $TE_{m,p,q}$  modes where the  $q$  is



larger than one. These higher order axial modes can be excited at magnetic fields just above those where the  $TE_{m,p,1}$  modes are reached. The practical consequence of this is that continuous frequency tuning on the order of several gigahertz has been observed for each of the fundamental modes excited in this gyrotron. A continuous bandwidth of 410 MHz around 31.8 GHz has been previously observed using higher order axial modes, up to  $q = 5$ , in a two-stage gyrotron amplifier experiment at the University of Maryland [111]. Several experiments in electron paramagnetic resonance (EPR) and dynamic nuclear polarization (DNP) might be dramatically simplified with a tunable oscillator that exploits this property.

The experimental gyrotron frequency corresponding to magnetic field tuning in the range 5.6 – 9.2 T is shown in Figure 5-3(b). The frequency was measured using a heterodyne receiver system described in Sec. 3.1.1. The data were taken concurrently with the data from Fig. 5-3 (a), in which the beam current was set near the threshold of oscillation for each mode. Further, the data in each  $TE_{m,p}$  mode were taken at unique voltages which are labeled on Fig. 5-3 (a). We observe continuous frequency tuning in each fundamental mode across a range of magnetic fields. The frequency tuning bandwidth is relatively large, notably with 1.8 GHz tuning at the 246 GHz  $TE_{5,2,q}$  modes and 2.34 GHz tuning at the 157 GHz  $TE_{2,2,q}$  modes. Further, the data show that a significant amount of power can be maintained across the frequency tuning range of a given mode. This is illustrated for the  $TE_{0,3,q}$  modes in Fig. 5-11(a), where the power measurements are taken as a function of the magnetic field and electron beam current. We can conclude that an average power of at least 5 W can be maintained from 237.9 to 238.6 GHz.

## Analysis

Prior to further analysis, we note that the mechanism of frequency tuning is qualitatively similar for each fundamental mode. Figure 5-14 is a plot of the experimental data from the fundamental modes of Figs. 5-3 (a) and (b), normalized to one magnetic field axis. That is, the data from each  $TE_{m,p,q}$  mode family are normalized to the magnetic field value which yields minimum start current for the mode. The frequency axis in the lower plot is then normalized with respect to the frequency of the first axial mode at that magnetic field. The start currents and normalized frequency tuning with respect to magnetic field resemble each other in functional form. For instance, in the upper plot, the local minima of the start oscillation current curves fall at approximately the same magnetic field values; in the lower plot, the frequency tuning rate,  $df/dB$ , is identical for each family of modes.

For the following discussion, we therefore focus our attention on the  $TE_{5,2}$  mode,

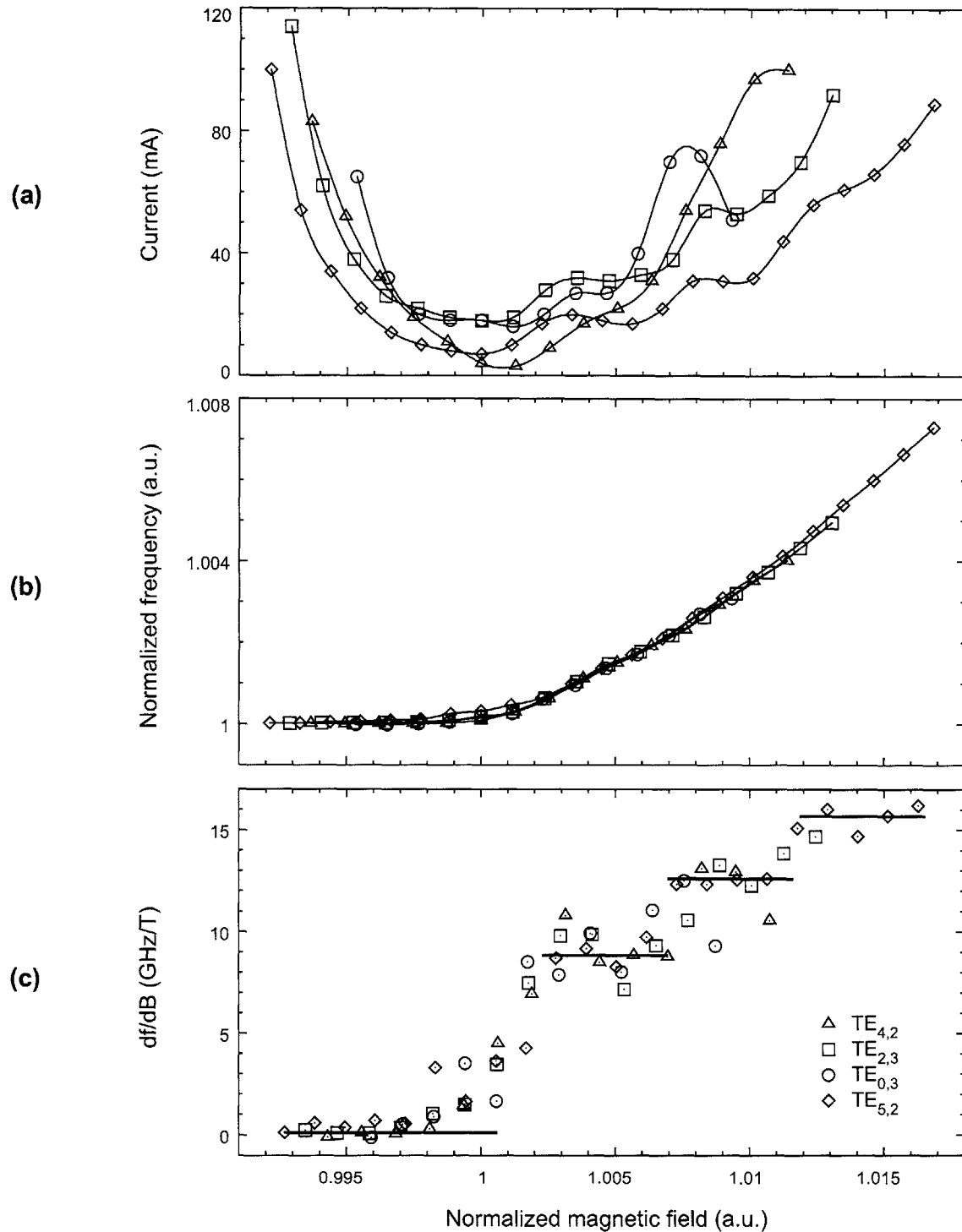


Figure 5-14: (a) Start oscillation currents, (b) frequency tuning, and (c)  $df/dB$  normalized to the frequency at the minimum start current versus magnetic field normalized to the field at the minimum start current of fundamental modes from 7.8 to 9.2 T.

which displays broad frequency tuning in isolation from other fundamental and second harmonic modes. First, using weakly irregular waveguide (so-called “cold cavity”) theory [65], we can calculate the resonator eigenfrequencies,  $Q$  values, and axial field functions of TE modes by solving a one-dimensional wave equation of the form

$$\left[ \frac{d^2}{dz^2} + k_z^2(z) \right] f(z) = 0, \quad (5.1)$$

where  $f$  is the longitudinal profile function and  $z$  is the longitudinal coordinate, with the boundary conditions of a cutoff wave in the input and propagating wave at the output. The analysis relies upon the dimensions of the cavity as well as the indices of the  $\text{TE}_{m,p}$  mode, but neglects coupling to other modes and the perturbing effects of the electron beam. Calculated field profiles lose the distinction between consecutive axial modes, approximating the continuous behavior observed in the experiment.

Second, by inspection of the uncoupled dispersion diagram (Figure 5-15) and the frequency tuning (Figure 5-16), it is clear that, above a threshold which lies approximately between the frequencies of the  $\text{TE}_{5,2,1}$  and  $\text{TE}_{5,2,2}$  cold cavity modes, the beam interacts with a backward propagating wave of the resonator. In this case, the RF frequency lies below the relativistic cyclotron frequency, and the device functions as a reflection-type gyro-BWO instead of a gyromonotron.

Using this information and the cold cavity frequencies and axial field profiles corresponding to the  $\text{TE}_{5,2,1}$ – $\text{TE}_{5,2,5}$  modes, we have applied linear theory to approximately calculate the frequency tuning in the  $\text{TE}_{5,2}$  mode. These five calculated eigenfrequencies are shown in Fig. 5-16 as solid circles, where each eigenfrequency is located at the magnetic field corresponding to the theoretical minimum starting current of that eigenmode. This value of magnetic field is selected because, at the minimum starting current, the effect of dispersion due to the electron beam is negligible and the linear theory should be valid. Since these data are indeed taken near the threshold of the starting current, the agreement between theory and experiment is very good. The starting current data are compared in Fig. 5-17 to theory, and there is a fivefold discrepancy in agreement.

However, the linear theory alone cannot completely describe the dynamics of the beam-wave interaction for reasons that have been previously enumerated. For example, the observation of continuous frequency tuning even between frequencies corresponding to the discrete axial modes of the cold cavity theory cannot be easily explained within the framework of linear theory. We therefore again apply the non-linear, time-dependent theory as implemented in MAGY to model the operating characteristics of this gyrotron. Using the EGUN-derived beam pitch ratio and the

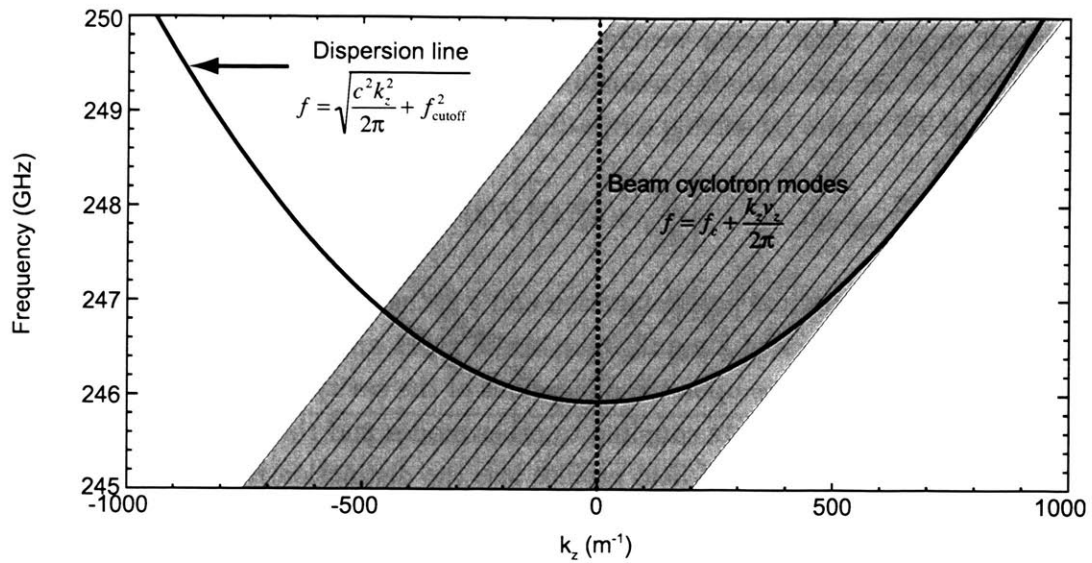


Figure 5-15: Dispersion diagram showing the region of interaction between the unperturbed  $\text{TE}_{5,2}$  waveguide dispersion curve and the experimentally observed Doppler shifted beam cyclotron modes. The intersection of the beam cyclotron modes with the waveguide mode at negative values of  $k_z$  implies interaction of the beam with a backward propagating wave.

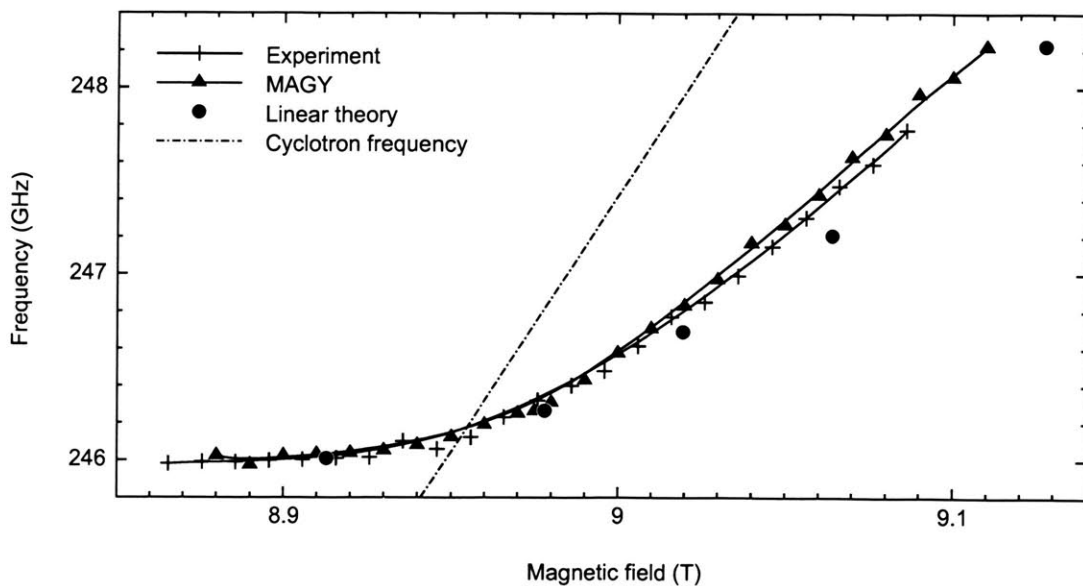


Figure 5-16: Linear theory (solid circles) and MAGY simulation (solid triangles) using EGUN calculated parameters of the frequency tuning of the  $\text{TE}_{5,2,q}$  modes compared to the experiment (+). The dotted line is the relativistic cyclotron frequency.

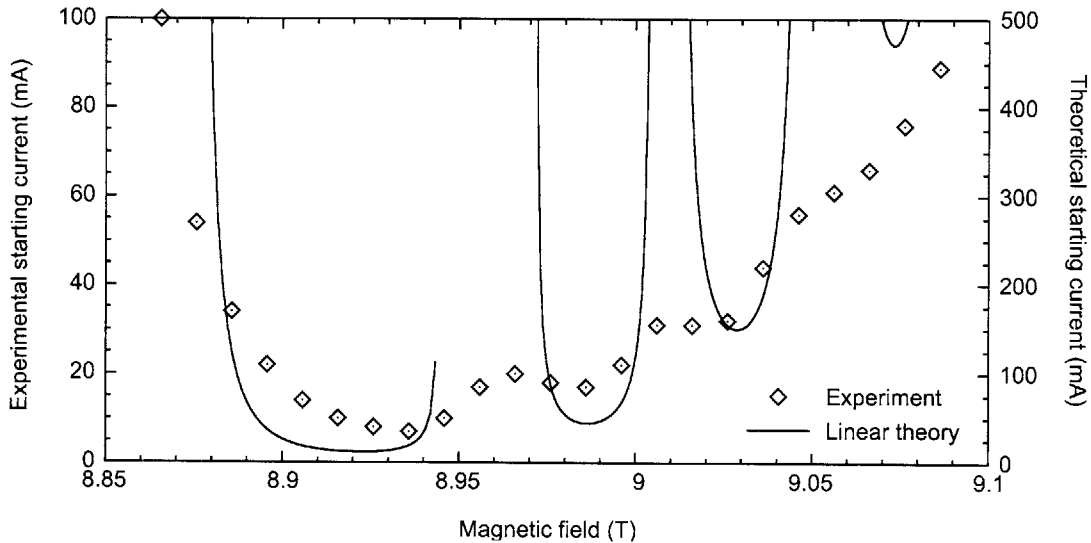


Figure 5-17: Linear theory (lines) using EGUN calculated parameters of the starting currents of the  $TE_{5,2,q}$  modes compared to the experimental data (diamonds).

adjusted perpendicular velocity spread to model thermal properties of the electron beam as previously described, the self-consistent MAGY simulations quantitatively predict continuous frequency tuning and monochromatic emission in the  $TE_{5,2}$  mode. The agreement between experiment and the predictions of MAGY is better than for the linear theory, even though the former depends on fewer adjustable parameters.

Detailed analysis of the axial field structures predicted by MAGY (Figure 5-18) reveal a continuous transition from lower to higher order axial modes, and this is the basis of the observed frequency tuning. The self-consistent axial field structures resemble those obtained from the cold cavity theory, except that, for frequencies greater than that of the  $TE_{5,2,1}$  cold cavity mode, the electric field is growing in the negative direction along the  $z$ -axis (*c.f.* Fig. 5-19). This is consistent with the observation of coupling to the backwards-propagating wave for higher order axial modes [112]. Further, we note that, for frequencies above that of the  $TE_{5,2,1}$  mode, there is a characteristic spatial oscillation of the power in the  $TE_{5,2}$  mode (*c.f.* Fig. 5-20) which results from interference of the backward propagating resonator wave with its non-synchronous reflection from the taper at  $z=0$  [12].

## 5.2 CW Experiment

*The results in this section are adapted from a manuscript: M.K. Hornstein, V.S. Bajaj, R.G. Griffin, and R.J. Temkin. Continuous-Wave Operation of a Second*

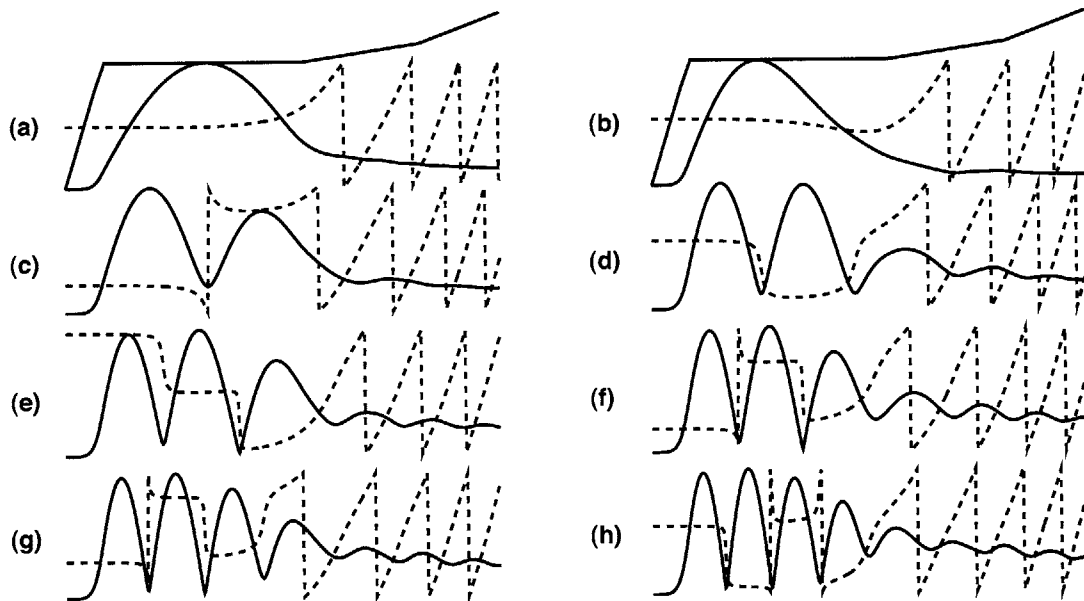


Figure 5-18: Self-consistent axial field and phase profiles for  $TE_{5,2,q}$  modes with  $q \geq 1$  as calculated from MAGY. The cavity geometry is indicated above each column, and we have displayed the normalized voltage amplitude. The frequency increases from 246.0 GHz in (a) to 248.1 GHz in (h).

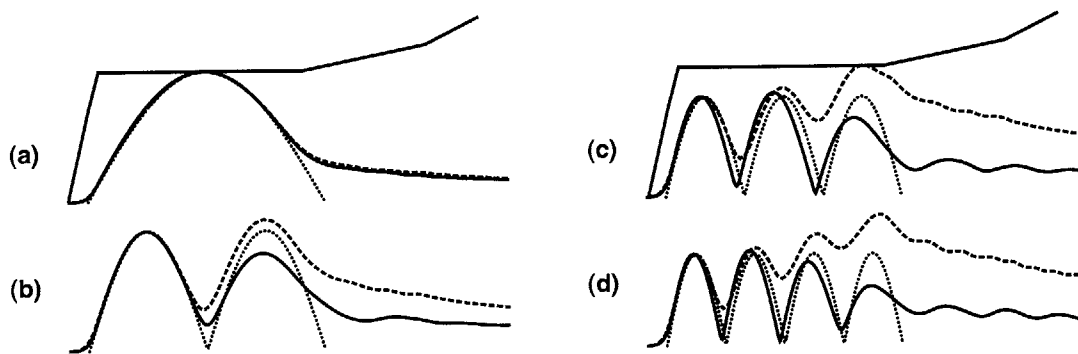


Figure 5-19: Self-consistent axial field profiles for  $TE_{5,2,q}$  modes with  $q \geq 1$  as calculated from MAGY (solid lines) compared with cold cavity (dashed lines) and sinusoidal (dotted lines) field profiles. The cavity geometry is indicated above the column.

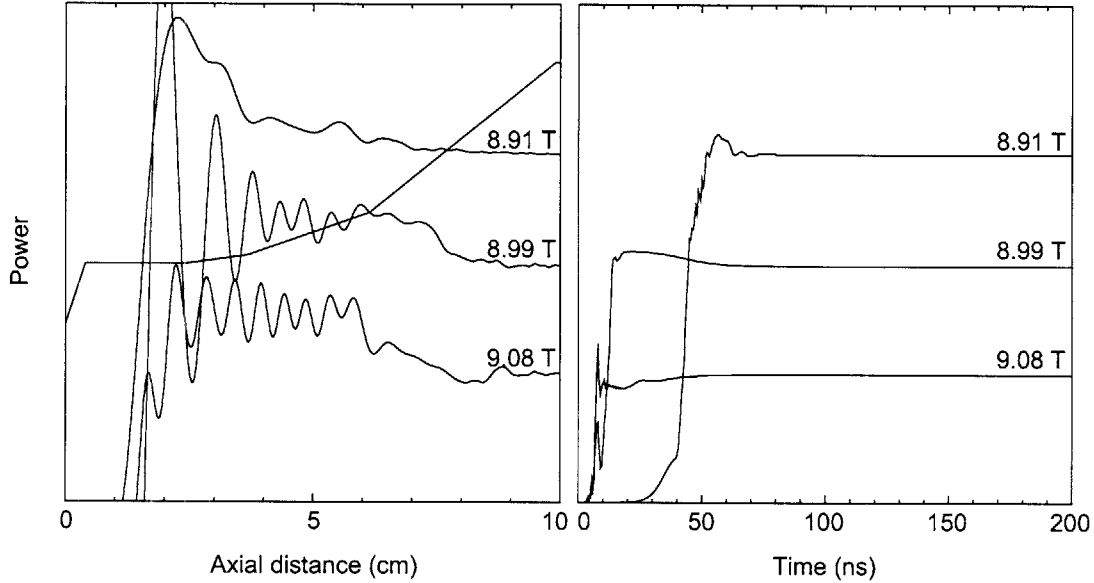


Figure 5-20: Spatial dependence of the power throughout the cavity (in the  $TE_{5,2}$  mode) at three magnetic fields. At frequencies greater than that of the  $TE_{5,2,1}$  cold cavity mode, there is a spatial oscillation pattern which we interpret as the interference of the backward propagating wave with its non-synchronous reflection [12].

Table 5.3: CW experimental operating parameters

Experimental parameters	Min.	Max.
Duty cycle (%)	–	100
Beam voltage (kV)	0	15
Beam current (mA)	0	140
Main magnetic field	8	9.2
$\Delta$ cathode magnetic field (T)	$-8.5 \times 10^{-2}$	$8.5 \times 10^{-2}$

*Harmonic Gyrotron Oscillator at 460 GHz* [113].

There have been very few CW gyrotron experiments at high frequencies. Table 1.1 shows only six different CW gyrotrons from Univ. Sydney [36], Fukui Univ. [38], IAP [37, 114], and MIT [1, 40] generating frequencies above 207 GHz at output powers ranging from a fraction of a Watt to a kilowatt.

While the physics of a gyrotron can be nearly completely characterized in short pulse (microsecond to millisecond) operation, many engineering issues remain which must be addressed in the design of a high frequency continuous-wave gyrotron that are nontrivial. These include passing an extremely energetic electron beam through an increasingly narrow interaction structure which changes criteria for the selection process of the design mode, the design of a robust collector that can dissipate high average power, the magnetic field limitations of a CW magnet, a cooling circuit, and a very good vacuum pumping conductance throughout the tube.

After the gyrotron's operation was characterized using short pulses, the Spellman HV power supply (described in Section 4.3.1) was connected in replacement of the modulator initially using pulses of millisecond and second lengths. The pulse capabilities of the CW power supply are shown in Fig. 4-12. However, we discovered that a better method was through the continuous application of low voltage. Due to the substantial gas load produced in the collector, the tube performance during this conditioning procedure was carefully monitored, and no arcing or permanent degradation was observed. This process is akin to activation of the gun, where the heater temperature is held constant and the emission current increases over time with increasing cathode voltage at continuous duty, and the collector is outgassed as a result. Finally, the collector has dissipated in excess of 1.8 kW of electron beam power, sufficient to achieve the operating parameters of 12.4 kV and over 100 mA, with no adverse effects.

A parametric study of the second harmonic design mode and neighboring modes involves variation of the electron beam voltage and current, main magnetic field, gun magnetic field, and the alignment of the vacuum tube with respect to the room temperature bore of the superconducting gyrotron magnet. The electron beam voltage and current were varied up to 15 kV and 140 mA while the main magnetic field was varied up to 9.2 T and the gun magnet up to  $\pm 8.5 \times 10^{-2}$  T with respect to the cathode field. The experimental parameters are summarized in Table 5.3. All measurements were taken at the end of a 2 m long copper waveguide of 2.54 cm inner diameter, which couples directly to the output window, unless otherwise specified. The alignment of the tube may be slightly different in this configuration than in the previous two experiments because the gyrotron tube was removed from the magnet



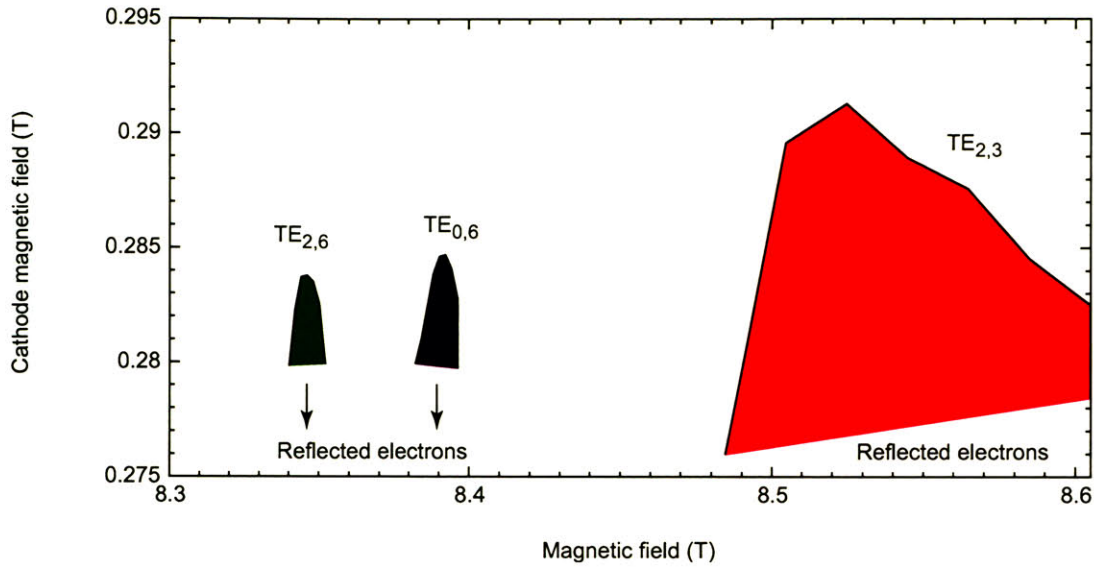


Figure 5-21: Mode map for the design mode and nearby competing fundamental  $TE_{2,3}$  mode at 12.4 kV and 100 mA for the cavity and cathode magnetic fields.

in the interim. However, tube alignment was never performed in CW mode due to the potentially disastrous effects of CW interception of the body components, where a beam power locally of 5 W could overheat a ring in the beam tunnel.

### 5.2.1 Mode Map

Figure 5-21 is a mode map which was generated during CW operation charting the regions of parameter space in which the modes in the vicinity of the  $TE_{0,6}$  design mode can be excited. Since the design mode is of relatively low order, the modes are spaced apart and there are few possibilities of simultaneously excited modes in the present gyrotron. In fact, in the region of interest, there are only two possible second harmonic modes, the  $TE_{2,6}$  and  $TE_{0,6}$ , and one competing fundamental mode, the  $TE_{2,3}$ . For the present mode map, we have varied two main parameters, the main magnetic field and the cathode magnetic field, to determine the operational limits of each mode. The cavity magnetic field is an obvious parameter choice because the electron cyclotron frequency is directly proportional to it in addition to the proportionality of the detuning parameter. The cathode magnetic field, adjustable through varying the gun coil, affects the magnetic compression which changes the beam radius.

## 5.2.2 Second Harmonic

The variation of the output power of the  $TE_{0,6}$  design mode with beam current is depicted in Fig. 5-22(a). The power in the operating mode was measured using the Scientech calorimeter described in Chapter 3. The magnetic field was chosen from the pulsed results shown in Fig. 5-8 depicting the relative efficiency as a function of the voltage and magnetic field. After oscillations begin around 77 mA, the power is linear with current. A maximum CW output power of 8.4 W is achieved at beam parameters of 135 mA and 12.4 kV, yielding an efficiency of 0.5%. At the time of this writing and to the author's knowledge of the state-of-the-art of high power gyro-devices [115], this is a record CW power for this frequency. While this tube will cease to be experimental upon the completion of these characterizing experiments and from that time onward will be wholly dedicated to dynamic nuclear polarization, a decision was made to not increase the beam power past this point in order to avoid deleterious effects on the collector, electron gun, and tube performance.

The optimum CW operating voltage was verified in Fig. 5-22(c). The CW result compares favorably with the pulsed result of Fig. 5-8 yielding an optimum beam voltage of 12.4 kV. In our diode electron gun, the electron velocity pitch factor (also known as the alpha) changes rapidly with cathode magnetic field, along with other factors such as main magnetic field and cathode voltage (*c.f.* Fig. 4-9). This rapid change is illustrated in Fig. 5-23. A first-order attempt at holding the alpha constant was made in the voltage optimization measurement by maintaining a constant body current signal. The small but nonzero body current is attributed to reflected electrons originating from an unusually high alpha estimated at 2.4, and is less than 2% of the total beam current in most cases. Since we do not have an alpha probe in our experiment, an experimental illustration of the change in alpha with cathode magnetic field can be inferred from the change in body current and is shown in Fig. 5-22(d). Here, both the power and body current are shown with changing magnetic field. The body current increases from zero to four milliamperes with decreasing cathode magnetic field (increasing alpha) while the power increases with decreasing cathode magnetic field (increasing alpha and increasing beam compression) until a point where the overall beam quality suffers. A discrepancy between the cathode magnetic field values in Figs. 5-22(d) and 5-23 may emanate from several factors, including the accuracy to which the actual cathode magnetic field is known and the precise location of the gun coil with respect to the cathode.

In Fig. 5-22(b) the experimentally measured continuous duty power of the design  $TE_{0,6,1}$  mode with varying magnetic field is compared with the theoretical results from a self-consistent nonlinear theory. In the theoretical model we assumed 30% losses

Table 5.4: Frequency dependence on operating parameters

Parameter	Sensitivity
Beam current	0.4 MHz/mA
Magnetic field	3.0 GHz/T
Beam voltage	50 MHz/kV
Cathode magnetic field	1.3 GHz/T

in the quasi-optical mode converter. A conductivity one-fifth that of ideal copper is used based on cavity thermal load measurements (Sec. 5.2.4). From electron gun simulations, a guiding center spread of 5.5% is derived, in addition to the transverse velocity spread of 6% and pitch factor of 2.4, which are both consistent with EGUN. At beam parameters of 100 mA and 12.4 kV, a power of nearly 5 W is recorded. However, the theory shows a slightly elevated power of 7 W indicating that either the mode converter is less efficient than previously assumed or that the beam quality is below that which is expected. There is no present explanation for the difference in width of the theoretical and experimental curves. The optimal magnetic field agrees with the result of the pulsed second harmonic experiment, shown in Fig. 5-8.

### 5.2.3 Frequency Pulling

The dependence of the emission frequency on the operating parameters is an important metric of the frequency stability of the gyrotron. The dependence of the emission frequency of the TE<sub>0,6</sub> design mode on the operating parameters such as the beam current, main magnetic field, beam voltage, and cathode magnetic field was characterized using a heterodyne frequency system. The heterodyne receiver system is highly accurate due to a phased locked loop which is capable of stabilizing the local oscillator to 1 Hz. Only a single parameter was varied for each measurement in order to simulate operation. While the beam voltage is not likely to change during operation, the control of the output power by feedback will cause the beam current to vary accordingly. The main magnetic field will drift downward at a specified rate over long periods of time and the cathode magnetic field may vary due to heating of the gun coil.

The measured frequency pulling characteristics of the gyrotron are plotted in Fig. 5-24. The total frequency change observed is within 30 MHz. The frequency dependence on operating parameters is summarized in Table 5.4. The pulling effects on frequency by the magnetic field are proportional to  $\omega/Q$  [18]. While the second harmonic mode has high frequency, it also has a very high quality factor. Comparing

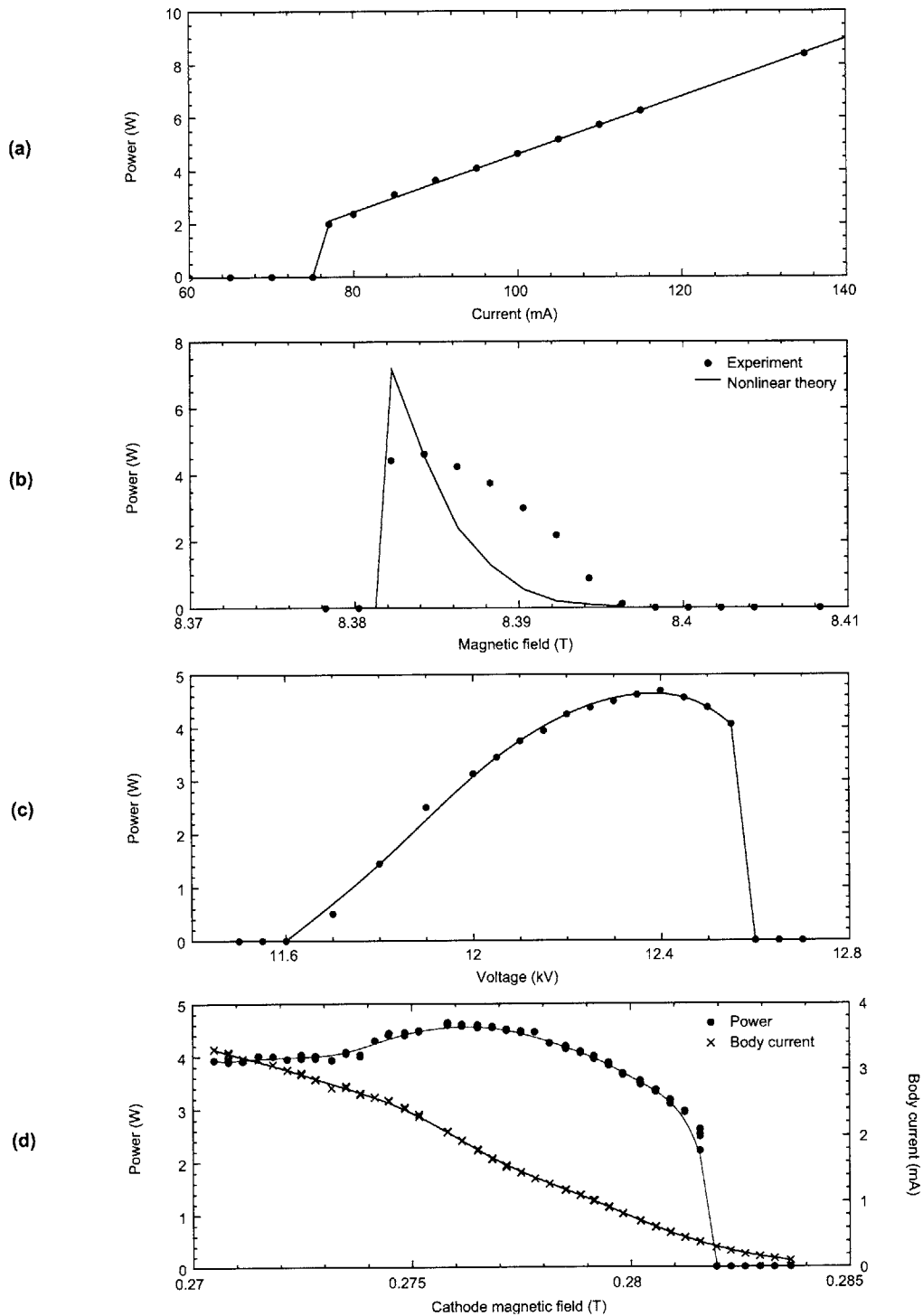


Figure 5-22: CW output power measured in the  $TE_{0,6}$  second harmonic mode as a function of (a) beam current, (b) main magnetic field, (c) voltage, and (d) cathode magnetic field. Unless otherwise indicated, the experimental parameters are 12.4 kV, 100 mA and 8.384 T.

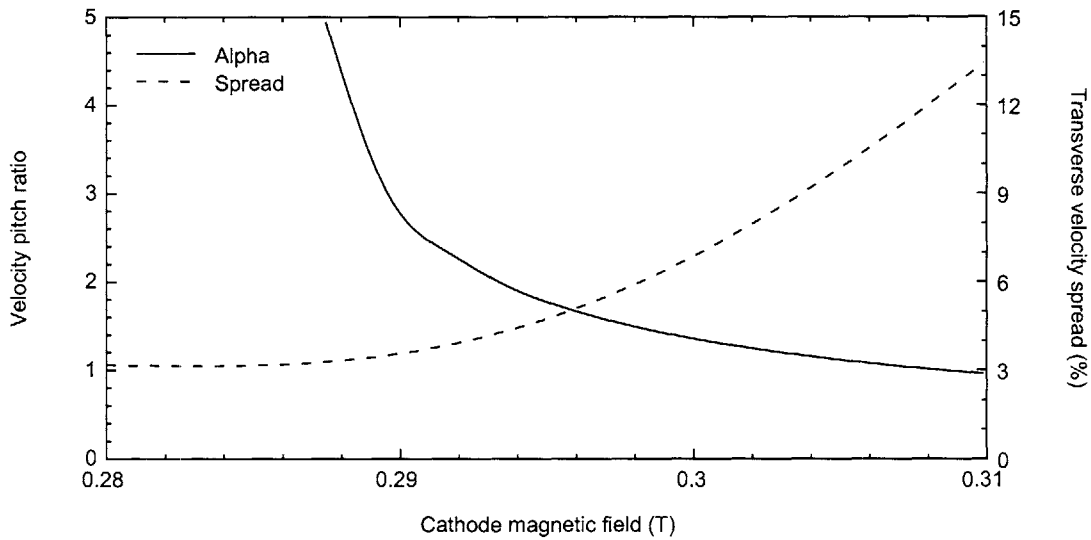


Figure 5-23: EGUN simulations for varying cathode magnetic fields at 12.4 kV and 100 mA.

the frequency sensitivity from Tables 5.4 and 4.1 we find that the values are more than twice for the second harmonic at 460 GHz compared to the fundamental at 140 GHz. The dependence of the frequency on the beam current (*c.f.* Fig. 5-24(a)) is negative, which is opposite to the positive dependence measured by Kreisler et al. [18].

The frequency pulling effects of the cathode voltage  $V_c$  and main magnetic field  $B$  in Figs. 5-24(b) and (c) have opposing slopes. For a given beam current, the observed shift in emission frequency resulting from changes of either the main magnetic field or the beam voltage is due to the effect on the cyclotron frequency,  $\omega_c (= eB/\gamma m_e)$ , where  $\gamma (= 1 + V_c/511)$  is the relativistic factor, and the cathode voltage  $V_c$  is in kilovolts. If the magnetic field alone is varied, the resulting frequency pulling will have a positive slope, and if the voltage is varied, the frequency pulling will have a negative slope. However, coordinated changes in both the magnetic field and cathode voltage may leave the cyclotron frequency unchanged such that there is no change in the emission frequency. The same nonlinear theory as was used to simulate the power as a function of magnetic field yields results for the frequency pulling, which are compared with experimental data in Fig. 5-24(b) with coinciding slope.

### 5.2.4 Ohmic Losses

At high frequencies, a significant portion of the power generated in the cavity is not extracted and is instead deposited in the cavity walls in the form of ohmic heating.

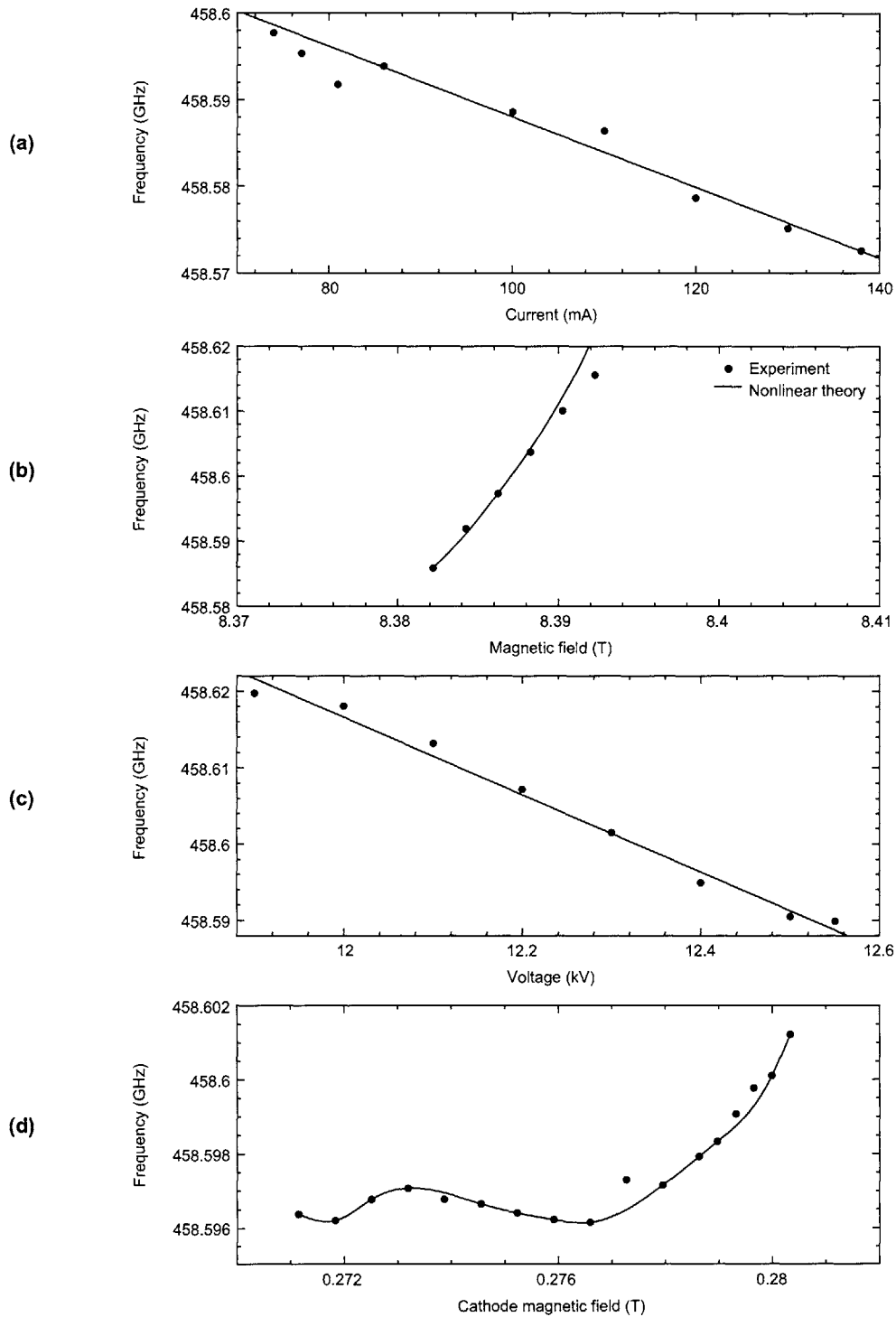


Figure 5-24: Frequency tuning of the  $TE_{0,6}$  second harmonic mode with (a) beam current, (b) main magnetic field, (c) voltage, and (d) cathode magnetic field. Unless otherwise indicated, the experimental parameters are 12.4 kV, 100 mA and 8.384 T.

These ohmic losses are given by the ratio of diffractive to ohmic  $Q$  multiplied by the output power,

$$P_{\text{ohmic}} = \frac{Q_{\text{diffractive}}}{Q_{\text{ohmic}}} P_{\text{out}}. \quad (5.2)$$

The method, materials, and process of fabrication of the cavity are the main contributions to the experimental value of the ohmic losses. For example, the properties of the material (in our case copper), in particular the electrical conductivity and surface roughness, as well as machining anomalies such as irises, in essence determine the ohmic losses. The theoretical ohmic efficiency as a function of the conductivity of copper for the second harmonic  $\text{TE}_{0,6,1}$  mode is shown in Fig. 5-25. The ohmic efficiency, or the RF efficiency, is the fraction of output power with respect to the total power generated in the cavity. Starting with an RF efficiency near 40% at the conductivity of ideal copper ( $5.8 \times 10^7$  S/m), the RF efficiency rapidly decreases as the quality of copper degrades. For comparison, the RF efficiency as a function of diffractive  $Q$  assuming a conductivity half that of ideal copper is shown in Fig. 5-25. Here the RF efficiency decreases rapidly with increasing diffractive  $Q$ .

A measurement of the ohmic losses in the  $\text{TE}_{0,6}$  second harmonic design mode of the 460 GHz gyrotron was made possible by the data acquisition capabilities of the computerized control system. By measuring the flow rate and change in temperature of the cavity cooling water, the amount of power transferred from the cavity to the water could be calculated (wet calorimetry). The temperature of the cavity cooling water was simultaneously measured at both the inlet and outlet of the cavity with separate thermistors, where the measurement was taken as close to the cavity as possible to prevent heat transfer between the cooling hose and the ambient. Assuming that the water is in good thermal contact with the cavity and that the cavity is thermally isolated from any other source of heat internal or external to the tube (such as the collector which is isolated by a ceramic insulator), this is equivalent to measuring the thermal load on the cavity. A period of up to several minutes was allowed for thermal equilibrium to be reached.

Using wet calorimetry, the ohmic power distribution was measured for gyrotron output powers up to 4 W. The output microwave power was measured using dry calorimetry. The results of these measurements are shown in Fig. 5-26 and Table 5.5. The RF efficiency is nearly constant with output power and the cavity thermal load is linear with output power. The observed RF efficiency of 24% is approximately 8% less than the theoretical value. From Fig. 5-25, the theoretical ohmic efficiency assuming half the conductivity of ideal copper is shown to be 32%. The electrical conductivity required to match the experimental results ranges between one-quarter

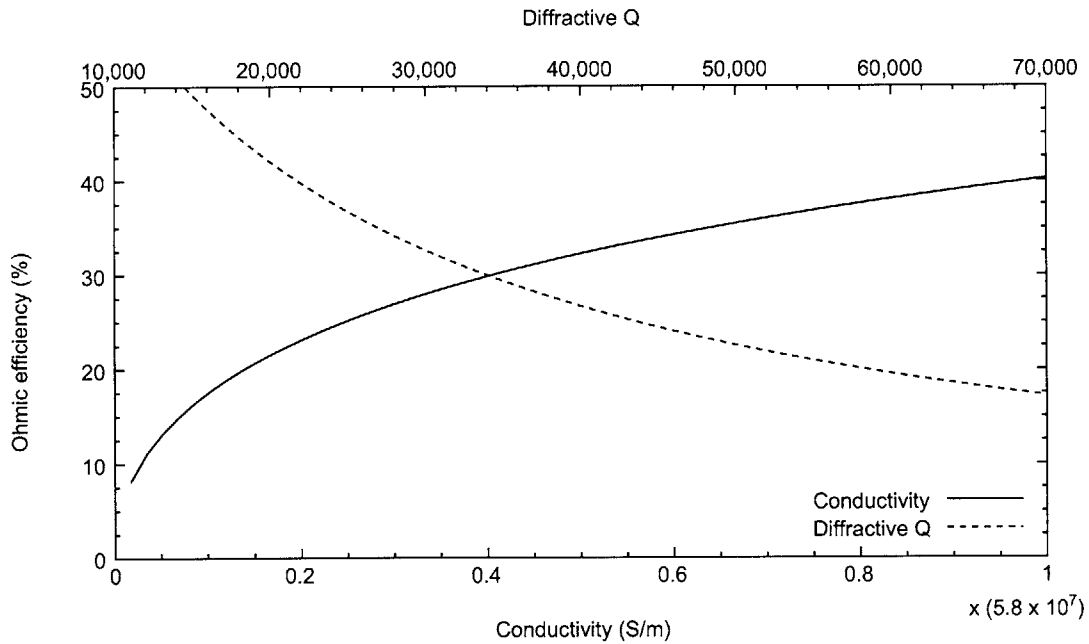


Figure 5-25: Theoretical RF efficiency as a function of the conductivity of copper and diffractive  $Q$  for the second harmonic  $TE_{0,6,1}$  mode. The calculation assumes alternately a diffractive  $Q$  of 31,000 and half the conductivity of ideal copper.

Table 5.5: Measured and theoretical ohmic losses in the gyrotron cavity at 458 GHz

Output power (W)	Cavity thermal load (W)	RF efficiency (%)
0	0	-
2.5	7.9	24.0
3.75	12.1	23.6
4.1	13.5	23.3

Table 5.6: Design and measured parameters from the ohmic loss measurement of the gyrotron cavity at 458 GHz

	Design	Measured
Conductivity $\times (5.8 \times 10^7 \text{ S/m})$	0.5	0.25
Diffractive $Q$	31,000	47,000
RF efficiency (%)	32	24



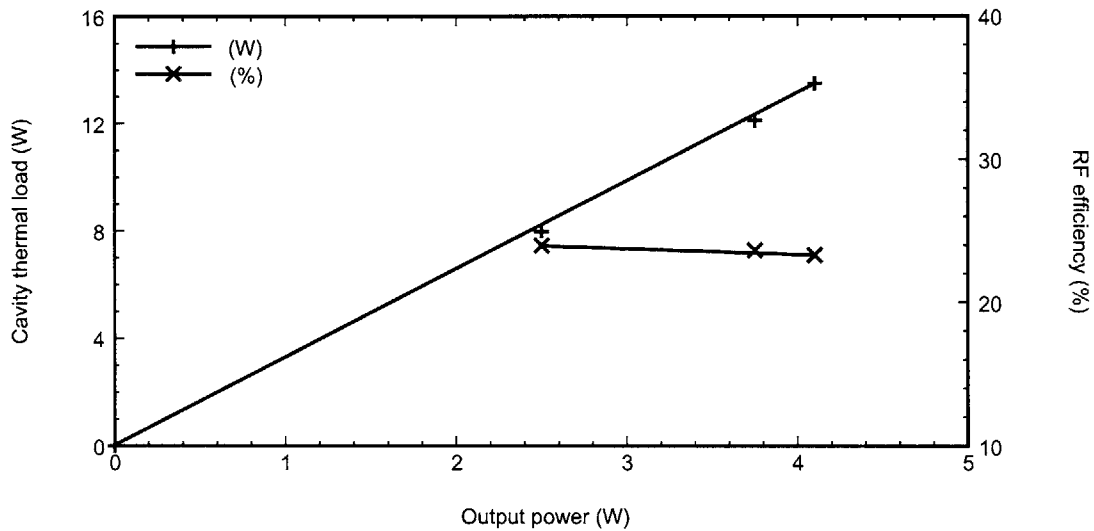


Figure 5-26: Cavity thermal load and RF efficiency as a function of measured output power using cavity thermal load measurement for the second harmonic  $TE_{0,6,1}$  mode.

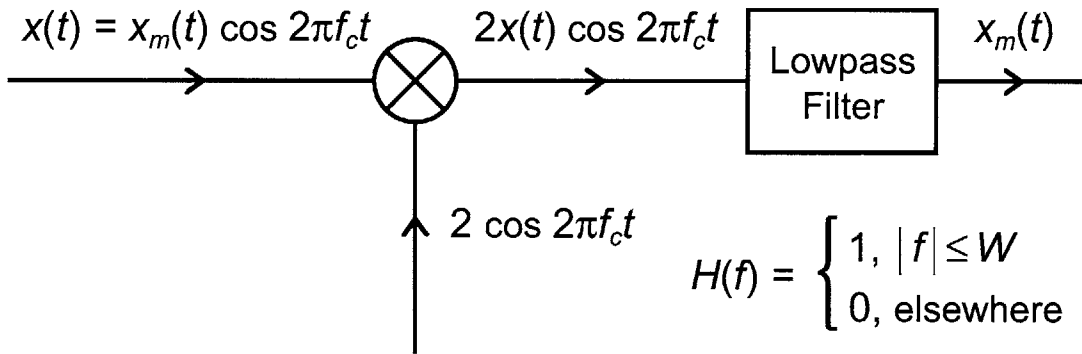


Figure 5-27: Block diagram of a simple homodyne detector [13].

and one-fifth that of ideal copper. Another possible cause of the excessive cavity losses is an increased cavity diffractive  $Q$  factor, incurred from the implementation of the shallow output taper. Figure 5-25 shows that an increase in diffractive  $Q$  of 1.5 times from 31,000 to 47,000 could account for the additional ohmic losses. The design and measured values for the ohmic loss measurement are summarized in Table 5.6. Both the increase in diffractive  $Q$  and decrease in conductivity are within reasonable bounds and in reality it is probably a combination of the two contributing to the slightly elevated ohmic losses.

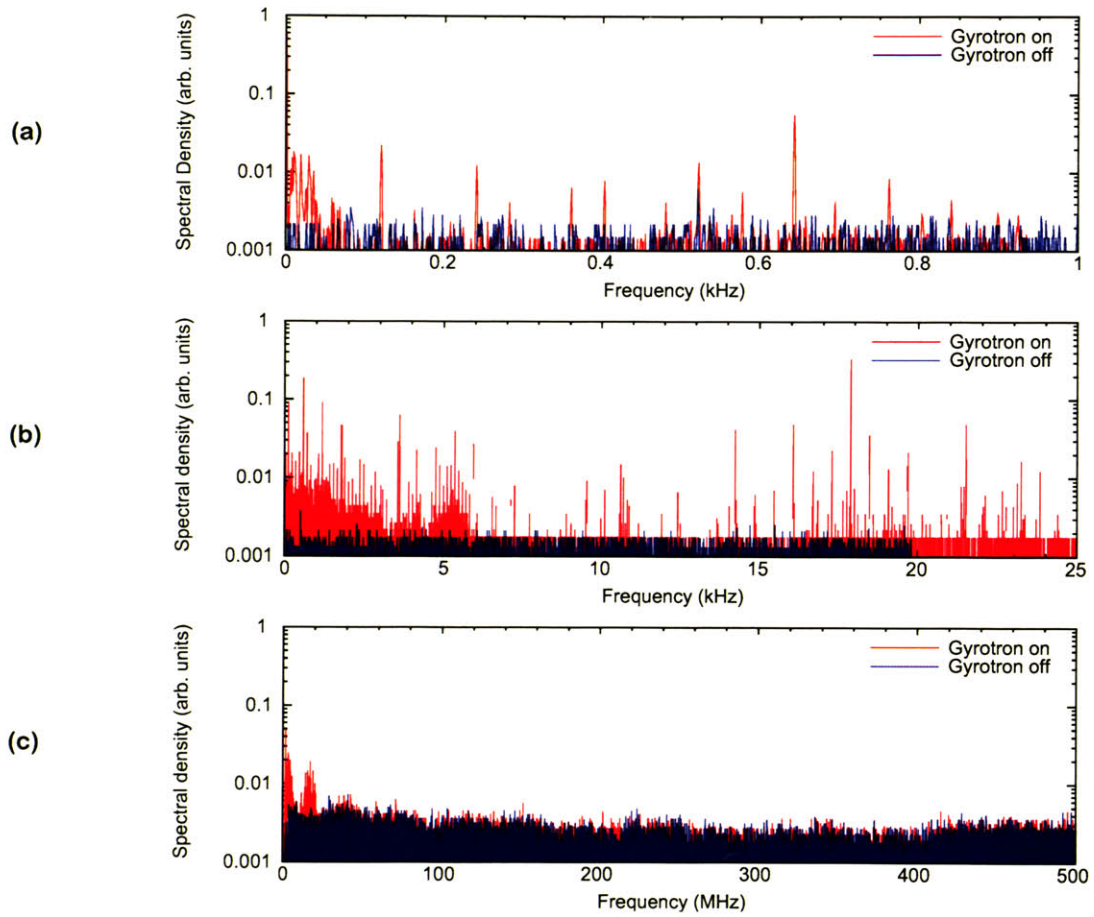


Figure 5-28: Homodyne measurements of the technical noise for the second harmonic  $TE_{0,6,1}$  mode.

## 5.2.5 Homodyne Measurements

The 460 GHz time domain signal is an amplitude modulated (AM) signal which can be demodulated yielding both the linewidth and technical noise of the device. The homodyne detector, depicted in Fig. 5-27, uses a local oscillator which is synchronized in frequency to the carrier of the signal, essentially reversing the amplitude modulation process. The output of the modulation of the AM signal  $x(t)$  with a local oscillator  $2 \cos 2\pi f_c t$  of the same frequency can be written as [13]

$$2x(t) \cos 2\pi f_c t = 2x_m(t) \cos^2 2\pi f_c t \quad (5.3)$$

$$= x_m(t) + x_m(t) \cos 4\pi f_c t \quad (5.4)$$

where the trigonometric identity

$$\cos^2 \phi = \frac{1}{2} + \frac{1}{2} \cos 2\phi \quad (5.5)$$

has been applied. The signal  $x_m(t)$  can then be recovered by a lowpass filter. In this setup, the local oscillator signal must be synchronized in phase with the carrier signal.

An overmoded horn directed at the gyrotron output beam coupled a sample of the gyrotron radiation into the homodyne receiver. In our case, the main center line frequency of the gyrotron acts as a local oscillator; this frequency beats with any other frequencies that are generated by the gyrotron in the harmonic mixer, including those generated by spurious or competing gyrotron modes. The receiver is a simplification of the heterodyne frequency system, consisting of a mixer followed by three intermediate frequency (IF) amplifiers whose amplification bandwidth is from approximately 0.1–1,000 MHz, and a low pass filter with 520 MHz cutoff frequency. Thus, the gyrotron frequencies between 0.1 and 520 MHz are amplified, digitized, and passed through an FFT. If the mixer is saturated, the truncation will create artifacts.

The results of homodyne measurements on the second harmonic  $TE_{0,6}$  design mode over 1 kHz, 25 kHz, and 500 MHz bands are shown in Figure 5-28. Since the amplifiers do not pass DC, these signals are presumed to be well below the gyrotron center line frequency. The technical noise in the gyrotron is apparent in the tens of kilohertz (*c.f.* Fig. 5-28). The high voltage power supply is a likely source of the noise in this band. The specifications for the ripple on the power supply are 0.03% rms below 1 kHz and 0.75% rms above 1 kHz. In addition, the filament output is at 38 kHz. The gyrotron signal at higher frequencies shows little contamination (*c.f.* Fig. 5-28(c)).

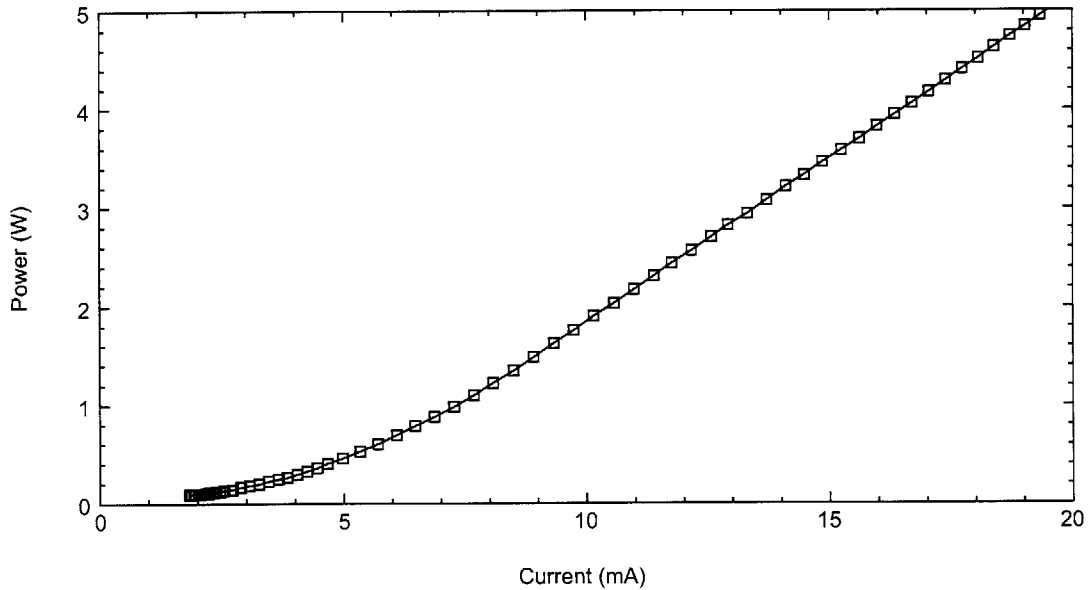


Figure 5-29: CW output power in the  $TE_{2,3}$  mode as a function of beam current at 3.5 kV and 8.38 T.

### 5.2.6 Low Voltage Fundamental $TE_{2,3}$ Mode

The nearest mode to the  $TE_{0,6}$  second harmonic design mode in magnetic field is the fundamental  $TE_{2,3}$  mode. The studies of the  $TE_{2,3}$  fundamental mode reveal that the mode can be excited at very low voltage, less than 3.5 kV, with less than 7 W of beam power. The low voltage cannot be explained through simulations of the electron gun. Measurements of the power show that the mode starts at 2 mA (*c.f.* Fig. 5-29). A starting current of 2 mA can be obtained using linear theory with beam alpha above 1.8. In Fig. 5-30 the experimental start currents are compared with linear theory using beam alpha 2.5 and 10% velocity spread to good agreement in the longitudinal mode with a single variation. However, the simulation and experiment begin to diverge as the number of longitudinal variations increase. The mode also exhibits a wide frequency tuning range, shown in Fig. 5-31.

Average power measurements were made during the experiment using a laser calorimeter. Figure 5-32 depicts measured CW power data of the fundamental  $TE_{2,3,q}$  modes around 233 GHz as a function of beam current and magnetic field. A calorimeter was used to measure the radiation, and the beam voltage was fixed at 3.5 kV. Over 12 W of average power were recorded with an efficiency in excess of 7%.

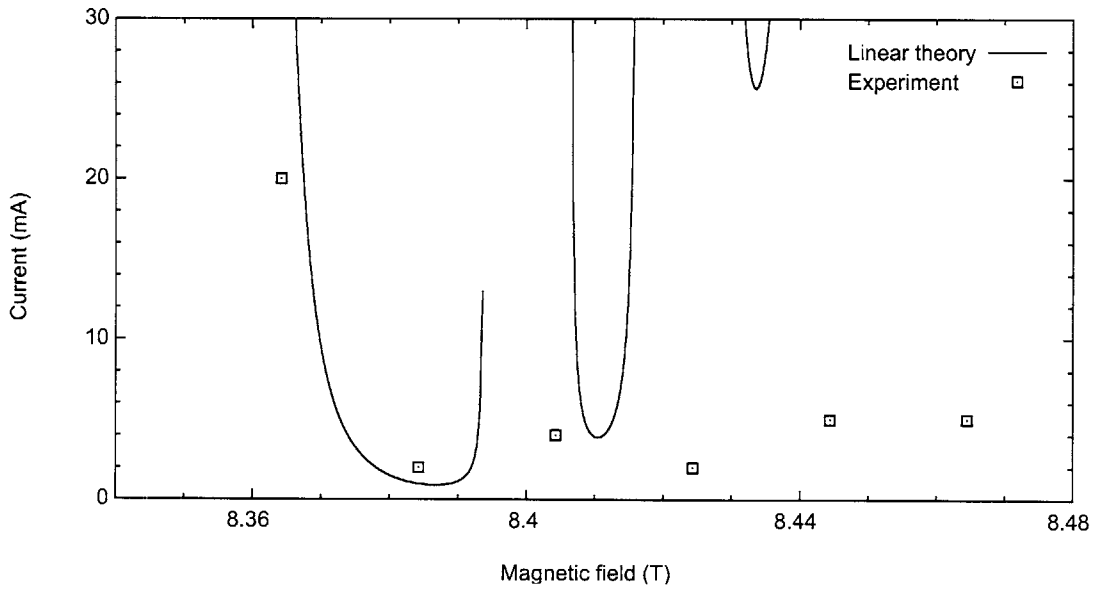


Figure 5-30: CW start current data in the TE<sub>2,3</sub> mode at 3.5 kV compared to linear theory using alpha 2.5 and 10% transverse velocity spread.

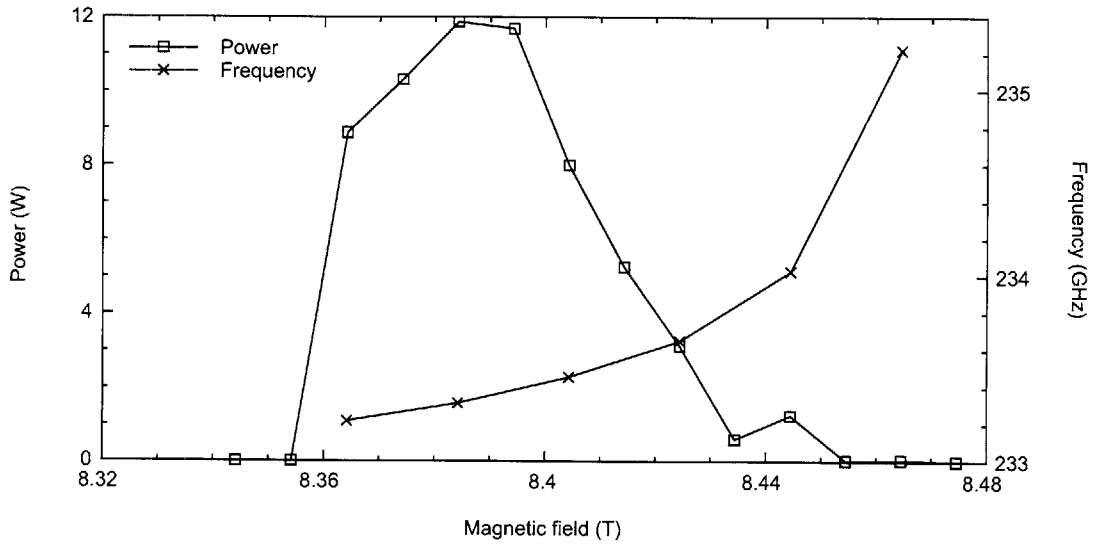


Figure 5-31: CW output power and frequency in the TE<sub>2,3</sub> mode as a function of magnetic field for 50 mA and 3.5 kV.

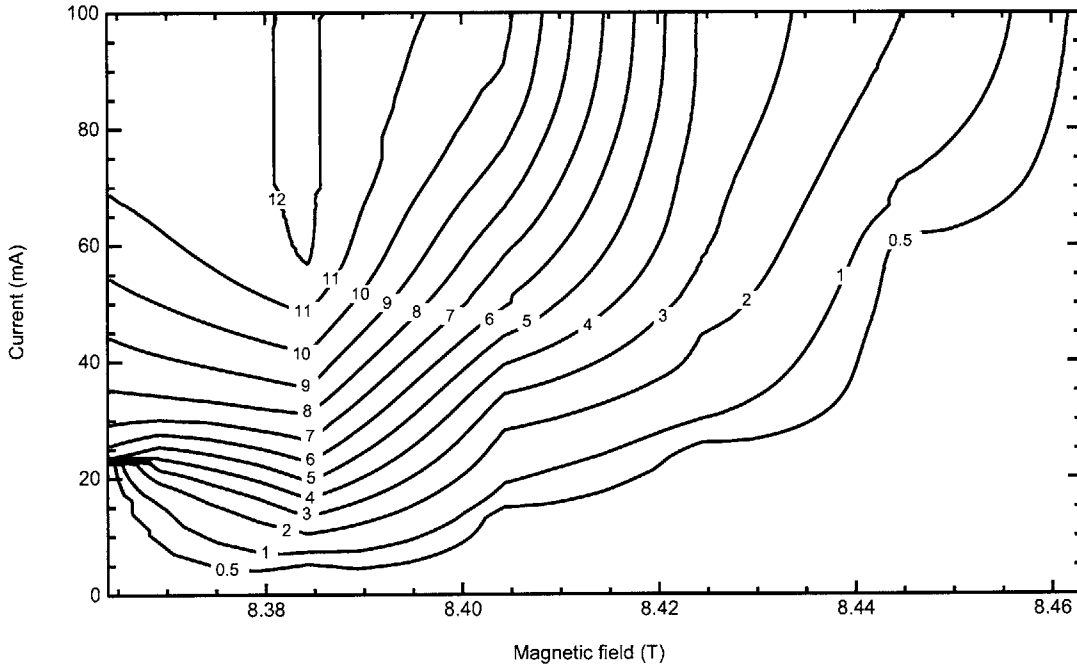


Figure 5-32: Contour plot of measured CW power data of the fundamental  $TE_{2,3,q}$  modes in watts as a function of beam current and magnetic field.

### Axial mode competition of the $TE_{2,3,q}$ modes

It is possible for axial mode competition to occur when the resonance curves of modes with differing axial indices overlap [116]. The axial mode locking phenomenon has been studied in detail in a harmonic-multiplying, inverted gyrotwystron at 31 GHz in the  $TE_{4,2,q}$  modes [111]. The axial structure of the modes of a cylindrical resonator along the  $z$  axis can be described by

$$f(z) = \sin\left(\frac{q\pi z}{L}\right) \quad (5.6)$$

where  $q$  is the axial index and  $L$  is the resonator length. The  $Q$  factor of the axial modes can be estimated as

$$Q_q \propto \frac{1}{q^2} Q_{D, \min} \quad (5.7)$$

where  $Q_{D, \min} (= 4\pi (L/\lambda)^2)$  is the minimum diffractive  $Q$  factor for open cylindrical cavities. A parameter  $P$  defined as the ratio of the sum of halfwidths of resonance curves of two neighboring axial modes to their frequency separation expresses the

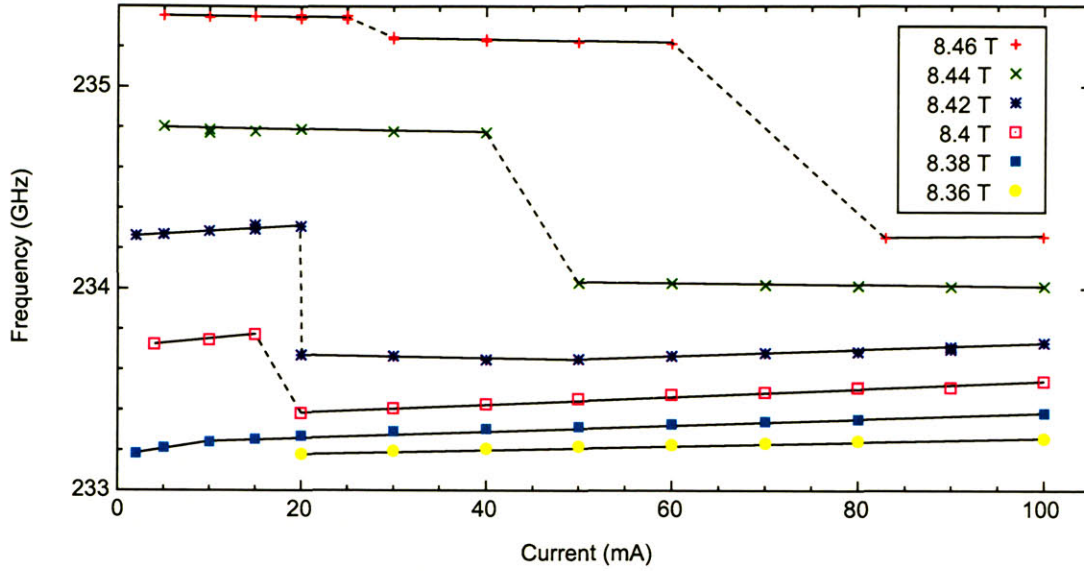


Figure 5-33: Heterodyne measured frequencies of the axial  $TE_{2,3,q}$  fundamental modes at low voltage as a function of beam current and magnetic field.

Table 5.7: Cold cavity frequencies of the  $TE_{2,3,q}$  modes

$q$	Frequency (GHz)
1	233.148
2	233.411
3	233.844
4	234.411
5	235.250

overlapping between successive axial modes and is given by [116]

$$P \simeq \frac{1}{\pi} \frac{(q+1)^2 + q^2}{(q+1)^2 - q^2}. \quad (5.8)$$

From (5.8), the overlapping becomes larger as the axial index  $q$  increases due to the broadening of the resonance curves.

Figure 5-33 shows heterodyne frequency data for the  $TE_{2,3,q}$  modes at 3.5 kV and as a function of beam current up to 100 mA, where the main magnetic field has been varied from 8.36 to 8.46 T in 0.02 T intervals. As the beam current is increased, the frequency is continuously pulled until a current threshold where the frequency discretely drops by an interval that is consistent with excitation of the  $q - 1$  axial mode. Table 5.7 lists the cold cavity frequencies for the  $TE_{2,3,q}$  funda-

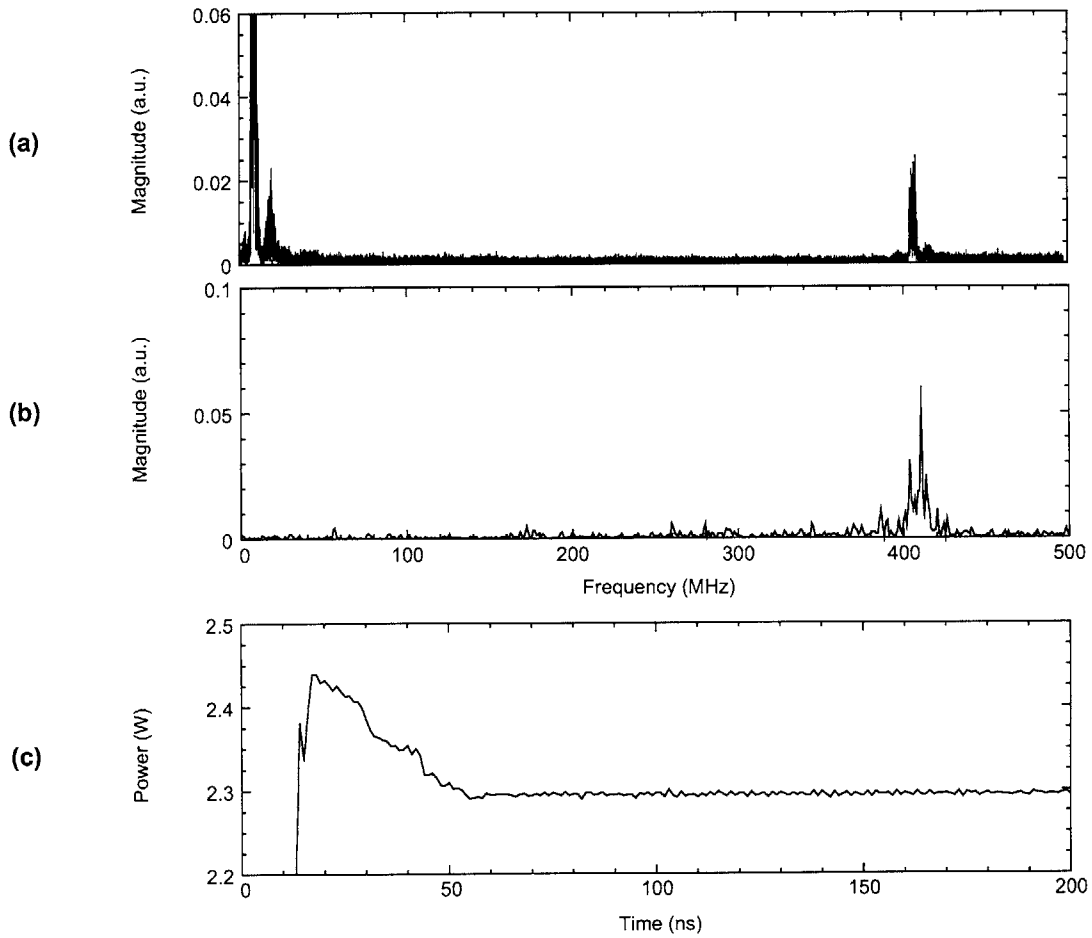


Figure 5-34: (a) Experiment (homodyne) compared to (b) MAGY simulation of the  $TE_{2,3,q}$  fundamental modes at low voltage (3.5 kV) and 8.42 T depicting multiple frequencies separated by 400 MHz corresponding to consecutive longitudinal modes (c) and its corresponding time domain.



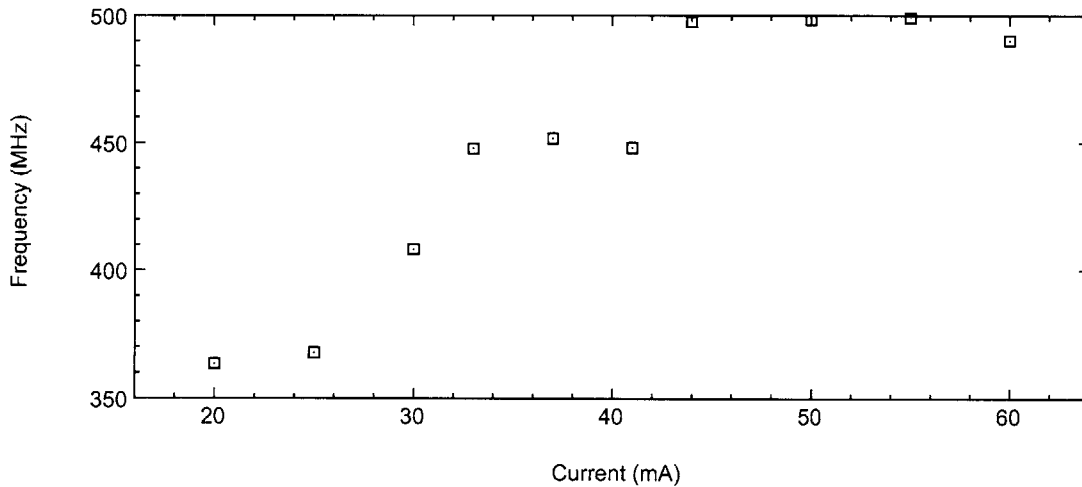


Figure 5-35: Homodyne frequency data for the  $TE_{2,3,q}$  fundamental modes at low voltage (3.5 kV) and 8.42 T as a function of beam current.

mental modes. At the transitional current, both axial modes are excited with equal amplitude, and afterward the gyrotron exhibits nearly single-mode oscillations accompanied by low-amplitude oscillations of another axial mode with pulsations of the phase difference. These low-amplitude oscillations were observed via homodyne measurements and were verified by MAGY. Figure 5-34(b) is a MAGY simulation of the  $TE_{2,3,q}$  fundamental modes at low voltage (3.5 kV) and 8.42 T depicting multiple frequencies separated by 400 MHz, corresponding to consecutive longitudinal modes. The results of homodyne measurements at 8.42 T with increasing beam current is shown in Fig. 5-35 which suggests that a mode mixture is always present, though the weaker mode is very small in amplitude compared to the dominating mode which is captured through the heterodyne measurements. In the second harmonic heterodyne measurements, axial mode competition is not seen through homodyne or heterodyne frequency measurements.

### 5.2.7 Hollow Dielectric Waveguide

Overmoded cylindrical hollow dielectric waveguide is an attractive method for low-loss transmission of Gaussian radiation over long distances. Consisting of a cylinder of dielectric medium filled with air or vacuum, the dielectric waveguide can couple to the Gaussian mode as the  $HE_{1,1}$  mode. For  $HE_{mp}$  modes (where  $m \neq 0$ ) in hollow dielectric waveguide with radius  $a$  and refractive index  $n$ , the attenuation constant is

Table 5.8: Measured and theoretical losses in 2.54 cm diameter G10 epoxyglass hollow dielectric waveguides

Mode	Frequency (GHz)	Length (cm)	Wall thickness (mm)	Total loss (dB)	Loss (dB/m)	Theoretical loss $n = 1.5$ (dB/m)
TE <sub>0,6</sub>	458	66	1.59	1.0	1.5	0.4
TE <sub>0,6</sub>	458	123	6.35	2.2	1.8	0.4
TE <sub>2,6</sub>	456	66	1.59	1.0	1.5	0.4
TE <sub>2,3</sub>	233	66	1.59	4.5	6.8	1.5

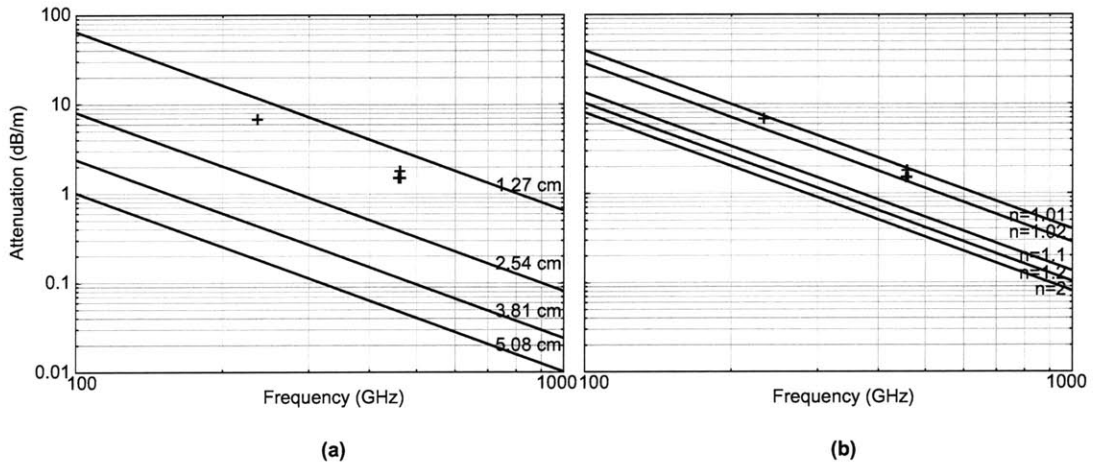


Figure 5-36: Theoretical attenuation (in dB/m) versus frequency of the HE<sub>1,1</sub> mode in (a) 1.27 cm, 2.54 cm, 3.81 cm and 5.08 cm diameter dielectric waveguide with refractive index  $n = 1.5$  (b) 2.54 cm diameter dielectric waveguide with refractive index of  $n = 1.01$ ,  $n = 1.02$ ,  $n = 1.1$ ,  $n = 1.2$ , and  $n = 2$ . Measured attenuation in 2.54 cm G10 epoxyglass is marked with pluses.

given by [117]

$$\alpha_{mp} = \left(\frac{\nu_{mp}}{2\pi}\right)^2 \frac{\lambda^2}{a^3} \frac{\frac{1}{2}(n^2 + 1)}{\sqrt{n^2 - 1}} \text{ (Np/m)}, \quad (5.9)$$

where in the Gaussian-like HE<sub>1,1</sub> mode,  $\nu_{mp} = \nu_{\text{HE}_{1,1}} = 2.405$ . The attenuation constant is proportional to  $\lambda^2/a^3$ , therefore the losses can be reduced by choosing a large radius relative to the wavelength.

Table 5.8 shows the measured losses at fundamental and second harmonic frequencies for hollow G10 epoxyglass waveguides with 2.54 cm inner diameter and lengths varying from 66 to 123 cm. The unit losses are calculating neglecting the coupling loss and compared with theoretical losses using (5.9) for refractive index of  $n = 1.5$ . The refractive index  $n = 1.5$  is chosen as an average refractive index for dielectrics

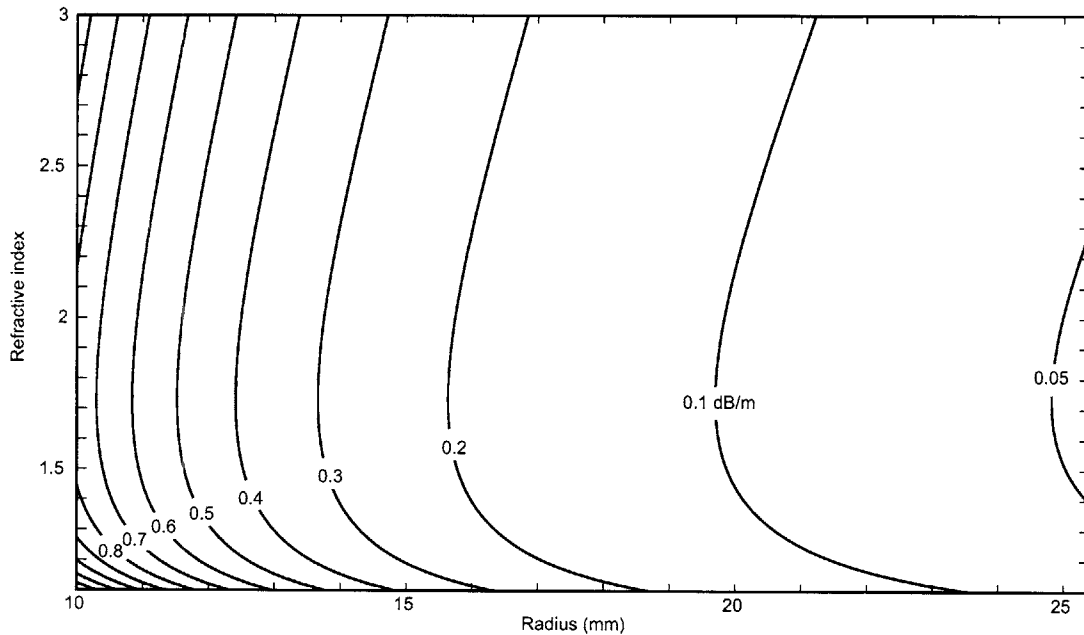


Figure 5-37: Contour plot of the theoretical attenuation (in dB/m) versus refractive index and radius of the  $HE_{1,1}$  mode at 460 GHz in hollow dielectric waveguide.

based on [104] and Fig. 5-37, where it can be seen that choosing any refractive index between 1.4 and 3.0 does not significantly change the attenuation. Using  $n = 1.5$ , the measured losses are higher than the calculated losses. This is also illustrated in Fig. 5-36(b). This discrepancy could be accounted for by coupling losses, since the waveguide of 2.54 cm inner diameter is not matched to the beam waist and was instead chosen to match the size of the window flange. Losses in excess to theory can additionally either be due to the roughness of the inner surface of the dielectric waveguide [118] or a bend in the hollow waveguide [117]. The attenuation can be reduced by choosing a larger radius waveguide (*c.f.* Figs. 5-36(a) and 5-37) and implementing a taper from a radius which couples more efficiently to the beam waist.

Measured losses in various 2.54 cm diameter hollow dielectric waveguides at 460 GHz are compared. The dielectric materials G10 (epoxyglass), canvas laminate, acrylic, acetal, and nylon were chosen for availability, machinability, heavy walls, and length. Fused quartz and Pyrex tubing were not available at the time of the measurement, are not easily machined, and are not manufactured in sufficient lengths. Various lengths of hollow dielectric waveguides were used to retrieve the coupling loss and unit loss. The results are shown in Fig. 5-38 and Table 5.9. Figure 5-38 is a plot of the losses versus length of the waveguides. The coupling loss and unit loss can be recovered as the  $y$ -intercept and slope of the curves, respectively. The lowest unit loss

Table 5.9: Measured losses in various 2.54 cm diameter hollow dielectric waveguides at 460 GHz

Material	Wall thickness (mm)	Loss (dB/m)	Coupling loss (dB)	Refractive index at 300 GHz
Acrylic	3.18	1.0	1.0	1.61 [119]
Canvas laminate	6.35	1.3	0.6	–
G10 (epoxyglass)	6.35	1.4	0.5	–
Acetal	6.35	1.7	0.2	–
Nylon	6.35	2.2	-0.2	1.72 [120]

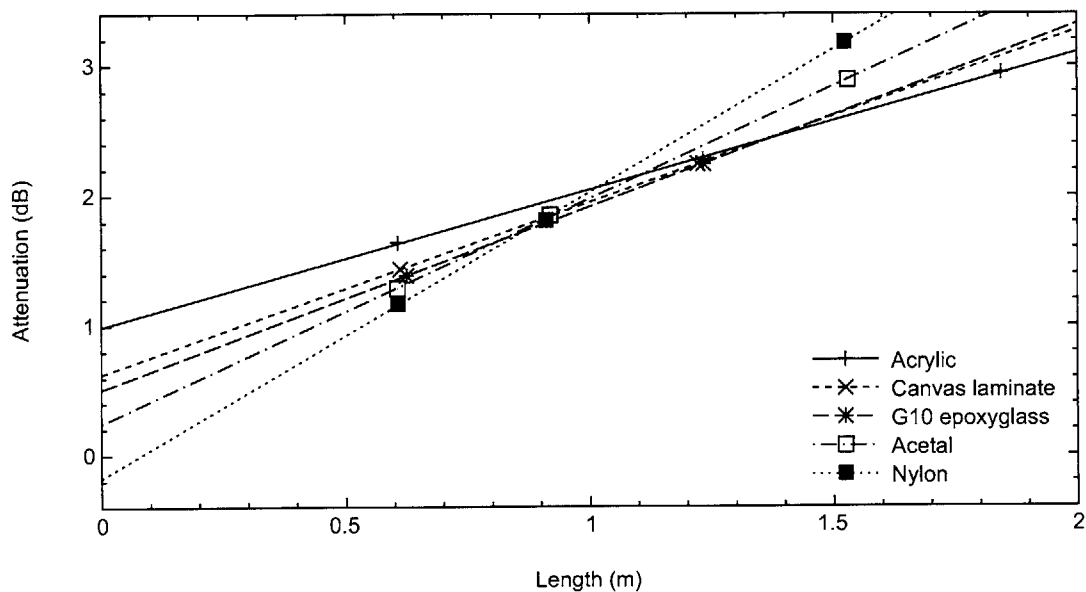


Figure 5-38: Plot of the experimental attenuation (in dB) versus length at 460 GHz in a variety of 2.54 cm diameter hollow dielectric waveguide.

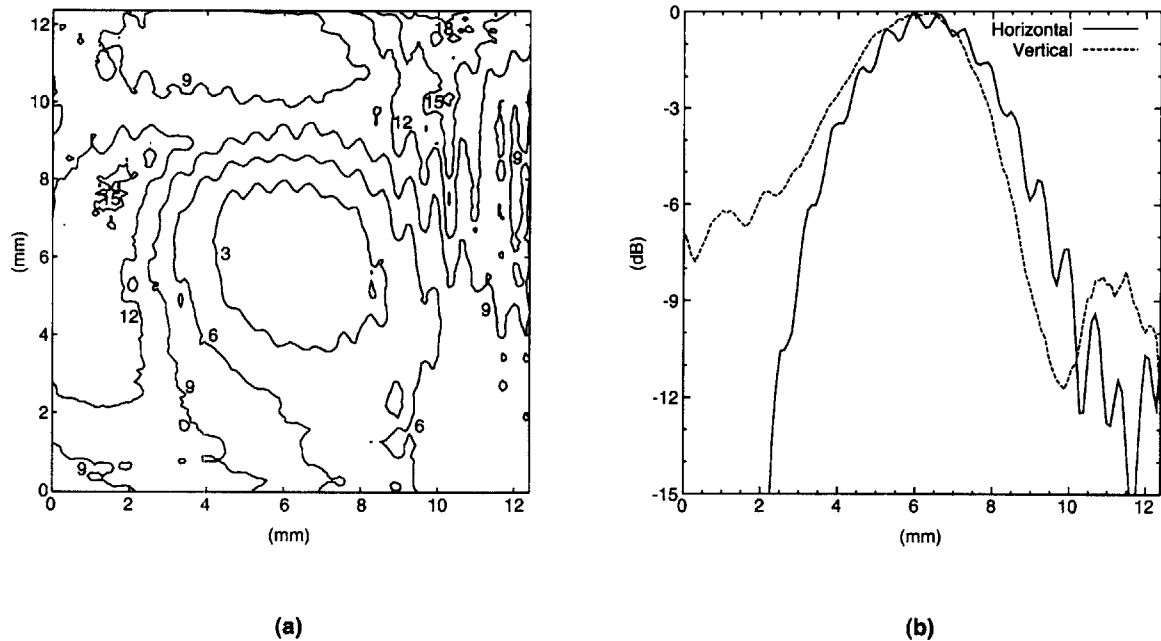


Figure 5-39: Logarithmic radiation intensity pattern (in normalized dB) of the mode-converted  $TE_{0,6}$  mode captured by a pyroelectric camera (a) two dimensional (b) one dimensional in the horizontal and vertical dimensions at the peak.

measured was 1.0 dB/m for the acrylic tube. The unit losses for the G10 epoxyglass and canvas laminate were close, at 1.4 and 1.3 dB/m. This is likely because the dominating factor in the material composition and therefore the refractive index is the epoxy. The coupling losses measured were consistent for each material type, but inconsistent across the five materials. Further, the coupling loss for nylon was negative! It is not known what is the cause of this discrepancy, though it is conjectured that the effective radius may be different in the various dielectrics. The measurements were recorded with the waveguide centered on the window, and accordingly another possibility is that the gyrotron beam is not centered in the window.

Due to the nature of the extrusion of acrylic, it is manufactured with a thinner wall. The wall thickness for the acrylic waveguide was 3.18 mm, which was half of the wall thickness of all the other dielectric waveguides. With the 460 GHz freespace wavelength of 0.65 mm, the wall thickness of 3.18 mm is approximately five wavelengths whereas the wall thickness of 6.35 is nearly ten wavelengths. Of course, the number of wavelengths increases in a dielectric material.

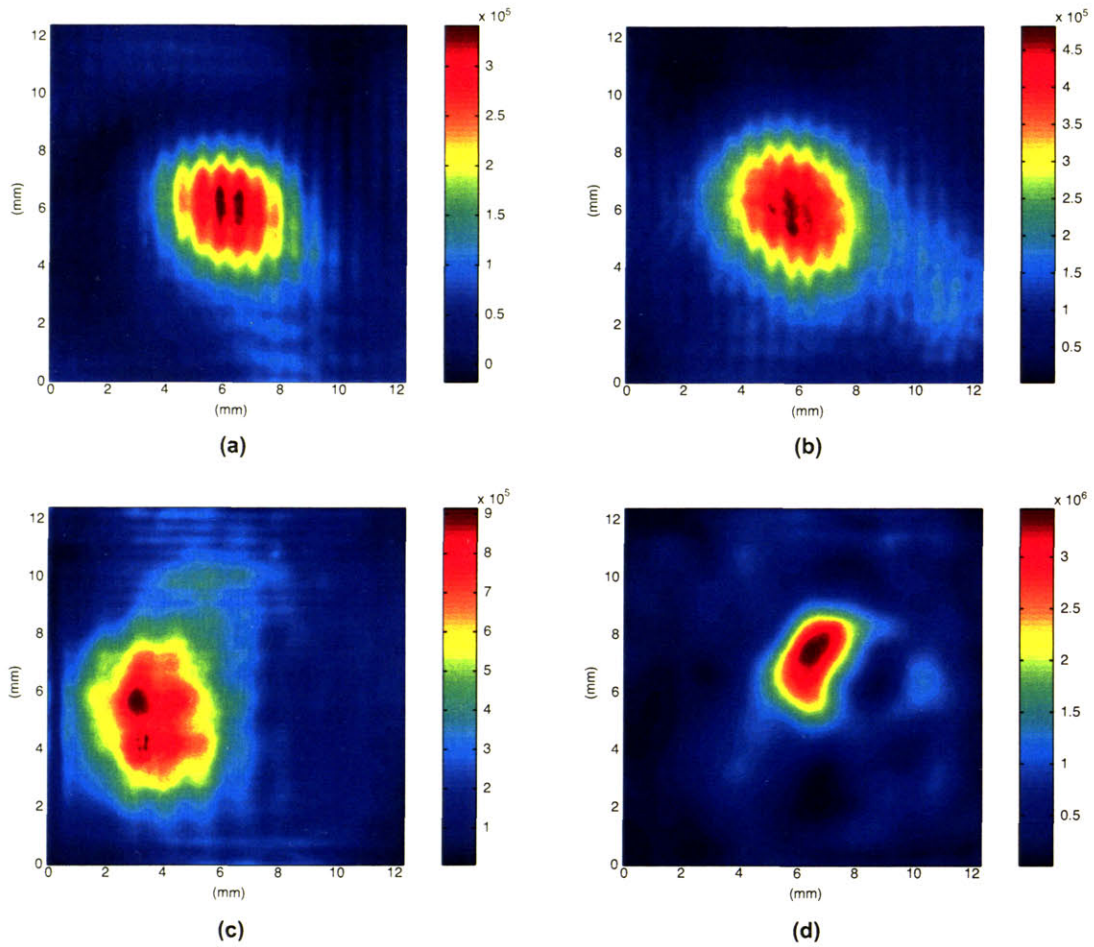


Figure 5-40: Linear radiation intensity patterns of the mode-converted (a)  $TE_{0,6}$  (b)  $TE_{2,6}$  (c)  $TE_{2,3}$  and (d)  $TE_{2,2}$  modes captured by a pyroelectric camera.

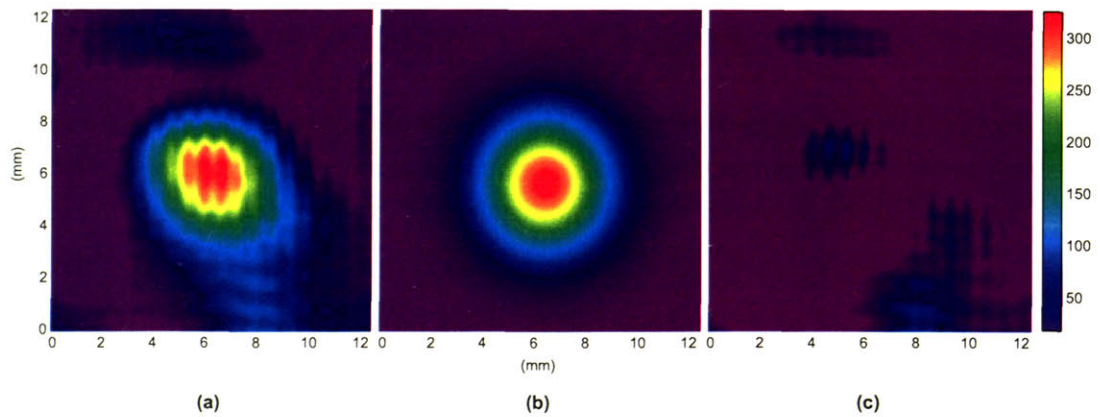


Figure 5-41: Linear radiation intensity pattern of the mode-converted  $TE_{0,6}$  mode (a) smoothed data captured by a pyroelectric camera (b) Gaussian fit (c) difference between experiment and fit.

Table 5.10: Beam waists of the mode converted radiation fields from Fig. 5-40 as calculated by the best fit Gaussian

TE <sub><i>m,p</i></sub> mode	Frequency (GHz)	<i>x</i> waist (mm)	<i>y</i> waist (mm)	Ellipticity ( <i>y/x</i> )	Ellipticity (%)
TE <sub>0,6</sub>	459	4.697 ± 0.038	4.911 ± 0.040	1.045	4.3
TE <sub>2,6</sub>	456	6.423 ± 0.028	5.630 ± 0.024	0.876	12.3
TE <sub>2,3</sub>	233	5.246 ± 0.020	6.597 ± 0.025	1.257	20.5
TE <sub>2,2</sub>	157	2.997 ± 0.017	3.814 ± 0.022	1.273	21.4

### 5.2.8 Radiation Patterns

The transmission of the microwave beam begins with the quasi-optical mode converter. The quasi-optical mode converter consists of a cylindrical waveguide with a step cut and a cylindrical focussing mirror. The waveguide antenna converts the higher order transverse electric gyrotron output into a linearly polarized beam and the focussing mirror collimates it.

Using the Pyrocam described in Section 3.1.3, we measured the output field intensity of several frequencies corresponding to the converted TE<sub>0,6</sub>, TE<sub>2,6</sub>, TE<sub>2,3</sub>, and TE<sub>2,2</sub> modes at the mouth of a 2.54 cm inner diameter dielectric epoxyglass waveguide. Figure 5-40 shows the four intensity patterns on a linear scale. The mode converter works well for TE<sub>*m,p*</sub> modes where  $m \ll p$ . In Fig. 5-40, the TE<sub>0,6</sub> and TE<sub>2,6</sub> modes have been converted fairly well into Gaussian beams, while the TE<sub>2,3</sub> and TE<sub>2,2</sub> modes have not. Table 5.10 shows the beam waists of the four modes as calculated by a best-fit Gaussian with 95% confidence interval.

The TE<sub>0,6</sub> mode-converted beam is displayed in Fig. 5-39 with a normalized logarithmic scale. At 460 GHz, a Gaussian fit (*c.f.* Fig. 5-41(b)) determined that the measured beam is slightly elliptical with a waist size in *y* of  $4.911 \pm 0.040$  mm and a waist size in *x* of  $4.697 \pm 0.038$  mm, where the beam waist is given by  $1/e^2$  from the maximum intensity or -8.7 dB.

A rectangular grid diffraction pattern is observed on the high frequency (233–460 GHz) intensity patterns (*c.f.* Figs. 5-40(a)-(c)) that is not observed on a lower (157 GHz) frequency (*c.f.* Fig. 5-40(d)) intensity pattern. A diffraction pattern was also observed in a 70 mJ, CO<sub>2</sub> (10.6 μm) laser beam at CERN using a Spiricon Pyrocam [121]. The spacing of the elements in the pyroelectric array is 100 μm, which may cause interference with the wavelengths in the hundreds of microns; the 460 GHz wavelength is 650 μm. Another possibility suggested by Spiricon [90] is the lack of an anti-reflection coated window on the Pyrocam III. A polyethylene window is used on

our Pyrocam. The Pyrocam III's window protects it against foreign objects entering the camera and thereby destroying the crystal in addition to providing protection to the sensor from the effects of humidity. The window requires an anti-reflection coating, else the two surfaces of the window will create interference fringes from a collimated light source which manifest themselves on the sensor as ripples in the beam.

## 5.2.9 Stability

The stability of the  $TE_{0,6}$  second harmonic and  $TE_{2,3}$  fundamental operation of the 460 GHz gyrotron was monitored for a period of one hour during which the gyrotron ran in complete CW mode. During this period, the power was held constant by proportional, integral, and derivative adjustments to the filament current. The output power was monitored by either a diode or laser calorimeter. In the case of the diode, the output power was referenced at the start and finish of the monitoring period with a calorimeter. All aspects of the experiment were monitored by the computerized control system and logged. These parameters include (but are not limited to) the power, pressure, beam voltage and current, filament current, and gun coil current.

A summary of the  $TE_{0,6}$  second harmonic results is shown in Fig. 5-42. A statistical analysis of excursions of the 458 GHz power signal from its setpoint over the hour long experiment using a diode for feedback, shown in Fig. 5-44, shows that power fluctuations are normally distributed and that the tolerances of the DNP experiment are met by the control system. Notably, the power was stable to 0.4% over the hour long period using feedback from either a diode or calorimeter. The pressure in both cases was low, but finally increasing with time. The increase in pressure was directly related to the increase in beam current required to maintain the constant output power. An increase in the electron gun ceramic compressed air pressure from 8 to 18 psi between the two separate hour duration stability tests at 460 GHz correlates with a reduction in the beam power increase over the hour long period from 36% to 23%. A summary of the fundamental  $TE_{2,3}$  results is shown in Fig. 5-43. Notably, the power was stable to within 0.2% over the hour long period using feedback from a diode. A summary of all stability results on the 460 GHz gyrotron are shown in Table 5.11.

In the fundamental case, the unregulated gun parameters, namely the filament current and beam current, did not change nearly as much as they did in the second harmonic case. While the rf output powers were comparable for both the fundamental and second harmonic controlled runs, their beam powers were widely differing by a factor of 20; where a beam power of 70 W was used for the fundamental, 1.4 kW



Table 5.11: Stability of the second harmonic  $TE_{0,6}$  and fundamental  $TE_{2,3}$  modes in the 460 GHz gyrotron

	$TE_{0,6}$ (diode)		$TE_{0,6}$ (calorimeter)		$TE_{2,3}$ (diode)	
	Avg.	Std. dev. (%)	Avg.	Std. dev. (%)	Avg.	Std. dev. (%)
Power (W)	3.76	0.35	3.13	0.42	4.69	0.19
Pressure ( $\times 10^{-8}$ Torr)	4.34	3.38	3.80	1.69	1.21	1.75
Beam voltage (kV)	12.40	0.02	12.40	0.02	3.50	0.04
Filament current (A)	2.55	1.03	2.52	0.65	2.36	0.26
Beam current (mA)	118.99	8.61	111.07	6.09	19.66	2.72
Gun coil current (A)	2.54	0.04	2.54	0.07	24.63	0.01

of beam power was used for the second harmonic. It is likely that the increase in beam current required to maintain a constant second harmonic output power is an effect due to the overheating of a component in the gyrotron. The temperature of the cavity was constant over the hour-long period and the frequency was unchanged, ruling out a thermal expansion of the cavity in a twofold manner. The other obvious gyrotron component that could be responsible for these effects is the electron gun. The ceramic break is the only component in the electron gun which is cooled in the present configuration, and this is achieved with low pressure compressed air. As noted previously, there was a strong correlation between increasing the air pressure with increased stability. In addition, while there are provisions for liquid cooling of the anode, the coolant channel remained unconnected in the present configuration.

### 5.3 Low Power $Q$ Measurements of the 460 GHz Cavity

Since conditioning a gyrotron can be a lengthy process, in order to minimize changes to the gyrotron's structure after fabrication and assembly, testing of all components before assembly is imperative. Most important of all components in the gyrotron is the interaction cavity, the structure that defines the generation of the microwaves. In order to verify that the gyrotron cavity functions as per design, we designed a low power test to measure the  $Q$  of the cavity at a mode which falls in the frequency range where we have an available broadband source. If the cavity resonates at the frequency of this mode with the appropriate  $Q$ , we can extrapolate that the cavity

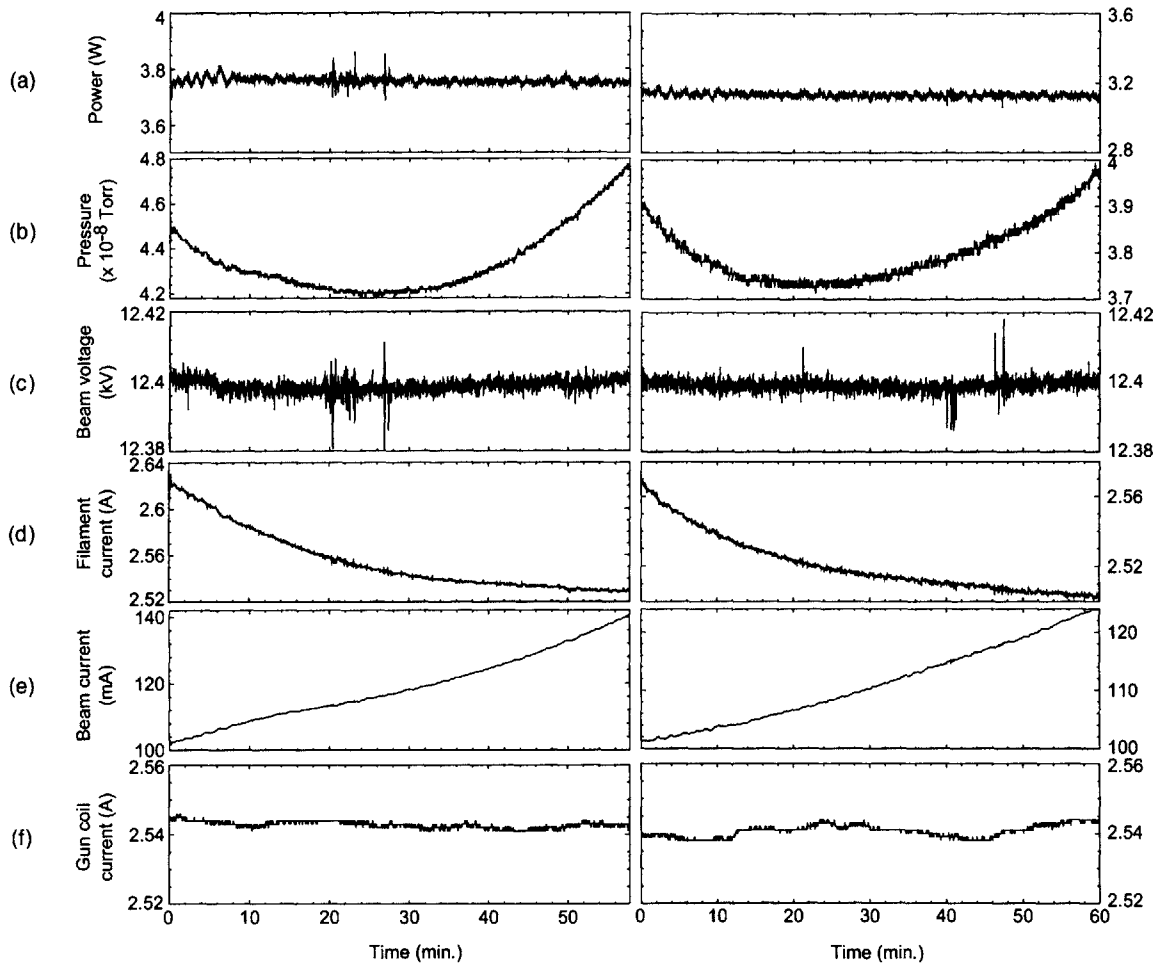


Figure 5-42: Two separate one hour duration stability tests of the (a) power, (b) pressure, (c) beam voltage, (d) heater current, (e) beam current, and (f) gun coil current for the  $TE_{0,6}$  second harmonic mode at 458 GHz using a diode (left) and calorimeter (right) to monitor the output power.

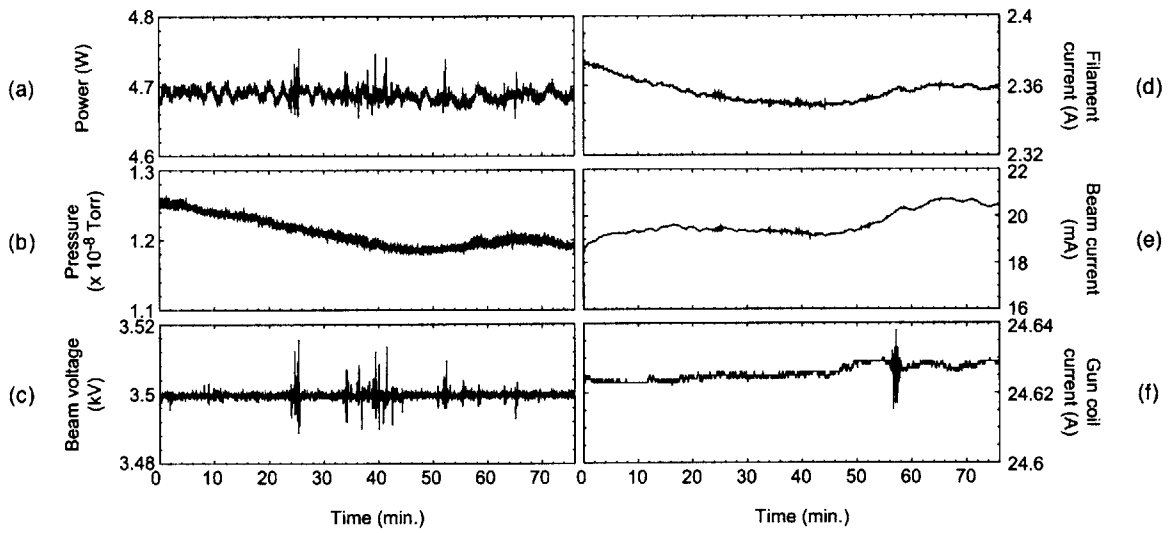


Figure 5-43: Stability of the (a) power, (b) pressure, (c) beam voltage, (d) heater current, (e) beam current, and (f) gun coil current over the period of one hour for the  $TE_{2,3}$  fundamental mode at 233 GHz using a diode to monitor the output power.

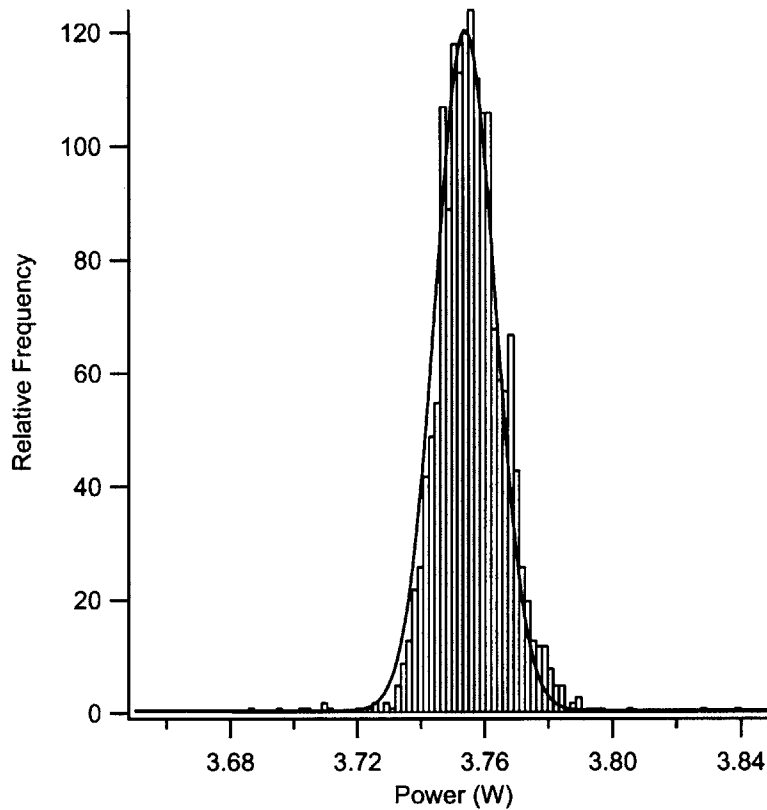


Figure 5-44: Statistical analysis of power fluctuations from setpoint for the diode controlled  $TE_{0,6}$  hour long run. The solid line is a Gaussian fit to the data.

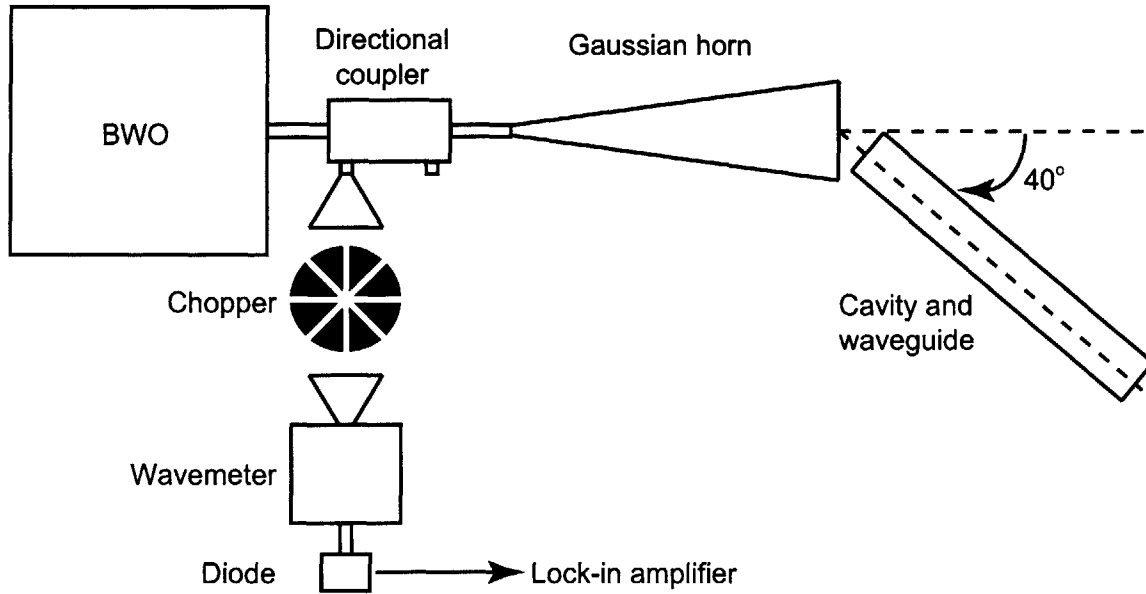


Figure 5-45: Arrangement of equipment for the 460 GHz cavity  $Q$  measurements.

Table 5.12: Cold test data and cold cavity simulation parameters of the  $TE_{0,2,q}$  and  $TE_{2,2,q}$  cavity modes.

Mode	Cold cavity		Experiment	
	Frequency (GHz)	$Q$	Frequency (GHz)	$Q$
$TE_{0,2,1}$	164.121	2,600	163.938	1,425
$TE_{0,2,2}$	164.459	630	–	–
$TE_{2,2,1}$	156.891	2,320	–	–
$TE_{2,2,2}$	157.245	590	157.218	786

will also function as per design at 460 GHz.

Figure 5-45 is an illustration of the experimental set-up used for cold test measurements. The backward wave oscillator (Insight Product Company, Model No. IPG-140-178) has the capability of tuning over a wide band from 113 to 173 GHz and is described in more detail in Sec. 3.1.8. The BWO output is in the rectangular  $TE_{1,0}$  mode. In our configuration, the source is connected to a directional coupler followed by a Gaussian horn, which converts the radiation into the quasi-Gaussian  $HE_{1,1}$  mode. This is then radiated into freespace in reverse through the cavity setup at the bounce angle  $\theta$  ( $= \tan^{-1}(k_{\perp}/k_z) = 40^\circ$ ) into the cylindrical focus mirror, waveguide, and finally into the cavity. The reflected signal from the -3 dB directional coupler is optically chopped at 100 Hz and recorded through a WR-6 (110–170 GHz) broadband detector diode (Pacific Millimeter, Model No. DD) and lock-in amplifier

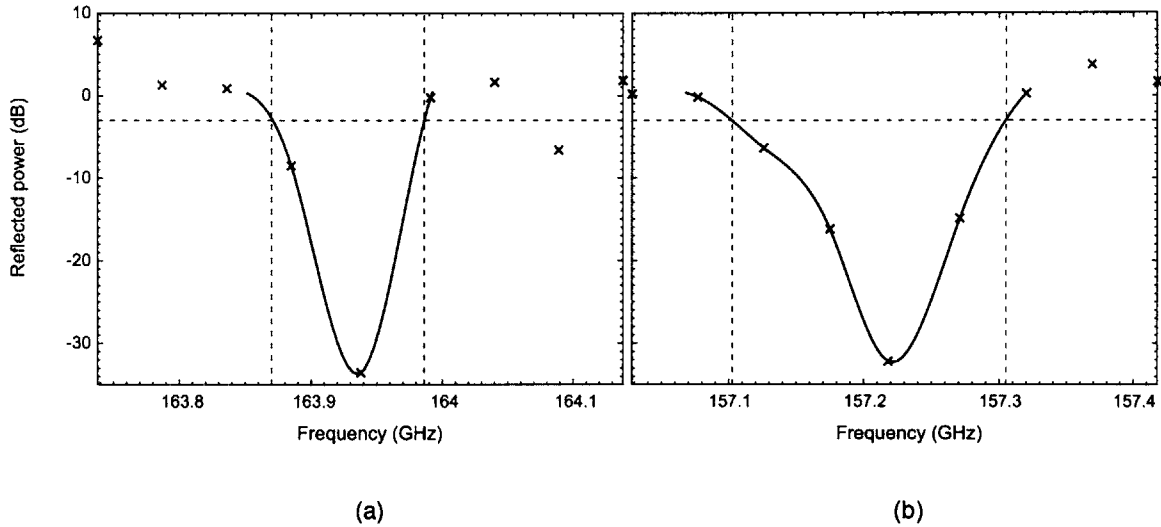


Figure 5-46: Measurement of a high  $Q$  mode around (a) 163.9 GHz (b) 157.2 GHz.

(Stanford Research Systems, Model No. SR830). The frequency is measured with a wavemeter, which has been calibrated against the frequency system. The frequency system (similar to the one described in Sec. 3.1.1) utilizes a local oscillator (LO) that spans 8 – 18 GHz. For these frequency measurements, the tenth harmonic of the LO is used. The diode signal obtained on the lock-in amplifier is normalized by a reference signal obtained by reflecting all power of the BWO by placing a metal plate over the Gaussian horn to filter out drift in the source.

Design and simulations of the 460 GHz gyrotron cavity were performed with the cold cavity code [65] which solves for the eigenmodes of a cold (beam absent) gyrotron cavity. The cylindrical interaction cavity is 2 cm long, has a radius of 2 mm, and ends in three tapers. The simulations were performed for the  $TE_{0,2,q}$  and  $TE_{2,2,q}$  modes around 156 to 165 GHz for  $q = 1$  and 2. The relevant cold cavity simulation parameters, the frequency and  $Q$ , are shown in Table 5.12.

Cavity modes measured around 163.9 GHz and 157.2 GHz with the described setup are depicted in Fig. 5-46. The FWHM of the mode at 157.218 GHz is 200 MHz yielding a total  $Q$  ( $= \text{FWHM}/f$ ) equal to 786. The FWHM of the mode at 163.938 GHz is 115 MHz yielding a total  $Q$  equal to 1,425. These modes can likely be identified as the  $TE_{2,2,2}$  and  $TE_{0,2,1}$  modes as seen in Table 5.12. Both the  $Q$  measurements and the frequencies of the two cold tested modes match reasonably well with the cold cavity theory.

## 5.4 Discussion

The 460 GHz experiment has successfully demonstrated that a gyrotron can efficiently produce several watts of average power at the second electron cyclotron harmonic in submillimeter wavelengths at low voltage. The efficiency of the gyrotron was verified with measurements of the cavity ohmic losses which also confirmed the ratio of diffractive to ohmic  $Q$ . The stability characteristics were studied over the duration of an hour, and demonstrated that the output power could be maintained to 0.4% under computer control. The limiting factor in operating at longer periods of time is likely the overheating of the electron gun. An existing anode cooling channel which was unused in the present experiments simply needs to be connected to the output water path of the cavity. Frequency pulling measurements determined that the stability of the frequency with respect to the beam voltage, beam current, and magnetic field drift was sufficient for DNP. The feasibility of various hollow dielectric waveguides for use in the transmission line was studied. With the lowest loss at 460 GHz of at least 1.0 dB/m for acrylic tubing, sections of the waveguide would only be useful over short distances in conjunction with the main transmission occurring in corrugated waveguide. The radiation pattern of the second harmonic design mode at 460 GHz shows that the beam is Gaussian with a 4% ellipticity and that the mode converter works reasonably well for several other observed second harmonic and fundamental modes.

Continuous broadband frequency tuning of the gyro-oscillator over a range of 2 GHz has been demonstrated in the fundamental modes, and we have presented non-linear and linear analyses of the results. Due to the inhomogeneous frequency dispersion of the interactions responsible for dynamic nuclear polarization effects in paramagnetically doped solids, either the microwave source frequency or the static magnetic field in the NMR spectrometer must be varied over a broad range to optimize the DNP experiment. Performing the latter presently requires the modification of high homogeneity superconducting magnets in the 9–16 T range to incorporate a magnetic sweep coil. Future gyro-oscillator designs which could exploit the broad tunability features described here might eliminate this complication of the experiment and extend applicability of DNP to any NMR spectrometer while still preserving the advantages of simple, low-voltage, CW operation.

The fundamental  $TE_{2,3}$  mode was excited with ultra low beam power, at an extremely low voltage below 3.5 kV while oscillations started with 2 mA of beam current. Axial mode competition was studied in this mode in the CW experiment. Homodyne measurements, confirmed by nonlinear analyses, demonstrate the presence of simultaneous axial modes, while heterodyne measurements show that one mode dominates

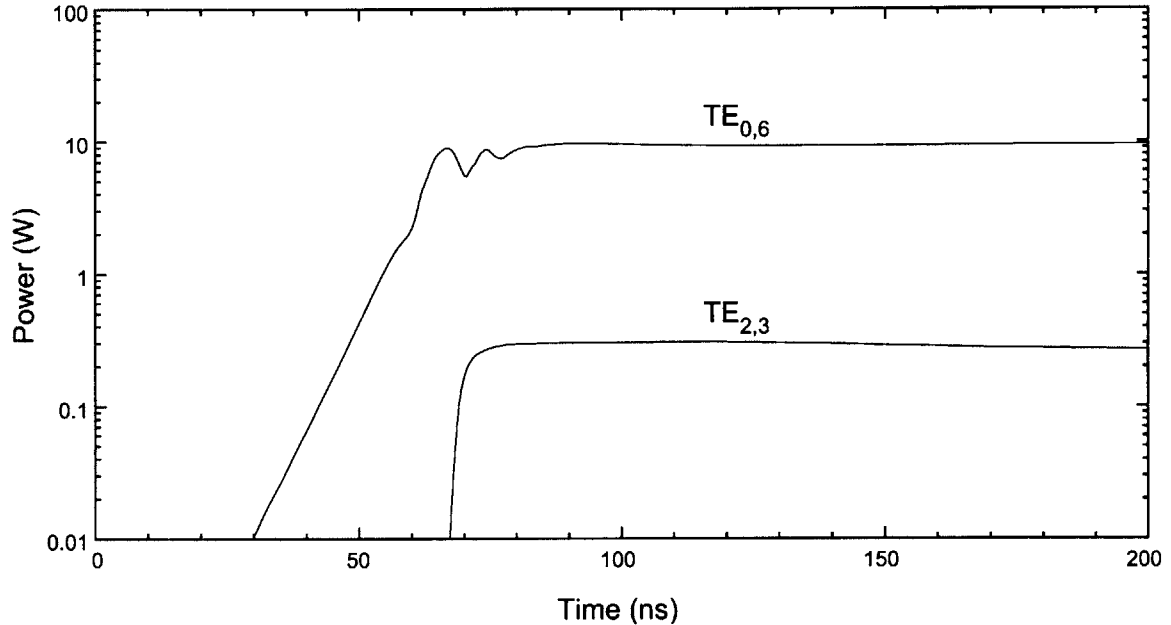


Figure 5-47: MAGY run at 13.1 kV, 100 mA, and 8.39 T showing mode cooperation between the  $TE_{0,6}$  and  $TE_{2,3}$  modes effectively lowers the starting current of the  $TE_{2,3}$  fundamental mode due to pre-bunching of the beam by the  $TE_{0,6}$  second harmonic mode.

the other by several orders of magnitude.

In initial short pulse experimental studies of the second harmonic  $TE_{0,6}$  design mode, we observed that the  $TE_{2,6}$  second harmonic mode was experimentally easier to quantify due to possible contamination of the  $TE_{0,6}$  design mode with the fundamental contrasted with the added isolation of the  $TE_{2,6}$  mode. However, in this regime, linear theory predicts a very high starting current for the fundamental  $TE_{2,3}$  mode. In order to explain these results, we used MAGY to simulate the beam-wave dynamics. First, in agreement with linear theory, MAGY predicts a starting current in single  $TE_{2,3}$  mode simulations which is well above the parameters of our experiment. In multifrequency, multimode simulations, however, the  $TE_{2,3}$  mode always oscillates with the  $TE_{0,6}$  second harmonic mode in a manner which suggests that excitation of the second harmonic mode is lowering the starting current for the fundamental mode. The calculated time evolution of RF power in the  $TE_{0,6}$  and  $TE_{2,3}$  modes (*c.f.* Fig. 5-47) shows that the  $TE_{2,3}$  mode amplitude is near zero until the second harmonic  $TE_{0,6}$  mode amplitude nears its steady-state value. Even after the fundamental mode begins to oscillate, its amplitude is so low that it may be below the threshold of detection. We believe this may be an example of mode cooperation, which has been treated theoretically [116, 122] and observed experimentally [109], and arises in this case due to favorable prebunching of the beam by its interaction at the second harmonic. The

contamination by the undesirable fundamental mode implies that the  $TE_{2,6}$  second harmonic mode might be preferred over the design mode. However, previous studies have concluded that such mode competition effects are sensitive to the beam start-up scenario, while all our simulations correspond to the sudden start-up case [123]. In CW operation, competition between the fundamental modes and the second harmonic design mode was not observed therefore it is likely that the observed effect was not mode competition but rather excitation of the fundamental mode during the rising and falling edge of the pulse.



## Chapter 6

# 250 GHz Gyrotron Experiments

*The results in the first two sections of this chapter are adapted from a manuscript: V.S. Bajaj, M.K. Hornstein, K.E. Kreisler, P.P. Woskov, R.J. Temkin, and R.G. Griffin. A long-term, stable, CW 250 GHz gyrotron with low second harmonic starting currents [92].*

The 250 GHz gyrotron is the critical component in performing the highest frequency dynamic nuclear polarization (DNP) experiments to date and is used in conjunction with a 380 MHz NMR spectrometer. The 250 GHz gyrotron was designed by Kreisler et al. [40] and is more fully described in [124]. Figure 6-1 shows an aerial photograph of the 250 GHz gyrotron, corrugated transmission system, and 380 MHz NMR magnet. In the center of the photograph, the beam splitter which allows for sampling of the power in the overmoded corrugated waveguide is visible. The beam splitter is shown in more detail in Fig. 6-2 and is discussed in Section 6.3.

Using the gyrotron, enhancements of nuclear spin polarization by dynamic nuclear polarization in static and spinning solids at a magnetic field strength of 9 T (250 GHz for  $g=2$  electrons, 380 MHz for  $^1\text{H}$ ) have been achieved [27]. Enhancements in these experiments can be summarized as follows;  $^1\text{H}$  enhancements of up to  $170\pm 50$  in  $1\text{-}^{13}\text{C}$ -glycine dispersed in a 60:40 glycerol/water matrix at temperatures of 20 K; significant enhancements in  $^{15}\text{N}$  spectra of unoriented *pf1*-bacteriophage; and enhancements on the order of 17 in two-dimensional  $^{13}\text{C}$ - $^{13}\text{C}$  chemical shift correlation spectra of the amino acid U- $^{13}\text{C}$ ,  $^{15}\text{N}$ -proline during magic angle spinning (MAS).

The 250 GHz gyrotron was examined in detail for four main purposes; to ascertain its operating characteristics, to observe and control its stability, to find second harmonic modes, and to increase its efficiency, three of which are important qualities for DNP. Section 6.1 describes the operating characteristics of the gyrotron and also details the stability of the gyrotron. Notably, the gyrotron has operated for more than 10 days under computerized control during DNP experiments. To determine

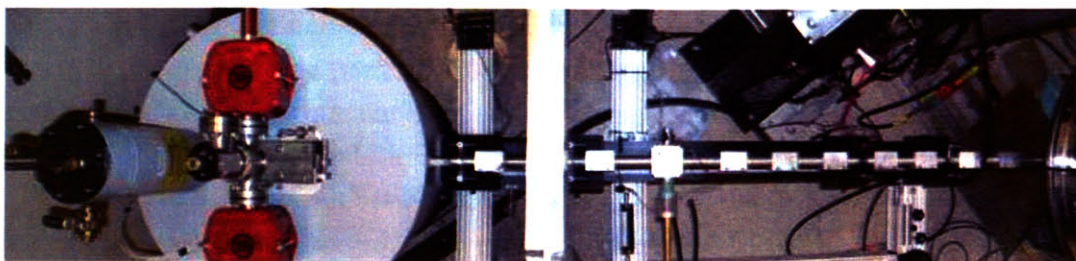


Figure 6-1: Aerial photograph of the 250 GHz gyrotron, corrugated transmission system, and 380 MHz NMR magnet.

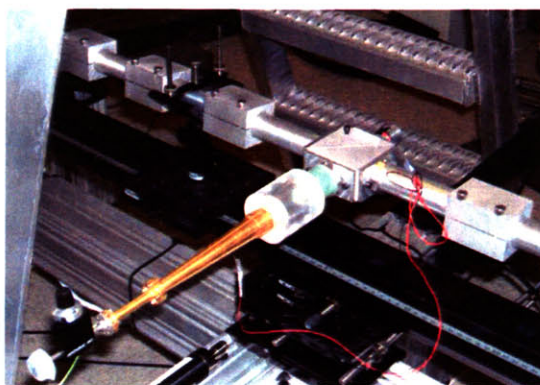


Figure 6-2: Photograph of the 250 GHz quasi-optical directional coupler.

the viability of designing a second harmonic gyrotron at 460 GHz, an experiment was conducted to search for the operating parameters of similar high frequency second harmonic modes in the 250 GHz gyrotron. Section 6.2 analyzes the low starting currents observed in the resulting search. In Section 6.3, we describe how we increased the efficiency of the gyrotron by implementing a corrugated waveguide transmission system with quasi-optical coupling to monitor the forward and reflected power and frequency. Due to a steady increase in the gyrotron output power under constant current regulation, active monitoring of the power is required as an input to the control system.

## 6.1 Characterization of the 250 GHz Gyrotron

While a number of experimental variables can influence the stability of DNP experiments, the stability requirements of the microwave signal for the application of dynamic nuclear polarization to quantitative measurements of internuclear distances and torsion angles are at most several percent. Since the stability of the gyrotron output power under these conditions has never been tested, it is important to bench-

mark its performance. This section summarizes the operational status and operating parameters of the 250 GHz DNP gyrotron under a variety of test conditions. The gyrotron was operated in CW mode for most of the measurements. The tests explore the output power, frequency, linewidth, intensity pattern, and stability of the output power over sustained operation. The results demonstrate that the requirements for DNP can indeed be met and that the gyrotron can be safely operated for times greater than 10 days, and that the power variation with feedback control can be maintained to less than 1%.

### 6.1.1 $TE_{0,3}$ Operating Mode

The 250 GHz gyrotron is normally operated in the  $TE_{0,3,2}$  mode at 12.2 kV and 21 mA. This can be explained by the simple fact that the NMR frequency is matched to the gyrotron frequency when the longitudinal mode with two variations is chosen over the  $TE_{0,3,1}$  longitudinal mode with one variation (*c.f.* Fig. 6-3). In addition, it also has a low start oscillation current and generates a sufficient amount of output power (*c.f.* Fig. 6-4) for DNP.

Figure 6-4 depicts the variation of the output power of the  $TE_{0,3,2}$  operating mode with beam current, which can be regulated by proportional control implemented in software. The power in the operating mode was measured using the Scientech calorimeter described in Chapter 3. The magnetic field value corresponds to the correct frequency for DNP experiments. At a beam voltage of 12.2 kV, the beam current was incremented manually in steps of 1 mA in the range from 10–26 mA through changes in the heater control voltage. The error was set to the average error of the other measurements. After oscillations begin at 10 mA, the result is an approximately linear correlation. A maximum CW output power of 7 W is achieved at beam parameters of 26 mA and 12.2 kV, yielding an efficiency of 2.2%. Even with the current controlled, the gyrotron output power is not constant over long periods of time, and so the calibration is strictly valid only in the initial stages of operation. Direct feedback on the gyrotron output power is discussed later.

In Fig. 6-3 the experimentally measured continuous duty power of the  $TE_{0,3,2}$  operating mode with varying magnetic field is compared with output frequency. The gyrotron should operate at a frequency of 250.5 GHz which corresponds to a proton frequency of 380 MHz. The operating magnetic field is determined by the optimum DNP enhancement which yields a point with a combination of optimal frequency and power. A sufficient amount of power is generated over a broad magnetic field range to allow a narrow amount of frequency tuning to be performed.

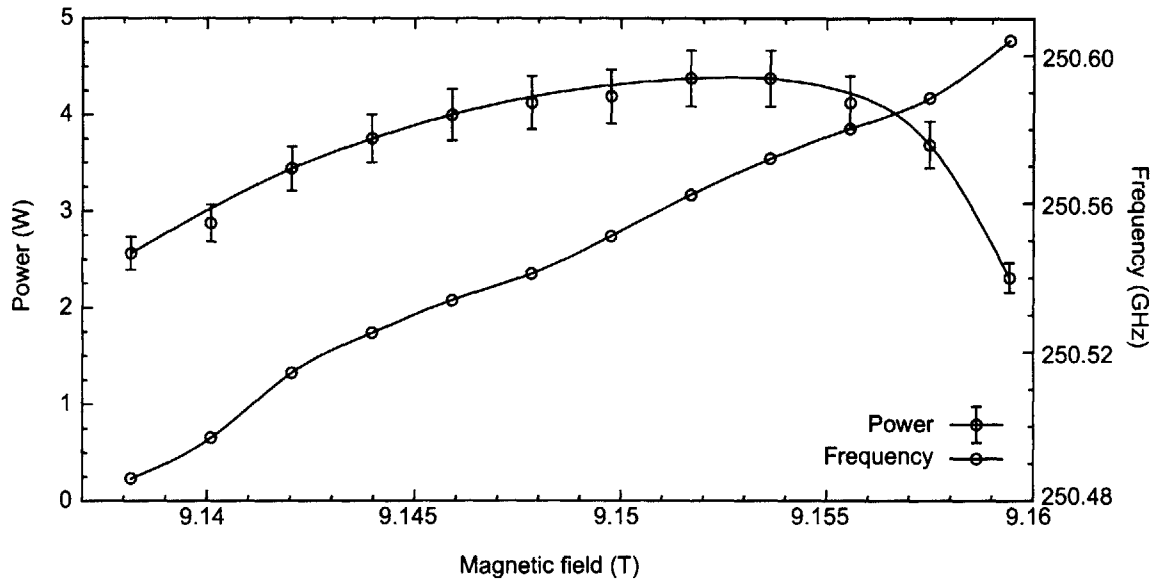


Figure 6-3: Frequency and power of the operating  $TE_{0,3,2}$  mode as a function of magnetic field.

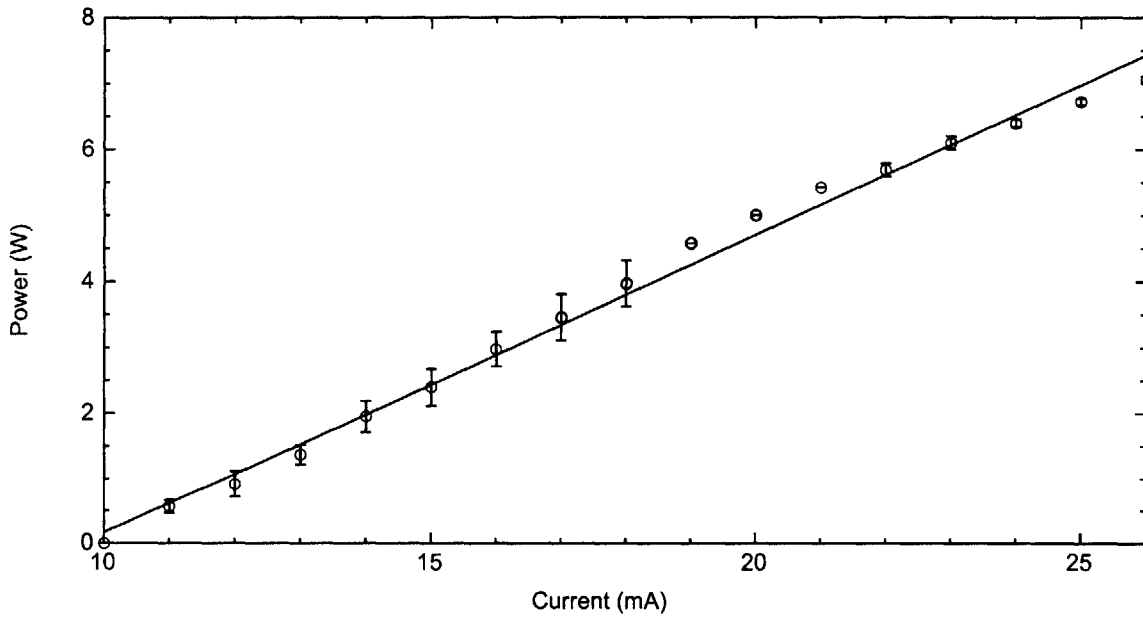


Figure 6-4: Power in the operating  $TE_{0,3,2}$  mode as a function of beam current.

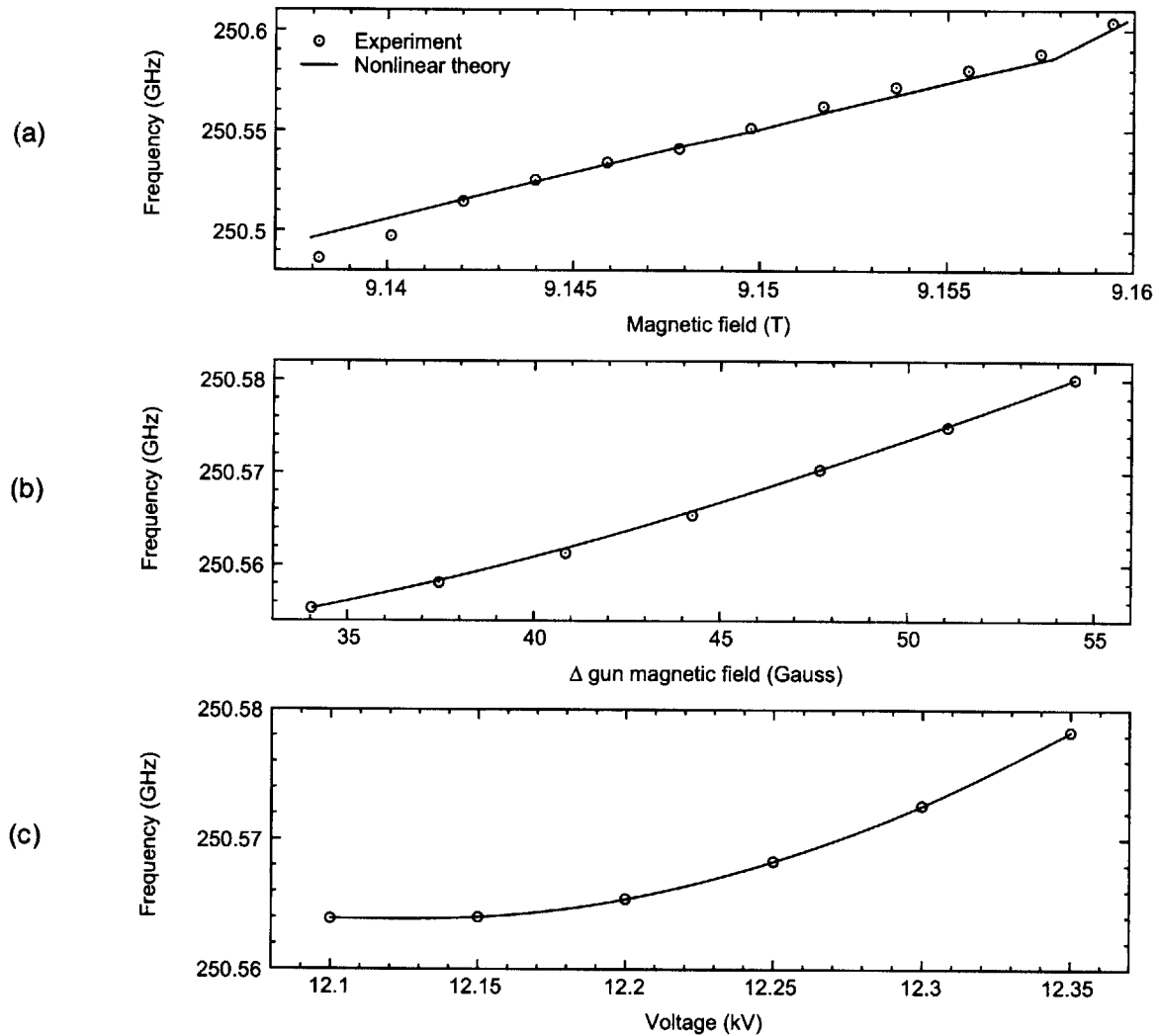


Figure 6-5: Frequency pulling of the operating  $TE_{0,3,2}$  mode by changing (a) the main magnetic field, (b) the gun magnetic field, and (c) the beam voltage.

## 6.1.2 Frequency Pulling

Frequency pulling can result from variation in the main or auxiliary magnetic fields, beam voltage, or beam current. This effect in gyrotrons has been observed and discussed in [18, 57, 125] and also in Section 5.2.3.

The measured frequency pulling characteristics of the 250 GHz gyrotron using the heterodyne frequency detection system (described in Sec. 3.1.1) in the operating  $TE_{0,3,2}$  mode are plotted in Fig. 6-5. The total frequency change observed is over 100 MHz. The frequency dependence on operating parameters is summarized in Table 6.1. Frequency pulling in the operating  $TE_{0,3,2}$  mode results from changing the main magnetic field by 0.02 T, the cathode magnetic field by 20 gauss, and the beam voltage by 250 V. Individually tuning the beam voltage and gun magnetic field resulted in 14

Table 6.1: Frequency dependence on operating parameters of the 250 GHz gyrotron in the  $TE_{0,3,2}$  operating mode

Parameter	Sensitivity
Magnetic field	5.3 GHz/T
Cathode magnetic field	12.3 GHz/T
Beam voltage	86 MHz/kV
Cavity temperature	< 1 MHz/°C

and 25 MHz of frequency tuning, respectively, while the main magnetic field yields the widest tunability of 118 MHz. This wide tunability is due to the use of the second longitudinal mode as the operating point. The operating frequency is also affected by the cavity temperature by less than 1 MHz/°C. A discussion of the frequency pulling effects at 460 GHz is located in Section 5.2.3.

### 6.1.3 Radiation Patterns

Radiation pattern measurements are an important diagnostic of a gyrotron. They can be used to deduce the functionality of internal components, such as a mode converter, and the measurements can be recorded at several planes to reconstruct the phase information. A Gaussian mode free of defects is critical to quasi-optical propagation and minimizing losses to the system. In our case, the beam is launched into free-space twice; first, the beam is launched into free-space internal to the gyrotron after the quasi-optical mode converter and second inside the DNP probe where the beam is focused and reflected into a vertical waveguide before it finally reaches the sample.

At 250 GHz, several techniques of measuring intensity patterns were compared. In this section, we consider a pyroelectric camera, thermal paper, and a quantitative technique utilizing liquid crystals that we have developed for millimeter waves. Previously, measurements of the beam at 250 GHz have been conducted with a mechanized scanner [124].

#### Liquid crystal

Liquid crystals can provide sub-micron resolution and temperature accurate to within a few degrees [126, 127]. In industry, 0.1 °C accuracy is obtainable from narrow-band (5 °C range) liquid crystals and 0.5 °C or better from broad-band ones. A combination of different ranges of liquid crystal sensitivity can provide good dynamic range. To recover the spatial power distribution numerically, the time-dependent change in color

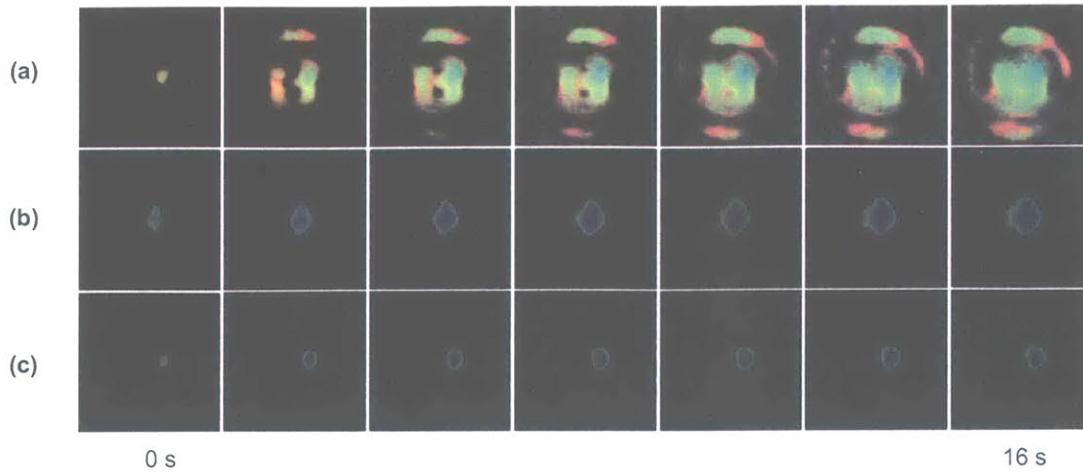


Figure 6-6: Intensity radiation pattern of the Gaussian output of the gyrotron operating in the  $TE_{0,3,2}$  mode as recorded by liquid crystal paper for (a) the gyrotron output and (b) and (c) after lengths of corrugated waveguide.

from the liquid crystal paper must be imaged, yielding the relative power at a given point. The color value (R,G,B) for each pixel is read as a function of time and converted to temperature. The results of several measurements in different dynamic ranges can be combined if necessary. The beam power can then be obtained from the rate of increase of the pixel temperature and the ambient temperature. Relative power measurements do not require the latter measurement. Liquid crystals have been previously used to qualitatively identify gyrotron radiation [128].

Liquid crystal measurements of the mode-converted  $TE_{0,3,2}$  mode were recorded over 16 seconds with a digital video camera from (a) the gyrotron output and (b) and (c) after two lengths of corrugated waveguide in Fig. 6-6. Since the liquid crystal sheet is nearly transparent to the electromagnetic radiation at 250 GHz, it only samples the radiation and therefore does not perturb the rf field profile in the waveguide or unconfined rf field profile. The colors of the liquid crystals change from black at the coldest through red and green with increasing temperature and finally reach indigo at the warmest. A unique (R,G,B) color corresponds to each temperature such that the temperature of the liquid crystals can be recovered through calibration. Continuous monitoring of the liquid crystal sheet via the digital video camera is essential to the measurement since the image is dynamic. While the power flow is normal to the liquid crystal sheet, the conductive heat transfer occurs in the surface of the sheet such that at steady state, the image will “bleed”. Through continuous monitoring of the image evolution, a video frame can be selected before steady state is established.

In this measurement, to eliminate reflected light we used an optical polarizing

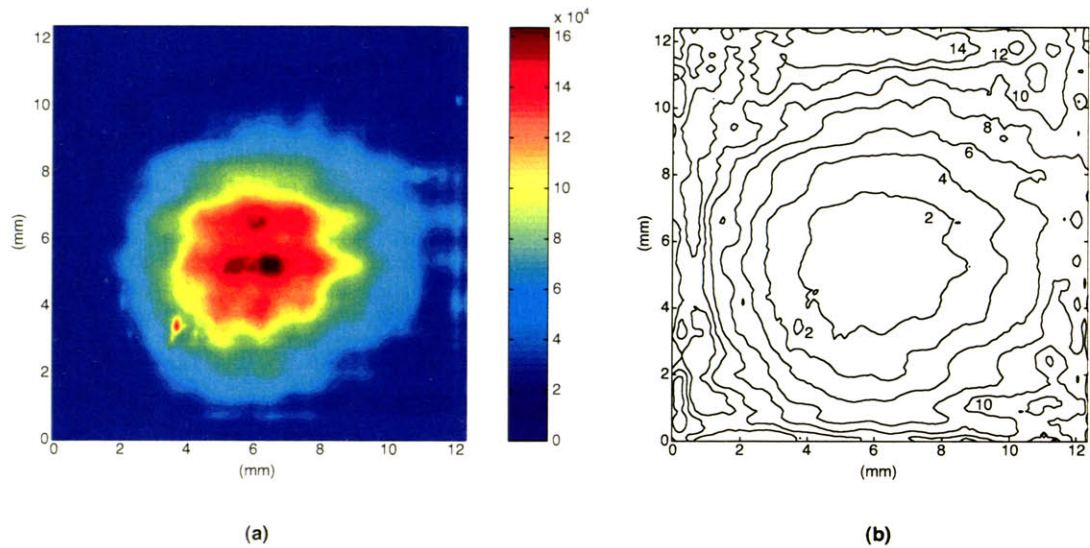


Figure 6-7: Intensity radiation pattern of the Gaussian output of the gyrotron operating  $TE_{0,3,2}$  mode as recorded by a pyroelectric camera (a) linear (b) logarithmic (normalized dB).

Table 6.2: Beam waist of the gyrotron output radiation field from the pyroelectric camera and liquid crystal method

	Liquid crystal	Pyroelectric	Theory
$x$ waist (mm)	$7.7 \pm 0.15$	$7.255 \pm 0.016$	6.99
$y$ waist (mm)	$7.0 \pm 0.1$	$6.605 \pm 0.015$	6.99
Ellipticity ( $y/x$ )	0.90	0.91	—
Ellipticity (%)	9.0	9.0	—

filter. The liquid crystals change the polarization of incident light. Thus, in a cross-polarized viewing system in which the incident light source is polarized (+) and there is a (-) viewing filter on the camera, then the only light that will reach the camera is that which has been reflected from the liquid crystals. This technique yields several orders of magnitude less noise and eliminates reflections to the video camera.

In Fig. 6-6(a), the gyrotron radiation is captured unguided, and it can be seen that the cross bore of the superconducting magnet provides some interference with the beam. Figures 6-6(b) and (c) show a small sidelobe which is also seen in the pyroelectric measurements.



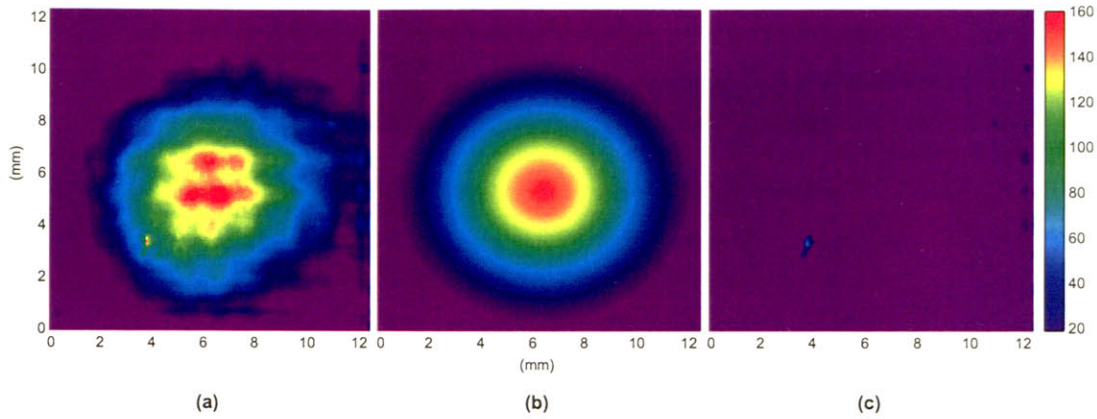


Figure 6-8: Linear radiation intensity pattern of (a) the mode-converted  $TE_{0,3}$  mode captured by a pyroelectric camera (b) Gaussian fit (c) difference between experiment and fit.

### Pyroelectric camera

A pyroelectric camera (Spiricon Pyrocamera III, Model No. PY-III-C-B, Serial No. 30507) was used to measure the radiation pattern of the mode-converted  $TE_{0,3,2}$  operating mode of the 250 GHz gyrotron with a beam current of 23 mA. Originally used as a laser beam diagnostic, here we present the first use at millimeter wavelengths of an array of pyroelectric elements. Such a technique has previously been used at Jefferson Lab in the terahertz regime [91]. The measurement, taken after a length of corrugated waveguide, is shown in Fig. 6-7 both in a linear and normalized logarithmic scale. The plots show a small sidelobe of -2 dB. At 250 GHz, a Gaussian fit (*c.f.* Fig. 6-8(c)) determined that the measured beam is slightly elliptical with a waist size in  $y$  of  $6.605 \pm 0.015$  mm and a waist size in  $x$  of  $7.255 \pm 0.016$  mm, where the beam waist is given by  $1/e^2$  from the maximum intensity or -8.7 dB. These results are summarized in Table 6.2.

The rectangular grid diffraction pattern observed on the intensity patterns is explained in Section 5.2.8.

### Thermal paper

Thermal paper is described in Section 3.1.3. Intensity patterns recorded with thermal paper are shown in Table 6.9 in Section 6.3.

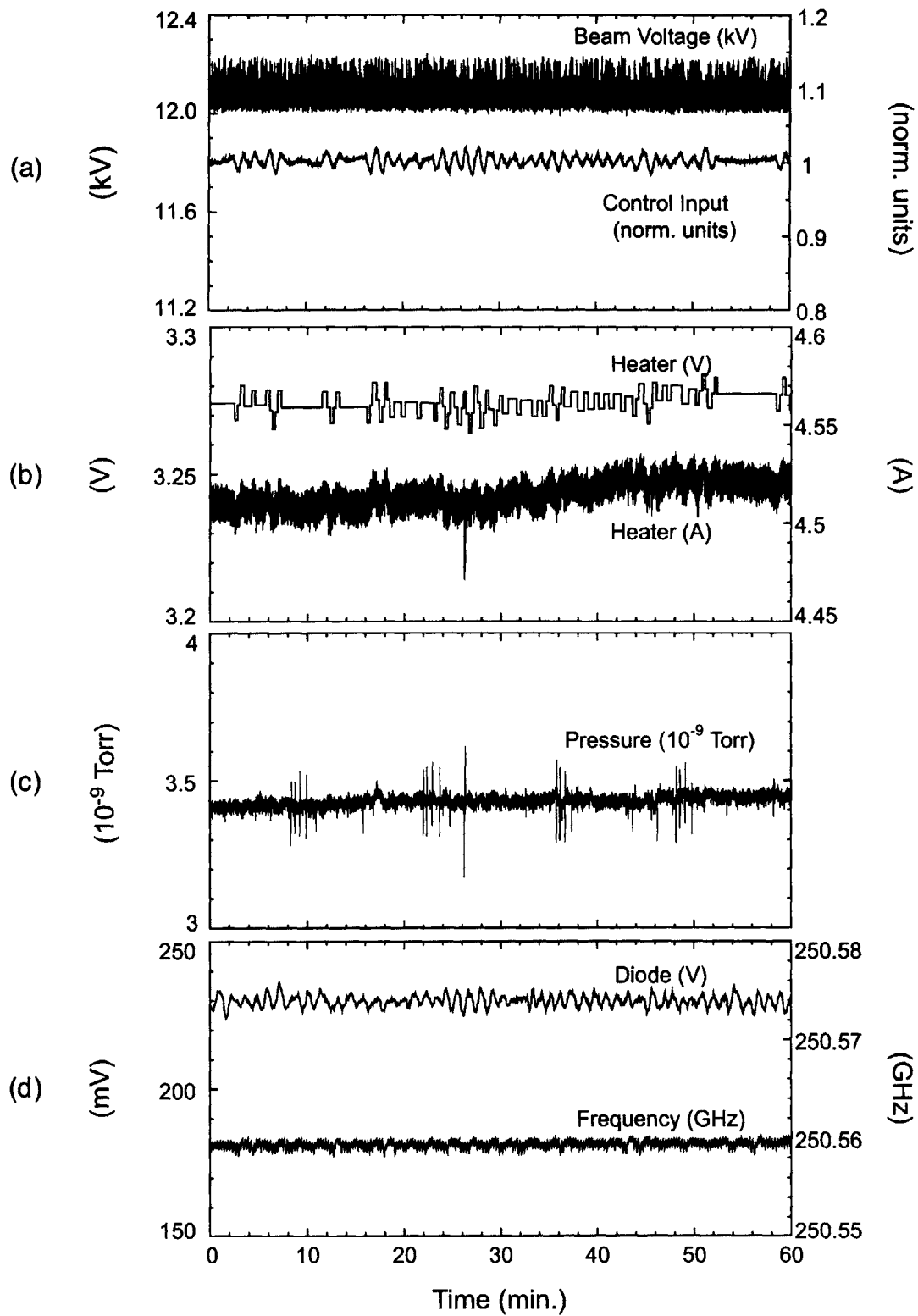


Figure 6-9: Stability of the  $TE_{0,3,2}$  operating mode over an hour of the (a) cathode voltage and beam current, (b) heater voltage and current, (c) pressure, and (d) power and frequency.

Table 6.3: Stability of the 250 GHz operating parameters

Technical parameter	Average value	Standard deviation	(%)
Filament voltage (V)	3.274	0.004	0.1
Filament current (A)	4.515	0.008	0.2
Beam voltage (kV)	12.090	0.047	0.4
Pressure ( $10^{-9}$ Torr)	3.430	0.019	0.5
Frequency (GHz)	250.559348	0.000359	0.000143
Diode (mV)	229.75	1.94	0.8

### 6.1.4 CW Long-term Stability and Control

The 250 GHz gyrotron has operated for more than 10 days continuously under computer control. Long-term stability of the gyrotron was monitored during a DNP experiment, where the gyrotron output power was monitored and controlled through the beam splitter and the gyrotron control system was modified to automatically record parameters of operation at regular intervals. A one hour period is representative of the fluctuations during this long-term operation, and as such is shown in Fig. 6-9. Stability of the operating parameters is summarized in Table 6.3. All parameters are stable to within one percent. Notably, the output power was stable within 0.8% (excluding initial and terminal phases). The frequency stability is discussed in Section 6.1.5.

#### Transient response

The output power is directly monitored and regulated by a PID controller which explicitly compensates for the transient response of the system. Figure 6-10 shows typical response curves for a sudden positive or negative step in the heater voltage (from 3.6 V to 3.7 V or vice versa). The pressure following a sudden or controlled shutdown is shown in Fig. 6-11. From these response curves, the optimal control parameters for a PID controller can be extracted using a variety of tuning rules. A Ziegler-Nichols analysis suggests a process dead time of  $57 \pm 8.5$  s and a maximum change in the detector voltage of  $(8.43 \pm 0.2) \times 10^{-9}$  V/s. Since the diode is operating in its linear range, the actual process rate is related to the detected rate by a scalar which can be estimated, on the basis of the calibration data, to be  $2.618 \pm 0.13$  W/ $\mu$ V. In practice, the parameters will have to be modified slightly to take into account the sampling rate of the digital controller and the precise integration method by which the integral correction is obtained. Also, it is clear from inspection of Figure 6-10

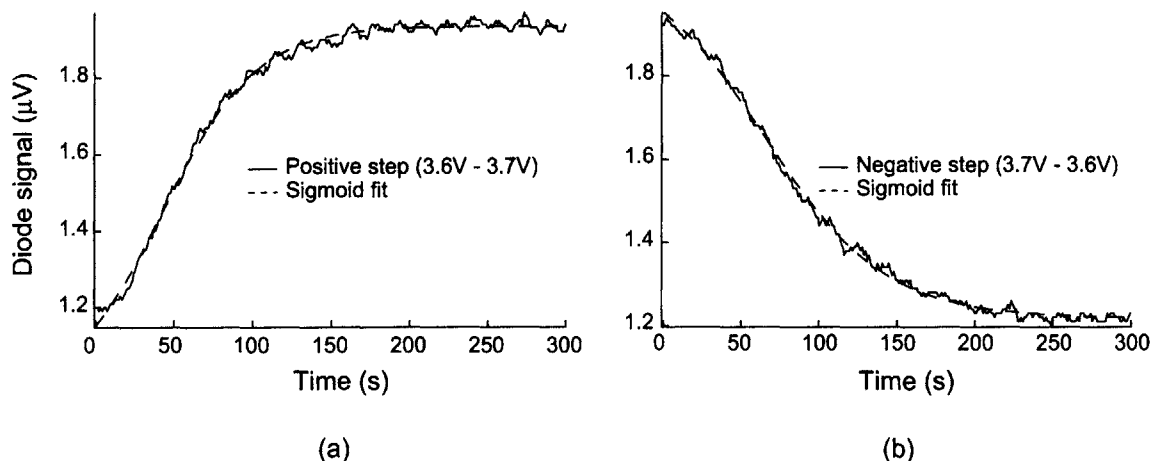


Figure 6-10: Representative transient response of the gyrotron to (a) positive and (b) negative step in the control voltage. The dashed line is a sigmoidal fit to the data from which optimal PID parameters were estimated. Note oscillations in the output power which persist even though the system is not under proportional regulation for these measurements.

that oscillations in the output signal persist even when the gyrotron is not under regulation of its output power. Thus, these oscillations do not arise from oscillatory control as originally suspected, but they must arise from some periodic noise in either the detection or the gyrotron power supplies. Fortunately, the time scale of these oscillations is such that it will not impact thermal mixing DNP experiments.

### 6.1.5 Linewidth

The radiation produced by the gyrotron has a finite linewidth which can be attributed to both natural and technical sources. The fluctuations of the technical parameters which dominate over the natural noise sources cause the broadening of the radiation linewidth in gyrotrons [129, 130]. Among these technical or operating parameters are the beam voltage, beam current, and external magnetic fields. In our case the technical noise is caused by the fluctuations of the high voltage, the filament, and the gun coil power supplies, and the pulsed nature of the recirculating chiller.

#### Heterodyne

The gyrotron linewidth in the  $TE_{0,3,2}$  operating mode was measured using the heterodyne receiver system described in Sec. 3.1.1. The linewidth of the gyrotron averaged over 32 shots is shown in Fig. 6-12. The linewidth is estimated at 300 kHz.

One of the reasons that the linewidth may be so broad is due to technical noise. Table 6.3 is a list of the average value, standard deviation, and percent deviation of

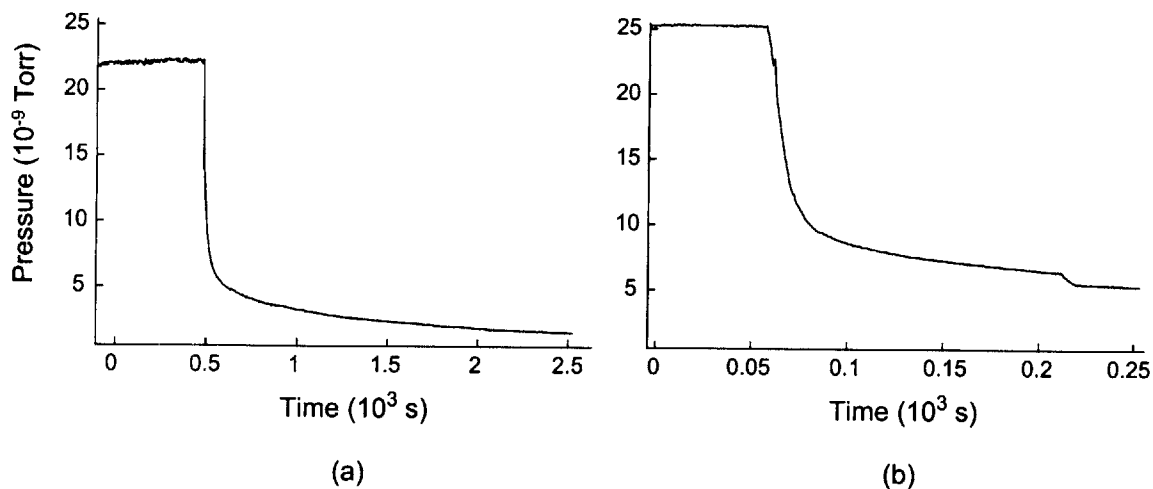


Figure 6-11: Response of the system to (a) sudden and (b) controlled termination of running power supplies. In (a), a power failure caused the accidental shutdown of the high voltage and heater supplies following three hours of CW operation, while, in (b), the high voltage output was gradually reduced over a period of 10–15 s, and the heater supply voltage was reduced over a period of thirty minutes, both following thirteen hours of CW operation.

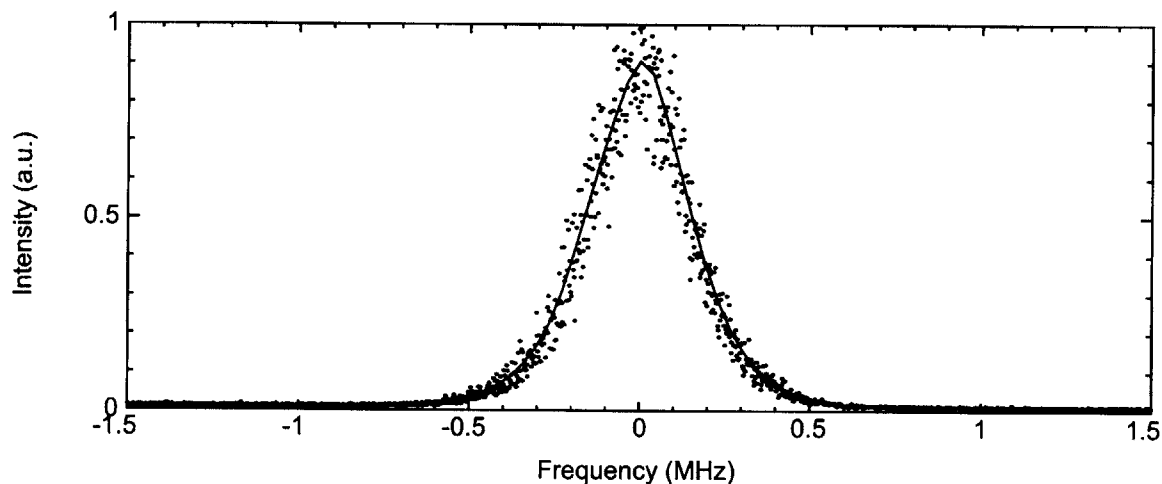


Figure 6-12: Linewidth measurement of the operating  $TE_{0,3,2}$  mode using the frequency measurement system.

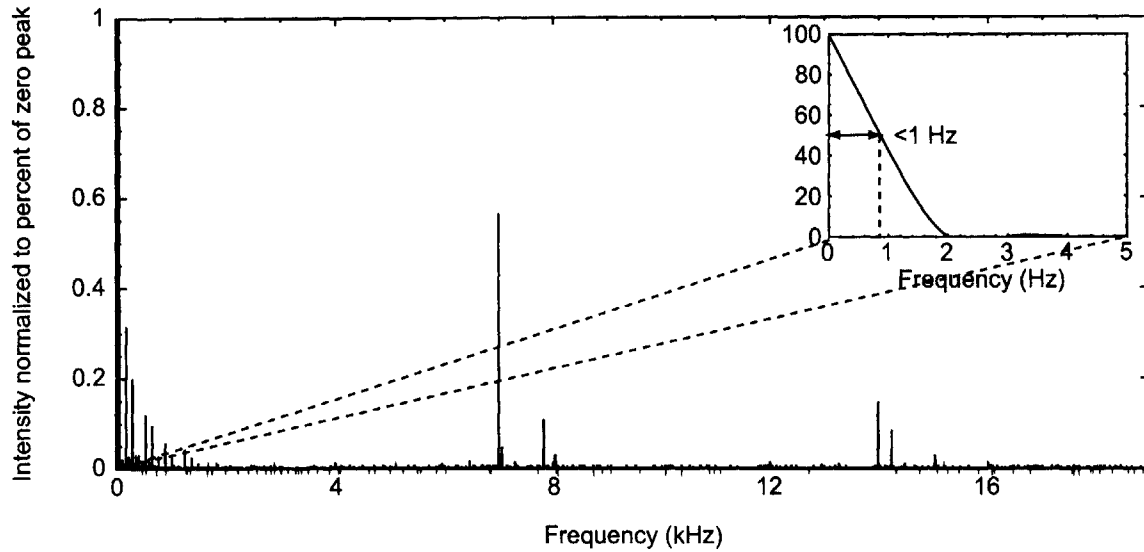


Figure 6-13: Homodyne measurement of the operating  $TE_{0,3,2}$  mode.

the contributing factors. Over the hour long period shown in Fig. 6-9, the standard deviation of the frequency is 359 kHz. The standard deviation of the beam voltage and current are 47 V and 8 mA, respectively. The standard deviation of the heater voltage and current are 4 mV and 8 mA respectively.

### Homodyne

The 250 GHz modulated signal is an amplitude modulated (AM) signal which can be demodulated yielding the linewidth of the device. The homodyne signal is shown in Fig. 6-13. We measured the instantaneous line width of the 250 GHz oscillator using a homodyne system and found it to be below the detection limit of a few Hz. There are sidebands every 60 Hz corresponding to the line modulation and sidebands spaced at 7 kHz at the switching frequency of the high voltage power supply. All sidebands are less than 1% in intensity. The previous linewidth measurement of several hundred kilohertz was limited by either the phase noise of the heterodyne receiver system or the technical noise.

## 6.2 Low Second Harmonic Starting Currents

The 250 GHz experiments were performed in pulsed mode with the same equipment used for the 460 GHz pulsed experiments, which is detailed extensively in Chapter 3, for the purpose of locating the second harmonic modes. The CW gyrotron was reverted to operation in a short pulse configuration with duration of 1-3  $\mu$ s and

Table 6.4: Second harmonic modes observed in the 250 GHz gyrotron.

Mode	Frequency (GHz)	Magnetic field (T)	Voltage (kV)	Start current (mA)
TE <sub>2,4,1</sub>	323.67	5.84	7.3	12
TE <sub>0,4,1</sub>	327.41	5.90	7.8	15
TE <sub>3,4,1</sub>	358.42	6.48	8.6	15
TE <sub>3,4,2</sub>	358.81	6.50	8.6	47
TE <sub>1,5,1</sub>	365.26	6.60	8.8	-

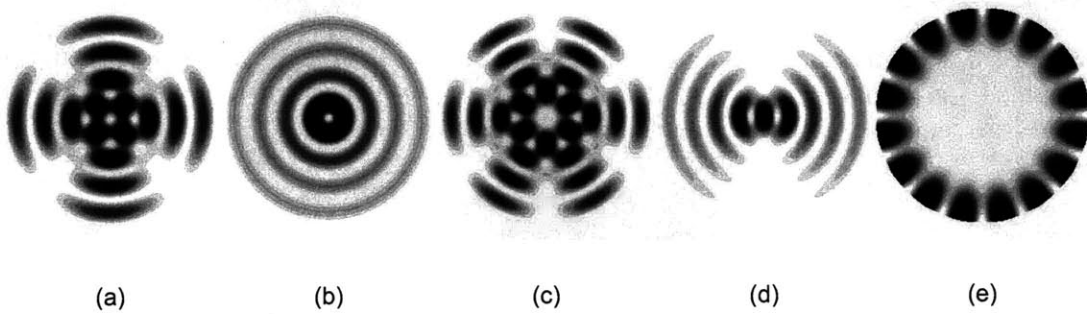


Figure 6-14: Intensity patterns of the harmonic modes observed in the 250 GHz experiment: (a) TE<sub>0,4</sub>, (b) TE<sub>2,4</sub>, (c) TE<sub>3,4</sub>, (d) TE<sub>1,5</sub>, and the fundamental waveguide mode (e) TE<sub>8,1</sub>.

repetition rate of approximately once per second. In this configuration, the low duty cycle allowed us to explore the physics of the second harmonic microwave generation in the gyrotron while avoiding potential damage due to beam interception or RF heating of internal components.

A parametric study was conducted to determine the operating parameters of several second harmonic modes in order to determine the feasibility of second harmonic operation in the 460 GHz experiment. Fundamental modes in the vicinity of the second harmonic modes or the operating TE<sub>0,3</sub> mode were also studied. To this end, operating parameters including the cavity and gun magnetic fields, beam current, and voltage were varied to map out the operating characteristics of the modes. The electron beam voltage and current were varied up to 15 kV and 120 mA while the main magnetic field was varied up to 9.2 T and the gun magnet up to  $\pm 8.5 \times 10^{-2}$  T with respect to the cathode field.

During the course of the experiment, four unique transverse second harmonic modes were observed from 5.8 to 6.6 T with starting current as low as 12 mA: the TE<sub>0,4,1</sub>, TE<sub>2,4,1</sub>, TE<sub>3,4,1</sub> (and TE<sub>3,4,2</sub>), and TE<sub>1,5,1</sub>, and these are enumerated in Table 6.4. The theoretical intensity patterns of several of the modes observed in the exper-

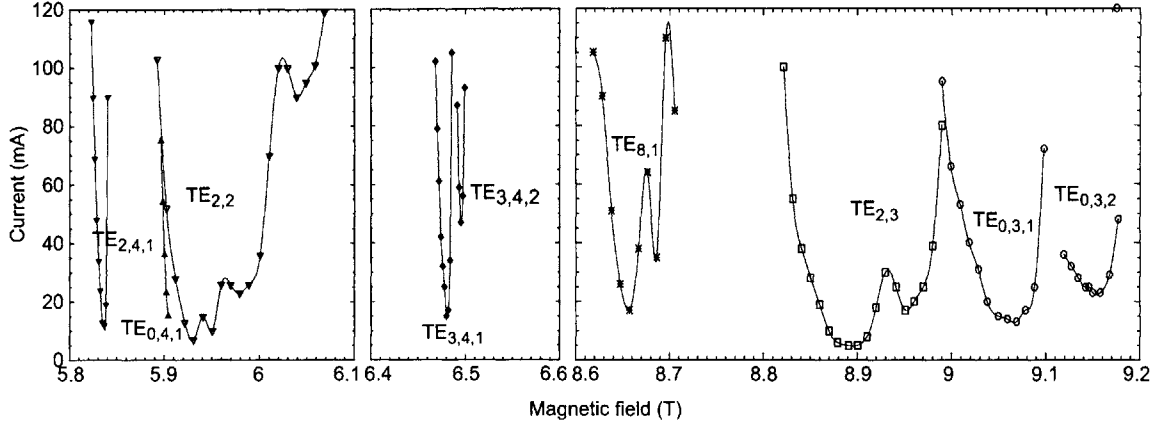


Figure 6-15: Summary of experimental starting current data vs. magnetic field recorded for resonant cavity modes from 5.8 to 9.2 T and up to 120 mA. Open symbols denote fundamental modes and filled-in symbols denote second harmonic modes.

iment are pictured in Fig. 6-14. Figure 6-15 summarizes the experimental starting current data as a function of magnetic field recorded for resonant cavity modes from 5.8 to 9.2 T and up to 120 mA. Open symbols denote fundamental modes and filled-in symbols denote second harmonic modes. It is of particular note that the three harmonic modes detailed in the experiment, the  $TE_{2,4,1}$ ,  $TE_{0,4,1}$ , and  $TE_{3,4,1}$  start oscillating at between 12 and 15 mA and that the  $TE_{3,4,2}$  second axial variation of a second harmonic mode begins oscillating at 47 mA.

Fig. 6-16 summarizes the experimental frequency tuning data as a function of magnetic field recorded near the starting current for resonant cavity modes from 5.8 to 9 T. Open symbols denote fundamental modes and filled-in symbols denote second harmonic modes. Data for the  $TE_{2,4,1}$ ,  $TE_{0,4,1}$ ,  $TE_{3,4,1}$ , and  $TE_{3,4,2}$  second harmonic modes is shown in addition to the  $TE_{2,2}$ ,  $TE_{8,1}$ , and  $TE_{2,3}$  fundamental modes. Table 6.5 summarizes the frequency tuning of the modes shown in Fig. 6-16, where, notably, 1.8 GHz tuning has been observed in the  $TE_{2,2}$  mode and 1.4 GHz in the  $TE_{8,1}$ , and, comparable to in the 460 GHz experiment, only tens of megahertz of tuning in the second harmonic modes. The magnetic frequency tuning of the fundamental modes has been previously analyzed in detail in Section 5.1.5.

The starting currents for the 250 GHz gyrotron calculated using linear theory, in Table 6.6, are much higher than the experimentally observed starting currents (*c.f.* Fig. 6-15). Among the possible explanation for this phenomenon are the electron beam, cavity shape, and window. An unintentional iris in the cavity resulting from an artifact of the machining and electroforming could lower the starting current by trapping the mode thereby raising the  $Q$ . Depending on the size and shape of the



Table 6.5: Frequency tuning for the observed modes between 5.8 and 9 T in the 250 GHz gyrotron.

$\text{TE}_{m,p,q}$	Harmonic number	$\Delta f$ (GHz)
$\text{TE}_{2,4,1}$	2	0.05
$\text{TE}_{0,4,1}$	2	-
$\text{TE}_{2,2,1}$	1	1.77
$\text{TE}_{3,4,1}$	2	0.02
$\text{TE}_{3,4,2}$	2	-
$\text{TE}_{8,1,1}$	1	1.36
$\text{TE}_{2,3,1}$	1	0.77

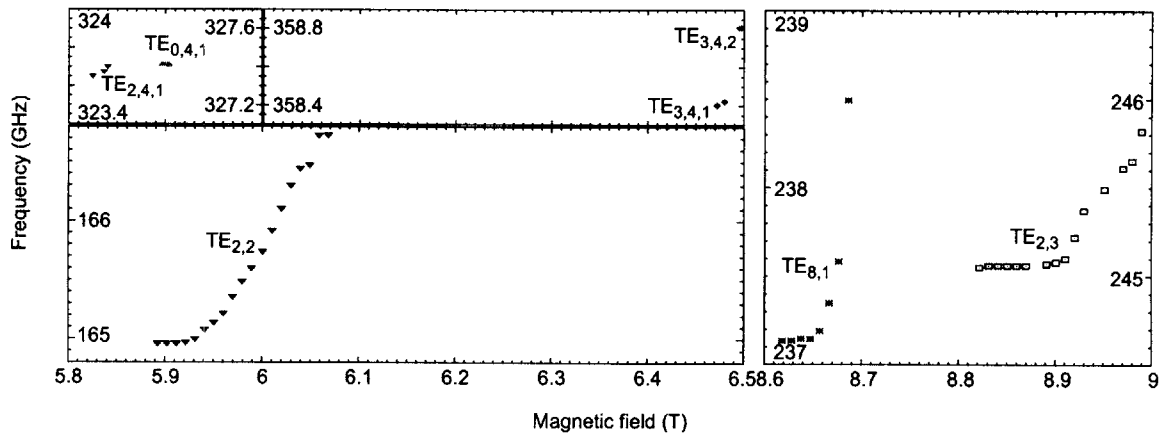


Figure 6-16: Summary of experimental frequency tuning data vs. magnetic field recorded for resonant cavity modes from 5.8 to 9 T near the starting current. Open symbols denote fundamental modes and filled-in symbols denote second harmonic modes.

Table 6.6: Minimum start current, and magnetic field and frequency for minimum starting current of  $q = 1$  modes from linear theory [19] vs. experiment

$\text{TE}_{m,p,q}$	Experiment			Theory		
	$B_0$	$I_{\text{st}}$	$f$	$B_0$	$I_{\text{st}}$	$f$
	(T)	(mA)	(GHz)	(T)	(mA)	(GHz)
$\text{TE}_{2,4,1}$	5.84	12	323.67	5.85	272	323.537
$\text{TE}_{0,4,1}$	5.90	15	327.41	5.92	361	327.301
$\text{TE}_{2,2,1}$	5.93	7	165.00	5.95	15	164.889
$\text{TE}_{3,4,1}$	6.48	15	358.42	6.49	226	358.286
$\text{TE}_{8,1,1}$	8.66	17	237.19	8.66	252	237.062
$\text{TE}_{2,3,1}$	8.89	5	245.07	8.93	9	244.966
$\text{TE}_{0,3,1}$	9.06	13	250.10	9.12	9	249.973

iris, it could either selectively enhance only the high frequency modes or affect all modes. In the 250 GHz gyrotron, nearly all of the modes including the  $\text{TE}_{0,4}$ ,  $\text{TE}_{2,4}$ , and  $\text{TE}_{3,4}$  second harmonic modes and the  $\text{TE}_{8,1}$  fundamental mode all have greatly reduced starting currents. Reflections from the window could also reduce the starting currents of selected modes by increasing the  $Q$ . However, this mechanism is not thought to be active because the effects of window reflections on the cavity operation which would be manifested as discrete segments in the magnetic frequency tuning data are not observed [18]. A third possibility is increased beam-wave coupling due to an off-axis beam.

### Off-axis beam

In this section we consider the effects on the starting current due to an off-axis beam. An off-axis beam could result from either a misaligned tube, a cross-bore that is not centered to the magnetic field, or from a skewed field resulting from the coupling of the NMR magnetic field to the gyrotron magnetic field in the region near the electron gun.

To illustrate this possibility, we have plotted the coupling coefficients, which are inversely proportional to the start oscillation current, of the design  $\text{TE}_{0,3}$  mode and the  $\text{TE}_{8,1}$  fundamental mode in Fig. 6-17. The design beam radius is 1.018 mm, which effectively couples the electron beam to the second radial maximum of the  $\text{TE}_{0,3}$  mode. The coupling to the experimentally observed  $\text{TE}_{8,1}$  whispering gallery mode should be poor except for interaction with electrons in the vicinity of the cavity wall. However in practice the mode enjoys a low starting current.

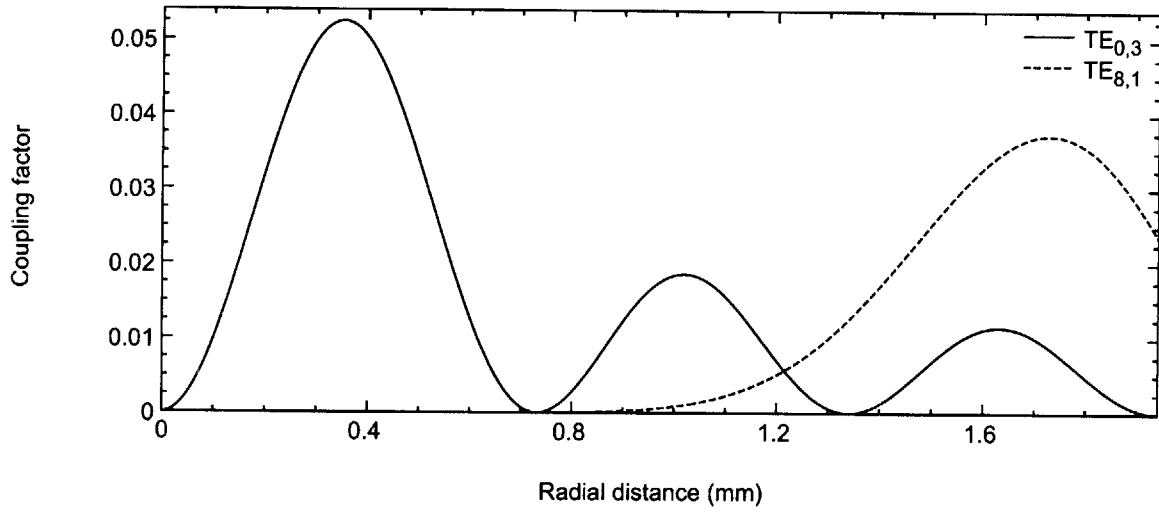


Figure 6-17: Coupling factor for the  $TE_{0,3}$  operating mode and the co-rotating  $TE_{8,1}$  fundamental mode. The operating electron beam radius is 1.018 mm.

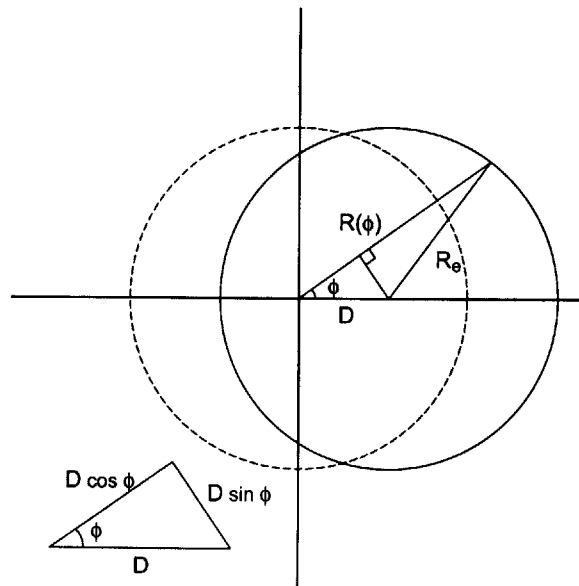


Figure 6-18: Electron beam shifted by the distance  $D$  (solid line) in the coordinate system of the resonator. The on-axis electron beam is indicated by the dashed circle.

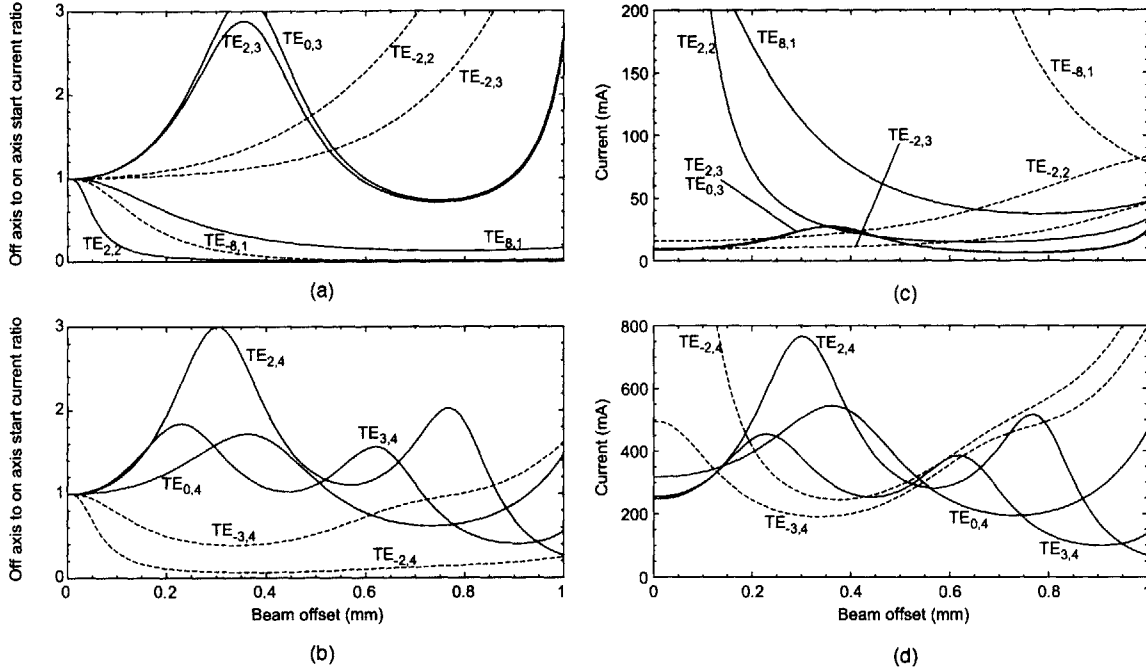


Figure 6-19: Ratio of off-axis to on-axis starting currents for observed (a) fundamental modes and (b) second harmonic modes. Off-axis starting currents for observed (c) fundamental modes and (d) second harmonic modes. The counter-rotating modes are represented by dashed lines.

The coupling coefficient for the off-axis beam can be determined by transforming the coordinate space for a shifted electron beam to the on-axis coordinate system (*c.f.* Fig. 6-18). Now the off-axis starting current can be addressed as the ratio of the off- to on-axis coupling coefficients multiplied by the on-axis starting current, which simplifies to

$$I_{\text{off axis}} = \frac{J_{m \pm n}^2(k_{\perp} R_e)}{J_{m \pm n}^2(k_{\perp} R(\phi))} \times I_{\text{start}} \quad (6.1)$$

where  $R_e$  is the beam radius and the beam radius of the off-axis beam transformed to the on-axis coordinate system is given by

$$R(\phi) = D \cos \phi + \sqrt{R_e^2 - D^2 \sin^2 \phi}. \quad (6.2)$$

The ratios of off-axis to on-axis starting currents are plotted in Fig. 6-19 for observed (a) fundamental modes and (b) second harmonic modes. The off-axis starting currents are plotted in Fig. 6-19 for observed (c) fundamental modes and (d) second harmonic modes. The counter-rotating modes are represented by dashed lines. The consequences of an off-axis shift of the electron beam with respect to the resonator are clear; even a 0.1 mm shift reduces the start current of the  $TE_{2,2}$  mode to 8% of

Table 6.7: Thermal load measurements on the 250 GHz gyrotron [20]

Current (mA)	Voltage (kV)	Beam power (W)	Cavity load (W)	Collector load (W)	Calorimeter (W)	RF efficiency (%)
4	12	48	0	37	0	-
8	12	96	0	85	0	-
12	12	144	11	127	3	21.43
16	12	192	24	150	5.7	19.23
20	12	240	31	189	8.4	21.38
24	12	288	37	221	10.3	21.75
28	12	336	47	260	12	20.34
32	12	384	51	292	13.9	21.37

the original on-axis starting current.

Since the cavity electron beam radius is slightly more than 1 mm and the cavity radius itself is slightly less than 2 mm, a beam offset of more than 0.9 mm will result in beam interception in the cavity and an offset of more than 0.6 mm will likely result in beam scraper interception. While the starting current for the counter-rotating second harmonic  $TE_{2,4}$  and  $TE_{3,4}$  modes are immediately decreased with a small beam shift, the starting current for the  $TE_{0,4}$  second harmonic mode is not diminished in the offset range that results in zero beam interception. Likewise, the  $TE_{8,1}$  fundamental mode requires a beam offset of 0.8 mm to enter the region of low current parameters in our experiment. In conclusion, there is no singular beam offset that will explain all of the lowered second harmonic starting current results.

### High $Q$ cavity

A high cavity  $Q$  is a second possibility for lowered starting currents that we will explore. From (2.62), the starting current is inversely proportional to the total cavity  $Q$ . In simulations, the conductivity of the oxygen-free copper used to electroform the cavity is assumed to be half that of ideal copper. A design value for the cavity diffractive  $Q$  of 6,000 was recovered from cold cavity simulations. Using these parameters, the expected RF efficiency for the 250 GHz  $TE_{0,3,1}$  mode is approximately 62%. In fact, according to the thermal load measurements in Table 6.7, the actual RF efficiency is closer to 21% [20]. In order to obtain an RF efficiency that is one-third as large as expected, there are two factors to be considered, as seen previously in Section 5.2.4. In the first scenario, the conductivity of the copper of the electroformed cavity

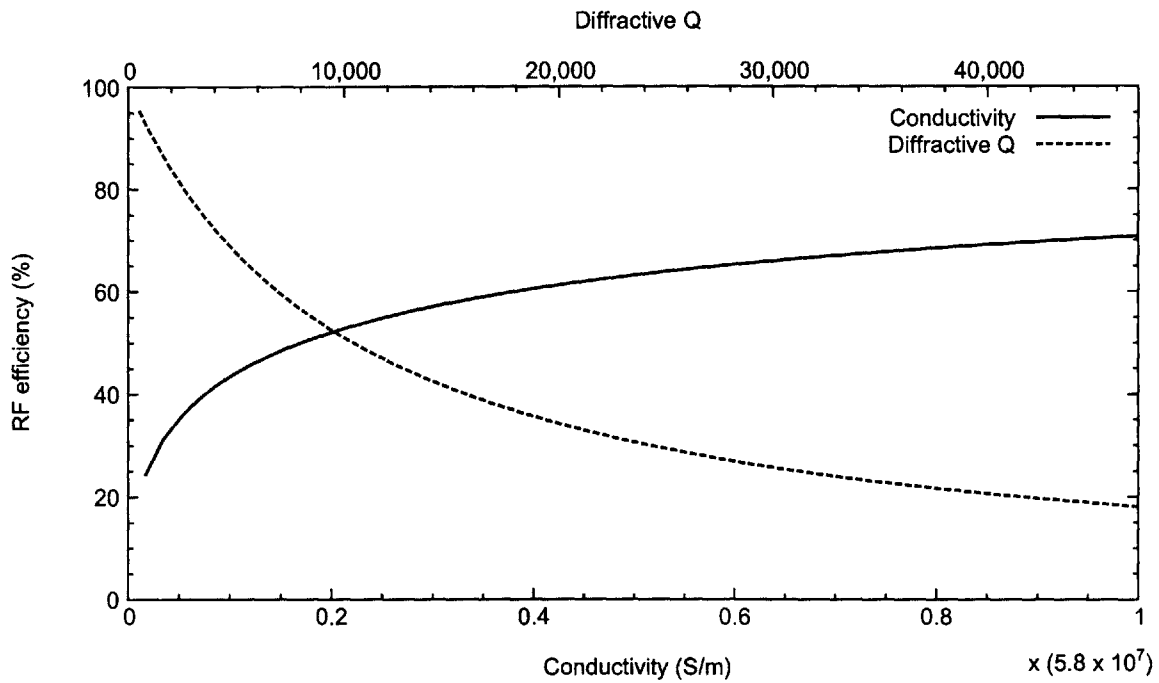


Figure 6-20: Theoretical RF efficiency as a function of the conductivity of copper and diffractive  $Q$  for the fundamental  $TE_{0,3,1}$  mode.

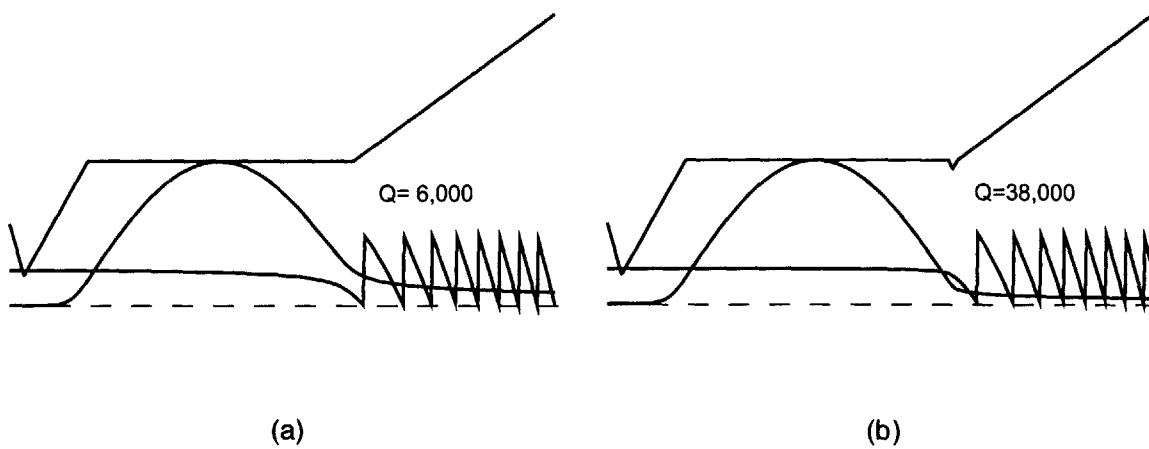


Figure 6-21: Cold cavity simulation showing the cavity and RF profile for the 250 GHz gyrotron cavity (a) without and (b) with an iris.

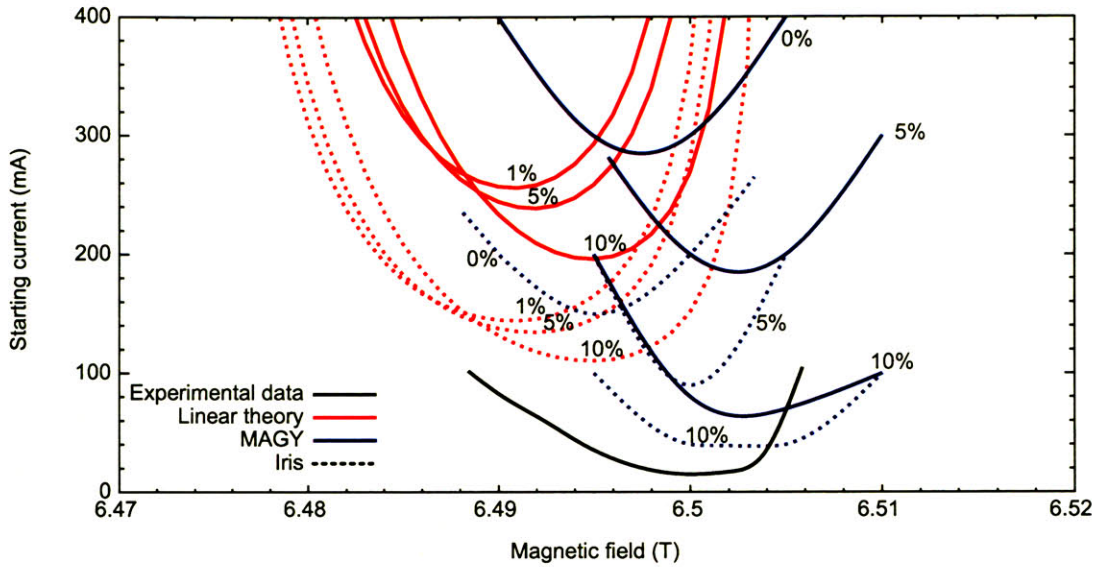


Figure 6-22: Starting currents for the second harmonic  $TE_{3,4,1}$  mode using linear and non-linear theory and for the case of the design cavity (lines) and with an iris added before the output uptaper (dotted lines). The percentages indicate the velocity spread simulated.

should be less than one-fiftieth of the conductivity of ideal copper. In the second case, the diffractive  $Q$  should be seven times higher than the design value. These are illustrated in Fig. 6-20. The first scenario seems highly unlikely, therefore we will focus on the second possibility.

The presence of a small iris before the output uptaper of the cavity can significantly increase the diffractive  $Q$  by the observed factor of seven. This is illustrated in cold cavity simulations for the  $TE_{0,3,1}$  mode in Fig. 6-21, where the frequency remains unchanged with or without an iris. An iris is consistent with the machining of discontinuous radii on the mandrel and can explain the elevated thermal load on the cavity. Most importantly, a high diffractive  $Q$  can significantly lower the starting currents of all modes. Figure 6-22 shows the starting current results of linear and non-linear simulations of the second harmonic  $TE_{3,4,1}$  mode. The nonlinear simulations with 10% transverse velocity spread and an iris of the variety depicted in Fig. 6-21 show the best agreement to the experimentally observed low starting current. The exact nature of the iris is unknown because the cavity cannot be removed from the gyrotron and this may account for the discrepancy between experiment and theory.

## 6.3 Corrugated Waveguide and Directional Coupler Experiment [2]

A 250 GHz corrugated transmission line with a directional coupler for forward and backward power monitoring has been constructed and tested for use with a 25-watt CW gyrotron for dynamic nuclear polarization (DNP) experiments. The main corrugated line (22 mm internal diameter (i.d.), 2.4 m long) connects the gyrotron output to the DNP probe input. The directional coupler, inserted approximately midway, is a 4-port crossed waveguide beamsplitter design. Two beamsplitters, a quartz plate and 10-wire array, were tested with output coupling of 2.5% (-16 dB) at 250.6 GHz and 1.6% (-18 dB), respectively. A pair of mirrors in the DNP probe transferred the gyrotron beam from the 22 mm waveguide to an 8 mm helically corrugated waveguide for transmission the final 0.58 m distance inside the NMR magnet to the sample. The transmission line components were all cold tested with a  $248 \pm 4$  GHz radiometer. A total insertion loss of 0.8 dB was achieved for  $HE_{1,1}$  mode propagation from the gyrotron to the sample with only 1% insertion loss for the 22 mm diameter waveguide. A clean Gaussian gyrotron beam at the waveguide output and reliable forward power monitoring were achieved for many hours of continuous operation.

### 6.3.1 Introduction

The recent availability of multiwatt CW power at 250 GHz for dynamic nuclear polarization (DNP) [27] and other diagnostic applications has created a need for efficient, moderate power transmission line and directional coupler components. Fundamental mode WR-03 waveguide components (0.86 x 0.43 mm inside dimensions) are not practical due to high insertion losses of  $\geq 8$  dB/m. High transmission efficiencies at 250 GHz can be achieved by using overmoded waveguide (cross section dimensions greater than a wavelength) or optical components. The most efficient overmoded waveguide mode is the  $HE_{1,1}$  mode in corrugated waveguide [131]. This mode also ideally couples to a free space Gaussian beam, which is optimum for achieving the smallest possible diffraction limited spot sizes for maximizing power concentration or spatial resolution in an experiment.

Corrugated waveguide transmission lines are a well-established technology widely used with gyrotrons at lower frequencies. Some examples are the transmission lines at 110 GHz on the DIII-D tokamak [132], at 140 GHz on the ADSEX-Upgrade tokamak [133], and at 84 and 168 GHz on the Large Helical Device (LHD) stellarator [134]. In this report we extend this technology to 250 GHz.



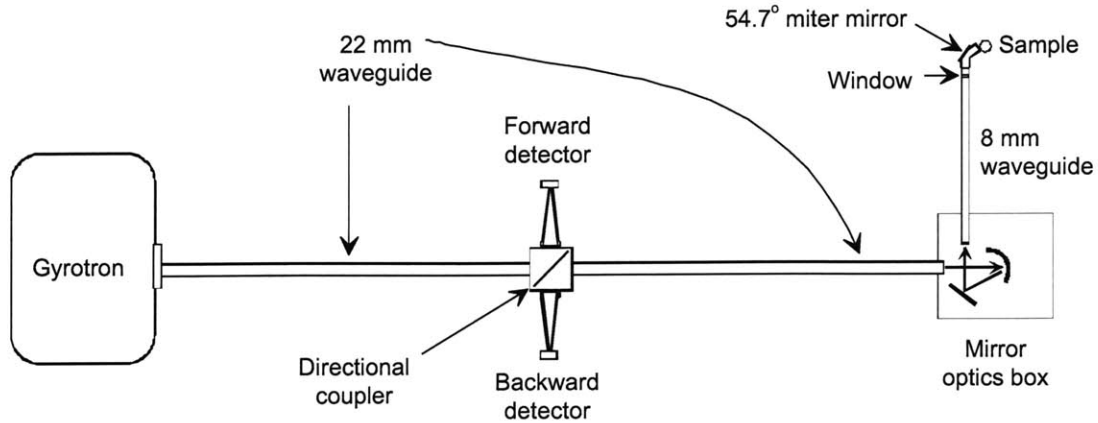


Figure 6-23: 250 GHz transmission line layout for DNP experiments.

In addition to efficient transmission, a directional coupler is required in most experiments to monitor forward and reflected power. In high power gyrotron transmission lines at lower frequencies this is typically accomplished with small coupling holes in the mirror of a miter bend. Practical considerations due to the high power levels and requirements for heat dissipation limit the coupling holes to linear arrays as used in the transmission lines at 110 GHz on DIII-D [135] and at 140 GHz on the Frascati Tokamak Upgrade [136]. To overcome the power coupling variations of a linear array when multiple modes are present in the transmission line, experiments with a two-dimensional array of holes in a copper film on a diamond substrate for heat dissipation have also been carried out [137]. In the work presented here a quartz optical beam splitter, which is practical at moderate power levels, was implemented inside a straight section of corrugated transmission line to provide full beam cross section coupling of both forward and reflected power. Thin wires stretched across the waveguide aperture in place of the quartz were also tested as an alternative beamsplitter.

### 6.3.2 Component Design

The layout and principal components of the 250 GHz transmission line for DNP experiments are illustrated in Figure 6-23. From the gyrotron the transmission line starts with a 22 mm diameter, 2.44 m long corrugated waveguide with a beamsplitter directional coupler near the middle. At the output of this waveguide a two-mirror optics unit focuses and directs the gyrotron beam into a smaller 8 mm diameter, 0.58 m long helically tapped corrugated waveguide. The two mirrors consist of a spherical 50 mm diameter, 50 mm focal length focusing mirror, and a 25 mm square flat steering mirror. At the sample end of the 8 mm waveguide a flat mirror, 54.7°

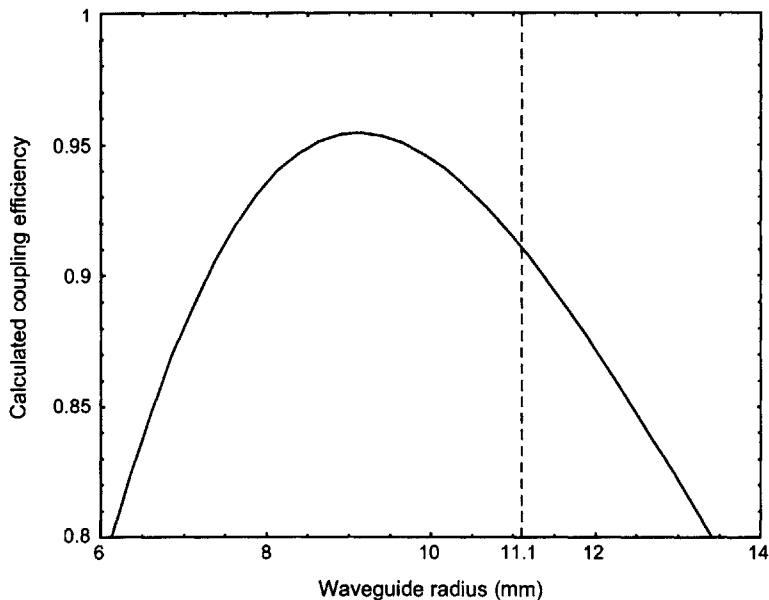


Figure 6-24: Calculated coupling efficiency of an elliptical Gaussian beam of  $10.04 \times 13.76$  mm waist cross section to a circular waveguide  $HE_{1,1}$  mode.

mitered waveguide bend directs the beam to the cryogenically cooled sample. A PTFE (Teflon) window is located in the 8 mm straight waveguide just before the miter bend. The 8 mm waveguide and sample are inside the bore of the magnet (not shown) for the DNP experiments. The 8 mm waveguide also serves the dual purpose of the central conductor of the coaxial line for the 30–300 MHz RF.

## Waveguide

The choice of the main waveguide diameter was based on an analysis of the gyrotron output. An internal Vlasov converter inside the gyrotron transforms the  $TE_{0,3}$  mode to a near Gaussian beam, launching it through a quartz window. Ray tracing analysis of the Vlasov coupler predicts a slightly elliptical beam waist at the window with minimum and maximum diameters of 10.04 and 13.72 mm. A calculation of coupling such an elliptical beam to a circular corrugated waveguide  $HE_{1,1}$  mode as a function of waveguide diameter is shown in Figure 6-24. The coupling efficiency is optimal with a waveguide diameter of about 18 mm. A somewhat larger waveguide diameter of 22.2 mm (7/8 inch) was finally chosen after initial gyrotron output power measurements immediately outside the magnet dewar side bore showed greater power output coupling using a larger diameter waveguide due to the presence of higher order modes. The compromise for the calculated coupling to the  $HE_{1,1}$  mode at this larger waveguide diameter is not significant, dropping only from 95% to 91%.

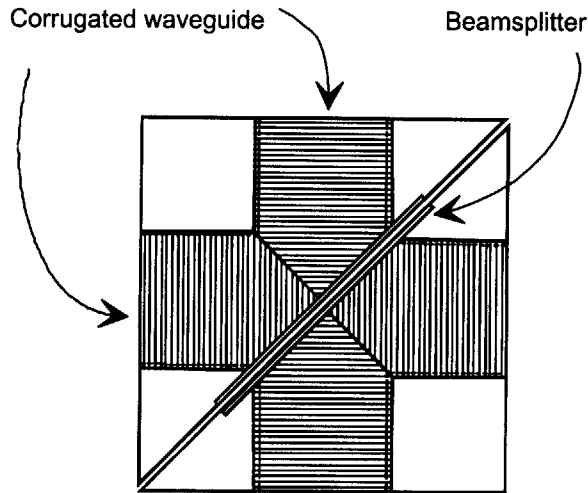


Figure 6-25: Design of the directional coupler fabricated from two corrugated waveguide corners that mate along the diagonal to hold the beamsplitter. One corner with a flat mirror along the diagonal would make a  $90^\circ$  waveguide miter bend.

The 22 mm diameter corrugated waveguide was fabricated from many short aluminum tube sections with a wall thickness of 3.2 mm (1/8 inch). The circumferential wall corrugations were 0.3 mm ( $0.25 \lambda$ ) deep and wide with a period of 0.4 mm ( $0.33 \lambda$ ). Two 0.254 m long and fifteen 0.124 m long waveguide sections and one 0.064 m long directional coupler block were assembled with outer diameter clamps to achieve the desired waveguide length.

The 8 mm waveguide was fabricated from copper tubing with a short section of stainless steel tubing welded in the middle to act as a cryogenic thermal break. The internal corrugations were machined with a rifling tap having a pitch of 2.5 grooves per mm (3 per  $\lambda$ ). The triangular groove depth was estimated to be between  $1/4 \lambda$  and  $1/8 \lambda$ . The total polarization rotation for propagating a 250 GHz beam through this waveguide due to the helical groove was estimated to be  $< 3^\circ$  using equation (2) in [138]. After machining, internal and external surfaces of this waveguide were flash coated with silver and then gold to provide good electrical conductivity to the RF and protection from corrosion.

### Directional coupler

The directional coupler design, illustrated in Figure 6-25, uses crossed corrugated waveguides that are split along a diagonal of the crossed waveguide intersection to accommodate a beamsplitter. The beamsplitter thickness and index of refraction determine the degree of reflective coupling from the main waveguide direction to the side waveguide ports. The reflectivity of a beamsplitter, assuming no absorption, is

given by the standard formula [139]:

$$\mathcal{R} = \frac{4\rho \sin^2\left(\frac{\delta}{2}\right)}{(1-\rho)^2 + 4\rho \sin^2\left(\frac{\delta}{2}\right)} \quad (6.3)$$

where  $\rho$  is the surface reflection given by the Fresnel equations and  $\delta$  is the phase difference between the beamsplitter front and back surfaces given by:

$$\delta = \frac{4\pi}{\lambda_0} n h \cos \theta_t \quad (6.4)$$

For the two orthogonal  $E$ -field polarizations parallel and perpendicular to the plane of incidence (the plane of Fig. 6-25):

$$\rho_{\parallel} = \left[ \frac{\tan(\theta_i - \theta_t)}{\tan(\theta_i + \theta_t)} \right]^2 \quad (6.5)$$

$$\rho_{\perp} = \left[ \frac{\sin(\theta_i - \theta_t)}{\sin(\theta_i + \theta_t)} \right]^2 \quad (6.6)$$

where in the above equations  $\theta_i$  and  $\theta_t$  are the angle of incidence and transmission, respectively at the beamsplitter as related by Snell' law of refraction ( $\sin \theta_i = n \sin \theta_t$ ),  $n$  is the beamsplitter index of refraction,  $h$  is its thickness, and  $\lambda_0$  is the gyrotron beam wavelength in vacuum.

A low coupling factor is achieved by a beamsplitter minimum in reflectivity. At 250 GHz fused quartz has an index of refraction of 1.955 [104] and for an incidence angle of  $45^\circ$  has a reflection minimum for a thickness of approximately 1 mm. Common microscope slides with this thickness and sufficient area ( $25 \times 50$  mm) to cover a 22 mm aperture at  $45^\circ$  are readily available and were used in the present experiments. Another advantage of this beamsplitter is that a visible laser beam can be introduced through a side port and its reflection off the beamsplitter can be aligned with the waveguide axis, facilitating downstream alignment of the transmission line and microwave optics.

A disadvantage of using a dielectric beamsplitter for signal coupling is that it is narrowband. Narrowband operation is not a limiting factor in this 250 GHz DNP experiment, since only the narrow gyrotron frequency is transmitted, but stability is important for monitoring power. Small changes to the beamsplitter parameters, for example due to thermal changes, could cause the coupling factor to drift. To overcome this potential limitation, experiments were carried out with thin wires stretched across the waveguide aperture as an alternative broadband beamsplitter approach.

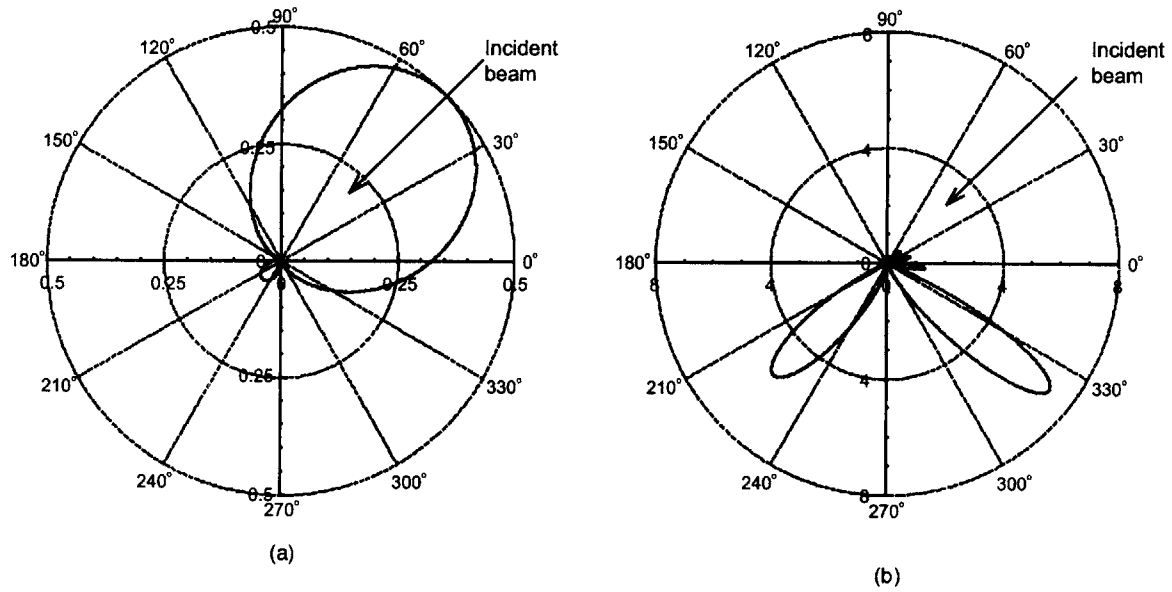


Figure 6-26: Scattered radiation patterns ( $P_s/P_o \times 10^3$ ) at 250 GHz by (a) one wire (36 gauge) and by (b) a ten wire array. The wires are arrayed with a spacing of  $1/4\lambda$  along the vertical axis of this figure with the wire axis normal to the figure plane. The incident beam is  $45^\circ$  from normal to the wire array plane with a  $HE_{1,1}$  beam profile corresponding to corrugated waveguide with  $ka = 58$ .

### Coupler with wires

The power scattered by a wire can be expressed as the product of its scattering cross section and the incident power density as:

$$P_S = \sigma P_D \quad (6.7)$$

where  $\sigma$  has units of area and  $P_D$  has units of power per unit area. In the following analysis we will only consider the electric field polarization normal to the wire axis because the scattering cross-section is smaller for this orientation and we desire a small coupling factor. For an infinitely long, small radius,  $a$ , wire such that the condition  $k_o a \ll 1$  is true the scattering cross-section is given by [140]:

$$\sigma_{\perp} = \frac{\pi^2 a \cos \Psi \left[ (k_o a \cos \Psi)^3 \left( \frac{1}{2} + \cos \phi \right)^2 \right]}{\cos^2 \Psi} \quad (6.8)$$

where  $\Psi$  is the angle between the incident beam and the normal to the wire axis and  $\phi$  is the angle between the direction of the scattered signal and the plane containing the incident beam and wire. In our present coupler design for a wire stretched across the waveguide aperture perpendicular to the plane in Figure 6-25,  $\Psi = 0^\circ$  and  $\phi = 90^\circ$ .

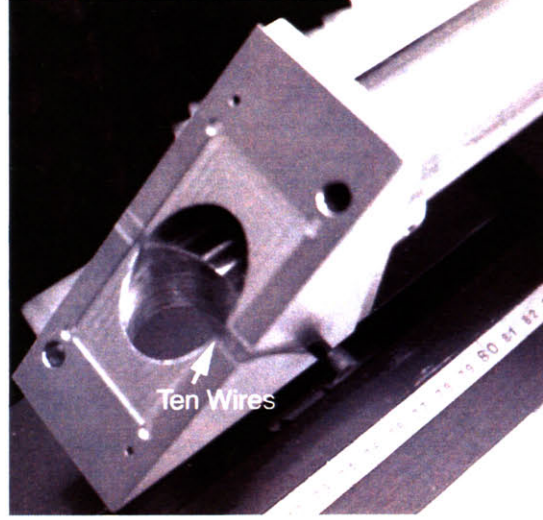


Figure 6-27: View of 10-wire, gauge 36 beamsplitter stretched across the diagonal face of the corrugated 4-port directional coupler block.

A 36 gauge wire with  $a = 63.5 \mu\text{m}$  has a value  $\sigma_{\perp} = 5.8 \times 10^{-3} \text{ mm}^2$  at 250 GHz ( $k_o = 5.24 \text{ mm}^{-1}$ ).

The power density of the  $\text{HE}_{1,1}$  mode inside a circular waveguide is best expressed in terms of the electric field density,  $E_D$ , as:

$$P_D = \frac{1}{2Z_o} E_D^2 \quad (6.9)$$

where  $Z_o = \sqrt{\mu_o/\epsilon_o}$  is the impedance of free space and the electric field density is given by [131]:

$$E_D = \sqrt{\frac{2P_o Z_o}{\pi}} \frac{1}{A} \frac{J_o\left(2.405 \frac{r}{A}\right)}{J_1(2.405)} \quad (6.10)$$

where  $P_o$  is the power of the gyrotron beam,  $A$  is the waveguide radius,  $r$  is the radius coordinate inside the waveguide, and  $J_o$  and  $J_1$  are Bessel functions.

According to (6.8), one wire will primarily backscatter the incident radiation (see the top of Figure 6-26). An array of wires is needed to impart directionality to the scattered signal away from the backward direction. The sum of the scattered electric field for an array of wire scatters can be calculated with the aid of the grating equation [141].

$$E_S = \sqrt{\sigma(\phi)} E_D(r_o) e^{ikr_o} \sum_{j=1}^n E_D(r_j) e^{ij\xi} \quad (6.11)$$

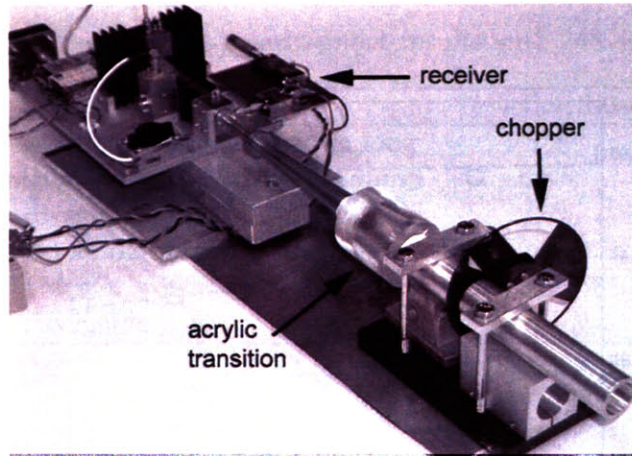


Figure 6-28: The 248 GHz heterodyne receiver used for cold test measurements.

where  $\xi$  is given by the grating equation as:

$$\xi = k_o d (\sin \theta_i + \sin \phi) \quad (6.12)$$

and  $d$  is the spacing of the wires and

$$r_n = \begin{cases} nd & \text{for } n \text{ odd} \\ (n + \frac{1}{2}) d & \text{for } n \text{ even} \end{cases} \quad (6.13)$$

The wire spacing needs to be less than the wavelength to minimize the number of side lobes in the radiation pattern. The radiation pattern for ten wires with a spacing of  $0.25 \lambda$  is shown in the lower part of Figure 6-26. The strongest radiation lobe is at about  $83^\circ$  to the incident beam with a scattering fraction of 0.0072 (-21.4 dB). The other strong radiation lobe is in the forward direction and does not contribute to the output coupling into the side port. The 10-wire side port coupling is not as optimal as with the quartz beamsplitter due to the slight angular offset, but it would be broadband. Figure 6-27 shows the 10-wire beamsplitter implemented on the diagonal face of the split 4-port corrugated block for measurements described below.

### 6.3.3 Cold Tests

A 248 GHz heterodyne radiometer was used to test the transmission efficiency of the waveguide components with broadband thermal radiation. The radiometer obtained from Millitech used a tripled 88.67 GHz Gunn local oscillator (LO) that was frequency stabilized to a 100 MHz crystal quartz reference. The intermediate frequency (IF)

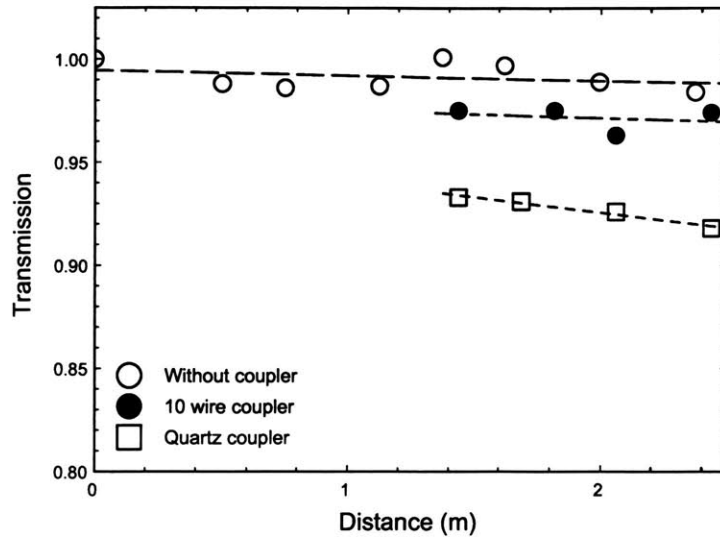


Figure 6-29: Cold test transmission measurements of the 22 mm diameter corrugated waveguide without and with two versions of the directional coupler.

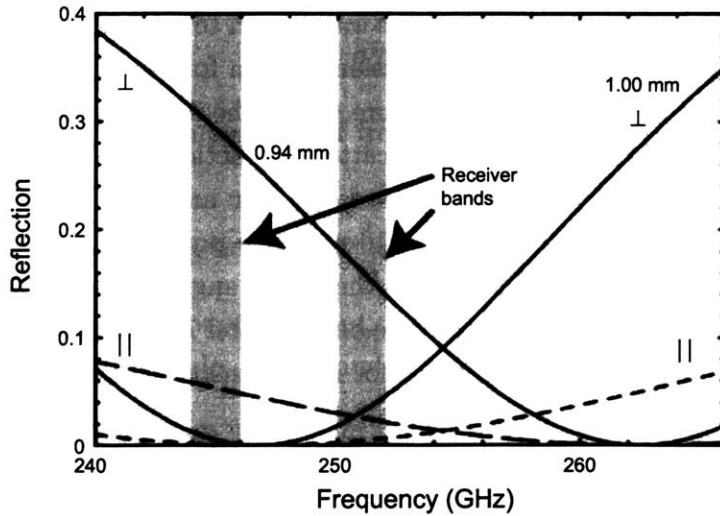


Figure 6-30: Calculated quartz ( $n=1.955$ ) beamsplitter reflectivity for a beam incidence at  $45^\circ$  for the two orthogonal polarization cases and two thicknesses.



Table 6.8: Cold test insertion loss measurement results with  $248 \pm 4$  GHz radiometer

Component	Insertion Loss
22 mm waveguide, 2.44 m long	1%
Quartz coupler (6.3% coupling)	6.8%
10-wire coupler (1.6% coupling)	2.6%
4-port block w/o beamsplitter	0.5%
Transfer mirrors and 8 mm waveguide	$15 \pm 3\%$

amplifiers covered the 2–4 GHz range. A corrugated horn with an internal semi-angle of  $2.5^\circ$  and an output aperture of 18 mm provided an  $HE_{1,1}$  mode field-of-view that was coupled to a 6.35 cm long 22 mm diameter corrugated waveguide section by a hollow acrylic plastic conical transition with an internal semi-angle of  $4^\circ$ . A second 12.4 cm long 22 mm diameter waveguide section was fixed relative to the first with a gap of about 1 cm for insertion of a chopper. A photograph of this setup is shown in Figure 6-28. The chopper permitted operation as a Dicke receiver [142] with lock-in amplifier phase sensitive detection. The double sideband (DSB) noise temperature was measured with a liquid nitrogen cooled thick (30 mm) pyramidal surfaced Eccosorb black body to be approximately  $T_r = 11,000$  K past the chopper at the end of the 22 mm diameter waveguide. Though the theoretical measurement precision with this receiver as given by  $T_r/\sqrt{Bt}$  [143] is  $0.2^\circ\text{C}$  for one second integration time ( $t = 1$  s) and the full receiver DSB ( $B = 4$  GHz), in practice it was at least several degrees due to electronics drift.

The transmission efficiency of the 250 GHz corrugated waveguide components was determined by measuring the increase in receiver noise temperature as the components were added to the end of the receiver-chopper assembly. The results for the 22 mm waveguide and the two versions of the directional coupler are shown in Figure 6-29. The top plot (open circles) shows the transmission efficiency of the straight waveguide sections as they were built up to the full 2.4 m length without any directional coupler. A small linearly increasing insertion loss was observed that totaled 1% for the complete waveguide. This is probably an upper limit for  $HE_{1,1}$  mode transmission efficiency, since it is likely that the receiver beam may have had some higher order mode content due to the acrylic transition and chopper waveguide gap.

In the next lower trace (solid circles) of Figure 6-29, a directional coupler using a 10-wire beamsplitter as described above was inserted into the 22 mm waveguide 1.37 m from the receiver assembly. The measured loss of this coupler at the insertion

location was 2.6%. In the lower trace (open squares) a directional coupler with a 1 mm thick quartz beamsplitter was inserted in the same position and measured a 6.8% insertion loss. Measurements of the noise temperature to the side port of the coupler for forward power coupling corresponded to 1.6% and 6.3% coupling fraction for the wire and quartz beamsplitters, respectively. Therefore some of the observed insertion loss is not coupled out to the monitoring port. A further measurement was made of the 4-port corrugated waveguide block without a beamsplitter and was found to have an insertion loss of about 0.5%. Consequently, the difference between the observed insertion loss and side coupling can be accounted for by the discontinuity of the crossed waveguide in the 4-port block.

The measured coupling fraction of 1.6% (-18 dB) with the 10-wire beamsplitter is 3 dB larger than the calculation above. This difference may be due to the approximate nature of the calculation for  $k_o a \ll 1$  where for the present case  $k_o a = 0.33$

The results for the coupler with the quartz beamsplitter can be understood with the aid of the calculations shown in Figure 6-30. The quartz reflectivity is a sensitive function of frequency and thickness. The beamsplitter thickness was measured to be  $0.94 \pm 0.02$  mm, one of the cases plotted in Figure 6-30. Integrating the beamsplitter reflectivity over the detection bands of the receiver results in a reflectivity of  $3.8 \pm 2\%$  for parallel polarization, the upper limit of which is close to the observed value. Rotating the quartz beamsplitter  $90^\circ$  on the waveguides axis to couple with the perpendicular polarization increased the measured coupling to 22%, which is also in agreement with the calculation of  $22.2 \pm 3\%$  for a 0.94 mm thick beamsplitter. For comparison, the case for a beamsplitter with a thickness of exactly 1 mm is also shown, which has a calculated parallel and perpendicular coupling of 0.24% and 1.7% respectively. Polishing the quartz beamsplitter to a precise thickness can be used to achieve almost any desired coupling factor less than -3 dB at a specific frequency.

The insertion loss of the two mirrors that transfer the millimeter-wave beam from the 22 mm waveguide to the 8 mm waveguide and the 8 mm waveguide was also measured and found to be  $15 \pm 3\%$ . It is likely that most of this loss can be accounted for by non-optimal threaded groove parameters and an elliptical distortion of the millimeter-wave beam caused by the spherical focusing mirror that is used at about  $30^\circ$  off axis. Table 6.8 summarizes the cold test insertion loss measurements.

### 6.3.4 Measurements with Gyrotron

The 22 mm diameter corrugated waveguide with the quartz 4-port directional coupler was tested with the CW gyrotron beam. Power was measured with a Model 362 Sci-entech calorimeter and mode patterns were obtained with thermal burn paper backed

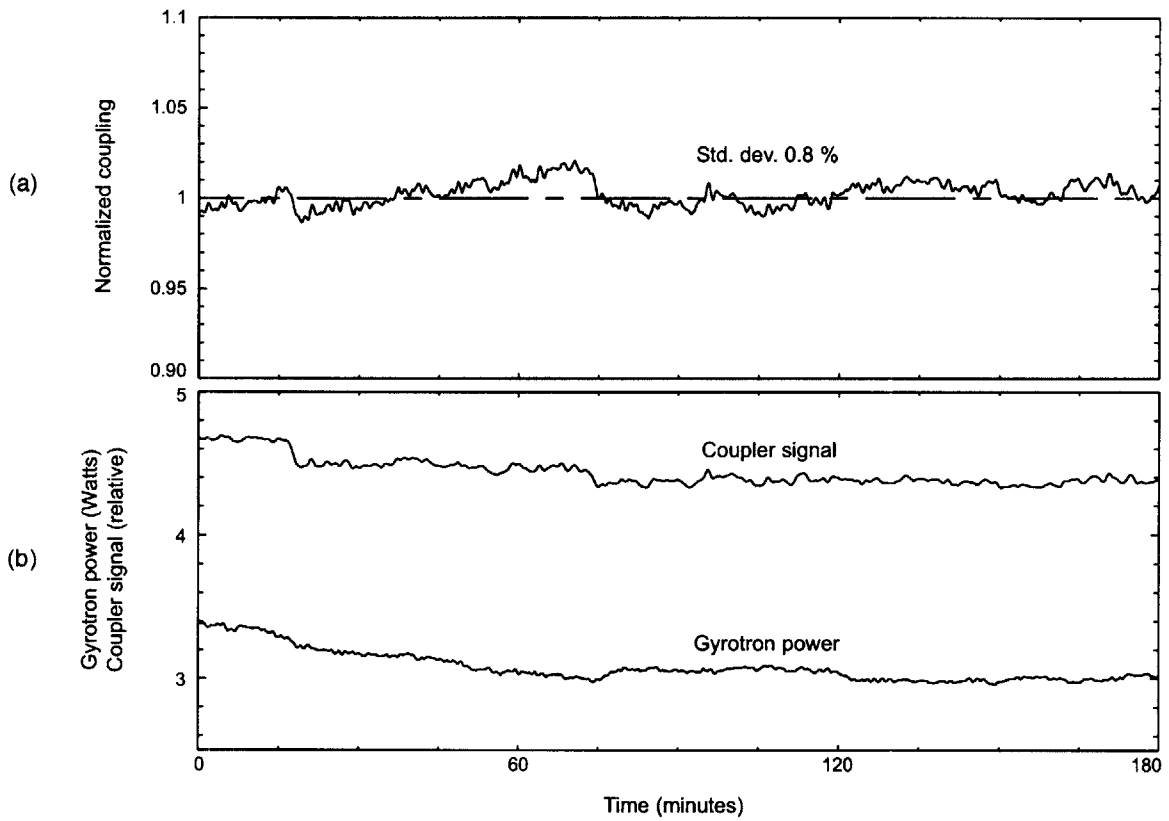
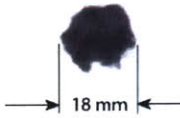
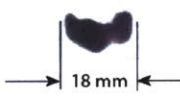
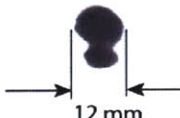
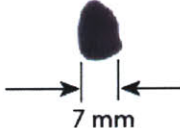
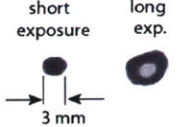


Figure 6-31: Three hour CW test of the quartz directional coupler stability, (a) normalized ratio of forward coupled signal and gyrotron power shown in (b).

Table 6.9: 250 GHz gyrotron beam measurements

Distance from Gyrotron Window (cm)	Burn Pattern	Power (W)
30 (no waveguide)		
38		4.5
100		
132 (after quartz coupler)		
244		4.1

by a flat sheet of eccosorb to enhance absorption. The power measurements were not corrected for the actual millimeter-wave absorption by the calorimeter detector element [144]. Table 6.9 summarizes the results. The gyrotron power output was set to about 5 watts for these measurements, which is adequate for the DNP experiments and allows very stable operation for periods of over 10 days. Operation with output power up to 25 watts is possible when long-term drift is not important.

The top burn pattern was taken without any waveguide immediately outside the gyrotron magnet side port, about 30 cm from the gyrotron window. The irregular appearance of the beam indicates the presence of higher order modes. However, the nonlinear absorption properties of the thermal paper may exaggerate the content of higher order modes. In the next entry, a 38 cm long section of the 22 mm waveguide was brought into near contact with the gyrotron window and aligned to maximize the power output. At this point the beam is significantly distorted and elongated in the horizontal direction. The next measurement was made after 1 m of waveguide was added to the output of the gyrotron window. The beam now has evolved to two vertically separated hot spots. In the next entry, with 132 cm of waveguide including the directional coupler the beam has become a smaller elliptically elongated spot. Finally, at the output of the full waveguide we have a single circular spot. Here two burn paper exposures are shown. The short exposure shows a small circular spot. In the longer exposure, the small circular spot has been burned from black to a lighter shade of gray making the outer regions of the beam visible, showing that the beam is circular over a large dynamic range. This suggests that the higher order gyrotron modes have been filtered from the beam by the 2.4 m long transmission through the corrugated waveguide. A power measurement of 4.1 watts was made at the waveguide output. This corresponds to an 11% loss relative to the first measurement of 4.5 watts near the gyrotron output.

The forward output coupling of the quartz directional coupler was also tested with the calorimeter. A coupled fraction of 2.5% was measured. This is lower than the cold test result because the quartz beamsplitter has a smaller reflectivity at the 250.55 GHz gyrotron frequency versus the two IF bands of the cold test receiver (*c.f.* Figure 6-30). The gyrotron frequency was accurately established by harmonically mixing with a frequency counted and PLL-regulated Gunn oscillator and performing a Fourier transform measurement of the IF frequency on a digital oscilloscope.

A 3-hour test of the directional coupler was also carried out to determine thermal stability with the gyrotron beam. A detector diode in WR-3 waveguide was matched to the forward power monitoring port with a 2.5° corrugated horn from Millitech, a 4° hollow acrylic taper, and a short section of 22 mm dielectric waveguide similar to

the setup of the 248 GHz radiometer described above. A thick pyramidal surfaced Eccosorb dump blocked the reflection monitoring port opposite the forward port for this test. The harmonic frequency measurement receiver was used to simultaneously monitor the gyrotron power in the main beam after the directional coupler by intercepting a small part of the beam at a distance. Figure 6-31 shows the results. The measured power levels are shown in Figure 6-31(b) and the normalized ratio of these signals is plotted in Figure 6-31(a). The coupling factor remains relatively stable over the three hour period. Drifts in the detection electronics can explain the observed deviation of 0.8% in the coupling factor.

This directional coupler design will require careful matching of the detector diodes and/or isolation when both forward and backward detectors are simultaneously implemented because they view each other cross the beamsplitter.

### 6.3.5 Conclusions

A corrugated waveguide with a full cross-section directional coupler for use with a moderate power CW 250 GHz gyrotron for DNP experiments has been fabricated and successfully tested. Precise measurements of small insertion losses and coupling factors were made possible with the use of a wide bandwidth radiometer,  $248 \pm 4$  GHz, for cold testing rather than a coherent source that would have had standing wave inaccuracies. The total transmission loss for an  $HE_{1,1}$  mode from the gyrotron to the sample was found to be about 0.8 dB over a total distance of 3 m with a directional coupler, an optical change in waveguide diameter, a Teflon window, and a miter bend. The actual loss was about 1.1 dB due to the presence of higher order modes in the gyrotron beam. However, with 5 watts output at the gyrotron 4 watts can be readily coupled to the sample, more than adequate for the DNP experimental requirements. Most of the insertion loss of about 0.7 dB occurs in the 0.58 m long, 8 mm diameter waveguide inside the DNP magnet probe and the associated two mirrors that transfer the gyrotron beam from the 22 mm diameter waveguide. Future improvements in the performance of this section of the transmission line system are possible by replacing the spherical mirror with an off axis parabolic mirror and improved corrugation parameters. The main 22 mm diameter, 2.44 m long waveguide with optimum corrugations was found to have an upper limit for  $HE_{1,1}$  mode transmission losses of only 1%.

The problem of monitoring forward power was solved with a 4-port crossed corrugated waveguide with a beamsplitter. Two types of beam splitters were tested, a narrow band thin quartz plate and a broadband 10-wire scattering array. The quartz plate has the advantage that a visible laser beam can be superimposed on

the millimeter-wave beam for alignment, but it has a disadvantage that it may be susceptible to frequency drift of the coupling factor under thermal loading by the gyrotron beam. The 10-wire scattering array is broadband and the wires are good thermal conductors, potentially making the 10-wire array coupling factor more stable at higher power. Both beamsplitters cold tested about as predicted and in the present 5 watt CW gyrotron tests the quartz beamsplitter did not reveal any problem with thermal drift. This directional coupler design along with the corrugated waveguide demonstrated here provide an efficient solution to the problem of transmitting and monitoring millimeter-wave beams at a frequency of 250 GHz.

## 6.4 Discussion

The 250 GHz gyrotron is situated in a nearly 50 gauss fringe field of a 380 MHz wide bore NMR magnet. While the center of the gyrotron magnet is shielded by the nature of its superconducting coils, the region of the electron gun remains unshielded. The electron beam characteristics are extremely sensitive at the region where the electrons are emitted and the second magnet may have consequences on the alignment and quality of the electron beam in the gyrotron tube.

Starting currents for the second harmonic modes of the gyrotron were as low as 12 mA. Two possible causes of the low starting currents in the various second harmonic and fundamental modes of the gyrotron discussed were an off-axis beam and a high  $Q$  cavity. The argument for an off-axis beam was discarded because there was no single beam offset that provided a unified solution to all modes without beam interception on the body. A high cavity  $Q$ , likely due to an iris, is the more reasonable cause of the low starting currents. This hypothesis is supported by thermal load data for the cavity which indicates that the ohmic losses are several times in excess of the design value.

The DNP probe incorporates an optical transmission section, which then couples to an over-moded waveguide which also serves as the center conductor of the RF coaxial transmission line. At the top of this line, a bend is made in over-moded waveguide to couple microwaves to the sample at the complement of the magic angle. Losses of approximately 7.5 dB at the top of the probe were measured using the setup previous to the installation of the corrugated waveguide, incorporating an overmoded smooth-wall waveguide. These losses were thought to have been incurred from diffraction losses inside the probe due to the launching into free space of a non-Gaussian beam. A smooth-wall waveguide does not transmit a mode which couples to a Gaussian. Instead, it transmits a combination of  $TE_{1,1}$  and  $TM_{1,1}$  radiation where the separate

modes can beat with each other, and, depending on the length of waveguide used, the output may not be in phase and will not yield a Gaussian. The  $TM_{1,1}$  mode also attenuates more rapidly than the  $TE_{1,1}$  mode. Corrugated waveguide, on the other hand, supports the  $HE_{1,1}$  mode which couples to a free-space Gaussian. The loss of power at the sample was reduced to 1.1 dB with the corrugated waveguide.

Under constant beam current regulation, the gyrotron output power steadily increases over time. The corrugated transmission system incorporates a quasi-optical directional coupler which allows the forward and reverse microwave power to be sampled, with very low insertion loss in the system. The beam splitter makes possible active monitoring of the power as an input to the control system which is the reason that the gyrotron output power can be held constant to less than 1% over long periods of time.



## Chapter 7

# Transmission System of a 140 GHz Gyrotron Oscillator

This chapter describes the mode purity and microwave transmission system of a 140 GHz gyrotron oscillator, the first collaborative effort of the joint series of Francis Bitter Magnet Laboratory and Plasma Science and Fusion Center DNP gyrotrons [41, 42]. A detailed analysis of the transmission system was performed in order to determine the efficiency of transmission and to minimize losses through design and implementation of several new components. For example, a new  $TE_{0,1}$  to  $TE_{1,1}$  waveguide mode converter was designed and implemented as the result of this effort.

Operating around 12.5 kV and 26 mA in millisecond pulses and approximately 50% duty, the 140 GHz gyrotron generates approximately 10 W of peak power in the  $TE_{0,3,1}$  mode. The power is transmitted to the DNP probe in the low-loss  $TE_{1,1}$  waveguide mode. To complete the process of transformation into the  $TE_{1,1}$  transmitted mode, the  $TE_{0,3}$  radiation is initially converted into the  $TE_{0,2}$  mode via an axisymmetric waveguide mode converter, followed by a  $TE_{0,2}$  to  $TE_{0,1}$  waveguide mode converter, both of which are located internal to the gyrotron. Also internal to the gyrotron is a  $90^\circ$  miter mirror to steer the radiation toward the 211 MHz NMR magnet and to block electrons which have not been deflected to the collector walls from striking the quartz window. A schematic of the 140 GHz gyrotron oscillator illustrating these features can be seen in Fig. 7-1.

The gyrotron output window, with a diameter of 1.27 cm, is followed by an external  $TE_{0,1}$  to  $TE_{1,1}$  waveguide mode converter, a miter bend, a vertical copper pipe, a second miter bend, a horizontal pipe, and a downtaper to fundamental waveguide, a circular to rectangular transition, a high-power directional coupler (-36 dB attenuation on both ports), and a  $90^\circ$  fundamental waveguide bend, before entering the NMR magnet from the top (*c.f.* Fig. 7-2). The  $TE_{0,1}$  to  $TE_{1,1}$  waveguide mode converter,

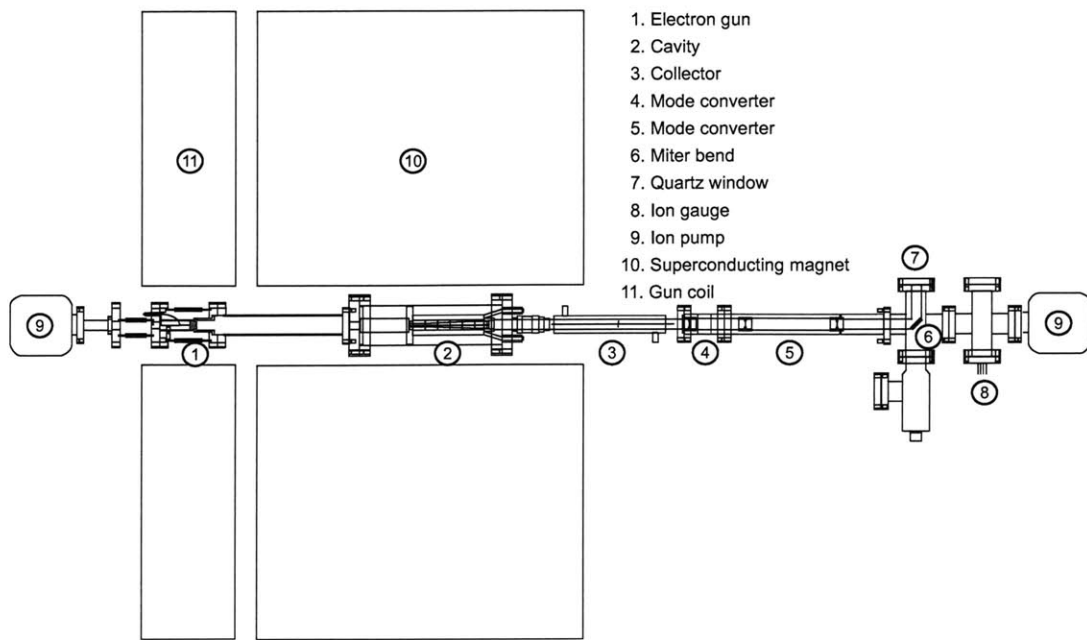


Figure 7-1: Schematic of the 140 GHz gyrotron oscillator indicating key components. The gyrotron tube is parallel to the plane of the floor.

shown in Fig. 7-3, is an asymmetrical periodically perturbed cylindrical waveguide. The  $TE_{0,1}$  to  $TE_{1,1}$  waveguide mode converter, also referred to as the “snake” due to its serpentine shape, has been fabricated from a section of cylindrical copper waveguide almost a meter long that has been perturbed periodically. In the old snake, these perturbations are held in place with clamps and can be adjusted manually with screws. The measured snake parameters are listed in Table 7.1.

In order for the transmission system to have optimum efficiency, the transmitting mode must have high single mode purity. As a metric of the mode purity, we first measured the radiation pattern from the output window of the gyrotron. To determine the snake mode converter efficiency, we also measured the radiation pattern from the mode converter output and analyzed the result. Based on these efforts, a new snake mode converter was designed, implemented, and tested. The new mode converter was the first of a series of iterative modifications that were made to the 140 GHz transmission system that resulted in significantly higher transmission efficiency.

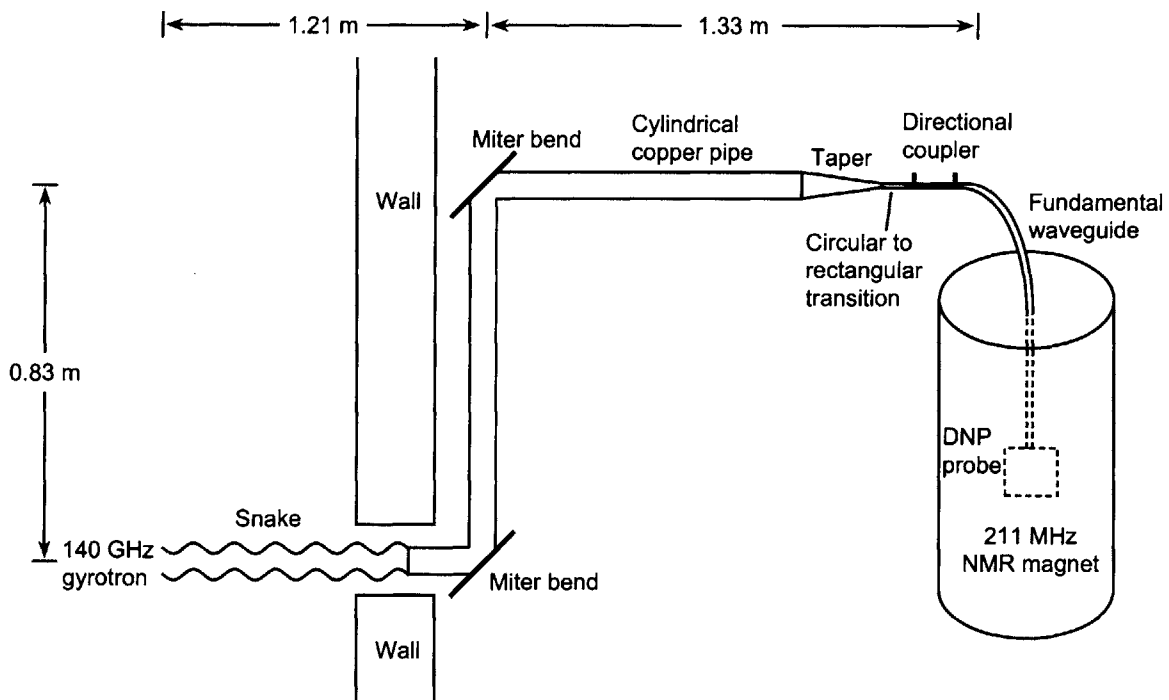


Figure 7-2: Schematic of the 140 GHz external transmission system, consisting of a  $TE_{0,1}$ - $TE_{1,1}$  snake mode converter, overmoded cylindrical copper waveguide with two miter bends, a taper to fundamental waveguide, a circular to rectangular transition, a directional coupler, and a fundamental waveguide bend, terminating at a 211 MHz ( $^1\text{H}$ )/140 GHz (electron cyclotron) DNP probe.

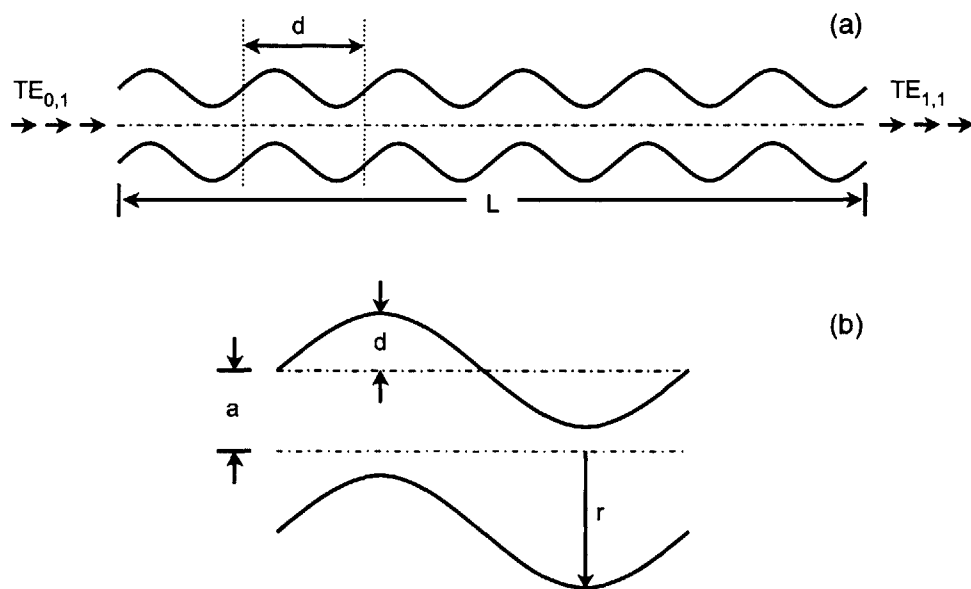


Figure 7-3: (a) Schematic of the  $TE_{01}$ - $TE_{11}$  snake mode converter, where  $a$  is the average waveguide radius,  $\delta$  is the perturbation,  $r(z) = a + \delta(z)$ ,  $d$  is a period, and  $L$  is the total length (b) close-up of one period [14].

Table 7.1: Measured snake parameters

Length of the snake $L$ (m)	0.93
Waveguide radius $a$ (mm)	6.35
Period length $d$ (cm)	13.3
Number of periods $N$	7

## 7.1 Two-Dimensional Radiation Pattern Measurements

The data acquisition system based on a mechanized scanner described in Sec. 3.1.3 was used for the field scans of the gyrotron output and snake output [89]. The attenuation level was adjusted until the diode signal reached a preset level, in our case, 10 mV. The gyrotron was set at a 2 Hz repetition rate. The slow repetition rate, along with the delay due to the motorized attenuator adjustments, results in a long scanning time. At the gyrotron window, a miter bend was placed followed by a short pipe of 1.27 cm radius. The miter bend was necessary due to the obstruction of a wall parallel to the gyrotron oscillator. In a second set of scans, the short pipe was replaced with the TE<sub>0,1</sub> to TE<sub>1,1</sub> waveguide mode converter. The scanner was placed about 5.08 cm away from the end of the open pipe (or snake). The cutoff waveguide attached to the diode detector is atuned to a single field polariation, thus each scan was repeated for both horizontal and vertical polarizations.

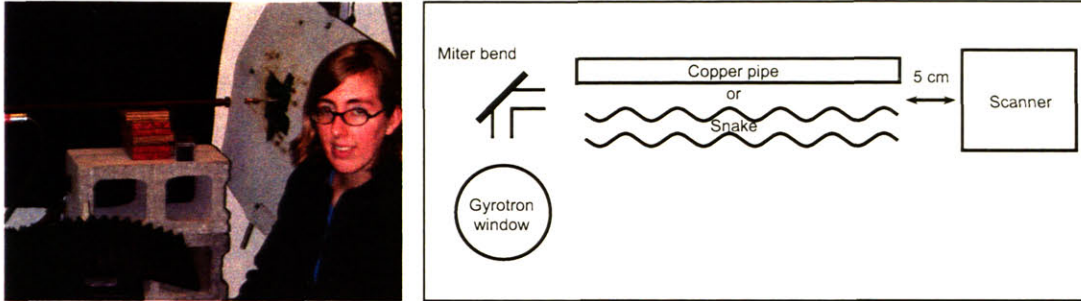
Since the relation

$$\frac{ka^2}{2z} > 1 \quad (7.1)$$

holds true, we know that we are operating in the near field, where  $a$  is the radius of the aperture (6.35 mm),  $z$  is the distance from the aperture (5.08 cm), and the frequency  $f$  ( $= ck/2\pi$ ) is 140 GHz. In this limit, the waveguide radiation fields should be appropriate for comparison.

### 7.1.1 Gyrotron Radiation Pattern Measurements

In the first set of scans, two-dimensional radiation patterns from the gyrotron output were measured using the apparatus described in the previous section in order to verify the quality of the TE<sub>0,1</sub> mode gyrotron output. The radiation exits the gyrotron window and is steered 90° with a miter bend in the plane of the floor to a copper pipe where it is radiated to the scanner over a 5 cm gap. The surface of the scanner not used to detect the radiation is covered with Eccosorb to prevent reflections. A block



(a)

(b)

Figure 7-4: (a) Photograph of the author and the setup for measuring the radiation mode patterns. The gyrotron is located off-screen to the left, and a miter bend steers the radiation toward the scanner. The scanner is located to the right and is covered with Eccosorb to prevent reflections. (b) Block diagram of the setup for measuring the radiation mode patterns.

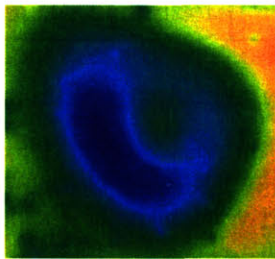


Figure 7-5: Liquid crystal recording of the  $TE_{0,1}$  gyrotron output.

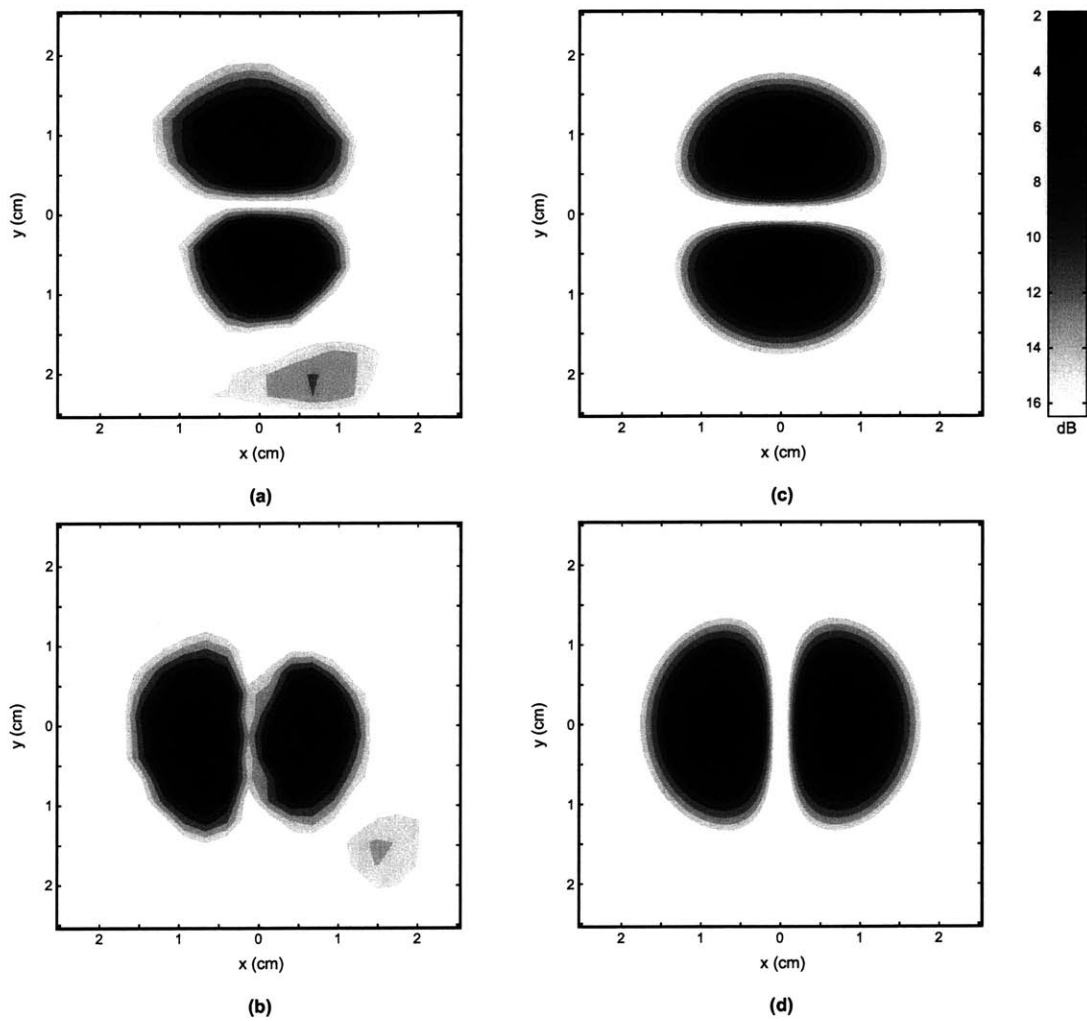


Figure 7-6: (a) Horizontal and (b) vertical polarizations of the gyrotron output at  $z = 5.08$  cm; (c) horizontal and (d) vertical polarizations of  $TE_{0,1}$  theoretical intensity; normalized dB contour plot

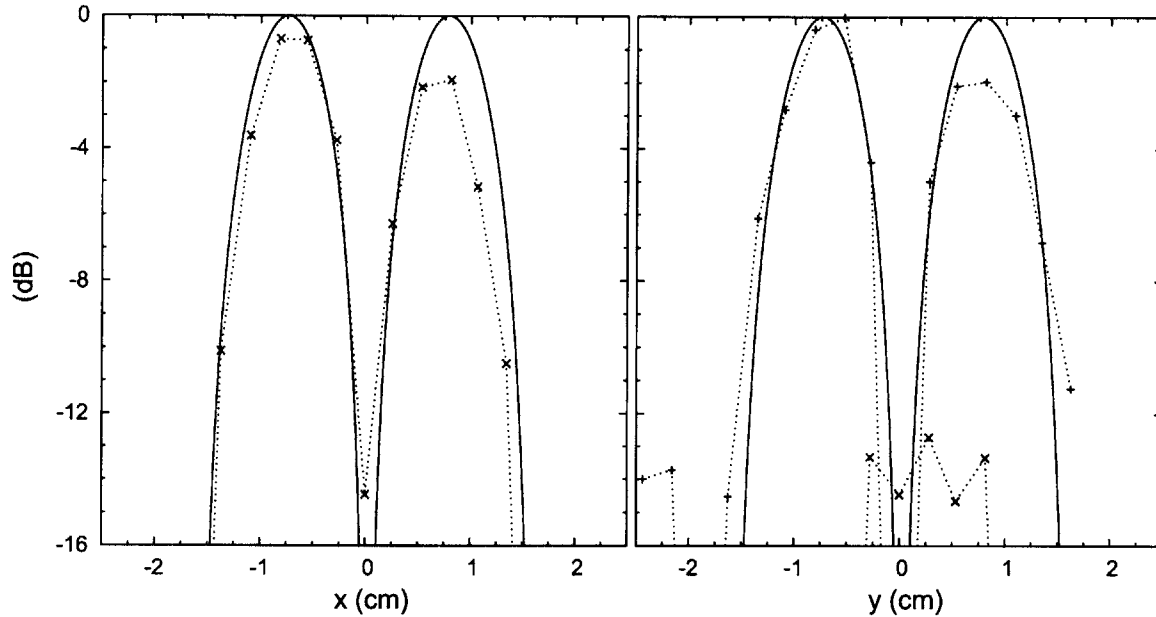


Figure 7-7: Gyrotron output at  $z = 5.08$  cm, (a)  $y = 0$ ; (b)  $x = 0$ ; the solid line represents the theoretical values, the  $\times$ 's the vertical polarization, and the  $+$ 's the horizontal polarization

diagram and photograph of the setup are shown in Fig. 7-4.

As an initial test, we irradiated the beam on a sheet of liquid crystal and took a still photograph with a digital camera (*c.f.* Fig. 7-5). A  $TE_{0,1}$ -like pattern can be seen, however the liquid crystals saturated quickly and were slightly damaged, potentially accounting for the nonuniform thermal distribution.

We used the scanner to obtain the data plotted in Figs. 7-6(a) and (b). Figures 7-6(a) and (b) show a two-dimensional scan of the horizontal and vertical polarizations of the gyrotron output at 5 cm in a normalized dB contour plot, where the maximum intensity is set to zero. When compared to the theoretical  $TE_{0,1}$  radiation patterns in Figs. 7-6(c) and (d), a sidelobe of low intensity is visible in Figs. 7-6(a) and 7-6(b) in the lower right of the scanned zone. One-dimensional slices taken at the  $y = 0$  and  $x = 0$  plane and compared to their theoretical  $TE_{0,1}$  counterparts are shown in Fig. 7-7, where the solid line represent the theoretical values,  $\times$  the vertical polarization, and  $+$  the horizontal polarization. The vertical polarization in Fig. 7-7(a) and the horizontal polarization in Fig. 7-7(b) match to theory reasonably well, and less than -12 dB of the vertical polarization was detected in the  $x = 0$  plane where there ought to have been none.

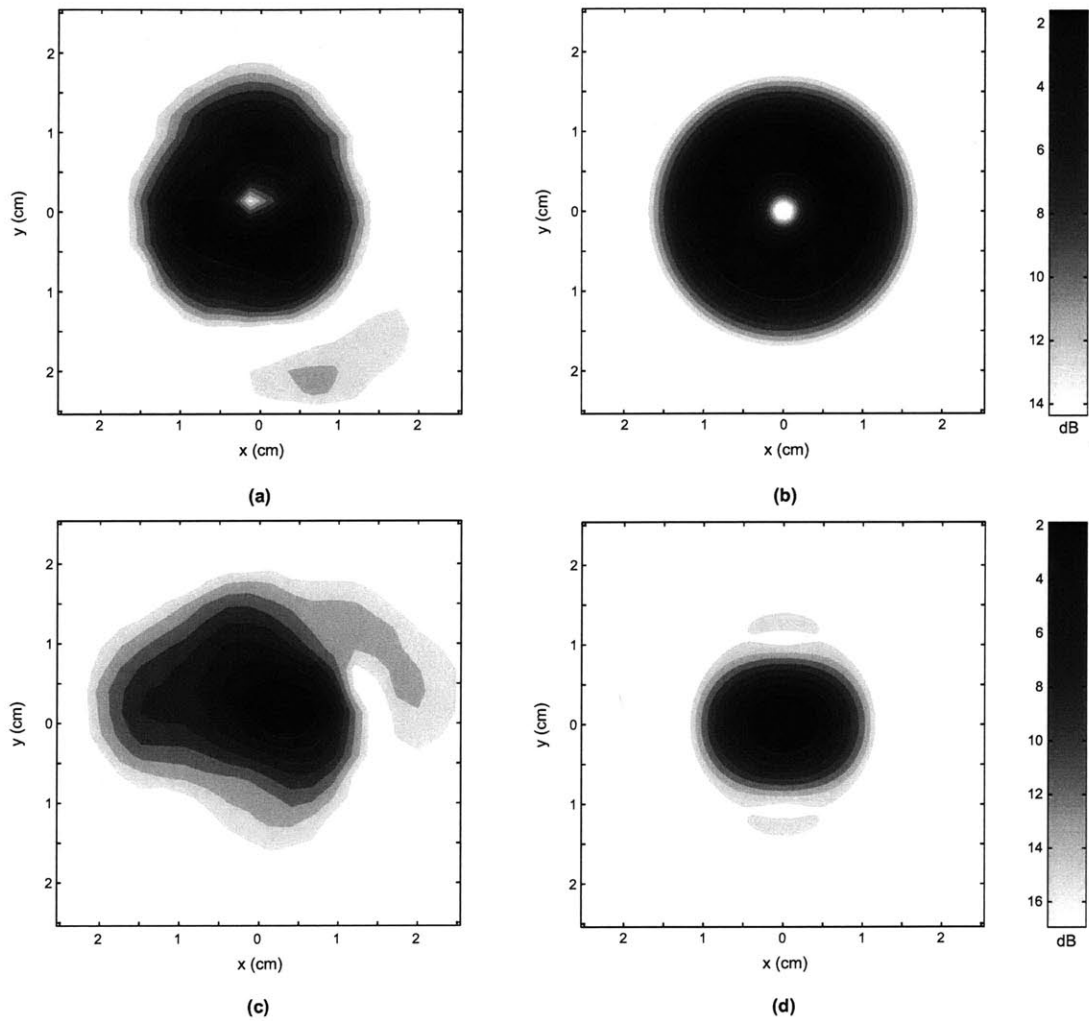


Figure 7-8: Sum of horizontal and vertical polarizations at  $z = 5.08$  cm of (a) gyrotron output, (b) theoretical  $TE_{0,1}$  waveguide mode, (c) snake output, and (d) theoretical  $TE_{1,1}$  waveguide mode in a normalized dB contour plot



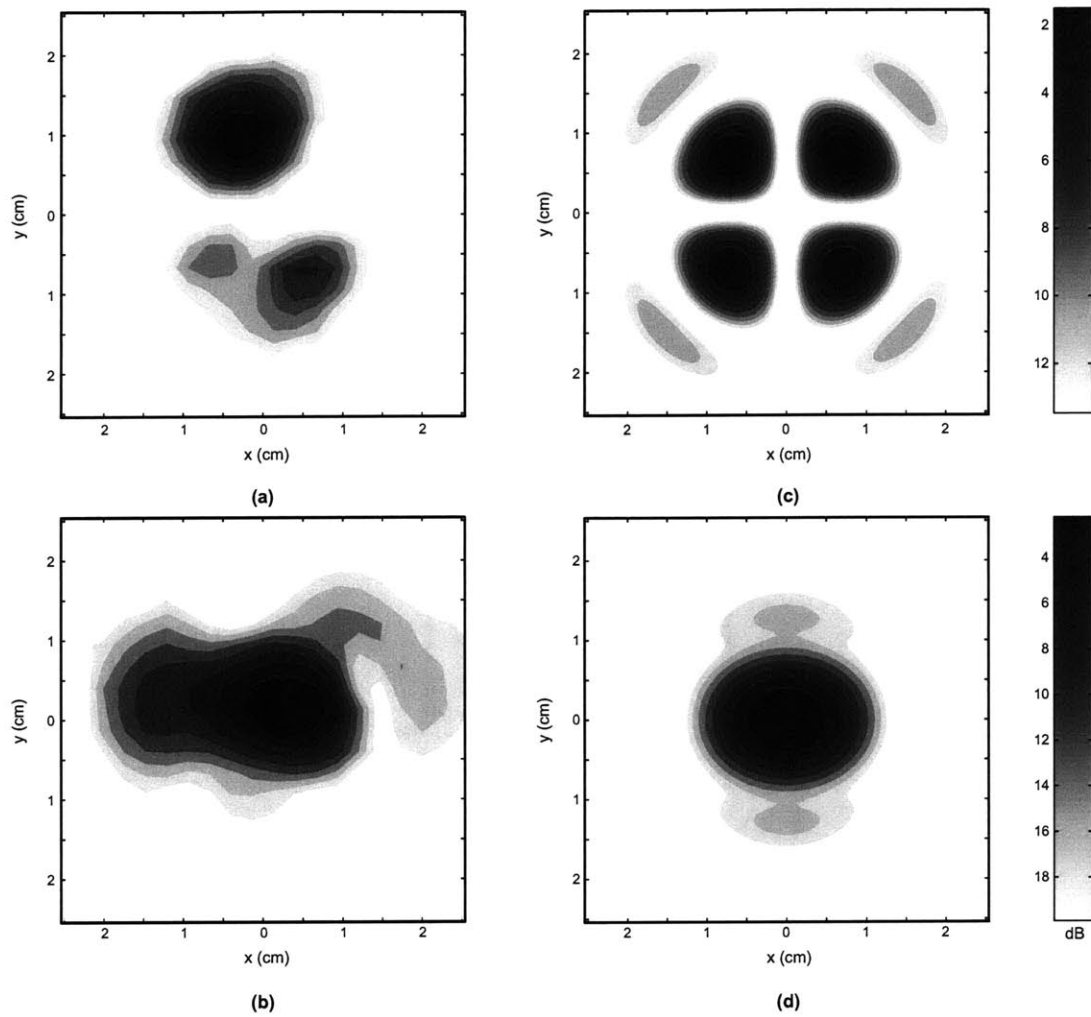


Figure 7-9: (a) Horizontal and (b) vertical polarizations of the snake output at  $z = 5.08$  cm; (c) horizontal and (d) vertical polarizations of  $TE_{1,1}$  theoretical intensity; normalized dB contour plot

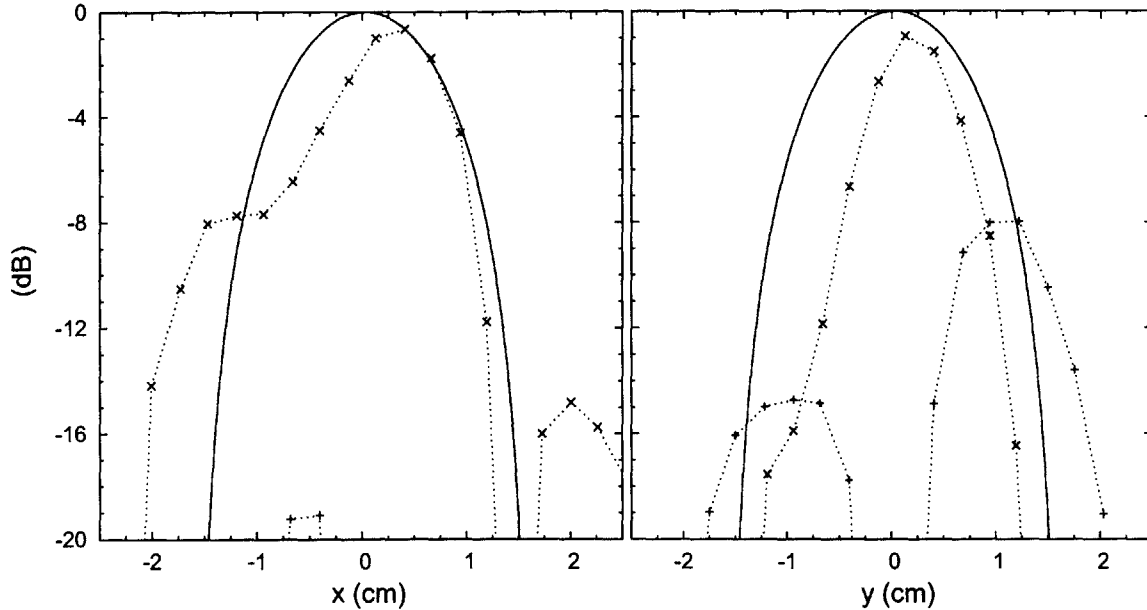


Figure 7-10: Snake output at  $z = 5.08$  cm, (a)  $y = 0$ ; (b)  $x = 0$ ; the solid line represents the theoretical values, the  $\times$ 's the vertical polarization, and the  $+$ 's the horizontal polarization

### 7.1.2 Old Mode Converter Radiation Pattern Measurements

In the second set of scans, we measured the radiation pattern from the snake using the scanning apparatus described previously in order to verify the functionality of the  $TE_{0,1}$  to  $TE_{1,1}$  mode converter. The radiation exits the gyrotron window and is steered  $90^\circ$  with a miter bend in the plane of the floor to the snake where it is radiated to the scanner over a 5 cm gap. The scanner is covered with Eccosorb to prevent reflections. A block diagram of the setup is shown in Fig. 7-4(b) and a photograph in Fig. 7-4(a).

We used the scanner to obtain the data plotted in Figs. 7-9(a) and (b) and 7-10. Figures 7-9(a) and (b) show a two-dimensional scan of the horizontal and vertical polarizations of the gyrotron output at 5 cm in a normalized dB contour plot, where the maximum intensity is set to zero. The horizontal polarization in Fig. 7-9(a) is a poor match to the theoretical  $TE_{1,1}$  pattern of Fig. 7-9(c) and is more reminiscent of the horizontal component of the  $TE_{01}$  mode, seen in Fig. 7-6(c). The vertical polarization of the snake output in Fig. 7-9(b) is a better match to its theoretical counterpart in Fig. 7-9(d). One-dimensional slices taken at the  $y = 0$  and  $x = 0$  plane and compared to their theoretical  $TE_{1,1}$  counterparts are shown in Fig. 7-10, where the solid line represent the theoretical values,  $\times$  the vertical polarization, and  $+$  the horizontal polarization. The vertical polarization in both Figs. 7-10(a) and 7-

10(b) match to theory in trend, however the horizontal polarization, which should be nearly absent resembles that of the  $TE_{0,1}$  mode more than the  $TE_{1,1}$  mode, indicating a probable error with the mode conversion.

### Mode converter analysis

To begin the the snake mode converter analysis, we added together the horizontal and vertical components of the gyrotron radiation patterns, likewise with the snake radiation patterns, to obtain the composite radiation pattern which is then compared to the theoretical  $TE_{0,1}$  or  $TE_{1,1}$  radiation pattern. These comparisons can be seen in Fig. 7-8 and they can be said to have the same shape.

Since the horizontally polarized component of the snake radiation pattern, Fig. 7-9(a), strongly resembles the theoretical horizontal component of the  $TE_{0,1}$  pattern, Fig. 7-6(c), instead of the theoretical  $TE_{1,1}$ , Fig. 7-9(c), we can first assume that the snake is not converting at 100% efficiency. Secondly we can assume that the horizontal polarization comes solely from the  $TE_{0,1}$  mode,

$$P_h = \frac{P_{0,1}}{2} \quad (7.2)$$

$$P_v = P_{1,1} + \frac{P_{0,1}}{2} \quad (7.3)$$

where  $P_h$  is the horizontal power from the snake radiation pattern,  $P_v$  is the vertical power component,  $P_{0,1}$  is the total power in the  $TE_{0,1}$  mode, and  $P_{1,1}$  is the total power in the  $TE_{1,1}$  mode. From this method, we can approximate that the  $TE_{0,1}$  to  $TE_{1,1}$  conversion efficiency of the snake is

$$\frac{P_{1,1}}{P_{1,1} + P_{0,1}} = 0.59. \quad (7.4)$$

Approximate analytical estimation [145] indicates that the snake converter has to be aligned with an accuracy of  $\pm 1^\circ$ . The misalignment angle  $\alpha$  (in radians) should be a factor of 2 to 3 smaller than  $\sqrt{4K/k}$ , where  $K$  ( $= \pi/(2Nd) = 0.017 \text{ cm}^{-1}$ ) is the  $TE_{1,1}$ - $TE_{0,1}$  mode coupling coefficient,  $N$  ( $= 7$ ) is the number of periods,  $d$  ( $= 13 \text{ cm}$ ) is the period, and  $k$  ( $= 2\pi/\lambda$ ). This angle corresponds to a shift in the tail of the snake of  $\pm 1 \text{ cm}$ . Assuming that the efficiency of mode conversion is 100% if the mode converter is perfectly aligned, the efficiency is reduced to 75% for a misalignment of  $2^\circ$ , and further to 20% for  $3^\circ$ .

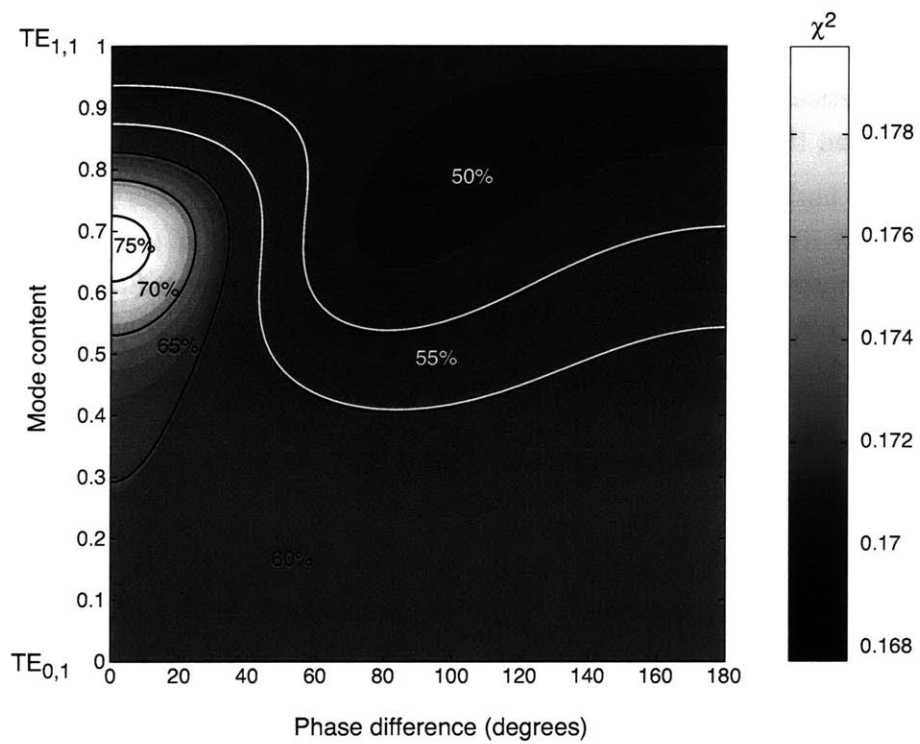


Figure 7-11: Statistical analysis of the mode converter radiation pattern assuming two modes present in the output, the TE<sub>1,1</sub> and TE<sub>0,1</sub>, and phase difference. Confidence levels are indicated by solid lines.

## Statistical analysis

Overmoded waveguide can support multiple propagating modes. Since each mode has a complex propagation coefficient, the intensity at successively sampled planes along the length of the waveguide will display a spatial interference pattern. The correct interpretation of mode spectra of waveguides on the basis of intensity measurements alone therefore requires phase reconstruction, a classic inverse problem for which a number of solutions have been proposed [], but for which a solution almost always involves sampling the intensity at several planes. In this case, there is enough information a priori about the mode content of the waveguide (*i.e.* that it is a mixture of two modes) for a single plane intensity scan to be informative, provided that each polarization component is separately measured. The diode detector apparatus is a polarization-sensitive detector; in combination with a digitally-controlled attenuator, it also has an extremely high dynamic range. In order to ascertain whether or not a detector that is insensitive to polarization can provide equivalent information, we first generated an aggregate data set consisting of a sum of the two intensity scans recorded from the output of the snake mode converter using the diode detector, each corresponding to a unique polarization. We then attempted to systematically fit the data on a grid of TE<sub>1,1</sub> and TE<sub>0,1</sub> mode content and relative phase. The goodness of the fit was analyzed using a statistical F-test to obtain confidence intervals for the measurement. The results of this statistical analysis show the entire fitting surface is enclosed by the 75% confidence contour. Thus, the separate measurement of each polarization component was critical for this analysis, and a detector measuring absolute intensity alone should not be expected to give informative results for the measurement of a single plane.

### 7.1.3 New Mode Converter Radiation Pattern Measurements

Using the coordinate system defined in Fig. 7-12, the radiation fields from the transverse electric (TE<sub>*m,p*</sub>) wave in hollow pipes of circular cross-section are given in spherical coordinates by [15]

$$E_r = 0 \quad (7.5)$$

$$E_\theta = j^{m+1} \frac{m\omega\mu}{2R} \left( 1 + \frac{k_z}{k} \cos \theta \right) J_m(k_\perp a) \frac{J_m(ka \sin \theta)}{\sin \theta} \sin m\phi e^{-jkR} \quad (7.6)$$

$$E_\phi = j^{m+1} \frac{ka\omega\mu}{2R} \left( \frac{k_z}{k} + \cos \theta \right) J_m(k_\perp a) \frac{J'_m(ka \sin \theta)}{1 - \left( \frac{k}{k_\perp} \sin \theta \right)^2} \cos m\phi e^{-jkR}, \quad (7.7)$$

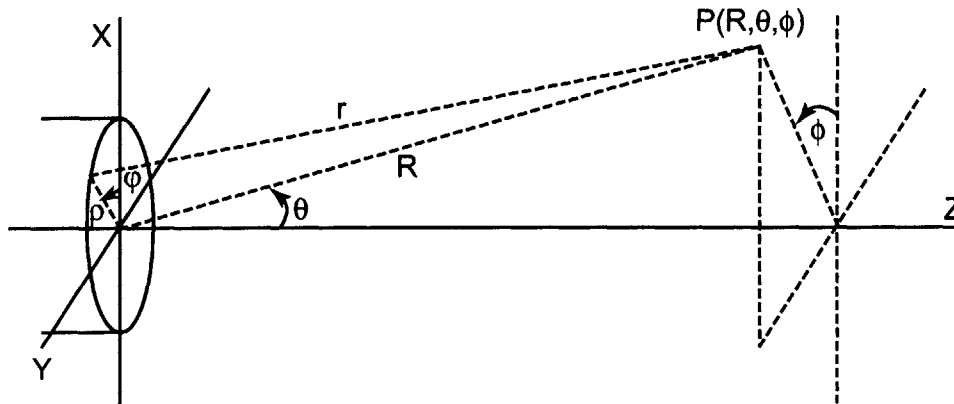


Figure 7-12: Coordinate system for calculating the radiation from a circular hollow pipe [15].

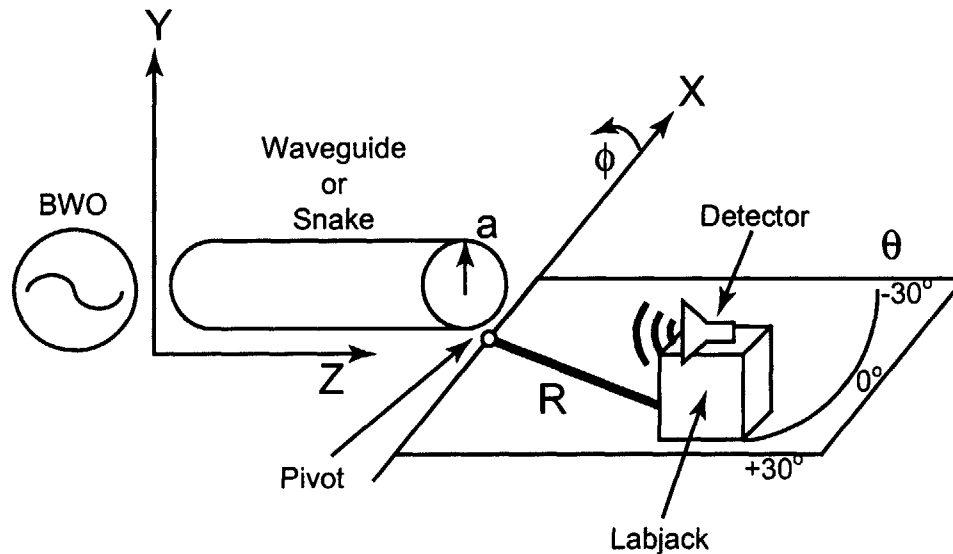


Figure 7-13: Setup of the apparatus for the 1D radiation scans.

where  $\nu_{mp}$  ( $= k_{\perp}a$ ) is the  $p^{\text{th}}$  root of  $J'_m(x)$ , the coordinates  $(R, \theta, \phi)$  are defined in Fig. 7-12, the vertical polarization refers to  $E_{\phi}$  (or the E-field polarized in the  $\hat{y}$ -direction) and the horizontal polarization refers to  $E_{\theta}$  (or the E-field polarized in the  $\hat{x}$ -direction).

This section describes the testing of the mode purity of the new snake (compared to the old snake) in the transmission line by measuring the one-dimensional radiation pattern. The pattern is measured by a diode which is rotated through a large angle in a single plane. This method is used to cold test the new (and old) snake and to hot test the new snake. The cold tests use the chopper and lock-in amplifier setup described in Sec. 3.1.7 to reduce the noise floor of the measurement. The cold tests are performed using the BWO (*c.f.* Sec. 3.1.8) as the source and the hot tests used

Table 7.2: Theoretical mode content of the radiation field from a TE<sub>1,1</sub> to TE<sub>0,1</sub> mode conversion in the new snake.

Power (%)	Mode	Phase
93.8	TE <sub>0,1</sub>	-89°
0.3	TE <sub>1,1</sub>	-131°
5.5	TE <sub>1,2</sub>	17°
0.4	TE <sub>2,1</sub>	56°

the 140 GHz gyrotron oscillator. The setup is shown in Fig. 7-13 which also labels the axes of the coordinate system used. A diode detector and variable attenuator are mounted onto a labjack which is fixed to an arm which has a pivot. The pivot point is located directly beneath the aperture of the launching waveguide. The diode and attenuator unit was incrementally rotated along the polar angle  $\theta$  at a fixed radius. At each angle, the variable attenuator was adjusted to maintain a constant diode signal. The horn was mounted in the orientation for detecting separately  $E_\theta$  and  $E_\phi$ . In the cold tests, the signal is chopped before it reaches the detector and read by a lock-in amplifier for signal enhancement. The radiation was manually measured over an arc of approximately 60° in 1° increments.

### Cold test of new snake

Figure 7-14 shows the far-field radiation scan of the output of the new snake at a distance of 41 cm using the BWO as the 140 GHz radiation source. The vertical polarization is represented by ×'s, the horizontal polarization by +'s, and the theory is shown by the solid line. The design simulations (*c.f.* Sec. 7.2.1) indicate that the power in the modes present at the exit of the mode converter should be broken down into the percentages shown in Table 7.2. When comparing one mode to another, their amplitudes should be normalized such that the integral of the radiation in one mode is equivalent to the other [146]. The theory matches the data up to -12 dB, below which there is the unexpected horizontal component, which should not be present. It may exist if the scan was not taken precisely at  $y = 0$ , or rather because the BWO radiation scan (*c.f.* Fig. 3-12) does not emit a pure mode and itself has this TE<sub>0,1</sub>-like component present. Alternately, it may be a residue from the cross-coupling from the other polarization. However, it is more than 10 dB below the intensity of the vertical polarization and is therefore not significant.

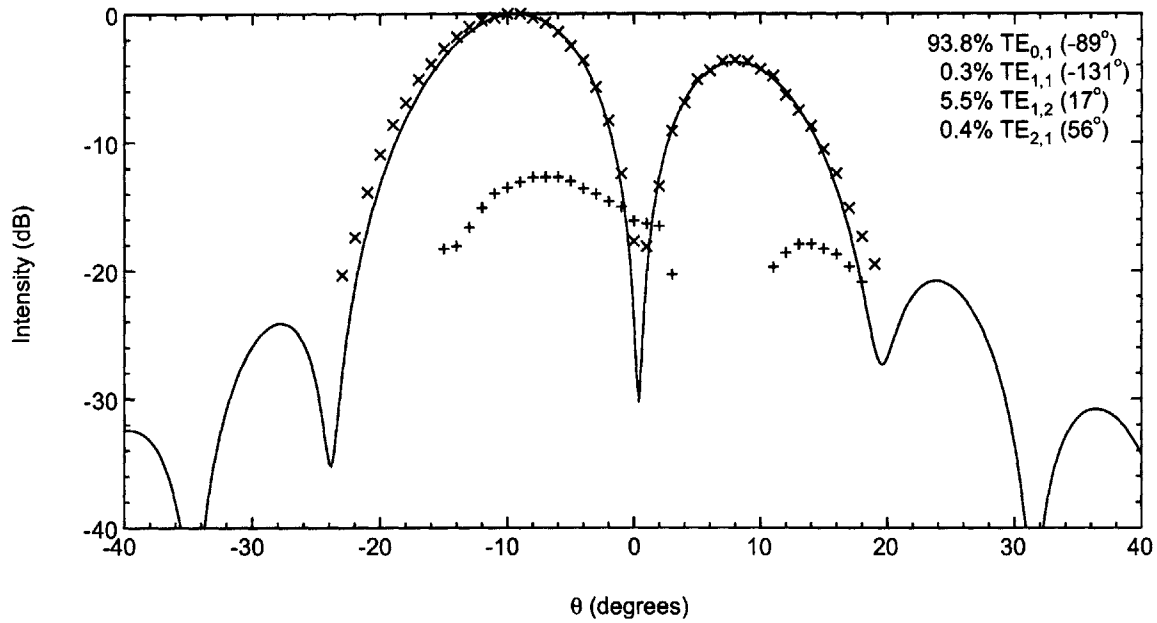


Figure 7-14: Far-field radiation scan of the output of the new snake at 41 cm using the BWO as the source. The vertical polarization is represented by  $\times$ 's, the horizontal polarization by  $+$ 's, and the theory is shown by the solid line. The theoretical mode content of the snake is in the upper right-hand corner.

Table 7.3: Theoretical mode content of the radiation field from a  $TE_{0,1}$  to  $TE_{1,1}$  mode conversion in the new snake.

Power (%)	Mode	Phase
0.3	$TE_{0,1}$	$58^\circ$
93.75	$TE_{1,1}$	$-98^\circ$
5.3	$TE_{1,2}$	$-63^\circ$
0.6	$TE_{2,1}$	$-86^\circ$



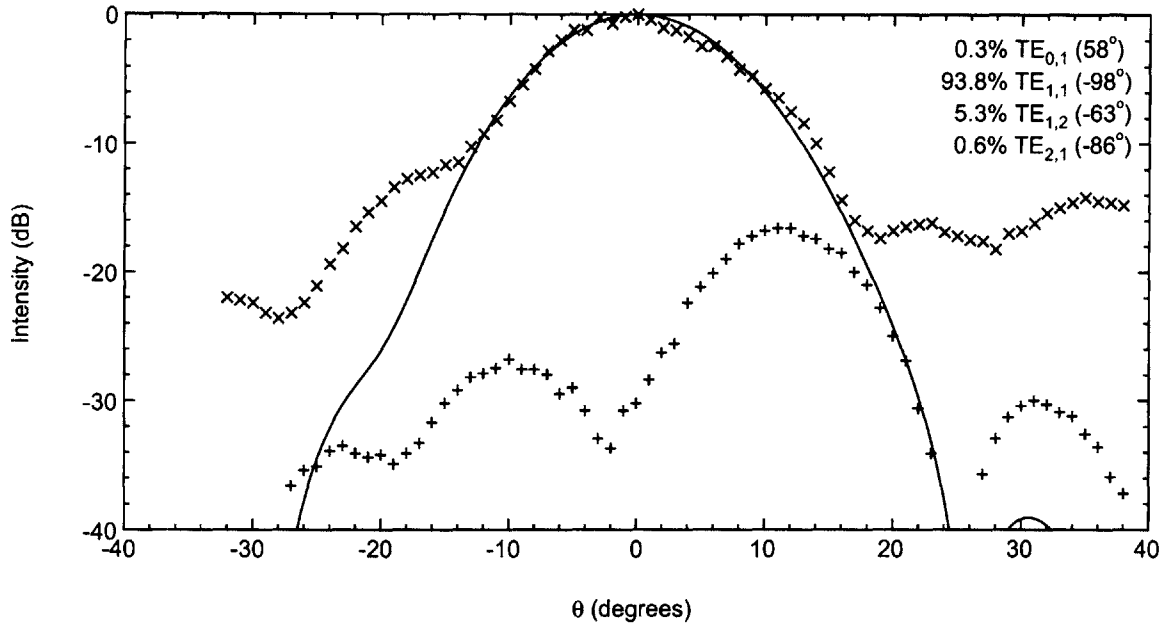


Figure 7-15: Far-field radiation scan of the output of the new snake at 41 cm using the 140 GHz gyrotron as the source. The vertical polarization is represented by  $\times$ 's, the horizontal polarization by  $+$ 's, and the theory is shown by the solid line. The theoretical mode content of the snake is in the upper right-hand corner.

### Hot test of new snake

Figure 7-15 shows the far-field radiation scan of the output of the new snake at a distance of 41 cm using the 140 GHz gyrotron as the source. The vertical polarization is represented by  $\times$ 's, the horizontal polarization by  $+$ 's, and the theory is shown by the solid line. The design simulations (*c.f.* Sec. 7.2.1) indicate that the output power of the mode converter should be broken down into the mode percentages and phases shown in Table 7.3. The theory matches the data up to -15 dB, below which there is the unexpected horizontal component, which should not be present. The horizontal component may exist if the scan was not taken precisely at  $y = 0$  or from cross-coupling in the detector. However, since it is more than -15 dB below the intensity of the vertical polarization it is therefore not significant.

### Cold test of old snake

Figures 7-16 and 7-17 show the far-field radiation scans of the output of the old snake in the forward and reverse configuration at a distance of 41 cm using the BWO at 140 GHz as the source. The vertical polarization is represented by  $\times$ 's, the horizontal polarization by  $+$ 's, and the theory is shown by the solid line. Since the  $TE_{1,1}$  mode is launched into the mode converter, it should function oppositely to its expected

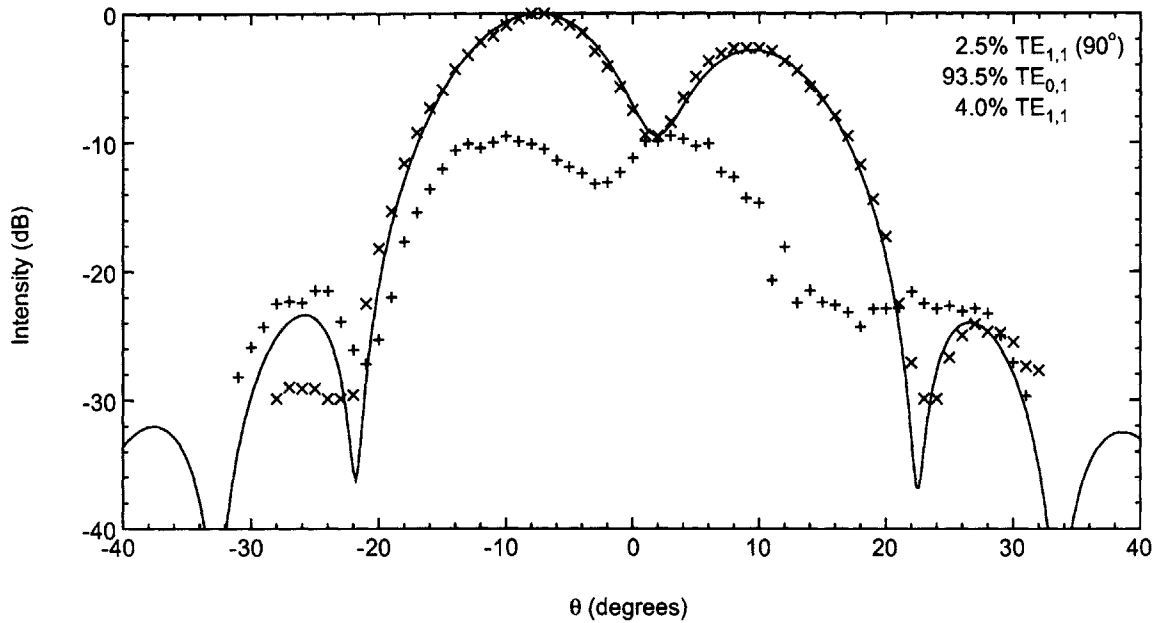


Figure 7-16: Far-field radiation scan of the output of the old snake in the forward configuration at 41 cm using the BWO as the source. The vertical polarization is represented by  $\times$ 's, the horizontal polarization by  $+$ 's, and the theory is shown by the solid line. The mode content of the theory data is in the upper right-hand corner.

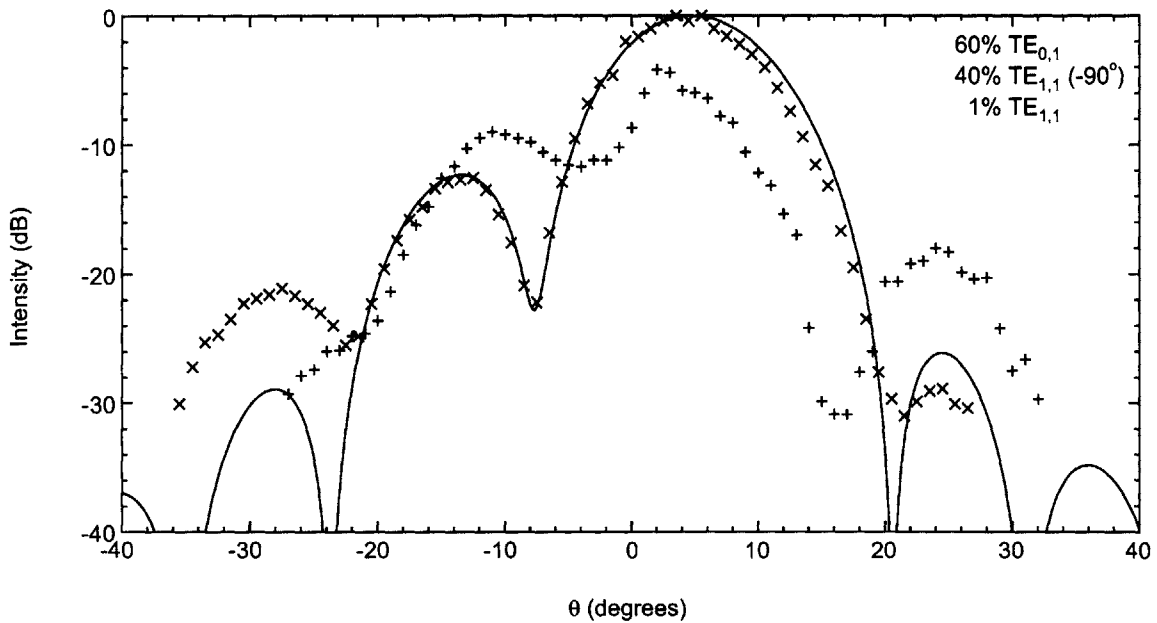


Figure 7-17: Far-field radiation scan of the output of the old snake in the reverse configuration at 41 cm using the BWO as the source. The vertical polarization is represented by  $\times$ 's, the horizontal polarization by  $+$ 's, and the theory is shown by the solid line. The mode content of the theory data is in the upper right-hand corner.

gyrotron performance and the output radiation should be a pure  $TE_{0,1}$  mode. The mode conversion efficiency in the forward configuration is 93.5% when only examining the vertical polarization, however the horizontal polarization (which should not be present) is recorded at -10 dB below the intensity of the vertical polarization. The output of the old snake in the reverse configuration is extremely poor. The mode conversion efficiency is 60% if only examining the vertical polarization, however the horizontal polarization (which should not be present) is recorded at only -5 dB below the intensity of the vertical polarization. The old snake is clearly malfunctioning in a reversed configuration. The snake should be symmetric; with an input of the  $TE_{0,1}$  mode the output should be  $TE_{1,1}$  and vice versa regardless of the configuration being in reverse.

## 7.2 Modifications to the 140 GHz Transmission System

Several modifications were iteratively applied to the 140 GHz transmission system in the direction of improving its performance. They include a new snake mode converter, an overmoded miter bend near the probe, adjustment for the direction of the beam exiting the window, correction for a beat between two consecutive miter mirrors, and a corrugated waveguide. The experimental losses were measured in each configuration.

### 7.2.1 Design of a New $TE_{0,1}$ - $TE_{1,1}$ Waveguide Mode Converter

Based upon the previous assessment, the snake mode converter is inefficiently converting the  $TE_{0,1}$  gyrotron output radiation into the  $TE_{1,1}$  mode for transmission, causing heavy losses in the taper and fundamental waveguide. The design of a new  $TE_{1,1}$  to  $TE_{0,1}$  snake mode converter is presented in this section. Tests on the new snake mode converter were presented in Section 7.1.3

#### Two-mode approach

This section contains the design summary of a  $TE_{0,1}$  to  $TE_{1,1}$  converter using the two-mode approach described in [147]. Conversion of a circular  $TE_{0,1}$  mode to the  $TE_{1,1}$  mode can be achieved by an asymmetrically periodically pipe, perturbed in one plane. This serpentine structure is often referred to as a “snake” (*c.f.* Fig. 7-3). The

radius of this snake can be written as

$$r(z, \varphi) = a + \delta(z, \varphi) \quad (7.8)$$

where  $a$  is the waveguide radius and  $\delta$  is the perturbation. The perturbation can be written in terms of a sinusoid,

$$\delta(z, \varphi) = a\varepsilon_1 \cos\left(\frac{2\pi}{d}z - \varphi\right) \quad (7.9)$$

where  $2\pi/d = |k_{z01} - k_{z11}|$ ,  $k_{z01} (= \sqrt{k^2 - \nu_{01}^2/a^2})$  and  $k_{z11} (= \sqrt{k^2 - \nu_{11}^2/a^2})$  are the propagation constants for the TE<sub>0,1</sub> and TE<sub>1,1</sub> modes,  $\nu_{01} = 3.8317$ , and  $\nu_{11} = 1.8412$ . A coupling coefficient  $K_{01}$  in the TE<sub>0,1</sub> to TE<sub>1,1</sub> conversion is defined such that

$$K_{01} = \frac{1}{R} \left[ \frac{g_1(ka)^2 - h_1}{(k_{z01}a k_{z11}a)^{\frac{1}{2}}} + g_1 (k_{z01}a k_{z11}a)^{\frac{1}{2}} \right] \quad (7.10)$$

where  $R$  is the radius of curvature,  $k_{zmp}$  is the propagation constant,  $\nu_{mp}$  is the  $p^{\text{th}}$  zero of  $J'_m$ , and the parameters  $g_1$  and  $h_1$  are defined by

$$g_1 = 2^{\frac{1}{2}} \nu_{01} \nu_{11}^2 (\nu_{11}^2 - 1)^{-\frac{1}{2}} (\nu_{01}^2 - \nu_{11}^2)^{-2} \quad (7.11)$$

$$h_1 = g_1 \frac{(\nu_{01} + \nu_{11})}{2}. \quad (7.12)$$

The coupling coefficient can be rewritten as

$$K_{01} = -K_{10}^* = i \frac{1}{2\pi} \frac{\nu_{01}^2 \nu_{11}^2 / a^2}{\sqrt{k_{z01} k_{z11}} \sqrt{\nu_{11}^2 - 1} \nu_{01}} \varepsilon_1 \pi. \quad (7.13)$$

Considering only the two modes of interest and their respective amplitudes  $A_0$  and  $A_1$  we obtain

$$\frac{dA_0}{dz} = K_{01} A_1 \quad (7.14)$$

$$\frac{dA_1}{dz} = -K_{01}^* A_0 \quad (7.15)$$

and solve for the amplitudes

$$A_0(z) = \cos |K_{01}|z \quad (7.16)$$

$$A_1(z) = \sin |K_{01}|z. \quad (7.17)$$

Table 7.4: Inputs to the two-mode approach

Length of the snake $L$ (m)	0.93
Waveguide radius $a$ (mm)	6.35
Frequency $f$ (GHz)	140

Table 7.5: Optimum two-mode approach snake parameters

Period length $d$ (cm)	13.0
Number of periods $N$	7.16
Perturbation $a\varepsilon_1$ (mm)	0.3

The length of the period  $d$  is

$$d = \frac{2\pi}{|k_{z01} - k_{z11}|} \quad (7.18)$$

where  $N$  ( $= L/d$ ) is the number of periods. From

$$\sin(|K_{01}|Nd) = 1 \quad (7.19)$$

$$|K_{01}|Nd = \frac{\pi}{2} \quad (7.20)$$

we can finally solve for  $\varepsilon_1$ ,

$$\varepsilon_1 = \frac{\pi}{Nd} \frac{\sqrt{k_{z01}k_{z11}}\sqrt{\nu_{11}^2 - 1}\nu_{01}a^2}{\nu_{01}^2\nu_{11}^2}. \quad (7.21)$$

With a waveguide radius of 6.35 mm and total snake length of 0.93 m, we find an optimized period of 13.0 cm and about seven periods. The perturbation  $a\varepsilon_1$  is found to be 0.3 mm. The optimized parameters are listed in Table 7.5.

### Multi-mode approach

Since multiple modes are too difficult to keep track of analytically, simulations must be performed in order to completely analyze the mode conversion [146]. Using a mode conversion code [148] to analyze multiple modes on our measured snake parameters, a conversion efficiency of 93% is determined. The other modes present at the end of the snake are 5%  $\text{TE}_{1,2}$ , 0.3%  $\text{TE}_{0,1}$ , and 0.6%  $\text{TE}_{2,1}$ . The conversion efficiency of the snake in the multi-mode approach is detailed in Table 7.6. If the number of periods on the snake are increased from seven to eight, the conversion efficiency will increase from 93 to 96%.

Table 7.6: Conversion efficiency of the snake in the multi-mode approach

Mode	Efficiency (%)
TE <sub>1,1</sub>	93.8
TE <sub>1,2</sub>	5.3
TE <sub>2,1</sub>	0.6
TE <sub>0,1</sub>	0.3

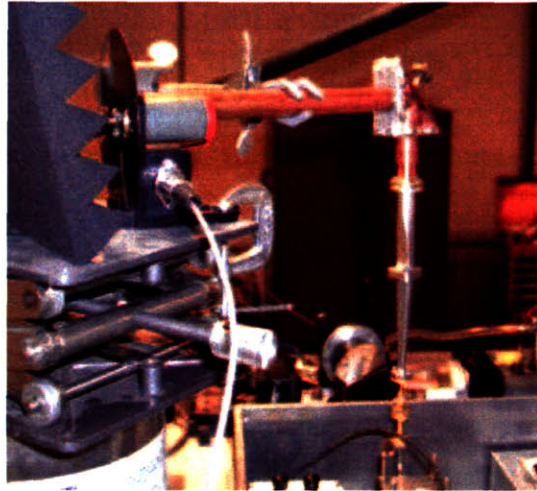


Figure 7-18: Photograph of the 140 GHz overmoded miter bend assembly in the insertion loss test setup. The chopper is on the labjack on the left side and the receiver is located on the bottom.

### Implementation

The wriggles of the new snake mode converter were carved into halves of a block of solid aluminum and a copper pipe was heated and set into the block, whereupon it was fastened.

### 7.2.2 Overmoded Miter Bend Near Probe

An overmoded miter bend assembly was designed by Woskov et al. [149] to replace the fundamental waveguide bend to the DNP probe, since fundamental waveguide in general is lossy. The miter bend featured a coupling hole to provide a proportional signal to the microwave power since this component would also replace the fundamental directional coupler.

The assembly consists of a 28.4 cm section of cylindrical copper waveguide of inner diameter 1.27 cm, a miter mirror with output coupling hole to provide a -30 dB signal

proportional to the microwave power, followed by a tapered segment of 7.0 cm length to a 1.19 cm inner diameter, a WR-42 circular to rectangular transition (Aerowave, Part No. 01-10(42)) connected to a rectangular WR-42 to WR-8 transition and is shown in Fig. 7-18. Measurements were taken with a 137 GHz heterodyne receiver using liquid nitrogen cooled Eccosorb as the source of radiation. The receiver double side bandwidth covered 135.5 -136.6 GHz and 137.4 - 138.5 GHz. The measurement approach was to use a single mode receiver with a multimode source rather than a single mode source with a multimode detector because our BWO is not isolated and is very sensitive to microwave circuit changes that precluded sensitive insertion loss measurements. The results show that the fundamental bend assembly had an insertion loss of -1.21 dB to a pure  $TE_{1,1}$  mode compared to -1.64 dB in the overmoded miter bend assembly.

Hot test results [150] show that the 140 GHz gyrotron system did not benefit significantly from the change to a new, oversized miter bend, therefore the setup was reverted to the previous configuration (*c.f.* Fig. 7-2). While the new miter bend assembly transmitted more power around the  $90^\circ$  bend, high losses were recorded after taper. As a result, power reaching the sample is not very different with the fundamental waveguide bend as compared to the new overmoded miter bend. The downtaper used after the miter bend was designed for a low frequency band where it operates in a single mode. Since it was not specifically designed for use with a mode at 140 GHz, the poor observed result can be accounted for.

### 7.2.3 Oblique Gyrotron Beam

The gyrotron beam was found to be angling upward with respect to the horizon, at an angle of more than two degrees. Three options for compensating for the upward tilt were identified and discussed. The first proposal was to rotate the gyrotron tube on axis to direct the beam downward by two degrees to achieve radiation propagating parallel to the plane of the floor. Second, the tilt-table support upon which the gyrotron rests could be translated to tilt the gyrotron beam downward and readjust the tube position to null out body current. The third possibility was to modify the transmission line to account for the tilt.

The advantages of the first two options are that the transmission line would not have to be modified. The disadvantage of the first option is the additional strain on a fragile glass electrical break section and water hoses that would constrain rotation, with an outside possibility that too much strain on the tube during the rotation could cause irreparable damage. The disadvantage of the second option is that in the stray magnetic field environment it could become a tedious job to reposition the tube

to null out the body current and still have high power millimeter-wave operation. In addition, continuous-wave body current could be extremely damaging to the internal components of the tube.

The third option of modifying the transmission line was the least invasive, therefore a short two degree waveguide bend was substituted at the tube output before the external mode converter, removing the need to move the gyrotron or modify the bulk of the transmission line after the short piece. In a bent circular waveguide, it is possible to convert the  $TE_{0,1}$  mode into the  $TM_{1,1}$ . In a cylindrical waveguide of radius  $a$  ( $= 0.635$  cm) and wavelength  $\lambda$  ( $= 0.214$  cm), since the curvature coupling coefficient is [146]

$$A_{01} = \cos \frac{\pi\theta}{2\theta_c} = 0.99 \quad (7.22)$$

where  $\theta_c$  ( $= 77.6\lambda/a = 26^\circ$ ) is the Jouguet critical angle, the mode conversion is negligible.

The total measured losses in this configuration were very low, totalling 4.5 dB.

## 7.2.4 Beat

We identified a beat in the 140 GHz transmission line in the vertical section of the overmoded cylindrical waveguide. A beat is caused by a mismatch somewhere in the system causing a reflection and standing wave. In our case, the reflection is between the miter mirrors, and its path length can be characterized as an integral multiple of

$$l = \frac{2\pi}{k_{z11} - k_{zmp}} \quad (7.23)$$

where  $k_{zmp}$  is the propagation constant for the interfering mode and  $k_{z11}$  is the propagation constant for the transmitting  $TE_{1,1}$  mode. We detected this issue by meticulous study of the transmission system in various abbreviated configurations and by noting that an increase in length of the vertical waveguide corresponded with an increase of transmitted power. As corrective action, the second miter bend of the transmission line was re-fabricated and installed.

## 7.2.5 Corrugated Waveguide

The waveguide ohmic wall loss is proportional to the square of the tangential magnetic field components at the wall, where in cylindrical waveguide these components are the axial magnetic field component  $H_z$  and azimuthal magnetic field component  $H_\phi$ . In overmoded metallic corrugated waveguide, when both the waveguide radius  $a$  becomes



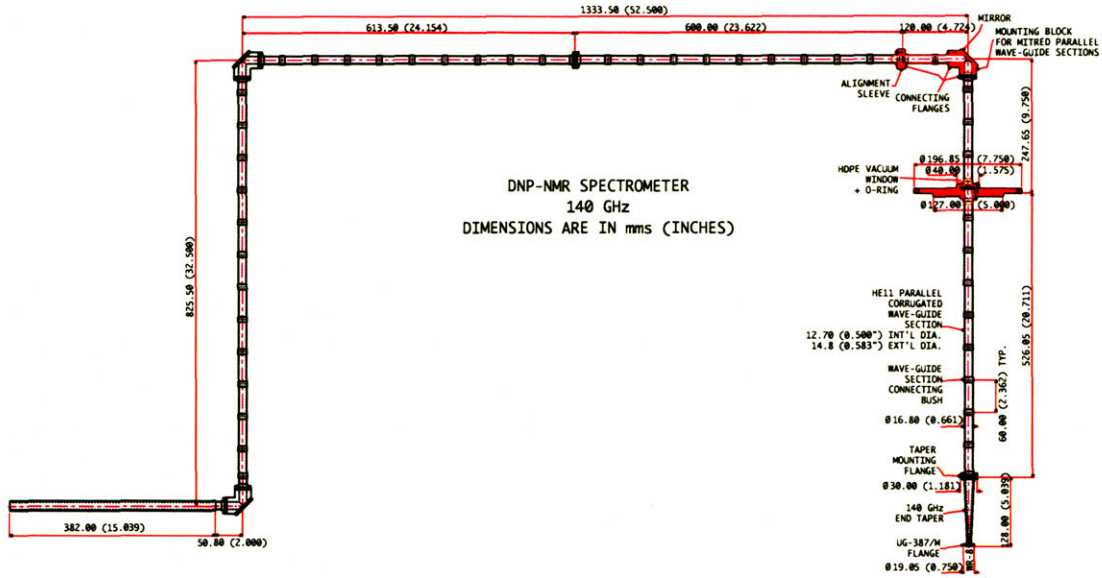


Figure 7-19: Corrugated waveguide transmission system for the 140 GHz gyrotron by Thomas Keating, Ltd. [16].

large and the period of corrugations becomes small compared to the wavelength, the waveguide wall will begin to resemble a surface with an anisotropic reactance [131],

$$Z_{\phi} = \frac{E_{\phi}}{H_z} \Big|_a = 0 \quad (7.24)$$

$$Z_z = -\frac{E_z}{H_{\phi}} \Big|_a \simeq jZ Z_0 \quad (7.25)$$

where  $Z$  is a normalized reactance and

$$Z_0 = \sqrt{\frac{\mu_0}{\epsilon_0}}. \quad (7.26)$$

The wall loss will then become small when the wavelength becomes small with respect to the radius. The mode which is supported in this waveguide configuration is the  $HE_{1,1}$  quasi-Gaussian mode which has very low fields at the walls. The  $HE_{1,1}$  mode couples directly to the fundamental free-space Gaussian mode with less than 2% loss.

Figure 7-19 shows a 140 GHz corrugated transmission system that was designed and built by Thomas Keating, Ltd. as a replacement for the copper smooth-wall waveguide transmission system. In addition to replacing the overmoded waveguide, the corrugated system would also replace the fundamental waveguide in the bore of the 211 MHz NMR magnet. However a requirement to make use of this waveguide is the construction of a new 211 MHz/140 GHz DNP probe which couples to the

corrugated transmission line. At the time of this writing, this has not occurred.

## 7.2.6 Theoretical Transmission Line Losses

Theoretical losses of the transmission system were calculated for comparison with the experimentally measured losses of various configurations. Both diffraction losses and ohmic losses were present in the system. Diffraction losses were present in the miter mirrors while mode propagation through the waveguide resulted in ohmic losses. The losses in two transverse electric modes are compared to the free-space coupling HE<sub>1,1</sub> mode.

### Diffraction losses

The miter bends in the transmission line can be modeled as gaps in a multimode waveguide and can be described by using both waveguide and optical properties. For the TE<sub>0,1</sub>, TE<sub>1,1</sub>, and HE<sub>1,1</sub> modes, the analytical solution for the total losses  $1 - |A_0|^2$ , where  $A_0$  is the normalized modal amplitude of the incident mode coupled to the waveguide, can be expressed as [151]

$$1 - |A_{01}|^2 = \frac{2}{\sqrt{\pi}} \frac{\nu_{01}^2}{3} \left( \frac{L}{k_0 a^2} \right)^{\frac{3}{2}} \quad (7.27)$$

$$1 - |A_{11}|^2 = \frac{2}{\sqrt{\pi}} \left[ \frac{1}{\nu_{11}^2 - 1} \sqrt{\frac{L}{k_0 a^2}} + \frac{\nu_{11}^2}{3} \left( \frac{L}{k_0 a^2} \right)^{\frac{3}{2}} \right] \quad (7.28)$$

$$1 - |A_{\text{HE}_{1,1}}|^2 = \frac{2}{\sqrt{\pi}} \frac{\nu_{\text{HE}_{1,1}}^2}{3} \left( \frac{L}{k_0 a^2} \right)^{\frac{3}{2}} \quad (7.29)$$

where  $A_{mp}$  is the modal amplitude,  $k_0$  ( $= 2\pi f/c$ ) is the wave number in free space,  $a$  is the waveguide radius,  $L$  is the gap length,  $\nu_{mp}$  is the Bessel function root of a TE <sub>$m,p$</sub>  mode, and  $\nu_{\text{HE}_{1,1}}$  is the root of the characteristic equation of the HE<sub>1,1</sub> mode. In our case, the frequency  $f$  is 140 GHz,  $a$  is 6.35 mm, and  $L$  is twice the waveguide radius, therefore the diffraction losses in the TE<sub>0,1</sub>, TE<sub>1,1</sub>, and HE<sub>1,1</sub> modes are 0.8 dB, 0.9 dB, and 0.33 dB, respectively.

## Ohmic losses

The ohmic losses in overmoded waveguide are generally small for our application. Power flow in a waveguide is of the form

$$P_T = P_0 e^{-2\alpha z}. \quad (7.30)$$

In order for energy to be conserved, the rate of decrease of the total power  $P_T$  must equal the time average power loss  $P_L$  per unit length,

$$P_L = -\frac{dP_T}{dz} = 2\alpha P_T. \quad (7.31)$$

The attenuation constant is defined as the ratio of the power lost per unit length and twice the power transmitted,

$$\alpha = \frac{P_L}{2P_T}. \quad (7.32)$$

For transverse electric modes, the power loss per unit length is given by

$$P_L = \frac{1}{2} R_s \int \int_S |\mathbf{H}_{\text{tan}}|^2 ds \quad (7.33)$$

where the magnetic field tangential to the waveguide walls  $\mathbf{H}_{\text{tan}}$  is composed of azimuthal and axial components

$$\mathbf{H}_{\text{tan}} = \mathbf{H}_\phi + \mathbf{H}_z. \quad (7.34)$$

The transmitted power is given by

$$P_T = \frac{1}{2} \text{Re} \int_0^{2\pi} \int_0^a (\mathbf{E} \times \mathbf{H}^*) \cdot \hat{\mathbf{z}} r dr d\phi. \quad (7.35)$$

For a cylindrical waveguide of radius  $a$ , the attenuation constant for transverse electric modes is given by [152]

$$\alpha = \frac{R_s}{a\eta_0} \frac{\frac{\nu_{mp}^2}{k^2 a^2} + \frac{1}{\nu_{mp}^2 - 1}}{\sqrt{1 - \frac{\nu_{mp}^2}{k^2 a^2}}} \quad (7.36)$$

where  $\delta$  ( $= \sqrt{1/\pi f \mu_0 \sigma}$ ) is the skin depth and  $R_s$  ( $= 1/\sigma\delta$ ) is the surface resistance. In our case, for a waveguide of radius 6.35 mm at 140 GHz, the ohmic losses for the  $\text{TE}_{0,1}$ ,  $\text{TE}_{1,1}$ , and  $\text{HE}_{1,1}$  modes are 0.015 dB/m, 0.16 dB/m, and 0.008 dB/m,

Table 7.7: 140 GHz theoretical transmission line losses for transmission of the TE<sub>0,1</sub>, TE<sub>1,1</sub>, and HE<sub>1,1</sub> modes.

Mode	Diffraction losses (dB)	Ohmic losses (dB/m)	Total losses (dB)
TE <sub>0,1</sub>	0.8	0.015	–
TE <sub>1,1</sub>	0.9	0.16	3.7
HE <sub>1,1</sub>	0.33	0.008	2.6

respectively.

### Total theoretical losses

The total theoretical losses of the transmission system until the downtaper can be obtained from the summation of the diffraction and ohmic losses which have previously been calculated. For the TE<sub>1,1</sub> mode, the total transmission losses are given by;

$$\begin{aligned}
 \text{TE}_{1,1} \text{ losses} &= 0.31 \text{ dB (snake efficiency)} \\
 &+ 0.16 \text{ dB/m} \times 1 \text{ m (snake ohmic)} \\
 &+ 0.16 \text{ dB/m} \times 2.5 \text{ m (waveguide ohmic)} \\
 &+ 0.9 \text{ dB} \times 2 \text{ (miter bends)} \\
 &+ 1 \text{ dB (downtaper ohmic)} \\
 &= 3.7 \text{ dB}
 \end{aligned}$$

For the HE<sub>1,1</sub> mode, the total transmission losses are given by;

$$\begin{aligned}
 \text{HE}_{1,1} \text{ losses} &= 0.31 \text{ dB (snake efficiency)} \\
 &+ 0.16 \text{ dB/m} \times 1 \text{ m (snake ohmic)} \\
 &+ 0.5 \text{ dB (efficiency of TE}_{1,1} - \text{HE}_{1,1} \text{ mode converter)} \\
 &+ 0.008 \text{ dB/m} \times 2.5 \text{ m (waveguide ohmic)} \\
 &+ 0.33 \text{ dB} \times 2 \text{ (miter bends)} \\
 &+ 1 \text{ dB (downtaper ohmic)} \\
 &= 2.6 \text{ dB}
 \end{aligned}$$

Table 7.7 summarizes the total theoretical transmission line losses for the TE<sub>0,1</sub>, TE<sub>1,1</sub>, and HE<sub>1,1</sub> modes. The TE<sub>1,1</sub> mode is presently used as the mode of propagation through the waveguide and miter bends. Conversion to the HE<sub>1,1</sub> mode would improve

Table 7.8: Losses in the 140 GHz transmission line in four configurations.

Component	Measured loss (dB)				Theor. loss (dB) [TE <sub>1,1</sub> ]
	[Old snake]	[New snake]	[Miter assembly]	[Oblique beam]	
	7 Feb 02	2 Jan 02	8 Mar 02		
Snake mode converter	1.0	1.0	1.0	–	0.47
Waveguide, two miter bends	1.5	1.4	1.4	–	2.2
Downtaper to fundamental w.g.	3.9	3.4	–	–	1
Circular-rectangular transition	1.7	1.5	–	–	–
Fundamental w.g. bend	0.6	0.6	–	–	–
Miter bend assembly	–	–	6.6	–	–
Total	8.7	7.9	9.0	4.5	3.7

the transmission system by more than 1 dB.

### 7.2.7 Summary of Experimental Losses

Using dry calorimetry, we measured the losses along the transmission system in the various configurations. This summary is presented in Table 7.8. The losses with the original configuration amounted to 8.7 dB. We found that the configuration involving the compensation for the oblique gyrotron beam most significantly reduced the transmission losses; the losses were reduced to 4.5 dB, which is comparable to the theoretical losses of 3.7 dB, since the theoretical losses in the fundamental waveguide are not considered. The other configurations, including implementation of the new snake and miter bend assembly, did not significantly reduce the transmission line losses; the losses with the new snake and the overmoded miter bend assembly resulted in total losses of 7.9 and 9.0 dB, respectively. The losses in these configurations are likely due to transmission of an impure mode and are predominantly incurred in the downtaper to fundamental waveguide.

## 7.3 Summary and Discussion

In this section, we discussed the transmission line of the 140 GHz gyrotron used in DNP studies, focusing on improving the losses. As the first stage in the 140 GHz transmission, we examined the mode purity of the gyrotron output and external mode converter output through two-dimensional radiation pattern scans. We presented the

two-dimensional experimental  $TE_{0,1}$  radiation patterns from both polarizations of the gyrotron in Figs. 7-6(a) and (b). An aggregate radiation pattern was generated from the combination of both polarizations and is shown in Fig. 7-8(a). We determined that the proper mode was being emitted from the gyrotron and that the internal mode converters were functioning properly because the captured radiation fields strongly resembled the theoretical radiation patterns, where the theoretical composite radiation is given in Fig. 7-8(b) and the theoretical polarizations in Figs. 7-6(c) and (d).

Similarly, we analyzed the two-dimensional radiation patterns from the  $TE_{0,1}$ - $TE_{1,1}$  “snake” external mode converter (*c.f.* Figs. 7-9(a) and (b)). An aggregate radiation pattern was generated from the combination of both polarizations and is shown in Fig. 7-8(c). The composite pattern was compared with the theoretical radiation pattern in Figs. 7-8(d) and the experimental polarizations were compared with the theoretical polarizations in Figs. 7-9(c) and (d). We concluded that since the horizontal polarization of the snake output strongly resembled that of the  $TE_{0,1}$  mode instead of the  $TE_{1,1}$  mode that it must not be functioning at optimum efficiency and that since this component should be very small in comparison to the vertical polarization that it must come mostly from the  $TE_{0,1}$  mode. From this, we calculated with this hypothesis in (7.2) through (7.4) that the old snake may be operating at as little as 60% efficiency.

A statistical plot was generated assuming that the composite output of the mode converter is a combination of the  $TE_{1,1}$  and  $TE_{0,1}$  modes at some phase difference. This analysis ignores the extra polarization information that was available. The fit resulted in a comparable efficiency to the previous estimate, however the results of the statistical analysis show the entire fitting surface is enclosed by the 75% confidence contour. Therefore, the separate measurement of each polarization component was deemed critical for mode content analysis, while a detector measuring absolute intensity alone should not be expected to give informative results for the measurement in a single plane.

Increase of the efficiency of the transmission system was accomplished through the scientific method. A new  $TE_{0,1}$  to  $TE_{1,1}$  waveguide mode converter was designed as the first in a series of iterative modifications to the 140 GHz transmission system to increase the power transmission efficiency. The design was carried out using both a two-mode and multi-mode approach yielding similar results. For the two-mode approach we found that the existing snake design was approximately accurate and with the multi-mode approach we found that increasing the number of periods from seven to eight would increase the snake efficiency from 93% to 96%. However, it

was determined that it was the fabrication of the snake that was lacking; the forced perturbations of the old snake had relaxed over time such that their amplitudes became nonuniform. The implementation of the new snake consisted of a serpentine groove carved into halves of a block of solid aluminum with a cylindrical copper pipe inserted into the groove. Since there are no clamps to release their hold, the new snake should retain its shape over extremely long periods of time.

Other configurations of the 140 GHz transmission system included an overmoded miter bend near the probe to replace the lossy fundamental waveguide bend, compensation for an oblique gyrotron beam, adjustment of the overmoded vertical copper smooth-wall waveguide to eliminate a beat frequency, and corrugated waveguide. We found that the configuration involving the compensation for the oblique gyrotron beam most significantly reduced the transmission losses to 4.5 dB from 9 dB. The reduced figure is comparable to the theoretical losses predicted of 3.7 dB, where the theoretical loss figure does not include the losses in the fundamental waveguide components and is for this reason almost certainly higher than the quoted figure. If the output waveguide couples to the gyrotron beam at an oblique angle, the radiation in the waveguide will spread uniformly throughout the cross-section and essentially become a “flashlight” beam; this type of beam will convert poorly in the mode converter resulting in higher losses ultimately incurred in the downtaper. The other configurations, including implementation of the new snake, did not significantly reduce the transmission line losses. The losses in these configurations are likely due to transmission of an impure mode and are predominantly incurred in the downtaper to fundamental waveguide.

Theoretical transmission line loss calculations show that conversion to and transmission in the  $HE_{1,1}$  quasi-Gaussian mode would increase the transmission efficiency by over 1 dB. Corrugated waveguide would need to be implemented since smooth-wall waveguide does not support this mode of propagation. A corrugated waveguide was purchased but, as of this writing, has not yet been installed.





# Chapter 8

## Conclusions

A continuous-wave second harmonic gyrotron oscillator at 460 GHz has successfully been demonstrated during the course of this work, allowing the highest field DNP experiments to date. The success of experiments on three gyrotron oscillators, at 460, 250, and 140 GHz makes an important contribution to the body of knowledge on the development of high frequency, CW, second harmonic, and low power gyrotrons. The 460 GHz gyrotron generates the highest CW power at this frequency to the author's knowledge. The 250 GHz gyrotron has been operated continuously for 10 days with good stability of the output power regulated under computerized control.

### 8.1 460 GHz Second Harmonic Gyrotron Oscillator

During the course of this work, the highest CW power at 460 GHz has been generated: over 8 W CW [113]. This achievement is the result of the title of the thesis research: a design and experimental study of a 460 GHz CW second harmonic gyrotron oscillator.

The gyrotron is a vacuum electron device that produces over 8 W of average power at the second harmonic of the electron cyclotron frequency through an interaction between a mildly relativistic electron beam and electromagnetic field in a static magnetic field. Design at high frequency, second harmonic, and low beam power is challenging because the latter two involve lower gain than at fundamental modes and all three necessitate higher  $Q$  cavities. However, ohmic loss introduces obstacles in attaining the high  $Q$  values necessary to lower the starting current into the range of the electron gun. The submillimeter wave regime is lacking in high average power devices, and this device generates the highest CW power at this frequency to the author's knowledge. The gyrotron, exhibiting stability under complete computer control, will

enable dynamic nuclear polarization, a type of sensitivity enhanced nuclear magnetic resonance applied to solid state NMR, at 700 MHz ( $^1\text{H}$ ).

The gyrotron's operation was characterized through both short pulses [1] and CW operation. Ohmic loss measurements at the second harmonic design mode confirmed the RF efficiency of the device. Nonlinear simulations verified the output power and overall efficiency.

Diagnostic radiation pattern measurements were performed using an array of pyroelectric sensors to simultaneously capture the entire beam. This measurement yielded an rf beam waist that was 4% elliptical for the 460 GHz design.

Hollow dielectric overmoded waveguide was tested at both the second harmonic and fundamental frequencies for feasibility in a low loss transmission system capable of delivering power to the NMR sample. Though experimental losses at 460 GHz that were somewhat higher than their predicted theoretical counterpart, the explanation likely lies in a combination of degradation due to surface roughness and curvature of the waveguide.

We demonstrated broadband continuous frequency tuning of the fundamental modes of the oscillator over a range of more than 2 GHz through variation of the magnetic field alone [1]. We interpret these results in terms of smooth transitions between higher order axial modes of the resonator and verified them with nonlinear and linear simulations.

The detailed studies of a low voltage fundamental  $\text{TE}_{2,3}$  mode reveal that the mode can be excited with less than 7 W of beam power at less than 3.5 kV. Using this mode, a study of axial mode competition was performed revealing that one axial mode dominated at a parameter set with small but finite contamination of another axial mode. Discrete transitions between axial modes were evidenced through variation of the beam current. Results were verified with nonlinear simulation.

## 8.2 250 GHz Gyrotron Oscillator Experiments

In a related experiment, second harmonic operation of a nominally 250 GHz gyrotron oscillator was characterized to verify the possibility of second harmonic excitation at 460 GHz. Fundamental operating parameters were also characterized. A computer-controlled stable CW source, the 250 GHz gyrotron was the first gyro-device specifically designed with the purpose of seamless integration into an NMR spectrometer [92].

Under complete computer control, the gyrotron's operation for over 10 days has been observed, yielding a power stability of better than 1% and frequency stability of

better than 400 Hz. This advance is due to two factors; first, a corrugated transmission system was designed and built to replace the smooth-wall waveguide enabling low loss quasi-Gaussian transmission, thereby extending this well-established technology to an even higher frequency of 250 GHz. The new corrugated transmission system incorporates a quasi-optical directional coupler which allows for the forward and reflected output power to be digitally sampled. Secondly, it was determined that constant beam current control is insufficient to regulate the gyrotron output power over long periods of time due to a slow drift in the output power over time. The control system was modified to allow regulation of the output power which is sampled directly from the beam splitter feedback.

The mode characterization experiments yielded results of extremely low second harmonic start oscillation currents, as low as 12 mA for a mode with one axial variation and as low as 47 mA for a mode with two axial variations. The low starting currents were attributed to an elevated cavity  $Q$  which is confirmed by previous cavity thermal load measurements. While initially an attractive theory, an off-axis beam is demonstrated to not be responsible for the low start currents.

Radiation intensity patterns were measured using three techniques: thermal paper, liquid crystal paper, and an array of pyroelectric sensors. The liquid crystalline technique was adapted from a technique employed in temperature measurements in electronic devices. Originally employed for use in diagnosing laser beams, we demonstrate the first use of a pyroelectric camera at millimeter frequencies.

### 8.3 140 GHz Gyrotron Oscillator Experiments

The study of the microwave transmission and mode conversion system of a 140 GHz gyrotron oscillator was presented. The 140 GHz gyrotron was the first gyro-device ever used for dynamic nuclear polarization. The losses were characterized under a succession of iterative configurations for optimization of power transmission. The iterations included the design and implementation of a new waveguide  $TE_{0,1}$  to  $TE_{1,1}$  mode converter. The result of this study was a reduction of the total loss of the transmission system from nearly 9 dB to 4.5 dB, a figure that approaches the theoretical loss figure calculated at 3.7 dB. Radiation pattern measurements using a mechanical scanner recorded for the gyrotron output and for the original waveguide mode converter and its replacement were used as a diagnostic for the mode converter design.

Table 8.1: Frequency dependence on operating parameters

Parameter	Sensitivity		
	460 GHz second harmonic	250 GHz fundamental	140 GHz [18] fundamental
Beam current	0.4 MHz/mA	–	30 kHz/mA
Magnetic field	3.0 GHz/T	5.3 GHz/T	1.1 GHz/T
Beam voltage	50 MHz/kV	86 MHz/kV	10 MHz/kV
Cathode magnetic field	1.3 GHz/T	12.3 GHz/T	–
Cavity temperature	–	< 1 MHz/°C	2.2 MHz/°C

## 8.4 Gyrotron Comparisons

Due to the experimentation in this work on three separate gyrotron oscillators with frequencies ranging widely from 460 through 140 GHz, it is possible to draw conclusions between the three experiments.

### 8.4.1 Frequency Pulling

A comparison of the frequency pulling at three frequencies in the second harmonic and fundamental is presented in Table 8.1. A simple argument tells us that the emission frequency  $\omega$  is  $n$  times the cyclotron frequency  $\omega_c$  and that the cyclotron frequency  $\omega_c (= eB/\gamma m_e)$  is proportional to the magnetic field  $B$  and inversely proportional to the voltage since the relativistic factor  $\gamma (= 1 + V_c/511)$  relies on the beam voltage. Based on this argument, the magnetic and voltage frequency pulling should be twice as great for the second harmonic as for the fundamental. The 460 GHz frequency sensitivity to operating parameters is indeed larger for the 460 GHz second harmonic than for the 140 GHz fundamental. However, the 250 GHz fundamental frequency sensitivity is larger than either. This can be explained by the use of the longitudinal mode with two variations as the operating mode.

### 8.4.2 Radiation Patterns

In the three experiments, radiation intensity patterns were measured using four techniques: a mechanized scanner with digital attenuator, thermal paper, liquid crystal paper, and an array of pyroelectric sensors. The liquid crystalline technique was used in the 250 GHz experiments and was adapted from a technique employed in temperature measurements in electronic devices. We present a technique for recovering

quantitative information applicable to millimeter and submillimeter-waves from these measurements. Originally employed for use in diagnosing laser beams, in the 250 GHz experiments we demonstrate the first use of a pyroelectric camera at millimeter-wave frequencies. The pyroelectric camera was also used with the 460 GHz gyrotron to image four different frequencies. Thermal paper was used in all three experiments to take quick permanent images of the beam. Thermal paper was especially useful in locating the beam axis of propagation.

## 8.5 Future Work

The studies described in this thesis have laid the groundwork for 700 MHz ( $^1\text{H}$ )/460 GHz DNP. The critical component, the 460 GHz gyrotron oscillator, has been designed, constructed, and successfully operated at continuous duty. However, several tasks remain in order to perform sensitivity-enhanced NMR through dynamic nuclear polarization.

Obviously, the gyrotron output power must be transmitted to the DNP probe. Initial studies have been conducted on the use of hollow dielectric waveguide as the transmission line. While for a fixed radius the transmission properties of dielectric waveguide become better with increasing frequency, initial measurements show that losses using an acrylic waveguide with 2.54 cm diameter at 460 GHz are 1.0 dB/m. Since the gyrotron needs to be located sufficiently remote (5 m) to the 16.4 T, 700 MHz NMR magnet in order to avoid the fringe field in the region of the electron gun, this is not a feasible option for a transmission system. A mitigating factor is that the theoretical losses in dielectric waveguide are significantly reduced by choosing a larger radius. This is countered by the difficulty of aligning large radius waveguide. Corrugated waveguide, which was successfully implemented at 250 GHz with very low insertion loss [2], is a likely candidate for the 460 GHz transmission system. Confined transmission has several advantages over quasi-optical transmission. Specifically for the DNP experiment, the gyrotron output power must couple successfully to the DNP probe. Since a DNP/NMR probe can be oriented in any direction inside the superconducting NMR magnet, there is no obvious way to guarantee repeatable alignment with the rf beam using quasi-optical transmission. Waveguide transmission has the added benefit of being confined and therefore safer for users than free-space transmission; a focused free-space rf beam can be extremely dangerous. Additionally, the alignment of waveguide is more rigid and easier than the alignment of mirrors, which may relax their position frequently and require an alignment laser to align the invisible rf beam each use. Finally, both mirrors and corrugated waveguide can

theoretically transmit the rf beam with low loss.

The gyrotron has only operated under computer control in the second harmonic design mode for a little over an hour at continuous duty. While this is sufficient for the most basic of DNP experiments, it is insufficient for the study of complex biological systems. It is possible that the gyrotron could be shut down intermittently to recover, however the underlying issue which should directly be confronted is likely a thermal issue in the electron gun. In the present configuration, the ceramic break is the only component in the electron gun which is cooled, and this is achieved with low pressure compressed air. To allow for longer periods of operation, the anode cooling channel, which presently is unconnected, should be directly connected to the recirculating chiller or to the output of the cavity cooling channel.

The final task to be completed in order to successfully perform DNP is to change the cavity radius. The actual gyrotron output frequency of 458.6 GHz is too far from the desired frequency of slightly above 460 GHz for the sweep coil in the NMR magnet to match. The cavity radius should be scaled by the appropriate factor and electroformed with a higher tolerance on the mandrel.

# Bibliography

- [1] Melissa K. Hornstein, Vikram S. Bajaj, Robert G. Griffin, Kenneth E. Kreischer, Ivan Mastovsky, Michael A. Shapiro, Jagadishwar R. Sirigiri, and Richard J. Temkin. Second harmonic operation at 460 GHz and broadband continuous frequency tuning of a gyrotron oscillator. *IEEE Trans. Electron Devices*, 52(5):798–807, May 2005.
- [2] P.P. Woskov, V.S. Bajaj, M.K. Hornstein, R.J. Temkin, and R.G. Griffin. Corrugated waveguide and directional coupler for CW 250 GHz gyrotron DNP experiments. *IEEE Transactions on Microwave Theory and Techniques*, June 2005.
- [3] J.P. Anderson. Private communication, May 2003.
- [4] V.A. Flyagin, A.V. Gaponov, I. Petelin, and V.K. Yulpatov. The gyrotron. *IEEE Transactions on Microwave Theory and Techniques*, 25(6):514–521, June 1977.
- [5] A. Hislop. Private communication. Pacific Millimeter Products., August 2002.
- [6] M.N. Afsar. Private communication, October 1983.
- [7] M.N. Afsar. Dielectric measurements of millimeter-wave materials. *IEEE Trans. Microwave Theory Techn.*, 32(12):1598–1609, December 1984.
- [8] J. Tarter. Private communication. Semicon Associates., November 2001.
- [9] Wayne McGhee. Private communication. Cryomagnetics, Inc., May 2001.
- [10] David Rayner. Private communication. Magnex Scientific., June 2002.
- [11] I. Ogawa, T. Idehara, and W. Kasperek. Design of a quasi-optical mode conversion system with variable output beam size. *Int. J. Electron.*, 87(4):457–467, 2000.
- [12] A.K. Ganguly and S. Ahn. Non-linear analysis of the gyro-BWO in three dimensions. *Int. J. Electron.*, 67(2):261–276, August 1989.
- [13] William M. Siebert. *Circuits, Signals, and Systems*, section 17.1, pages 508–519. MIT Press, Cambridge, Massachusetts, 1986.

- [14] J. Trulsen, P. Woskoboinikow, and R.J. Temkin. Circular waveguide mode converters at 140 GHz. Technical Report PSFC/RR-86-2, Massachusetts Institute of Technology, Plasma Fusion Center, Cambridge, MA, January 1986.
- [15] L.J. Chu. Calculation of the radiation properties of hollow pipes and horns. *J. Appl. Phys.*, 11:603–610, September 1940.
- [16] Richard Wylde. Private communication. Thomas Keating, Ltd., 2001.
- [17] David Chiasson. Private communication. Proteus Industries, Inc., February 2004.
- [18] K.E. Kreischer, B.G. Danly, P. Woskoboinikow, W.J. Mulligan, and R.J. Temkin. Frequency pulling and bandwidth measurements of a 140 GHz pulsed gyrotron. *Int. J. Elec.*, 57(6):851–862, December 1984.
- [19] M. Yeddulla, G.S. Nusinovich, and T.M. Antonsen. Start currents in an overmoded gyrotron. *Phys. Plasma*, 10(11):4513–4520, November 2003.
- [20] Kenneth E. Kreischer. Private communication, July 1999.
- [21] Frank C. de Lucia. Science and technology in the submillimeter region. *Optics and Photonics News*, 14(8):44–50, August 2003.
- [22] Daniel van der Weide. Applications and outlook for electronic terahertz technology. *Optics and Photonics News*, 14(4):48–53, April 2003.
- [23] Qing Hu, Benjamin S. Williams, Sushil Kumar, Hans Callebaut, and John L. Reno. Terahertz quantum cascade lasers based on resonant phonon scattering for depopulation. *Phil. Trans. R. Soc. Lond. A*, 362(1815):233–249, February 2004.
- [24] K.L. Felch, B.G. Danly, H.R. Jory, K.E. Kreischer, W. Lawson, B. Levush, and R.J. Temkin. Characteristics and applications of fast-wave gyrodevices. *Proceedings of the IEEE*, 87(5):752–81, May 1999.
- [25] R.W. Callis, W.R. Cary, S. Chu, J.L. Doane, R.A. Ellis, K. Felch, Y.A. Gorelov, H.J. Grunloh, J. Hosea, K. Kajiwara, J. Lohr, T.C. Luce, J.J. Peavy, R.I. Pinsky, D. Ponce, R. Prater, M. Shapiro, R.J. Temkin, and J.F. Tooker. Maturing ECRF technology for plasma control. *Nuclear Fusion*, 43(11):1501–1504, November 2003.
- [26] Toshitaka Idehara, Isamu Ogawa, Seitaro Mitsudo, Michael Pereyaslavets, Naoki Nishida, and Kiyohiko Yoshida. Development of frequency tunable, medium power gyrotrons (gyrotron FU series) as submillimeter wave radiation sources. *IEEE Trans. Plasma Sci.*, 27(2):340–354, April 1999.



- [27] V.S. Bajaj, C.T. Farrar, M.K. Hornstein, I. Mastovsky, J. Viereg, J. Bryant, B. Elena, K.E. Kreischer, R.J. Temkin, and R.G. Griffin. Dynamic nuclear polarization at 9 Tesla using a novel 250 GHz gyrotron microwave source. *J. Mag. Res.*, 160(2):85–90, February 2002.
- [28] T.L. Grimm, K.E. Kreischer, W.C. Guss, and R.J. Temkin. Experimental study of a megawatt 200-300 GHz gyrotron oscillator. *Fusion Technology*, 21(3):1648–1653, May 1992.
- [29] S. Mitsudo, Aripin T. Shirai, T. Matsuda, T. Kanemaki, and T. Idehara. High power, frequency tunable, submillimeter wave ESR device using a gyrotron as a radiation source. *Int. J. Infrared Millim. Waves*, 21(4):661–676, April 2000.
- [30] J.R. Sirigiri, K.E. Kreischer, J. Machuzak, I. Mastovsky, M.A. Shapiro, and R.J. Temkin. Photonic-band-gap resonator gyrotron. *Phys. Rev. Lett.*, 86(24):5628–5631, June 2001.
- [31] S. Spira-Hakkarainen, K.E. Kreischer, and R.J. Temkin. Submillimeter-wave harmonic gyrotron experiment. *IEEE Trans. Plasma Sci.*, 18(3):334–342, June 1990.
- [32] S. Fixler, J. Healey, T. Schultheiss, and J. Szot. Thermal analysis of cryogenically cooled linear accelerators. In *Proceedings of the 1989 IEEE Particle Accelerator Conference. Accelerator Science and Technology (Cat. No.89CH2669-0)*, pages 504–506. IEEE, Piscataway, NJ, USA, 1989.
- [33] R.Q. Twiss. Radiation transfer and the possibility of negative absorption in radio astronomy. *Australian J. Phys.*, 11:564–579, December 1958.
- [34] J. Schneider. Stimulated emission of radiation by relativistic electrons in a magnetic field. *Phys. Rev. Lett.*, 2(12):504–505, June 1959.
- [35] Andrei V. Gaponov. Interaction between electron fluxes and electromagnetic waves in waveguides. *Izv. VUZov Radiofizika (in Russian)*, 2:450–462, 1959.
- [36] K.D. Hong, G.F. Brand, and T. Idehara. A 150-600 GHz step-tunable gyrotron. *J. Appl. Phys.*, 74(8):5250–5258, October 1993.
- [37] N.I. Zaytsev, T.B. Pankratova, M.I. Petelin, and V.A. Flyagin. Millimeter- and submillimeter-wave gyrotrons. *Radio Eng. Electron. Phys. (USA)*, 19(5):103–107, May 1974.
- [38] T. Idehara, K. Yoshida, N. Nishida, I. Ogawa, M. L. Pereyaslavets, and T. Tatsu-kawa. CW operation of a submillimeter wave gyrotron (gyrotron FU IV) for high stability of the output frequency. *Int. J. Infrared Millim. Waves*, 19(6):793–801, June 1998.
- [39] T.B. Pankratova and G.S. Nusinovich. Experimental study of a diagnostic gyrotron. *Sov. Phys. Tech. Phys.*, 34(8):912–914, August 1989.

- [40] K.E. Kreischer, C. Farrar, R. Griffin, R. Temkin, and J. Viereg. A 250 GHz gyrotron for NMR spectroscopy. In *ICOPS 2000. IEEE Conference Record - Abstracts. 27th IEEE International Conference on Plasma Science*, page 198, New Orleans, LA, USA, June 2000. Plasma Sci. & Applications Committee of the IEEE Nucl. & Plasma Sci. Soc., IEEE, Piscataway, NJ, USA.
- [41] L.R. Becerra, G.J. Gerfen, B.F. Bellew, J.A. Bryant, D.A. Hall, S.J. Inati, R.T. Weber, S.Un, T.F. Prisner, A.E. McDermott, K.W. Fishbein, K.E. Kreischer, R.J. Temkin, D.J. Singel, and R.G. Griffin. A spectrometer for dynamic nuclear polarization and electron paramagnetic resonance at high frequencies. *J. Magn. Reson.*, 117:28–40, 1995.
- [42] J.S. Machuzak, P. Woskoboinikow, W.J. Mulligan, D.R. Cohn, M. Gerver, W. Guss, M. Mael, R.S. Post, and R.J. Temkin. 137-GHz gyrotron diagnostic for instability studies in Tara. *Review of Scientific Instruments*, 57(8):1983–1985, 1986.
- [43] V.S. Bajaj, M.K. Hornstein, R.J. Temkin, and R.G. Griffin. Dynamic nuclear polarization of biological systems at high magnetic fields. *To be submitted*, 2005.
- [44] R. E. Collin. *Foundations for microwave engineering*. IEEE Press, 2001.
- [45] K.E. Kreischer and R.J. Temkin. Linear theory of an electron cyclotron maser operating at the fundamental. *Int. J. Infrared Millim. Waves*, 1(2):195–223, June 1980.
- [46] Gregory S. Nusinovich. *Introduction to the Physics of Gyrotrons*. The Johns Hopkins University Press, Baltimore, 2004.
- [47] Julian Schwinger and D.S. Saxon. *Discontinuities in Waveguides*. Gordon and Breach, New York, 1968.
- [48] J. Mark Baird. Gyrotron theory. In Victor L. Granatstein and Igor Alexeff, editors, *High-Power Microwave Sources*, chapter 4, pages 103–184. Artech House, Boston, 1987.
- [49] Francis F. Chen. *Introduction to Plasma Physics and Controlled Fusion*, volume 1 of *Plasma Physics*, chapter 7, pages 225–285. Plenum Press, New York, second edition, 1984.
- [50] K.R. Chu and J.L. Hirshfield. Comparative study of the axial and azimuthal bunching mechanisms in electromagnetic cyclotron instabilities. *Phys. Fluids*, 21(3):461–466, March 1978.
- [51] Kwo Ray Chu, Adam T. Drobot, Harold Hwaling Szu, and Phillip Sprangle. Theory and simulation of the gyrotron traveling wave amplifier operating at cyclotron harmonics. *IEEE Trans. Microwave Theory Techn.*, 28(4):313–317, April 1980.

- [52] A.W. Fliflet. Linear and non-linear theory of the doppler-shifted cyclotron resonance maser based on TE and TM waveguide modes. *Int. J. Electron.*, 61(6):1049–1080, December 1986.
- [53] K.R. Chu and A.T. Lin. Gain and bandwidth of the gyro-TWT and CARM amplifiers. *IEEE Trans. Plasma Sci.*, 16(2):90–104, April 1988.
- [54] E. S. Weibel. Spontaneous growing transverse waves in a plasma due to an anisotropic velocity distribution. *Phys. Rev. Letters*, 2(3):83–84, February 1959.
- [55] Burton D. Fried. Mechanism for instability of transverse plasma waves. *Phys. Fluids*, 2(3):337, May 1959.
- [56] G.S. Nusinovich and R.E. Erm. Efficiency of the CRM-monotron with Gaussian axial structure of the high-frequency field. *Elektron. Tekh., Ser. 1, Elektron. SVCh*, 55, 1972.
- [57] A.W. Fliflet, M.E. Read, K.R. Chu, and R. Seeley. A self-consistent field theory for gyrotron oscillators: application to a low Q gyromonotron. *Int. J. Electron.*, 53(6):505–521, December 1982.
- [58] B.G. Danly and R.J. Temkin. Generalized nonlinear harmonic gyrotron theory. *Phys. Fluids*, 29(2):561–567, February 1986.
- [59] B.G. Danly and R.J. Temkin. Generalized nonlinear harmonic gyrotron theory. Plasma Fusion Center Report PFC/JA-85-6, Massachusetts Institute of Technology, Plasma Science and Fusion Center, Cambridge, Massachusetts, April 1985.
- [60] K.E. Kreischer and R.J. Temkin. Mode excitation in a gyrotron operating at the fundamental. *Int. J. Infrared Millim. Waves*, 2(2):175–196, March 1981.
- [61] G.S. Nusinovich. Toward a theory for optimizing the parameters of short wavelength gyrotrons. *Elektronnaya Tekhnika, Ser. Elektronika SHF*, 1(325), 1981.
- [62] J. J. Sakurai. *Modern Quantum Mechanics*. Addison-Wesley, 1994.
- [63] M. Petelin. One century of cyclotron radiation. *IEEE Trans. on Plasma Sci.*, 27(2):294–302, April 1999.
- [64] R. J. Temkin. Quantum mechanical formulation of gyrotron theory. Lecture series at the Massachusetts Institute of Technology.
- [65] Arne W. Fliflet and Michael E. Read. Use of weakly irregular waveguide theory to calculate eigenfrequencies, Q values, and RF field functions for gyrotron oscillators. *Int. J. Electron.*, 51(4):475–484, October 1981.
- [66] S.N. Vlasov, G.M. Zhislin, I.M. Orlova, M.I. Petelin, and G.G. Rogacheva. Irregular waveguides as open resonators. *Radiophys. Quantum Electron.*, 12(8):972–978, 1969.

- [67] S.N. Vlasov, L.I. Zagryadskaya, and I.M. Orlova. Open coaxial resonators for gyrotrons. *Radio Eng. Electron. Phys.*, 21(7):1485–1492, July 1976.
- [68] L.A. Vainshtein. *Open Resonators and Open Waveguides*, volume 2 of *Golem series in electromagnetics*. Golem Press, Boulder, Colorado, 1969.
- [69] B.Z. Katsenelenbaum. *Theory of Irregular Waveguides with Slowly Varying Parameters (in Russian)*. Izd-vo Akademii nauk SSSR, Moscow, 1961.
- [70] G. Reiter. Generalized telegraphist’s equation for waveguides of varying cross sections. *Proc. Instrn. Elec. Eng. Part B. Electronic and Communication Engineering*, 106(13):54–57, January 1959.
- [71] Francis Schneid. *Theory and Problems of Numerical Analysis. The Art of Computer Programming*. McGraw-Hill, New York, 1968.
- [72] J.R. Sirigiri. Starting current, ver. 1.0.1. Computer code based on linear theory, December 2003.
- [73] M. Botton, T.M. Antonsen, B. Levush, K.T. Nguyen, and A.N. Vlasov. MAGY: A time-dependent code for simulation of slow and fast microwave sources. *IEEE Trans. Plasma Sci.*, 26(3):882–892, June 1998.
- [74] W.B. Herrmannsfeldt. EGUN: An electron optics and gun design program. Technical Report SLAC-0331 UC-28, Stanford Linear Accelerator Center, Stanford, California, October 1988.
- [75] J. Cavanagh, W.J. Fairbrother, A.G. Palmer III, and N.J. Skelton. *Protein NMR Spectroscopy: Principles and Practices*. Academic Press, 1996.
- [76] D.A. Hall, D.C. Maus, G.J. Gerfen, S.J. Inati, L.R. Becerra, F.W. Dahlquist, and R.G. Griffin. Polarization-enhanced NMR spectroscopy of biomolecules in frozen solution. *Science*, 276:930–932, May 1997.
- [77] Joseph P. Hornak. *The Basics of NMR*. <http://www.cis.rit.edu/htbooks/nmr/>, Center for Imaging Science, Rochester Institute of Technology, Rochester, NY 14623-5604, IV edition, 2004.
- [78] C. Slichter and T. Carver. Experimental verification of the Overhauser nuclear polarization effect. *Phys. Rev.*, 102(4), May 1958.
- [79] A. Abragam and W. Proctor. *Compt. Rend.*, 246:2253, 1958.
- [80] R. A. Wind, M. J. Duijvestijn, C. Van Der Lugt, A. Manenschijn, and J. Vriend. Applications of dynamic nuclear polarization in  $^{13}\text{C}$  NMR in solids. *Progress in NMR Spectroscopy*, 17(1):33–57, 1985.
- [81] L.R. Becerra, G.J. Gerfen, R.J. Temkin, D.J. Singel, and R.G. Griffin. Dynamic nuclear polarization with a cyclotron resonance maser at 5 T. *Phys. Rev. Lett.*, 71(21):3561–3564, November 1993.

- [82] G.J. Gerfen, R.J. Temkin, and D.J. Singel. High frequency (140 GHz) dynamic nuclear polarization: Polarization transfer to a solute in frozen aqueous solution. *J. Chem. Phys.*, 102(24):9494–9497, June 1995.
- [83] V. Weis, M. Bennati, M. Rosay, J.A. Bryant, and R.G. Griffin. High-field DNP and ENDOR with a novel multiple-frequency resonance structure. *J. Magn. Reson.*, 140:293–299, 1999.
- [84] M. Rosay. *Sensitivity-Enhanced Nuclear Magnetic Resonance of Biological Solids*. PhD dissertation, Massachusetts Institute of Technology, Department of Chemistry, September 2001.
- [85] S. Spira-Hakkarainen. *Submillimeter Wave Harmonic Gyrotron*. PhD dissertation, Massachusetts Institute of Technology, Department of Nuclear Engineering, September 1989.
- [86] Dennis Froman and Gary Shelmire. Measuring laser output. <http://www.scientech-inc.com/laserpowernotes.htm>.
- [87] K.E. Kreischer, J.B. Schutkeker, B.G. Danly, W.J. Mulligan, and R.J. Temkin. High efficiency operation of a 140 GHz pulse gyrotron. *Int. J. Elec.*, 57(6):835–850, December 1984.
- [88] A. Hadni. Pyroelectricity and pyroelectric detectors. In Kenneth J. Button, editor, *Submillimeter Techniques*, number 3 in Infrared and Millimeter Waves, chapter 3, pages 111–180. Academic Press, New York, 1980.
- [89] P. M. Borchard. Design of a data acquisitioning system for near- and far field scans of the gyrotron. Bachelor’s project, Massachusetts Institute of Technology, Mechanical Engineering Department, May 1993.
- [90] Spiricon, Inc., 2600 North Main, Logan, UT 84341. *Pyrocam III Enhanced Pyroelectric Camera for IR and UV Laser Beam Diagnostics and Thermal Imaging*, August 2003.
- [91] Eric J. Lerner. Twenty watts of terahertz. *The Industrial Physicist*, 9(2):9, April 2003.
- [92] V.S. Bajaj, M.K. Hornstein, K.E. Kreischer, P.P. Woskov, R.J. Temkin, and R.G. Griffin. A long-term, stable, CW 250 GHz gyrotron with low second harmonic starting currents. *To be submitted*, 2005.
- [93] Rocoil Precision Rogowski Coils. How do Rogowski coils work? <http://www.rocoil.cwc.net/principle.htm>.
- [94] Stanford Research Systems, 1290-D Reamwood Ave., Sunnyvale, CA 94089. *Operating Manual and Programming Reference Models RGA100, RGA200, and RGA300 Residual Gas Analyzer*, revision 1.5 edition, February 2004.

- [95] Duniway Stockroom Corp., 1305 Space Park Way, Mountain View, CA 94043. *Instruction Manual Terranova Model 741 Ion Pump Power Supply*, rev081302sr edition, 2000.
- [96] Measuring temperature with an RTD or thermistor. <http://www.ni.com>, 2003.
- [97] Stanford Research Systems, 1290-D Reamwood Ave., Sunnyvale, CA 94089. *MODEL SR830 DSP Lock-In Amplifier*, revision 2.1 edition, July 2004.
- [98] William Mulligan. Private communication, November 2004.
- [99] I.G. Zarnitsina and G.S. Nusinovich. Stability of single-mode self-excited oscillations in a gyrotron. *Radiophys. Quantum Electron.*, 17(12):1418–1424, December 1974.
- [100] Spellman High Voltage Electronics Corporation, 475 Wireless Boulevard, Hauppauge, NY 11788. *Instruction Manual DF3 Series High Voltage Power Supply*, rev b edition, March 2002.
- [101] K.E. Kreischer, T.L. Grimm, W.C. Guss, and R.J. Temkin. The operation of a megawatt gyrotron in the submillimeter wave region. In *International Electron Devices Meeting 1989. Technical Digest (Cat. No.89CH2637-7)*, pages 751–754, Washington, DC, USA, December 1989. IEEE, New York, NY, USA.
- [102] Edward M. Purcell. *Electricity and Magnetism*, volume 2 of *Berkeley physics course*. McGraw-Hill, New York, 1985.
- [103] S.N. Vlasov and I.M. Orlova. Quasioptical transformer which transforms the waves in a waveguide having circular cross section into a highly directional wave beam. *Radiofizika*, 17:115–119, 1974.
- [104] J.W. Lamb. Miscellaneous data on materials for millimetre and submillimetre optics. *Int. J. Infrared Millim. Waves*, 17(12):1997–2034, December 1996.
- [105] H.A. Haus. *Waves and Fields in Optoelectronics*. Prentice-Hall, Englewood Cliffs, New Jersey, 1984.
- [106] V.S. Bajaj. Private communication, 2002.
- [107] Graham C. Goodwin, Stefan F. Graebe, and Mario E. Salgado. *Control System Design*. Prentice Hall PTR, 2001.
- [108] T. Idehara, T. Tatsukawa, I. Ogawa, T. Mori, H. Tanabe, S. Wada, G.F. Brand, and M.H. Brennan. Competition between fundamental and second-harmonic operations in a submillimeter wave gyrotron. *Appl. Phys. Lett.*, 58(15):1594–1596, April 1991.
- [109] T. Idehara and Y. Shimizu. Mode cooperation in a submillimeter wave gyrotron. *Phys. Plasmas*, 1(10):3145–3147, October 1994.

- [110] K.E. Kreisler, T. Kimura, B.G. Danly, and R.J. Temkin. High-power operation of a 170 GHz megawatt gyrotron. *Phys. Plasmas*, 4(5):1907–1914, May 1997.
- [111] J. Zhao, G. Nusinovich, H. Guo, J.C. Rodgers, and V.L. Granatstein. Axial mode locking in a harmonic-multiplying, inverted gyrotwystron. *IEEE Trans. Plasma Sci.*, 28(3):597–605, June 2000.
- [112] T.H. Chang, K.F. Pao, and K.R. Chu. Self-consistent effects on the starting current of gyrotron oscillators. *Int. J. Infrared Millim. Waves*, 24(9):1415–1420, September 2003.
- [113] M.K. Hornstein, V.S. Bajaj, R.G. Griffin, and R.J. Temkin. Continuous-wave operation of a second harmonic gyrotron oscillator at 460 GHz. *To be submitted*, 2005.
- [114] V.A. Flyagin, A.G. Luchinin, and G.S. Nusinovich. Submillimeter-wave gyrotrons: theory and experiment. *Int. J. Infrared Millim. Waves*, 4(4):629–637, July 1983.
- [115] M. Thumm. State-of-the-art of high power gyro-devices and free electron masers update 2003. Wissenschaftliche Berichte FZKA 6957, Forschungszentrum Karlsruhe in der Helmholtz-Gemeinschaft, Forschungszentrum Karlsruhe GmbH, Postfach 36 40, 76021 Karlsruhe, February 2004.
- [116] G.S. Nusinovich. Review of the theory of mode interaction in gyrodevices. *IEEE Trans. Plasma Sci.*, 27(2):313–326, April 1999.
- [117] E.A.J. Marcatili and R.A. Schmeltzer. Hollow metallic and dielectric waveguides for long distance optical transmission and lasers. *The Bell Syst. Tech. J.*, 43(4):1783–1809, July 1964.
- [118] Christopher C. Gregory and James A. Harrington. Attenuation, model, and polarization properties of  $n < 1$ , hollow dielectric waveguides. *Applied Optics*, 32(27):5302–5309, September 1993.
- [119] M.N. Afsar. Precision millimeter-wave measurements of complex refractive index, complex dielectric permittivity, and loss tangent of common polymers. *IEEE Trans. Instrum. Meas.*, 36(2):530–536, June 1987.
- [120] M. Halpern, H. P. Gush, E. Wishnow, and V. De Cosmo. Far infrared transmission of dielectrics at cryogenic and room temperatures: glass, fluorogold, eccosorb, stycast and various plastics. *Appl. Opt.*, 25(4):565–570, February 1986.
- [121] Richard Scrivens. CERN Spiricon: The first pictures. <http://scrivens.home.cern.ch/scrivens/lis/misc/mo/10109701.HTML>, October 1997.

- [122] G.P. Saraph, T.M. Antonsen, G.S. Nusinovich, and B. Levush. Nonlinear theory of stable, efficient operation of a gyrotron at cyclotron harmonics. *Phys. Fluids B*, 5(12):4473–4485, December 1993.
- [123] G.S. Nusinovich, O.V. Sinitsyn, L. Velikovich, M. Yeddulla, T. M. Antonsen, A.N. Vlasov, S. Cauffman, and K. Felch. Start-up scenarios in high-power gyrotrons. *IEEE Trans. Plasma Sci.*, 32(3):841–852, June 2004.
- [124] Jeffrey Robert Vieregg. A CW 250 GHz gyrotron oscillator for use in dynamic nuclear polarization. Bachelor’s project, Massachusetts Institute of Technology, Department of Physics, May 2000.
- [125] G.F. Brand, N.G. Douglas, M. Gross, J.Y.L. Ma, and Chen Zhiyi. Frequency detuning measurements in a low-power gyrotron. *Int. J. Infrared Millim. Waves*, 4(6):891–900, November 1983.
- [126] K. Azar, J.R. Benson, and V.P. Manno. Liquid crystal imaging for temperature measurement of electronic devices. In *Proceedings, Seventh Annual IEEE Semiconductor Thermal Measurement and Management Symposium (Cat. No.91CH2972-8)*, pages 23–33, Phoenix, AZ, February 1991. IEEE, New York, NY, USA.
- [127] D.J. Farina. Making surface temperature measurements using liquid crystal thermography. *Electronics Cooling*, 1(2):10–15, 1995.
- [128] Y. Carmel, K.R. Chu, M.E. Read, V.L. Granatstein, G. Faillon, P. Boulanger, E. Kammerer, and G. Mourier. A technique to identify electromagnetic modes in oversize waveguides. *IEEE Transactions on Microwave Theory and Techniques*, 32(11):1493–1495, November 1984.
- [129] O. Dumbrajs and G.S. Nusinovich. Effect of technical noise on radiation linewidth in free-running gyrotron oscillators. *Phys. Plasmas*, 4(5):1413–1423, May 1997.
- [130] G.S. Nusinovich and O. Dumbrajs. Technical noise in gyroklystrons and phase-locked gyrotron oscillators. *Phys. Plasmas*, 4(5):1424–1433, May 1997.
- [131] J.L. Doane. Propagation and mode coupling in corrugated and smooth-walled circular waveguides. In K.J. Button, editor, *Infrared and Millimeter Waves*, number 13, chapter 5. Academic Press, New York, 1985.
- [132] R.W. Callis, W.P. Cary, R. Ellis, Y.A. Gorelov, H.J. Grunloh, J. Lohra, J.J. Peavy, R.I. Pinsky, D. Ponce, and R. Prater. The 6 MW, 110 GHz ECH system for the DIII-D tokamak. In *IEEE Conference Record - Abstracts. 2002 IEEE International Conference on Plasma Science (Cat. No.02CH37340)*, page 294, Banff, Alta., Canada, May 2002. IEEE, Piscataway, NJ, USA.



- [133] F. Leuterer, M. Beckmann, H. Brinkschulte, F. Monaco, M. Munich, F. Ryter, H. Schutz, L. Empacher, G. Gantenbein, W. Forster, W. Kasperek, P. Schuller, K. Schworer, A. Borchegowski, A. Fix, V. Illin, L. Popov, V. Sigalaev, and E. Tai. Experience with the ECRH system of ASDEX-Upgrade. *Fusion Engineering and Design*, 53(1-4):485–489, 2001.
- [134] H. Idei, S. Kubo, T. Shimosuma, M. Sato, K. Ohkubo, Y. Yoshimura, Y. Takita, S. Kobayashi, S. Ito, Y. Mizuno, K. Tsumori, K. Ikeda, T. Notake, T. Watari, O. Kaneko, A. Komori, H. Yamada, P.C. de Vries, M. Goto, K. Ida, S. Inagaki, S. Kado, K. Kawahata, T. Kobuchi, T. Minami, J. Miyazawa, T. Morisaki, S. Morita, S. Murakami, S. Muto, Y. Nagayama, H. Nakanishi, K. Narihara, B.J. Peterson, S. Sakakibara, H. Sasao, K. Sato, K. Tanaka, Y. Takeiri, K.Y. Watanabe, I. Yamada, O. Motorjima, and M. Fujiwara. Electron cyclotron heating scenario and experimental results in LHD. *Fusion Engineering and Design*, 53:329–336, 2001.
- [135] J.L. Doane, H. Ikezi, and C.P. Moeller. Quasi-optic components in oversized corrugated waveguide for millimeter-wave transmission systems. In T.J. Parker and S.R.P. Smith, editors, *Proc. 23rd Int. Conf. Infrared and Millimeter-Waves*, Colchester, United Kingdom, 1998.
- [136] A. Simonetto, G. Solari, F. Gandini, G. Granucci, V. Muzzini, and C. Sozzi. Directional couplers-polarimeters for high-power corrugated waveguide transmission lines. *Fusion Science and Technology*, 40(3):247–252, November 2001.
- [137] C.P. Moeller, J. Lohr, and J.L. Doane. The measured performance of a millimeter wave beam splitter (in gyrotrons). In R.J. Temkin, editor, *Conference Digest. Twenty Seventh International Conference on Infrared and Millimeter Waves (Cat. No.02EX561)*, pages 307–308, San Diego, CA, September 2002. General Atomics;PSFC;IEEE, IEEE, Piscataway, NJ, USA.
- [138] P.P. Woskov and C.H. Titus. Graphite millimeter-wave waveguide and mirror for high temperature environments. *IEEE Transactions on Microwave Theory and Techniques*, 43(12):2684–2688, December 1995.
- [139] Max Born and Emil Wolf. *Principles of Optics*, section 7.6. Pergamon Press, New York, fifth edition, 1975.
- [140] G.T. Ruck, D.E. Barrick, W.D. Stuart, and C.K. Krichbaum. *Radar Cross Section Handbook*, volume 1, chapter 4. Plenum Press, New York, 1970.
- [141] R.H. Dicke. The measurement of thermal radiation at microwave frequencies. *Rev. Sci. Instrum.*, 17(7):268–275, 1946.
- [142] Matt Young. *Optics and Lasers: including fibers and optical waveguides*, chapter 6. Advanced texts in Physics. Springer, New York, fifth edition, 2000.

- [143] M.E. Tiuri. In J.D. Krauss, editor, *Radio Astronomy*, chapter 7. McGraw-Hill, New York, 1970.
- [144] F.B. Foote, D.T. Hodges, and H.B. Dyson. Calibration of power and energy meters for the far infrared/near millimeter wave spectral region. *Int. J. Infrared Millim. Waves*, 2(4):773–782, July 1981.
- [145] M.A. Shapiro. Private communication, February 2002.
- [146] B.Z. Katsenelenbaum, L. Mercader del Rio, M. Pereyaslavets, M. Sorolla Ayza, and M. Thumm. *Theory of Nonuniform Waveguides*, volume 44 of *Electromagnetic Waves*. The Institution of Electrical Engineers, London, United Kingdom, 1998.
- [147] C. Moeller. Mode converters used in the Doublet III ECH microwave system. *Int. J. Electron.*, 53(6):587–593, 1982.
- [148] S. Filchenkov. Private communication. Instit. Applied Physics, N. Novgorod, Russia.
- [149] P.P. Woskov. Private communication, February 2002.
- [150] M. Rosay. Private communication, January 2002.
- [151] D. Wagner, M. Thumm, W. Kasperek, G. A. Müller, and O. Braz. Prediction of TE-, TM-, and hybrid-mode transmission losses in gaps of oversized waveguides using a scattering matrix code. *Int. J. Infrared Millimeter Waves*, 17(6):1071–1081, 1996.
- [152] Robert E. Collin. *Field Theory of Guided Waves*, section 5.4, pages 349–354. The IEEE/OUP Series on Electromagnetic Wave Theory. IEEE Press, second edition, 1991.